UNIVERSITY OF CALGARY

Broadband Waveguide Quantum Memory for Quantum Communication

by

Erhan Saglamyurek

A THESIS

SUBMITTED TO THE FACULTY OF GRADUATE STUDIES

IN PARTIAL FULFILLMENT OF THE REQUIREMENTS FOR THE

DEGREE OF DOCTOR OF PHILOSOPHY

DEPARTMENT OF PHYSICS AND ASTRONOMY
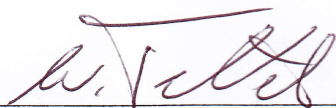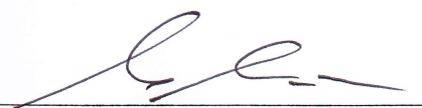

CALGARY, ALBERTA

JANUARY, 2013

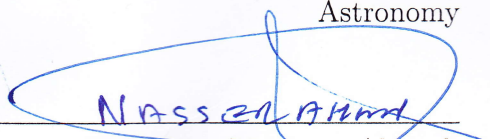# UNIVERSITY OF CALGARY

FACULTY OF GRADUATE STUDIES

The undersigned certify that they have read, and recommend to the Faculty of Graduate Studies for acceptance, a thesis entitled "Broadband Waveguide Quantum Memory for Quantum Communication" submitted by Erhan Saglamyurek in partial fulfillment of the requirements for the degree of DOCTOR OF PHILOSOPHY.
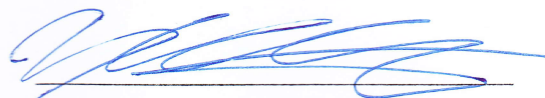
Dr. Wolfgang Tittel
Department of Physics and
Astronomy

Dr. Nasser Moazzen-Ahmadi
Department of Physics and
Astronomy

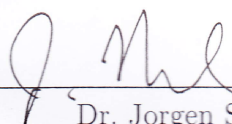Dr. Jorgen S. Nielsen
Department of Electrical and
Computer Engineering

Dr. Karl–Peter Marzlin
Department of Physics,
St Francis Xavier University
Antigonish, Nova Scotia

Dr. W. Randall Babbitt
Department of Physics,
Montana State University
Bozeman, Montana

12/17/2013
Date

Abstract

Quantum communication founds on the possibility to encode quantum states into photons and allows, for instance, the provable secure distribution of encryption keys. Despite a lot of progress during the past two decades, quantum communication still faces a distance barrier, which can be overcome by quantum repeaters whose currently most challenging ingredient is a memory for quantum states of light. In addition to robustness and ease of use, the requirements for such a quantum memory include high fidelity quantum state storage and the preservation of entanglement, sufficiently long storage time with on-demand recall, high efficiency, large bandwidth, and high multimode capacity. Six years ago, some of these properties had already been demonstrated using atomic vapor. However, practical solid-state memories were virtually unexplored in view of quantum state storage.

The main goal of this thesis was to realize a solid-state quantum memory for light with emphasis on meeting requirements for long distance quantum communication. First, we identified a potential material candidate, a thulium doped lithium niobate waveguide, and conducted spectroscopic investigations to assess its suitability for quantum state storage using a photon-echo type approach. Next, we demonstrated that our storage device is suitable for high fidelity quantum state storage and for the storage of photonic entanglement, and that its large spectral multimode capacity allows for on-demand selective recall in conjunction with standard spectral filters and frequency shifters. In addition, by performing two-photon interference experiments and Bell-state measurements, we found that our memory preserves not only quantum information, but, more generally, the entire photonic wave function, which further confirms its suitability for quantum repeaters as well as for linear optics quantum computers. Finally, we showed that our integrated device also allows for general temporal and spectral manipulation of individual quantum optical pulses, which paves the way towards on-chip quantum optical processors. While more work remains to be done, in particular to

improve memory efficiency and storage time, the large number of achievements, together with known ways to overcome the remaining obstacles, makes us confident that a quantum memory suitable for quantum repeaters will soon be built.

List of published papers and papers to be submitted

1. "Spectroscopic investigations of a Ti:Tm:LiNbO$_3$ waveguide for photon-echo quantum memory", N. Sinclair, E. Saglamyurek, M. George, R. Ricken, C. La Mela, W. Sohler, W. Tittel, *Journal of Luminescence*, Volume **130**, Issue 9, September 2010, Pages 1586–1593

2. "Broadband waveguide quantum memory for entangled photons", E. Saglamyurek, N. Sinclair, J. Jin, J. A. Slater, D. Oblak, F. Bussières, M. George, R. Ricken, W. Sohler and W. Tittel, *Nature*, **469** (7331): 512–515, 12 January 2011.

3. "Conditional detection of pure quantum states of light after storage in a Tm-doped waveguide", E. Saglamyurek, N. Sinclair, J. Jin, J. A. Slater, D. Oblak, F. Bussières, M. George, R. Ricken, W. Sohler and W. Tittel, *Physical Review Letters*, **108(8)**: 083602, 22 February 2012,

4. "Controllable-dipole quantum memory", K. Heshami, A. Green, Y. Han, A. Rispe, E. Saglamyurek, N. Sinclair, W. Tittel and C. Simon, *Physical Review A* **86**: 013813, 9 July 2012.

5. "Two-photon interference of weak coherent laser pulses recalled from separate solid-state quantum memories", J. Jin, E. Saglamyurek, N. Sinclair, J. A. Slater, D. Oblak, M. George, R. Ricken, W. Sohler and W. Tittel, *(To be submitted)*

6. "A Frequency multimode quantum memory featuring on-demand recall", N. Sinclair, E. Saglamyurek, H. Mallahzadeh, J. A. Slater, D. Oblak, M. George, R. Ricken, W. Sohler and W. Tittel *(In preparation)*

7. "Towards on-chip quantum optical processor using a waveguide quantum memory", E. Saglamyurek, N. Sinclair, D. Oblak, M. George, R. Ricken, W. Sohler and W. Tittel *(To be submitted)*

8. "State transformation in photon-echo quantum memory", A. Delfan Abazari, E. Saglamyurek, R. Ricken, W. Sohler, C. La Mela and W. Tittel *arXiv.org*:quant-ph 0910.2457, 2009.

Acknowledgements

First of all, I would like to thank my wife, Fatma, for her sacrifice, patience and support during my studies. I cannot express how thankful I am to her in words. I thank my sons, Mustafa and Enes, who always kept me motivated, for their patience as I could not spend much time with them when things were busy in the lab. I am truly indebted and thankful to my supervisor, Dr. Wolfgang Tittel, for giving me the opportunity to join his group as well as his guidance and support from the very beginning to the very end of my PhD studies. I hope that, during the last six years, I absorbed at least a little of his endless energy, practical thinking, deep insight, and intuition for solving problems.

I would like to thank all my co-workers for their contributions and help. More specifically, starting with the quantum memory team members, I am very grateful to Dr. Cecilia Le Mela, with whom I started building the lab from scratch, for guiding and motivating me and for her friendship to my family and me. I would like to thank my oldest lab-buddy, Neil Sinclair, for his help and support in this long journey and for his willingness to learn new things together. I am truly thankful to Dr. Daniel Oblak for sharing his experience and knowledge with me and for spending his precious time to read and help shape this thesis. I would like to thank Dr. Morgan Hedges, who has been my one of "on-demand consultants" while writing this thesis, for sharing his original ideas with me and for helping me to gain a better understanding of quantum memories.

From the entanglement team, I am very grateful to Josh Slater, who has been my other on-demand consultant during the last six years, for helping me understand the "quantum world" with his deep knowledge and with his teaching skills and, more importantly, for his exceptional help in every step of preparing this thesis right up until the last moment. I would like to thank Jeongwan Jin, who has been one of the people I enjoy working and talking with a lot, for his sincere support during my studies. His patient, open-minded and polite

Table of Contents

List of Tables

List of Figures and Illustrations

List of Abbreviations

Abbreviation	Definition
AFC	Atomic Frequency Comb
AOM	Acousto Optic Modulator
APD	Avalanche Photo Diode
AWG	Arbitrary Waveform Generator
BS	Beam Splitter
BSM	Bell-state Measurement
CHSH	Clauser-Horne-Shimony-Holt
CRIB	Controlled Reversible Inhomogeneous Broadening
CW	Continuous Wave
DLCZ	Duan-Lukin-Cirac-Zoller
EIT	Electromagnetically Induced Transparency
FWHM	Full Width at Half Maximum
GEM	Gradient Echo Memory
HOM	Hong-Ou-Mandel
LVT	Local Variable Theory
NV	Nitrogen Vacancy
PBS	Polarizing Beam Splitter
QED	Quantum Electrodynamics
Qubit	Quantum bit
RE	Rare-Earth
RF	Radio Frequency
SPDC	Spontaneous Parametric Down Conversion
TDC	Time-to-Digital Convertor

Chapter 1

Overview

Quantum communication is founded on the ability to encode quantum states into photons and transmit these photons between distant parties [1]. Quantum cryptography is currently the main application of quantum communication; it promises unconditionally secure transmission of information [2]. The main problem of existing quantum communication technologies is limited transmission distances, which is due to the loss across fiber-optics communication links in combination with the quantum no-cloning theorem, precluding one from perfectly copying and reproducing arbitrary quantum information as can be done in classical communication systems. The solution to this problem is to use quantum repeaters [3, 4]. The main idea behind this technology is to divide a communication channel into short links and use quantum entanglement to distribute quantum information between the links. Key ingredients in quantum repeaters are optical quantum memories, which synchronize the flow of quantum data by storing entanglement in such a way that it can be retrieved on demand [5, 6, 7]. The use of quantum memories is not limited to quantum communications; they are key hardware for linear optical quantum computers and potential tools for quantum metrology applications and fundamental tests of quantum mechanics [7].

This thesis details experimental efforts to build a quantum memory for light that satisfies the requirements for long distance quantum communication. It covers the steps from material spectroscopy to proof-of-principle demonstrations of key features of a quantum memory.

The structure of the thesis is as follows: First, I begin with introducing the basic elements of quantum communication. Next, I discuss the motivation to build a quantum memory and give an overview of quantum memory approaches. In the fourth chapter, I explain the basic principles of the Atomic Frequency Comb (AFC) quantum memory protocol, which is at the

core of the experimental implementations realized in this thesis. The fifth chapter covers spectroscopic investigations of a novel quantum memory material –a Tm:LiNbO$_3$ waveguide. In the sixth chapter, I present how we implement a broadband AFC in this memory material. Chapter seven reports the storage of single-photon-level pulses and eventually quantum information in our quantum memory. The following chapter is devoted to the experimental demonstration of storage of entangled photons. In chapter nine, two-photon interference, including a Bell state measurement, with optical pulses retrieved from two separate quantum memories is demonstrated. In the next chapter, the frequency multimode storage capabilities of our memory device is explored and, based on our experimental demonstration, the possibility of developing a new quantum repeater architecture with frequency-multimode AFC quantum memories is discussed. In chapter eleven, combining quantum state storage and coherent manipulation of quantum optical pulses within a memory is demonstrated. In the last two chapters, I draw conclusions and give an update on progress and future work.

Chapters 5, 7, 8, 9 and 11 contain published papers or papers close to being submitted. The requirement for each manuscript to be self-contained necessarily leads to some topical overlap.

This work would not have been possible without the collaboration of many people. In particular, this includes the members of our group's quantum memory team (myself, Neil Sinclair, Hassan Mallahzadeh, Dr. Daniel Oblak, Dr. Cecilia La Mela) and entanglement team (Josh A. Slater, Jeongwan Jin and Dr. Félix Bussières) as well as members from the group of Prof. Wolfgang Sohler at the University of Paderborn in Germany who fabricated the Tm:LiNbO$_3$ waveguides. My contributions to the investigations are detailed at the beginning of each chapter.

Chapter 2

Basic Elements of Quantum Communication

Quantum communication is the art of transferring quantum states from one place to another [1], and photons are naturally suited to carry quantum states. Thus, preparing, transmitting and measuring quantum states of photons are essential elements of quantum communication. In this section, I will briefly review these elements to provide a background for discussing the role of quantum memories in quantum communication. For a complete and detailed review, numerous resources such as [8, 9, 10] can be found in the literature.

2.1 Quantum Information (Qubits)

Quantum information is the quantum counterpart of classical information. Classical information is formed by the combination of bits that are the elementary piece of information. A classical bit can only be in one of two well-defined states, which are usually represented by "0" and "1". However a quantum bit, referred to as qubit, can also be simultaneously in both of these states, which is known as quantum superposition. Quantum superposition is at the heart of quantum mechanics and an essential ingredient of quantum information technologies.

A general representation of the state of a qubit is given by

$$|\psi\rangle = \alpha |0\rangle + \beta |1\rangle \tag{2.1}$$

where α and β are complex numbers, and called probability amplitudes for states $|0\rangle$ and $|1\rangle$, respectively[1]. One convenient way for visualizing a qubit state is to use the Bloch sphere representation shown in Fig 2.1. Any point on the Bloch sphere is defined by angles

---

[1] $|\alpha|^2$ and $|\beta|^2$ are probabilities for finding the qubit during a measurement in state $|0\rangle$ or $|1\rangle$, respectively. Note that $|\alpha|^2 + |\beta|^2 = 1$.
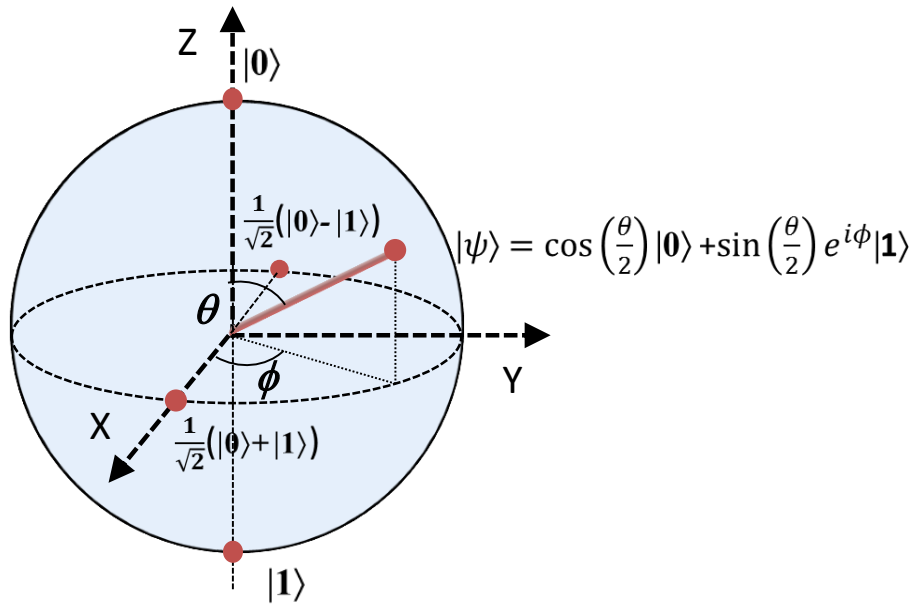
Figure 2.1: **Bloch sphere representation of a qubit state:** Any arbitrary pure state $|\psi\rangle$ is represented by a point, defined by angles θ and ϕ, on the Bloch sphere. Pure states represented by diametral (opposing) points on the Bloch sphere are orthogonal, e.g. $|0\rangle$ and $|1\rangle$, or $\frac{1}{\sqrt{2}}(|0\rangle + |1\rangle)$ and $\frac{1}{\sqrt{2}}(|0\rangle - |1\rangle)$.

θ and ϕ and corresponds to a pure quantum state [2]. In this representation, the probability amplitudes for a general qubit state are expressed by $\cos(\theta/2) \equiv \alpha$ and $e^{i\phi}\sin(\theta/2) \equiv \beta$, where θ and ϕ are angles defined with respect to the +Z-axis and +X-axis, respectively. ϕ describes the phase difference between the states $|0\rangle$ and $|1\rangle$ and makes qubits different from classical bits. Using these parameters, a qubit state is written in the following form:

$$|\psi\rangle = \cos\left(\frac{\theta}{2}\right)|0\rangle + e^{i\phi}\sin\left(\frac{\theta}{2}\right)|1\rangle \tag{2.2}$$

For example, the points on the poles of the Bloch sphere correspond to states $|0\rangle$ and $|1\rangle$, while the equator points represent equal superpositions of these states. The pair of states that are represented on each side of any defined axis through the center of the Bloch sphere, for example $|0\rangle$ and $|1\rangle$, or $\frac{1}{\sqrt{2}}(|0\rangle + |1\rangle)$ and $\frac{1}{\sqrt{2}}(|0\rangle - |1\rangle)$, are orthogonal states. A set of

---

[2]The points inside the Bloch sphere correspond to mixed states.

orthogonal states forms a basis for any qubit state, meaning that any qubit state can be written in terms of these states.

2.1.1 Preparation of Photonic Qubits

The preparation of photonic qubits consists of two steps. In the first step, individual photons need to be generated. The generation of single photons can be realized with various techniques such as using single atoms and ions, or single quantum dots as emitter, or non-linear processes like spontaneous parametric down conversion (SPDC), which can be employed to build heralded-single-photon sources as done in this thesis (see Chapter 7). With the non-linear techniques, multi-photon emission probability is not completely suppressed, yielding "approximate" single-photon sources.

The second step is to encode quantum states into the produced photons. In this process, quantum states are imprinted into a photonic degree of freedom such as polarization, time or frequency. For example, using an imbalanced Mach-Zehnder interferometer, a qubit can be encoded into two well-defined temporal modes of a photon. Such so-called time-bin qubits are used in this thesis (see Chapter 7).

2.1.2 Measurement of Photonic Qubits

The concept of the measurement of a qubit is fundamentally different from the concept of a classical measurement[3]. First of all, the measurement of a qubit is an "attempt" to determine the state of qubit, whose result is generally probabilistic. Therefore, in principle, determining a single photon state requires many measurements on an ensemble of identical qubits. Secondly, in the general case, a measurement disturbs the state of the qubit and the output of the measurement (the state found) is the new state after the measurement[4].

---

[3]This statement holds, in general, for any quantum mechanical measurement.

[4]In a typical photonic qubit measurement, the photon is destroyed upon its detection. In this situation this statement doesn't tell much. On the other hand, in principle, it is possible to perform a measurement without destroying the photon. This is often referred to as a quantum non-demolition measurement.

The term "projection" is used for a quantum mechanical measurement. In a projection measurement, a given input qubit state $|\psi_i\rangle$ is projected onto a qubit state $|\psi_p\rangle$ (projection state), which happens with probability[5],[6]

$$p = |\langle\psi_p| |\psi_i\rangle|^2. \tag{2.3}$$

This probability (the amount of overlap) depends on the input state and the state to be projected onto. If both states are equal or orthogonal, the measurement result is deterministic; that is 1 and 0, respectively. For example, this is the case when state $|\psi_i\rangle = \frac{1}{\sqrt{2}}(|0\rangle + |1\rangle)$ is projected onto $|\psi_p\rangle = \frac{1}{\sqrt{2}}(|0\rangle \pm |1\rangle)$. This situation is usually referred to as performing the measurement in the basis of the input state. On the other hand, if the input state and the projection states are neither equal nor orthogonal, the measurement probabilities deviate from 0 and 1. In the case of minimum overlap between the states, for example when the state $|\psi\rangle = \frac{1}{\sqrt{2}}(|0\rangle + |1\rangle)$ is projected onto $|0\rangle$ and $|1\rangle$, the probabilities of finding either result are equal to 0.5. This case is referred to as performing a measurement in an unbiased basis with respect to the basis used to prepare the qubit. The described properties of a measurement of qubit is the key for most applications of quantum communication.

Linear optical elements and single photon detectors are the building blocks of a measurement apparatus for photonic qubits. For instance, the measurement of time-bin qubits can be done using an imbalanced Mach-Zehnder interferometer, which is composed of two beam splitters, a phase shifter and a single-photon detector as described in Chapter 7 and 8. In general, the role of a projection measurement apparatus is to transform an input qubit state into a superposition of a set of orthogonal states, each in a distinguishable mode (temporal, spatial or spectral). Thus the detection of a photon in one of these modes projects the qubit onto the corresponding state.

---

[5]The other equivalent expression is $\langle\psi|_i \left(|\psi\rangle_p \langle\psi|_p\right) |\psi\rangle_i$; it is written in terms of the projector operator.

[6]If the input state is not a pure quantum state, a density matrix formalism needs to be used for this calculation.

2.1.3 No–Cloning Principle

This principle is the essence of the security of quantum key distribution (the most mature application of quantum communication). Furthermore it is also of fundamental importance as it is related to the impossibility of sending information faster than the speed of light [11, 12]. The no–cloning theorem states that it is impossible to perfectly copy an unknown quantum state [13]. To understand the basic idea, imagine that we want to copy an input quantum state $|\psi\rangle$ to another input state that is initially in state $|0\rangle$, using our copy machine. This means that after the copying process we should have two output states that are the same as $|\psi\rangle$. This process can be represented by $\hat{U}\left(|\psi\rangle \otimes |0\rangle\right) = |\psi\rangle \otimes |\psi\rangle$ where $\hat{U}$ is an unitary operation applied to the input states. Similarly, if an input state $|\phi\rangle$ that is orthogonal to $|\psi\rangle$ needs to be copied, the process should result in $\hat{U}\left(|\phi\rangle \otimes |0\rangle\right) = |\phi\rangle \otimes |\phi\rangle$. The question is now what would be obtained when one attempts to copy a more general state like $(\alpha |\psi\rangle + \beta |\phi\rangle)$, which is an arbitrary superposition of $|\psi\rangle$ and $|\phi\rangle$. In this case, using the linearity of quantum mechanics, the input states of the copying machine can be written as $\hat{U}\left((\alpha |\psi\rangle + \beta |\phi\rangle) \otimes |0\rangle\right) = \alpha\hat{U} |\psi\rangle \otimes |0\rangle + \beta\hat{U} |\phi\rangle \otimes |0\rangle$. When the copying operation is applied to the individual terms, it can be easily verified that in the general case, $\hat{U}\left((\alpha |\psi\rangle + \beta |\phi\rangle) \otimes |0\rangle\right) \neq (\alpha |\psi\rangle + \beta |\phi\rangle) \otimes (\alpha |\psi\rangle + \beta |\phi\rangle)$, where the right-hand side of the expression is the desired result. The equation is satisfied only in the case in which $\alpha = 0$ or $\beta = 0$. Therefore, it is impossible to perfectly copy an unknown quantum state. Nevertheless, in principle it is possible to make imperfect copies of quantum states by designing quantum cloning machines. For example, the universal quantum cloner that is the most well-known of such constructions allows one to obtain the two clones of an arbitray unknown input state with fidelity (amount of overlap between the input and the clone) of 5/6 [14].

At this point, it is worth to mention the difference between a classical memory and a quantum memory from a conceptual perspective in the view of the above discussions. A quantum memory converts an input photon state to a different form for storage, for example

from photonic state to atomic state, and later on reverses this operation. This allows, in principle, achieving a fidelity of one. On the other hand a classical memory device performs a measurement on an input state, records it and is then able to make an arbitrary number of imperfect clones. Taking into account all possible projection measurement settings, the average storage fidelity of a classical memory for an arbitrary qubit is 2/3 [15] [7]. This value is often used as a benchmark to demonstrate the quantum nature of a memory device.

2.2   Entanglement

The exact definition of a two-particle (bi-partite) entangled state is that it cannot be written as a product state of its two individual systems :

$$|\psi\rangle \neq |\psi\rangle_1 \otimes |\psi\rangle_2 \equiv |\psi\rangle_1 |\psi\rangle_2 \tag{2.4}$$

Entanglement leads to correlations between measurement outcomes obtained from separate quantum mechanical systems, such as two qubits, that in certain cases, cannot be explained by local (hidden) variable models, i.e. that violate a Bell-inequality [16].

In addition to their fundamental importance for the interpretation of quantum theory, two-qubit entangled systems are main ingredients in quantum communication. The states, $|0\rangle_1 |0\rangle_2$, $|0\rangle_1 |1\rangle_2$, $|1\rangle_1 |0\rangle_2$ and $|1\rangle_1 |1\rangle_2$, where indices 1 and 2 denote the first and the second particle, form a basis for two-qubit systems. Superpositions of these states such as $(\alpha |0\rangle_1 |0\rangle_2 + \beta |1\rangle_1 |1\rangle_2)$ are entangled qubit states. The states known as maximally entan-

---

[7]Why a classical memory cannot reach unit fidelity can be understood intuitively using the Heisenberg uncertainty principle. The information about a quantum state is contained in phase and amplitude which are conjugate variables. These variables cannot be measured with better accuracy than what is allowed by the Heisenberg uncertainty principle. Hence, perfect reconstruction is impossible.

gled states or Bell-states have the following form [8],

$$\left|\phi^{\pm}\right\rangle = \frac{1}{\sqrt{2}} \left(\left|0\right\rangle_1 \left|0\right\rangle_2 \pm \left|1\right\rangle_1 \left|1\right\rangle_2\right) \tag{2.5a}$$

$$\left|\psi^{\pm}\right\rangle = \frac{1}{\sqrt{2}} \left(\left|0\right\rangle_1 \left|1\right\rangle_2 \pm \left|1\right\rangle_1 \left|0\right\rangle_2\right) \tag{2.5b}$$

They are central to most applications of quantum communication.

Entanglement between photons (photonic entanglement) can be used to establish secret keys, or to distribute quantum information by means of teleportation. Moreover, entanglement can be reversibly transferred between different systems (such as photons and atoms) as is experimentally demonstrated in this thesis (see Chapter 8 and a brief review article on this work by J. Longdell [17]). In addition, it can be swapped as will be summarized in Sect. 2.6. For these reasons entanglement is considered as a main resource for quantum communications.

Photonic entanglement can be generated using various degrees of freedom such as polarization, time, or frequency. Among these possibilities, polarization and time-bin entanglement have attracted a lot of attention due to the simplicity of manipulating quantum states encoded in these degrees of freedom. SPDC is currently the most widely used technique to produce entangled photons and it is employed in some experiments described in this thesis (see Chapter 8).

2.3 Measuring Entanglement

The existence of entanglement in two-particle systems, in our context between two photons, can be verified using different approaches, all requiring one to perform joint projection measurements on the particles as schematized in Fig 2.2. One of the standard approaches is to re-construct the quantum state of the two-particle system, i.e. the density matrix, which

---

[8]These four states also form a basis for two-qubit systems.
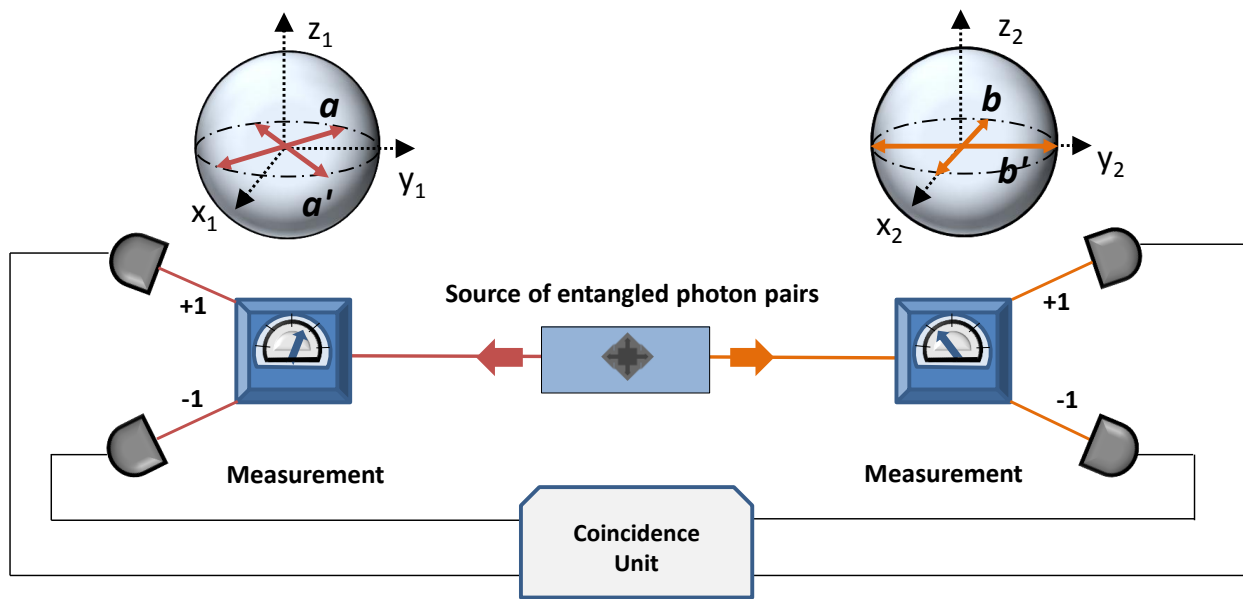
Figure 2.2: **A measurement apparatus to find the correlations between entangled particles:** The Bloch spheres on each particles side depict the projection settings required for a CHSH Bell-inequality test.

gives full information about the system. Once the density matrix is known, the amount of entanglement within the system can be quantified (see Chapter 8).

Another standard approach for the verification of entanglement is a Bell-Inequality test, explored by John Bell [16]. Strictly speaking this test reveals the non-local nature of two-particle states (if any), which is a stronger criterion than the one of being entangled. Therefore the Bell inequality constitutes a cornerstone in the interpretation of quantum mechanics.

The main procedure in a Bell-test is to quantify the correlations between entangled particles for different projection measurement settings. The CHSH (Clauser-Horne-Shimony-Holt) inequality is one of the most well-known forms of the Bell inequalities [18]. It requires four different pre-defined sets of joint projection measurements (see Fig. 2.2). From each measurement result a correlation coefficient is determined[9]. The correlation coefficients allow

---

[9]A correlation coefficient quantifies the strength of the correlations between the outcomes of the measurements performed on the particles. It varies between -1 and 1. Values of 1, -1 and 0 indicate the observation of perfect correlations, perfect anti-correlations and no correlations, respectively.

one to calculate a parameter, called the S-parameter (Bell-parameter):

$$S = |E(\boldsymbol{a},\boldsymbol{b}) + E(\boldsymbol{a'},\boldsymbol{b}) + E(\boldsymbol{a},\boldsymbol{b'}) - E(\boldsymbol{a'},\boldsymbol{b'})| \tag{2.6}$$

where $\boldsymbol{a},\boldsymbol{a'}$ and $\boldsymbol{b},\boldsymbol{b'}$ refer to the projection settings for the first photon and the second photon, respectively, and E is the corresponding correlation coefficient. Classical models based on the assumption of locality (generally referred to as local hidden variable theories–LVT) predict that the S-parameter has a maximum value of 2,

$$S_{LVT} \leq 2 \tag{2.7}$$

On the other hand, quantum mechanics predicts that the S-parameter is bounded by $2\sqrt{2}$. As a result, a violation of the Bell inequality (Eqn. 2.7) proves not only the existence of quantum entanglement but also quantum non-locality since there is no local classical model that can reproduce the observed results predicted by quantum mechanics. This test was also performed in this thesis; details can be found in Chapter 8.

2.4 Bell-State Measurement

A Bell-state measurement is a projection measurement that projects the quantum state of a two-qubit system onto one of the Bell states shown in Eqn. 2.5a and 2.5b. A 50/50 beam splitter with 2 input and 2 output ports is the most common tool to carry out this measurement for photonic qubits. The two photons are sent into different input ports and interfere at the beam splitter. The photons exiting the beam splitter are detected by single-photon detectors at the output ports. Coincident detections can project the state of the photons onto one of the Bell-states. For instance, detecting two photons in different output ports and orthogonal states (i.e. one in $|0\rangle$ and one in $|1\rangle$) corresponds to a projection onto the $|\psi^-\rangle$ state, and detecting both photons in the same output and in orthogonal states corresponds to a projection onto the $|\psi^+\rangle$. When one inspects the quantum states of two-qubits transformed after a beam splitter, it can be seen that the projection onto
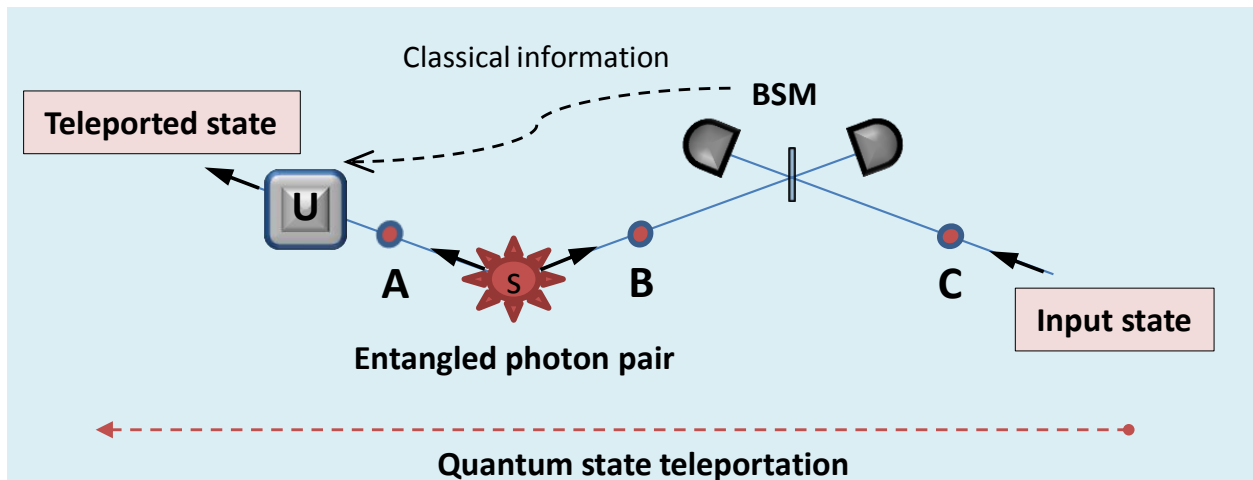
Figure 2.3: **Quantum teleportation:** Photon C, which carries the state to be teleported, and photon B, which is entangled with photon A, meet at the beam splitter for a Bell-state measurement (BSM). The detections after the beam splitter project the state of B and C onto one of the Bell-states. The information about which Bell-state has been projected onto is sent to the location of photon A. Based on this information, a unitary transformation ($\mathbf{U}$) is applied to photon A. This process results in the teleportation of the state of photon C to photon A.

$|\phi^+\rangle$ and $|\phi^-\rangle$ never occurs. It has been shown in [19] that this limitation of the success probability to 50% is intrinsic to the use of linear optics. The other important point is that for a successful Bell-state measurement, the photons that meet at the beam splitter must be indistinguishable in all-degrees of freedom, namely polarization, temporal, spatial and spectral degrees, as discussed in Chapter 9.

The Bell-state measurement is particularly important when one or two of the input qubits are entangled with other photons. In this case, it allows for quantum state teleportation and entanglement swapping, which are key processes in quantum communication as discussed in the next sections.

2.5 Quantum Teleportation

Quantum teleportation is one of the most interesting, surprising and useful applications of quantum entanglement [20]. It is the process of transferring an unknown quantum state from one place to another with no transmission of the carrier. To perform this process with linear optics, as schematically shown in Fig 2.3, the required elements are a pair of maximally entangled photons (labeled A and B), a photon that carries the quantum state to be teleported (labeled C) and a Bell-state measurement between photon C and one member of the entangled pair, say photon B. The initial quantum state of the three-photon system is given by

$$|\psi\rangle_{ABC} = \frac{1}{\sqrt{2}} \left(|0\rangle_A |0\rangle_B + |1\rangle_A |1\rangle_B \right) \otimes \left(\alpha |0\rangle_C + \beta |1\rangle_C \right) \tag{2.8}$$

where the first and second term in the product belong to the state of the entangled photons $(|\phi^+\rangle)$ and the state to be teleported, respectively. When the Bell-state measurement is performed on photon B and photon C, the state of these photons can be projected onto one of the Bell-states, let's say onto $|\psi\rangle_{BC} = \frac{1}{\sqrt{2}} \left(|0\rangle_B |1\rangle_C - |1\rangle_B |0\rangle_C \right)$. In this case, the resulting state of photon A is

$$|\psi\rangle_A = \langle\psi|_{BC} |\psi\rangle_{ABC} = \left(\beta |0\rangle_A - \alpha |1\rangle_A \right). \tag{2.9}$$

According to this result, immediately after the Bell-state measurement, the state of photon C is transferred to photon A with flipped bits (i.e. α and β are swapped) and a π phase difference. To recover the original state, classical information that reveals which Bell-state has been measured is sent to the location of photon A. The necessary unitary transformation, which depends on the resulting Bell-state projection, is applied to the state of photon A. This finalizes the teleportation of state from photon C to photon A. As seen, quantum teleportation requires classical communication, since the result of a Bell-state measurement is probabilistic. Therefore this scheme does not allow communications faster than the speed of light.
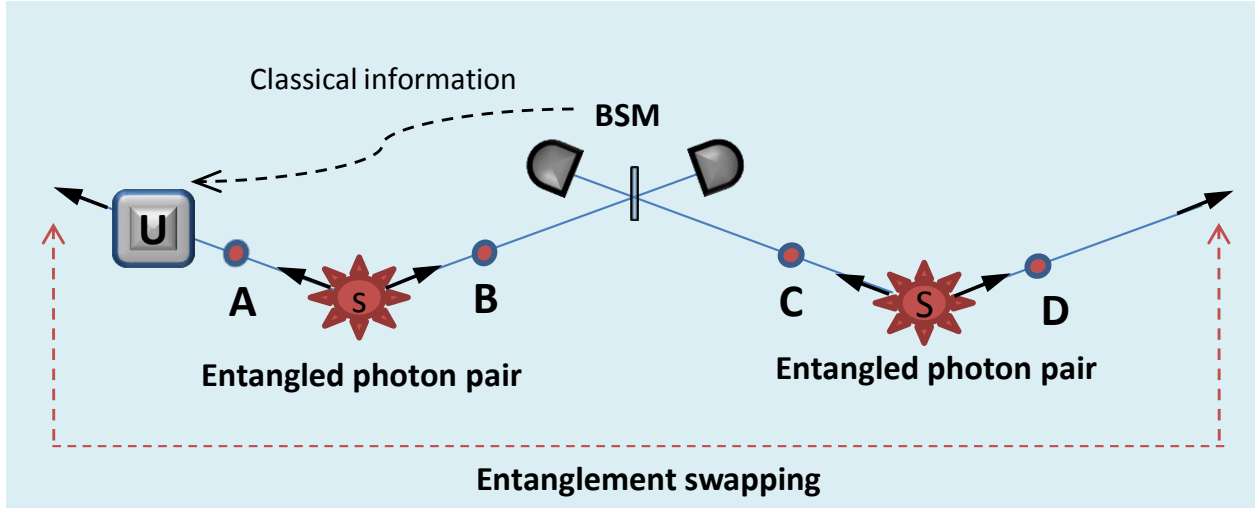
Figure 2.4: **Entanglement swapping:** Two pairs of entangled photons A-B and C-D are involved in the process. One member of each entangled photon pair (photons B and C) meet at the beam splitter where their joint state is projected onto the set of Bell-states. The information about which Bell-state has been projected onto is sent to the location of photon A and photon D. Based on this information, unitary transformations, shown by **U** is applied to photon A or photon D. After this step, the initial entangled state is now established between A and D.

2.6 Entanglement Swapping

The idea is very similar to that of quantum teleportation and so entanglement swapping is also known as teleportation of entanglement [21]. In this case, two pairs of entangled photons (A-B and C-D) are involved, as shown in Fig 2.4. The initial state of the four-photon system is given by

$$|\psi\rangle_{ABCD} = \frac{1}{\sqrt{2}} \left(|0\rangle_A |0\rangle_B + |1\rangle_A |1\rangle_B \right) \otimes \frac{1}{\sqrt{2}} \left(|0\rangle_C |0\rangle_D + |1\rangle_C |1\rangle_D \right) \qquad (2.10)$$

where each term in the product corresponds to a maximally entangled photon state ($|\phi^+\rangle$). One member of each pair (B and C) is subjected to a Bell-state measurement. When the state of photon B and photon C is projected onto one of the Bell-states, for example onto $|\psi\rangle_{BC} = \frac{1}{\sqrt{2}} \left(|0\rangle_B |1\rangle_C - |1\rangle_B |0\rangle_C \right)$, the resulting state is

$$|\psi_{AD}\rangle = \langle\psi|_{BC} |\psi\rangle_{ABCD} = \frac{1}{\sqrt{2}} \left(|0\rangle_A |1\rangle_D - |1\rangle_A |0\rangle_D \right). \qquad (2.11)$$

According to this result, immediately after the Bell-state measurement, photon A and photon D, which have never interacted before, become entangled. Similarly, to establish the original entangled state, a unitary transformation is applied to the entangled photons following the classical communication regarding the result of the Bell-state measurement. Entanglement swapping is key process for long distance quantum communication as will be discussed in Sect. 3.1.

2.7   Long-distance Quantum communication

In quantum communication, optical-fiber is a natural choice as a medium for transmitting photons between distant parties since classical optical communication relies on fiber-optics technology[10]. Optical-fibers can be considered low-loss media. For example, the transmission loss through a standard fiber for telecommunication wavelengths (about 1.5 μm) is only 0.22 dB per km. On the other hand, since loss scales exponentially with distance, the overall loss becomes very significant over large distances. In general, this is not a serious issue in classical optical communication because optical signals can be amplified at intermediate stages of a communication channel so that loss can be compensated. However, this solution cannot be applied in quantum communication due to no-cloning theorem, as discussed in Sec. 2.1.3. The solution to this problem is to use quantum repeaters proposed by Briegel *et al.* [3]. Quantum repeaters will be the main focus of the next section.

---

[10]There are also efforts to establish long-distance quantum communication through free-space using satellites. The detailed discussion of this approach is beyond the scope of this thesis.

Chapter 3

Quantum Memory for Quantum Communication

As discussed in the previous chapter (see Sect. 2.7), the main problem of existing quantum communication technologies is the limited tranmsmission distances, which can be overcome using quantum repeaters. The essential ingredients of quantum repeaters are quantum memories, which allow storage and retrieval of quantum states of light. In this chapter, I will first explain the basic operation of a quantum repeater with emphasis on the role of optical quantum memories. Next, I will describe the requirements that an optical quantum memory needs to satisfy for quantum repeaters. After that, I will give an overview on widely-known quantum memory protocols in view of these requirements. I conclude the chapter with a brief report of the state-of-the-art for quantum memories.

3.1   Optical Quantum Memories For Quantum Repeaters

The distribution of entanglement over long distances is the common goal in quantum repeater proposals. However, how to create entanglement and how to use quantum memories in this task is different, depending on the quantum repeater proposal. There are two widely known approaches [4]. In one of them, known as the Duan-Lukin-Cirac-Zoller (DLCZ) protocol, the processes of the generation and storage of entanglement are combined into the same system [22]. In the other quantum repeater approach, which is the motivation for our quantum memory development, these processes are carried out by independent systems [23]. The main elements in this approach are sources of entangled photon pairs, quantum memories to store entangled photons, and Bell-state projection measurements, as schematically shown in Fig. 3.1. To understand the operation of this quantum repeater, imagine that, ultimately, we would like to distribute quantum information between A and D. We start by dividing the
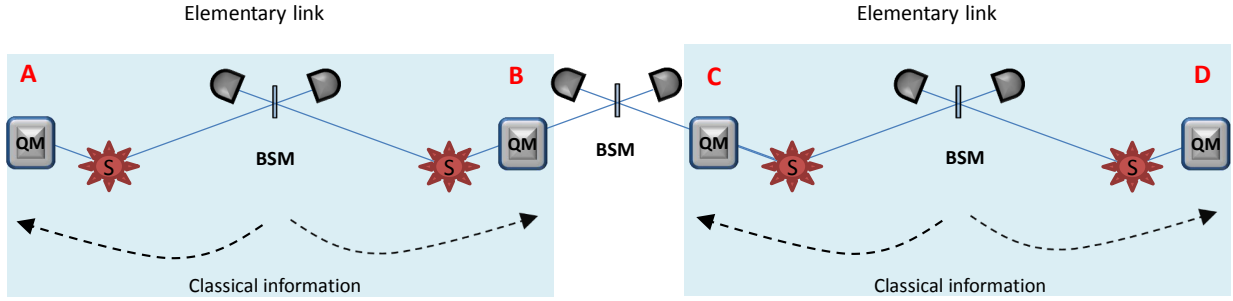
Figure 3.1: **A quantum repeater link based on quantum memories and entangled photon pair sources.** The entire link in this example consists of two elementary links that extend from node A to node B and from node C and to node D, respectively. Each elementary links contains two quantum memories (QM), two entangled photon sources (S) and a beam splitter for Bell-state projection measurements (BSM) plus two single photon detectors. The sources in each elementary link are placed close to the quantum memories, but far from the beam splitter. In this way, a successful Bell-state measurement indicates that the quantum memories are charged with photons, and also projects the memories onto an entangled state. The central beam splitter between the two elementary links allows for distributing entanglement between the two far ends of the entire link through entanglement swapping with photons recalled from neighboring quantum memories upon demand (i.e. once entanglement has also been established across the adjacent elementary link).

channel into two elementary communication links, (A-B and C-D) and first try to distribute entanglement across the first elementary communication link, consisting of two independent photon pair sources and two quantum memories. In this link, each source emits entangled photon pairs. One member of each entangled pair is stored in the quantum memories located at A and B, while the other members meet at the Bell-State measurement beam splitter. Detecting the photons after the beam splitter may project the joint quantum state of the stored photons, which have not directly interacted, onto a maximally entangled state (Bell state). As a result, entanglement is established between the quantum memories at A and B by means of entanglement swapping or teleportation of entanglement (see Sec. 2.6). Now imagine that we would like to extend entanglement between link A-B and A-D. To this end, entanglement also needs to be created between C and D in the same way. Once entanglement is generated between A and B and between C and D, the photons are retrieved from the

17

memories located at B and C and a Bell-state measurement establishes the entanglement between A and D.

Typically the probability of simultaneously creating entanglement in each link is quite low, because of the transmission loss over the links and the probabilistic nature of existing photon pair sources. Therefore, the main role of the quantum memory devices is to store entangled photons and hold them until the entanglement is also created across the adjacent link. To carry out this function, there are three necessary requirements for a quantum memory: First of all, it must able to store and preserve entanglement. That is the topic of Chapter 8. Secondly, it must not degrade the photonic wavefunction in any degree of freedom during storage, which is required for Bell-state measurement to be performed successfully. That is covered in Chapter 9. Finally, it must allow on-demand read-out for the synchronization, as discussed in Chapter 10. In addition to these requirements, implementing practical quantum repeaters with sufficiently high rate of entanglement swapping requires quantum memories with large bandwidth and large multimode storage capabilities, which are demonstrated in Chapter 6 and 10, respectively. Other requirements and performance criteria [7] will be discussed in the next section.

3.2   Performance Criteria for Quantum Memories

3.2.1   Fidelity

The faithful storage of quantum states is one requirement of a quantum memory device, meaning that quantum states must be stored and retrieved without too much degradations. A measure known as the quantum "Fidelity" is often used to quantify how faithfully a quantum state is stored. It amounts to the overlap between the input and retrieved quantum states, conditioned on successful retrieval (this definition holds for encoding of quantum information into discrete quantum variables, as in thesis). The fidelity is typically assessed by storing different input quantum states and analyzing the retrieved states, as shown in

Chapter 7. Furthermore, since photons need to be in entangled quantum states in a quantum repeater implementation, a quantum memory must preserve entanglement during storage, which can be verified by assessing the so-called Entanglement of Formation before and after storage, as demonstrated in Chapter 8.

3.2.2 Efficiency

For the purpose of storing single photons, efficiency is defined as the probability of retrieving an input photon out of a quantum memory. Ideally, a quantum memory should have unit efficiency. Although generally fulfilling this criterion is a significant technical challenge, recent, and very promising, quantum memory developments have demonstrated up to 90% efficiency [24, 25]. According to Ref. [4], this is sufficient to achieve quantum key distribution over 1000 km.

3.2.3 Storage Time

In the operation of quantum repeaters, quantum memories at the end-point of an elementary link must be able to store entangled photons and hold them until the entanglement is also created across the adjacent link, as described in Section 3.1. In this procedure, the knowledge that the two memories are charged with entangled photons is obtained from a successful Bell-State measurement in the middle of the elementary link (see Fig. 3.1). This information is sent to the memory locations using classical signals. When two memories at the node connecting two adjacent elementary links are known to be charged with entangled photons, the photons are retrieved from the memories and projected onto a Bell state to create entanglement between these elementary links. In this configuration, in the best case (assuming that entanglement is deterministically created across each elementary link) the storage time of the quantum memories must equal the time it takes a photon to travel from an entangled source to the Bell state measurement at the center of the elementary link and the classical signal to travel back (this is equivalent to the communication time across the

elementary link). For example, if the length of a fiber-based elementary link is set to be 100 km, the memory storage time needs to be at least 500 μs. Decreasing this distance would relax the requirement of long storage time at the expense of using more quantum memories in the communication link.

3.2.4 Bandwidth

In order to achieve high-rate data transfer, in optical communication systems information is encoded into short laser pulses that are on the order of picoseconds. Similarly for practical quantum communication systems, the duration of the single photon pulses has to be short. Since the frequency bandwidth of a Fourier-limited pulse is inversely proportional to its duration, the acceptance bandwidth of a quantum memory must be large. Thus, quantum memory bandwidths of GHz are desirable to practically integrate quantum communication into existing classical communication systems.

3.2.5 Multimode Capacity

The ability to simultaneously store more than one photon defines the multimode storage capacity of a quantum memory, which is crucial for practical realization of quantum repeaters. Without this ability, only one attempt at establishing entanglement between the nodes of an elementary link can be made per communication round trip time, because it would be necessary to ensure that the memory is emptied for the next attempt. In this case, the success rate of entanglement swapping would be very small. However, with multimode quantum memories, several attempts per communication round trip time in an elementary link can be made either successively with temporal multimode or simultaneously with spectral or spatial multimode storage capabilities [4]. The multimode capacity of a memory depends on the quantum memory approach [26]. Also, the multimode capacity of a quantum memory is directly related to the bandwidth capacity and storage times of the memory. The product of these two, known simply as time-bandwidth product, is proportional to the multimode

20

capacity.

3.2.6 Practicality and Compatibility

From a practical point of view, a quantum memory device should have minimal complexity and should not require expensive and bulky resources. In addition to these requirements, the integration of quantum memories with existing photonic and fiber-optic communication technologies needs to be simple. For instance, the storage wavelength of a quantum memory should preferably be in the fiber-optic communication band or compatible with the standard laboratory equipments. Thus quantum repeaters based on photon pair sources and quantum memories have an advantage compared to the DLCZ-type quantum repeaters, since for the former the wavelength of each member of the photon pair can be customized to match either the fiber-optic communication band or the quantum memory storage wavelength, as also shown in our experiments. Robustness and compactness are other important factors, when trying to build a reliable quantum repeater. Hence, the development of solid-state quantum memory, as opposed to e.g. laser cooled atoms, is highly desirable.

3.3   Optical Quantum Memory Approaches

To build a quantum memory for light, numerous protocols and physical media such as single atoms, gaseous or solid-state atomic ensembles have been proposed, as reviewed in [6] and [7] [1]. In one class of quantum memory implementations, which is known as DLCZ-type memories, mentioned in Section 3.1, the quantum memory and single photon source is fashioned from a single atomic ensemble. Basically, in this approach, a quantum state is created in-memory. In the other class, a quantum state encoded in a photon is input to a quantum memory that allows reversible mapping of the quantum state of this photon. In the following, I will discuss in further detail widely-known quantum memory protocols that

---

[1]See Sec. 2.1.3 for the discussion of the concept of quantum memory.

fall in the latter class.

3.3.1 Photon-Echo Based Quantum Memory Protocols

Photon-echo based optical data storage has been an active field of research since 1980 [27, 28]. In particular, photon-echo based implementations in cryogenically cooled rare-earth (RE) ion doped crystals have became attractive due to their large bandwidth and large multimode optical data storage and processing capabilities with long storage times [28].

The photon-echo process relies on absorbing input light in an ensemble of atoms, each with slightly different transition frequency, and then time reversing the absorption, which leads to a re-emission of the input light, known as an echo [29]. Rare-earth ions doped into crystals at cryogenic temperatures are particularly suitable for this process, since they possess a large naturally-broadened inhomogeneously broadened absorption profile composed of many narrow absorption lines, each featuring long coherence times. In the traditional photon-echo based storage schemes, the read-out mechanism that triggers the re-emisson of input light is a strong optical π-pulse[2]. However, this approach is not suitable for storing single photon quantum states. When a strong read-out pulse is absorbed by the medium, it causes excitations of many ions that can decay with spontaneous and/or stimulated photon emission. These photons add noise that screens the detection of a stored photon. To overcome this fundamental problem, different methods, based on modifying the retrieval process, have been proposed in the last decade. In the following, the modified photon-echo based storage schemes for single photon quantum state storage will be summarized.

Controlled Reversible Inhomogeneous Broadening (CRIB)

The initial proposal of the CRIB protocol is due to S. A. Moiseev and S. Kröll in 2001 [30] and allows for quantum state storage in atomic vapor, where inhomogenous broadening arises

---

[2]The term, π-pulse, will be used very often in the following sections. It refers to the pulse area that amounts to a π rotation of the atomic state as described in the Bloch sphere. When atoms, initially in the ground state, resonantly interact with a π pulse, it transforms the atomic state to the excited state.

from doppler shifts. After that, three groups independently developed the CRIB protocol [31, 32, 33] and made it suitable for solid-state quantum memory. Since then, different versions of this protocol have been proposed and experimentally realized in rare-earth doped crystals and in warm rubidium gas ensembles.

The implementation of CRIB in RE doped crystals starts with an inhomogeneously broadened absorption profile as shown in Fig. 3.2 [34]. The first step is to generate a single narrow absorption line on a zero-absorption background by performing frequency selective optical pumping (Fig. 3.2a). In this process, all atoms, except the ones whose transition match the narrow absorption line, are removed to long-lived shelving states that do not interact with the optical pulses to be stored. The next step is to broaden this line in a controlled way by applying a spatially varying external electric or magnetic field, depending on the properties of the storage medium. Electric fields can be used with materials that exhibit a DC Stark effect, which allows for a controlled shift of atomic transition frequencies (see Chapter 5).

Upon application of a spatially inhomogeneous field, an artificial inhomogeneous broadened absorption is obtained as represented in Fig. 3.2b. At this stage, the medium is ready for photon storage and the broadened absorption feature corresponds to the memory bandwidth that photons will be mapped onto. After absorbing an input photon, the atoms start picking up different phases due to their different frequencies [3]. The accumulated phase of each atom is proportional to the detuning of each atom (j) and the elapsed time, $\Delta\phi_j = \Delta\omega_j \Delta t$. To reverse this process and trigger the re-emission of the photon, the polarity of the external field is reversed at time τ leading to the reversal of the detuning of the atoms : $\Delta\omega_j \to -\Delta\omega_j$, leading to rephasing (Fig. 3.2c). Rephasing at time 2τ results in the re-emission of a photon in the originally encoded quantum state.

In general, for complete time reversal, the photon must be retrieved in the backwards

---

[3]This statement does not accurately describe the storage of a single photon in an atomic ensemble. Absorption of a photon in the ensemble results in a collective atomic state (Dicke state) that is a superposition of all possible single atomic excitations, as described in Section 4.2. Therefore, more accurate statement is that the different terms in the Dicke state pick up different phase due the different atomic frequencies.
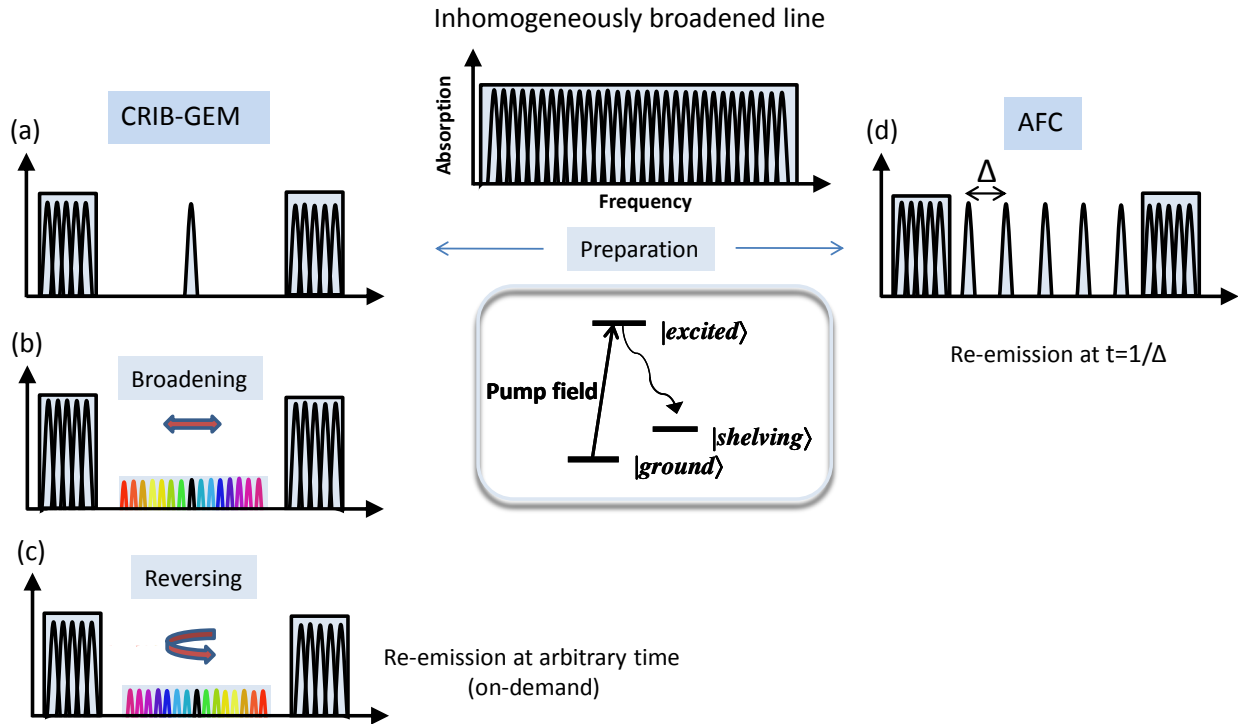
Figure 3.2: **Implementation of the CRIB and the AFC protocol in RE doped crystals.**

direction, which requires additional steps known as phase-matching, as described in [34]. In theory, with optimal preparation of the memory and backward retrieval, unit retrieval efficiency can be achieved.

In the scheme described above, quantum state encoded into a single optical excitation (more precisely, its coherence) is mapped onto optical transition of the atoms, which in principle requires only a two-level atomic (ignoring, for the sake of the argument, shelving states required for optical pumping). On the other hand, the typical achievable coherence time of the optical transitions in rare-earth systems are hundreds of microsecond and that limits the storage times to less than a millisecond. The way to extend the storage time is to transfer the optical coherence onto spin transitions, which have, in general, much longer coherence times. As shown in Fig. 3.3a, this processes can be done by applying two π-pulses:
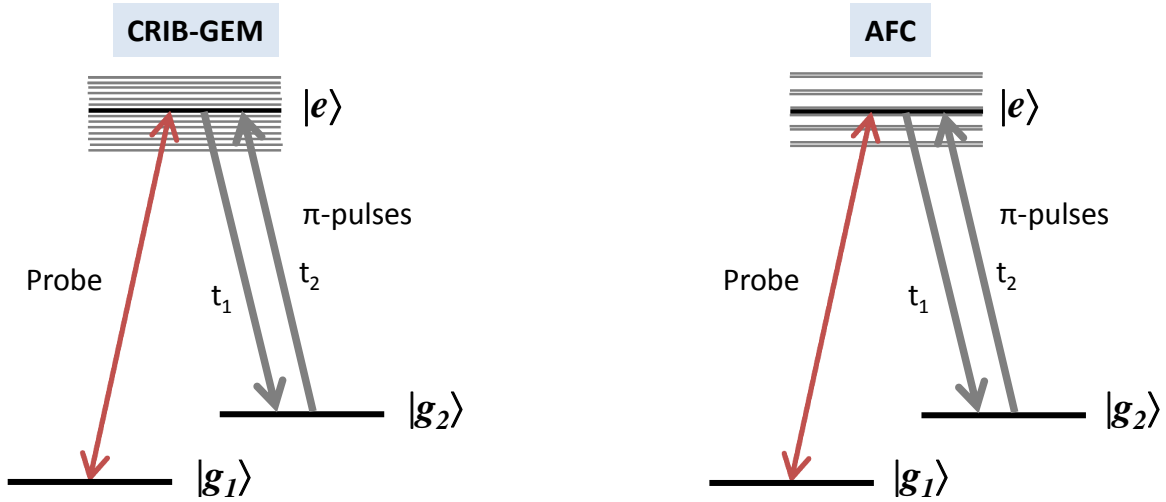
Figure 3.3: **Full CRIB and AFC protocols.**

the first maps the optical coherence onto the spin states and the second converts the spin coherence back to the optical coherence (see Section 4.5). Also, applying these pulses in counter-propagating directions allows for satisfying the phase matching conditions required for unit efficiency. Despite these advantages, implementing this scheme is more demanding, as it requires a three-level atomic system. Furthermore, applying strong π-pulses brings noise-related technical difficulties in single-photon level experiments.

Another version of this protocol is the Gradient-Echo Memory (GEM) approach that employs a linearly varying external field across the propagation direction of light in the storage medium [35]. This avoids the re-absorption of photons during retrieval in forward direction. In this case, even without the phase matching operation, 100% read-out efficiency is possible.

One variant of the GEM protocol is Raman-GEM [36, 37]. In this approach, photonic quantum state is directly mapped to spin coherence via an optical control field that mediates an off-resonant Raman interaction. For instance, in an implementation with a warm Rb gas system, a magnetic field gradient along the medium is used to artificially broaden the off-resonant Raman transition by introducing a varying amount of Zeeman splitting in the

spin transitions. Reversing the magnetic field in the presence of the control field starts the rephasing process and allows recovering the stored optical signal [36]. An attractive feature of Raman-GEM with gas ensembles is that room temperature is sufficient for operation. Also, it does not require the preparation of an initial narrow absorption line by optical pumping.

The bandwidth of quantum memories based on these protocols are typically limited by the energy level structure, the strength of external fields and the sensitivity of the memory media to the external fields. In RE systems, in principle, the separation between long-lived magnetic sub-levels determines the maximum achievable bandwidth, which can vary from a few MHz to hundreds of MHz depending on the material. In warm vapour, reaching high magnetic fields with sufficiently fast switching times is another technical difficulty for implementing large-bandwidth memories.

The CRIB-based quantum memories have better multimode storage capacity [38, 26, 35] than the most of the quantum memory protocols. In principle, increasing the multimode capacity for a given storage time requires increasing the broadening of the initial absorption line by increasing the field strength, which allows storing shorter pulses. However, a larger bandwidth reduces the effective absorption per frequency interval, resulting in decreased retrieval efficiency. Consequently, higher multimode capacity, with unchanged efficiency, requires higher optical depth. In the CRIB, the multimode capacity scales linearly with optical depth.

Atomic Frequency Comb Protocol (AFC)

Quantum memory implementations based on atomic frequency comb are the main focus of this thesis. The AFC protocol was proposed for quantum state storage and experimentally demonstrated by M. Afzelius and his colleagues in 2008 [39, 40]. It is inspired by the Accumulated-Photon-echo technique that was used for long-term optical data storage [41]. The AFC scheme relies on the interaction of input photons with an atomic ensemble that possesses a series of equally separated absorption lines on a zero-absorption background,

called an Atomic Frequency Comb, as shown in Fig. 3.2d. RE doped crystals are suitable media for AFC, since they have a naturally broadened absorption line that can be tailored into a comb-like spectrum using frequency selective optical pumping methods. When an input photon is mapped to an AFC medium, it is absorbed by the atoms that form the teeth in the AFC structure. Then, the atomic dipoles start dephasing due to their different detuning, as in the case of CRIB. However, differently from CRIB, the rephasing happens automatically without external control because of the discrete and periodic structure of the atomic transition frequencies. When the time reaches $T = 1/\Delta$, where Δ is the spacing between the peaks in Hz, complete rephasing occurs and the input photons are re-emitted in the forward in the originally encoded quantum state. While in this standard two-level AFC scheme, the storage time is pre-set and determined by the prepared peak spacing, it is possible to achieve on-demand recall, as well as recall in the backward direction by reversibly mapping the optical coherence onto a spin transition with π pulses as in the three-level CRIB protocol [39]. Also, we will discuss an alternative method to achieve read-out on demand in Chapter 10.

With the phase matching operation and optimal AFC parameters, the retrieval efficiency can reach up to 100%. The most attractive features of the AFC protocol are its excellent multimode and large bandwidth capacities [39]. Unlike other quantum memory protocols, the multimode and bandwidth capacity is independent of optical depth. Simply adding more peaks to the AFC increases the bandwidth and the number of modes to be stored, provided that inhomogeneous broadening is sufficiently large. In Chapter 4, the principles of the AFC protocol will be explained further.

Modified Two-Pulse Echo Schemes

As discussed in the previous sections, for the implementation of the CRIB and the AFC protocols in RE doped crystals, spectral tailoring of the inhomogeneous absorption profile using optical pumping techniques is a necessary step. However, in most of the situations,

this procedure is not easy for preparing an efficient memory. During the optical pumping, some of the atoms that are supposed to form the absorption peaks in the prepared spectral feature are unavoidably excited due to off-resonant interactions, resulting in loss of optical depth. Motivated by this problem, there have been recent protocols that remove the necessity of optical pumping and use naturally broadened lines [42, 43]. The idea behind these protocols originates from the traditional two-pulse photon echo technique that requires a strong rephasing π-pulse for read-out. As discussed in Section 3.3.1, this strong optical pulse causes substantial spontaneous and stimulated emission, resulting in reduced fidelity, i.e. masking of the recalled photon by noise photons. To eliminate this problem, the modified two-pulse photon echo schemes propose applying two π-pulses at different times, either in appropriately selected directions [42] or under inhomogenously applied electric fields [43], so that the primary echo and the associated spontaneous emission can be suppressed. On the other hand, the coherence still evolves in the medium and the stored photon comes out in a second re-phasing cycle. In theory, with sufficiently high optical depths, the efficiency can be 100%. The main difficulty in these techniques is the precise control of the π-pulses. To suppress the noise during the read-out stage, the medium must experience identical pulse areas. Any small deviation from this optimal condition can introduce noise that can pollute the stored single photon.

3.3.2 Electromagnetically Induced Transparency (EIT) based Quantum Memories

The EIT-based quantum memory protocol was one of the first developed approaches [44]. This protocol can be implemented in different media, including RE solid-state systems [6, 7, 45]. The most familiar type of the EIT phenomenon [46] requires a three-level atomic scheme with two ground levels and a common upper level, as shown in Fig. 3.4a. For EIT based light storage, two light field must act on the medium. One is the weak signal light (the probe) to be stored and the other is a strong optical field that controls the storage and read-out stages, as shown in the figure. In the absence of the control field, the signal field would be
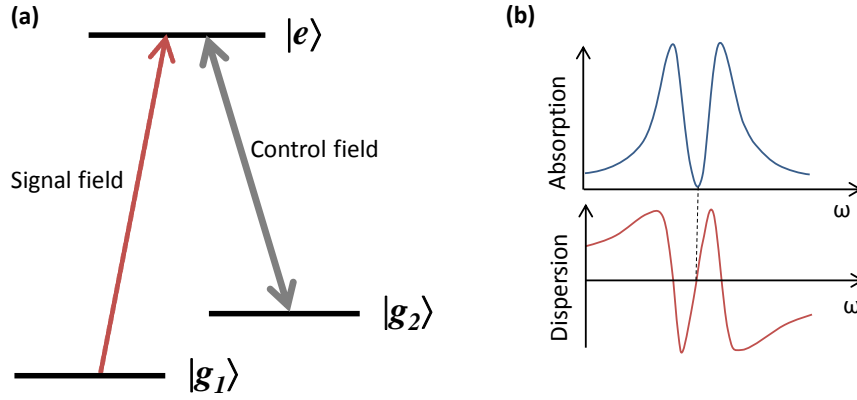
Figure 3.4: **EIT based storage protocol.**

partially or fully absorbed by the medium. Applying the control field induces a transparency window that allows the transmission of the signal field through the medium. According to the Kramer-Kronig relations, a change in the absorption profile is always accompanied with a change in the dispersion profile. In the EIT case, the transparency window results in a steep refractive index change, as shown in Fig. 3.4b. Consequently, the group velocity of the signal field is substantially reduced as it propagates in the medium. This is known as the slow-light effect [47]. The crucial point is that while the signal travels slowly through the medium, it can be stopped by adiabatically switching off the control field that creates the EIT condition. In this case, the coherence is trapped between the two ground levels. To release the signal from the medium, the control field is adiabatically switched back on and then the light is retrieved.

The EIT-based storage protocol has been experimentally demonstrated many times in various media such as single atoms, warm and cold gas ensembles and RE solid systems [6, 7]. Its realization with warm atomic vapour have become commonplace, since these systems are easily accessible and their spectroscopic properties are well known. However, there are only a few demonstrations of storage at the single-photon level using EIT scheme in a warm gas ensemble [48, 49, 45]. These experiments are complicated by a control field that generates
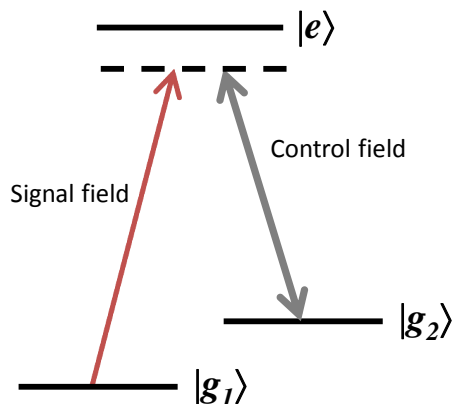
Figure 3.5: **Off-Resonant Raman based storage protocol.**

noise during the read-out stage [6]. Nevertheless, there are promising proof-of-principle storage experiments at the single-photon level using the EIT scheme in ultracold atoms and single atoms in high finesse cavities [50, 51, 52].

The poor scaling of the bandwidth of the EIT based quantum memories is the main issue for practical use. The width of the transmission window that sets the quantum memory bandwidth is given by the intensity of the control field. To reach bandwidths on the order of MHz, high powered control fields need to be applied, which worsens the noise problem. Finally, although EIT based quantum memories in atomic ensembles are capable of storing multimode quantum information, their multimode performance is quite poor and scales with the square of optical depth [26], which is worse than the CRIB and AFC approaches.

3.3.3 Off-Resonant Raman based Quantum Memories

The inital idea of this storage protocol came from E. Polzik and his colleagues [53] in 2000. Further it was developed by Nunn *et al.* [54] and Gorshkov *et al.* [55]. It is similar to EIT based storage in terms of memory operation, but brings important practicalities.

As in the EIT-based storage scheme, a three-level atomic system is coupled to a signal field that is to be stored, and a strong field that controls the storage and retrieval stages

as shown in Fig. 3.5. The main difference between the off-resonant Raman scheme and the EIT scheme is that, in the former, the signal and the control fields are far off-resonant to the upper level. Upon application of the strong far off-resonant control field, a virtual level is effectively created and this level mediates the transition to the other ground level, resulting in the storage of the coherence in the spin ground states. The memory bandwidth is determined by the intensity of the control field and can reach up to GHz, as demonstrated in recent experiments with a warm Cesium gas ensemble [56]. Similar to EIT in warm gas system, the noise arising from the control field is an issue, but here this problem is less severe as the off-resonant control field is less likely to excite the upper level. As in the EIT scheme, its multimode capacity is very limited and scales with the square root of optical depth [26]. On the other hand, its large bandwidth and the possibility to use warm atomic vapour make this approach attractive for quantum repeaters.

3.4   State of the Art and Progress in the Thesis

The development of quantum memories has progressed rapidly during the last decade and several impressive experimental achievements give hope that a high performance optical quantum memory for long distance quantum communications will be built in near future. Towards this end, a quantum memory has to meet the set of criteria discussed in Section 3.2. The goal of initial quantum memory experiments has been to demonstrate the possibility to meet each criterion, at least individually. Also, many quantum memory demonstrations have been performed with storage of classical light (laser pulses attenuated to the single photon level), since interfacing a memory with sources of non-classical light (e.g. single photons or entangled photons) entails additional challenges.

Among the milestones of quantum memory development, the implementation of high efficient quantum memories is probably the most encouraging. In 2010, using the GEM-protocol in a Pr^{3+}:Y_2SiO_5 crystal, a retrieval efficiency of up to 69% was demonstrated

with weak coherent pulses at the single photon level [24]. In another demonstration, up to 89% quantum memory efficiency was shown to be feasible using a GEM-Raman memory in warm Rb gas systems [25]. In terms of storage time, the storage of strong pulses during 2 s using the EIT protocol in a $Pr^{3+}:Y_2SiO_5$ crystal is a very important achievement [57]. The largest demonstrated quantum memory bandwidth is 5 GHz, accomplished using the AFC protocol in a $Tm^{+3}:LiNbO_3$ waveguide during this thesis [58]. Also to be noted in this context, a demonstration based on the off-resonant Raman protocol in a warm Cesium gas ensemble achieved a 1.5 GHz bandwidth with a high time-bandwidth product [59]. In terms of multimode capacity, AFC-based quantum memory demonstrations have achieved the highest performance. In 2010, the storage of 64 temporal modes with weak coherent pulses at the single photon level was realized in a $Nd^{3+}:Y_2SiO_5$ crystal [60]. Later on, the storage of a pulse train that contained more than 1000 bright pulses was demonstrated in a Tm:YAG crystal [61]. Finally, the possibility to store multiple frequency modes using a broadband AFC memory featuring on-demand recall was demonstrated as a part of this thesis (see Chapter 10).

Reversibly mapping photonic entanglement into-and-out of a quantum memory was demonstrated only in a few experimental studies. The main challenge to realizing this key ingredient of a quantum repeater is the substantial mismatch between the bandwidths of quantum memories and entangled photons provided from conventional spontaneous parametric downconversion (SPDC) sources. The first demonstration was in 2008 and used the EIT scheme in an ultra-cold atomic ensemble [5]. In 2011, as a part of this thesis [58] as well as in the work of Clausen *et al.* [62], time-bin entangled photons were successfully stored in AFC based solid-state quantum memories. Around the same time, the storage of polarization entangled photons was demonstrated in a cold atomic ensemble using the EIT protocol [63]. Also, the storage of continuous variable entangled states was realized in 2011 using an ensemble of cesium atoms [64].

Two-photon interference of photons recalled from separate quantum memories, which is a key process in the operation of a quantum repeater, has been demonstrated for the first time as a part of this thesis (Chapter 9). In addition, combining storage and manipulation of quantum optical pulses within an integrated quantum memory, which is important for realizing quantum networks and quantum computers was achieved in this thesis (Chapter 11).

The progress summarized above is very promising. However, to date, no approach (defined by a specific material and protocol) has been able to meet all requirements, and the challenge for the next few years will thus be to combine all these pieces into one single quantum memory implementation.

Chapter 4

Atomic Frequency Comb Quantum Memory Protocol

After having presented an overview of various quantum memory approaches in the previous chapter, I now detail the basic principles of the atomic frequency comb quantum memory protocol from an experimental perspective. First, I describe single photon storage using an AFC. Next, I discuss main memory parameters and their impact on efficiency, storage time, bandwidth and multimode capacity. In view of these explanations, I also detail the potential advantages and the technical difficulties to implement a high performance AFC memory. The main focus of this chapter will be on issues relate to implementing the AFC protocol with rare-earth doped crystals. However most of the discussions hold for other suitable media as well.

4.1 General Description

The basic form of the AFC scheme relies on the interaction of an input light field with a medium that has a comb-shaped absorption spectrum. There are two general descriptions of the storage and retrieval processes in an AFC medium. In the first [39], the input light is absorbed by atoms constituting the AFC. Each atom is treated as an oscillating electric dipole such that the collective behavior of all atomic dipoles define a macroscopic polarization of the ensemble. The resulting ensemble polarization leads to a coherent re-emission of the input light field, which is called an echo. In the other description [65], an AFC medium acts as a spectral filter to the input field such that the input light field's spectrum is modified during the propagation through the medium. The resulting light spectrum yields a set of time-delayed pulses in the time domain, which are called echoes. The former treatment is based on the absorption and re-emission of the input field, while the latter considers the
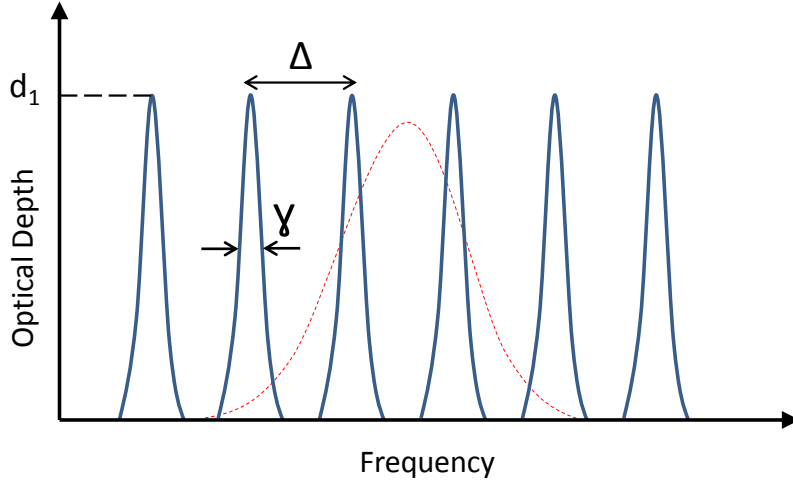
Figure 4.1: .
An idealized AFC structure composed of a series of equally spaced absorption peaks on a zero-absorption background. The dashed line represents the spectrum of a light pulse to be mapped onto the AFC.

transmission of the input field given by the spectrum-tailoring medium. Interestingly, both descriptions have the same predictions on the properties of output light field. In the rest of my thesis, I will use the absorption description to explain the storage and retrieval processes.

4.2   Photon Storage in AFC

A visual representation of an idealized AFC structure that is composed of equally spaced narrow absorption peaks on a zero absorption background is shown in Fig. 4.1. The width of each peak and the spacing between the peaks are denoted by γ and Δ, respectively. The y-axis corresponds to the optical depth and d_1 is the optical depth on resonance with an absorption peak. The dashed line inside the figure represents the spectrum of an input photon to be stored. Before a single photon enters the medium, assuming that all the atoms are in the ground state, the quantum state of the atom-photon system is given by the product state,

$$|1\rangle_{in} \otimes |g_1, \cdots g_j, \cdots g_N\rangle \tag{4.1}$$

35

where the first and second ket correspond to a photonic and a collective atomic state composed of N atoms, respectively. When a photon enters the AFC medium, it is absorbed, but there is no way to know by which atom. In this case, the photonic excitation is converted into a collective atomic excitation, which is an equal superposition of all excitation configurations expressed as,

$$\frac{1}{\sqrt{N}} \sum_{j=1}^{N} c_j e^{i2\pi\nu_j t} e^{-ikz_j} \left| g_1, \cdots e_j, \cdots g_N \right\rangle \tag{4.2}$$

where ν_j is the transition frequency of the jth atom with respect to the input photon's carrier frequency, i.e. the detuning. z_j and c_j are the position within the medium and the excitation probability amplitude for each atom, respectively. The term e^{-ikz_j} shows that the spatial phase information of the input field is imprinted on the atoms along the medium. Immediately after the absorption, the different constituents of the state in 4.2 start accumulating different phases that are proportional to their detunings, as represented by the term $e^{i2\pi\nu_j t}$. This process is called dephasing. If the width of the AFC peaks is sufficiently narrow compared to the spacing between them, then, to a good approximation, the frequency of each atom can be labeled by $m_j\Delta$, where m is an integer. The state can then be written as

$$\frac{1}{\sqrt{N}} \sum_{j=1}^{N} c_j e^{i2\pi m_j \Delta t} e^{-ikz_j} \left| g_1, \cdots e_j, \cdots g_N \right\rangle , \tag{4.3}$$

Due to the periodic nature of the atomic frequency distribution, the phases evolve to automatically rephase. When the time reaches $t = n(1/\Delta)$, where n is an integer, all the time-dependent phases become integer multiples of 2π, meaning that all the terms are in phase. At this moment, the macroscopic polarization becomes maximum and the input light is re-emitted in the originally encoded state. Ideally, all the atoms then come back to the ground level, resulting in unit-efficiency recall and the initial state given by Equation 4.1. When an input photon is re-emitted at a rephasing time with $n \geq 2$, the output photon is referred to as a higher order echo. Typically the first order echo ($n = 1$) has a much higher emission probability than the higher order echoes. Therefore, in the following, only the first

order echo will be considered.

4.3   Retrieval Efficiency

The parameters that determine the efficiency of an AFC based memory are the width (γ) and shape of the absorption peaks (i.e. Gaussian, Lorentzien, square etc.), the spacing between the peaks (Δ), the optical depth (d_1) and non-zero absorption background (d_0), which results from an imperfect AFC preparation. Assuming that the peaks have Lorentzian shape, an approximate analytic expression for the retrieval efficiency, in the case of a forward propagating echo, is given by [39, 40],

$$\eta_f = (d_1/F)^2 e^{-7/F^2} e^{-d_1/F} e^{-d_0} \tag{4.4}$$

where F is the finesse of the comb defined by $F = \Delta/\gamma$. As the comb peaks approach a delta function in shape, the finesse increases.

The terms in the above equation can be qualitatively explained. The first term represents a collective re-emission factor, as having higher d_1 means that more atoms participate in the collective re-emission process, resulting in higher retrieval probability. On the other hand, increasing F for a given d_1 reduces this probability due to the fact that having larger spacing (transmission windows) in the AFC effectively decreases the optical depth. The second term is the dephasing factor. With a higher finesse, the assumption of $\nu_j = m_j \Delta$, made in the previous section, becomes more valid and gives rise to more complete rephasing. The third term characterizes the re-absorption of the emitted light during its propagation in the medium, which can be re-emitted as high order echoes. Similar to the first term, having larger effective optical depth by increasing d_1 and/or decreasing F, increases the probability of the echo being re-absorbed by the medium, causing a decrease in the efficiency of the first order echo. The final term represents irreversible absorption due to the non-zero absorption background formed by atoms that do not participate in the collective re-emission.

As one can see, all the terms except the last, are coupled. Therefore some optimization is required to determine the configuration with experimentally accessible AFC parameters that gives the best efficiency. If there are no limits imposed to the AFC parameters, the maximum achievable efficiency is 54% due to the re-absorption effect.

One way to achieve unit efficiency is to trigger re-emission in backward direction. This can be done with two different approaches. One approach is to transfer the optical coherence to some other levels, preferably between two long-lived spin states and then convert it back by applying two counter-propagating π-pulses at different times [39]. This operation satisfies the phase matching condition and also allows on-demand recall, as explained in the next section. The other approach to achieve backwards propagation is to prepare a spatially varying frequency comb structure [66]. This can be accomplished by performing the optical pumping with counter propagating pulse sequences. In each case, for the backward propagating echo, the retrieval efficiency is approximately given by

$$\eta_b = (1 - e^{-(d_1/F)})^2 e^{-7/F^2} e^{-d_0} \tag{4.5}$$

In contrast to the forward propagating echo case, having a larger optical depth (d_1) always results in larger efficiency, as can be seen from the first term in the above expression, as re-absorption of the echo is eliminated.

A third way to achieve unit efficiency is to place the AFC medium into an impedance matched Fabry-Perot cavity [67, 68]. In this arrangement, the input mirror's reflectivity is decreased depending on the effective optical depth of the medium. Due to the strong interaction between the light and the medium inside the cavity, unit efficiency is already possible with moderate optical depths and without phase matching operations.

4.4 Storage time

An important characteristic of the basic AFC protocol is that the storage time is pre-set and inversely proportional to the spacing of the prepared peaks. Having longer storage times means preparing more closely spaced peaks and narrowing the width of the peaks accordingly in order to keep the efficiency the same. However, in real implementations there is a limit. The homogeneous linewidth sets a fundamantal limit to the teeth width, as will be discussed in the next chapter. In other words, the coherence time, which is inversely proportional to the homogeneous linewidth, sets the the upper bound for the storage time in a given material and transition.

4.5 On-Demand Retrieval

The full AFC protocol, featuring on-demand recall, requires a three-level atomic configuration with two ground levels that share a common excited level. This is usually called a Λ system. In addition to this, an auxiliary level may be needed to shelve the atomic population removed during optical pumping to create the grating. In a typical implementation with RE doped crystals, different magnetic sublevels are used to construct a Λ system with shelving states, due to their long coherence times and lifetimes. The full AFC protocol featuring on-demand recall with this type of atomic level scheme is presented in Fig. 4.2. In the protocol, first, an input photon's state is mapped onto the coherence between ground $|g\rangle_1$ and excited level $|e\rangle$ through the standard AFC protocol. Before the re-emission (at a time given by the peak spacing) takes place, applying a π-pulse on-resonant with the $|g\rangle_2 \leftrightarrow |e\rangle$ transition transfers the coherence onto the spin transition between two ground states, $|g\rangle_1$ and $|g\rangle_2$. At this stage, the AFC dephasing process stops, assuming that the spin transition does not have any broadening. When the coherence needs to be retrieved in a photonic mode, another π-pulse is applied to convert the coherence back onto the optical transition. From this moment, the atoms' phases continue to evolve and end up with the complete rephasing
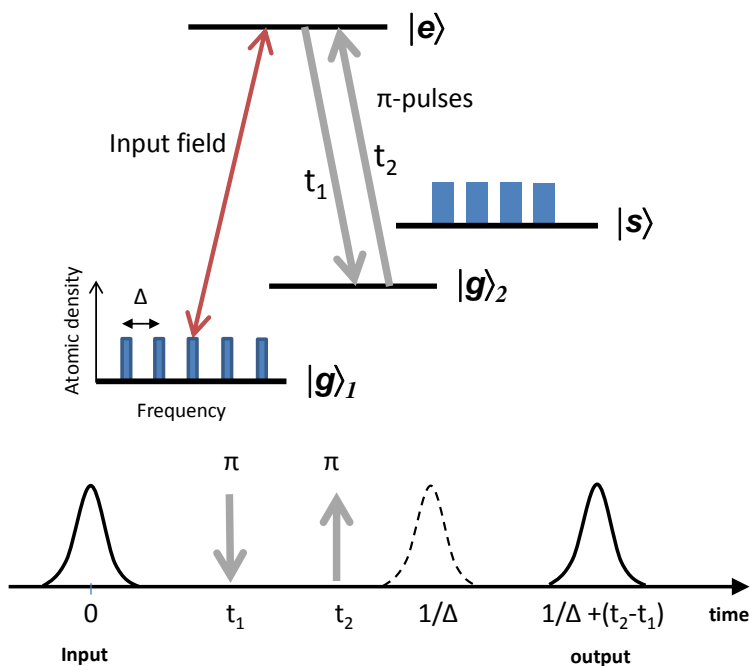
Figure 4.2: **The full AFC protocol featuring on-demand recall.** In the first step, an AFC is prepared between excited level $|e\rangle$ and ground level $|g\rangle_1$ by a frequency-selective population transfer to a long-lived shelving level $|s\rangle$. Upon absorption of input photons, the optical coherence is automatically mapped onto the $|g\rangle_1 \leftrightarrow |e\rangle$ transition. The application of a π-pulse that is resonant with the $|g\rangle_2 \leftrightarrow |e\rangle$ transition, at time t_1 maps the coherence onto the spin transition $|g\rangle_1 \leftrightarrow |g\rangle_2$. From this moment, the AFC phase evolution stops. When the coherence needs to be read-out, another π-pulse at time t_2 is applied, mapping the coherence back to the optical transition. Then the atomic phases' continue to evolve, giving rise to the re-emission of the stored photons at $T = 1/\Delta + (t_2 - t_1)$

as in the standard AFC scheme. The time difference of the application of the π pulses at t_1 and t_2 determines the storage time and thus on-demand readout can be achieved, as shown at the bottom of Fig. 4.2. Also, this scheme allows extending the storage time beyond the coherence time of the optical transition, since generally the coherence time for spin transitions is much longer than for optical transitions. A final point is that the application of the π-pulses in counter-propagating directions fulfills the phase matching conditions, which is required for unit efficiency, as discussed in the previous section.

Despite these advantages, there are a few technical issues that make the experimental

realization of the full AFC scheme at the single photon level quite demanding and challenging. First of all, it requires two ground level ($|g\rangle_1$ and $|g\rangle_2$) in addition to the population shelving state $|s\rangle$. Thus, it cannot be implemented with Tm:LiNbO$_3$ (the material investigated in this thesis), as this material lacks a third magnetic sub-level as discussed in the next two chapters. Secondly, the π-pulses must be precisely set and their spectra must be sufficiently broad to cover the entire AFC. The precision requirement of π pulses in combination with their high intensities make it quite difficult to operate the memory at the singe photon level due to the noise problems, discussed in Chapter 3.

The final issue is that the existence of inhomogeneity in the spin transitions requires RF pulse sequences to rephase spin dephasing, which brings more complications to an implementation. Despite these challenges, there have been promising demonstrations of the full AFC scheme with strong probe pulses [69, 70]. Extensive research by different research teams is progressing towards single photon level storage with the full AFC protocol.

In addition to the scheme described above, there are alternative ways to achieve on-demand recall with AFC. In brief, one way could be to combine the basic AFC approach with the CRIB-type protocols [58, 71]. In RE media that feature the DC Stark effect, controlled dephasing and rephasing can be added to the intrinsic phase evolution of the AFC by applying spatially varying electric fields, exactly as in the CRIB-type protocols (Section 3.3.1). With this technique, the input photons can be retrieved on-demand at discrete times given by the multiple of the first re-emission time of the AFC. However, the efficiency will be low for non-delta shaped absorption peaks.

Another possibility, which is exploited for the first time in this thesis, is to interpret the concept of "on-demand readout" from the operational perspective of quantum repeaters in an alternative way. In fact, the term "on-demand readout" suggests an adjustment of the "recall time" or "temporal mode" of the stored photon. However, considering that the central process in practical quantum repeaters is the simultaneous storage of several modes in

a quantum memory and retrieval of a single mode from all the stored modes, the meaning of "on-demand recall" can be translated into "selective recall". As demonstrated in Chapter 10, this selective recall can be implemented with a frequency multimode AFC that features only "pre-set delay". This replaces the requirement of on-demand recall in the time domain by on-demand recall in the frequency domain. This leads to significantly relaxed experimental challenges.

4.6 Bandwidth

Implementations of AFC memory with RE doped materials are very attractive in terms of the memory bandwidth, since the RE crystal generally possess very large inhomogenously broadened absorption lines that can be shaped into wide-comb structures. However, in practice, the energy level structure of RE media puts limitations on the bandwidth. Usually, in the preparation of an AFC via an optical pumping process, groups of atoms with certain transition frequencies are removed from the ground state $|g\rangle_1$, to a long-lived shelving state $|s\rangle$, that does not interact with the pulses to be stored (see Fig. 4.2). These frequency intervals form the troughs (transmission windows) of the AFC and the atoms that are left in the ground state build up the teeth (absorption peaks).

In order to avoid any interaction between the atoms moved to the shelving state and the optical pulse to be stored, the frequency separation between shelving state $|s\rangle$ and ground state $|g\rangle_1$ has to be larger than the bandwidth of the pulse. Generally speaking, this level separation, which depends on the RE material, sets limit for the bandwidth of an AFC. In some RE materials the level splitting can be varied with a magnetic field and thus allows tunable bandwidth limits. The bandwidth limitation imposed by level structures can be alleviated under certain conditions, which is part of our implementations and discussed in Sect.6.2.

4.7 Multimode Capacity

The multimode storage capability of a quantum memory refer to its ability to simultaneously store more than one mode as discussed in Chapter 3. Being closely linked to its large bandwidth capacity, the AFC protocol also has an excellent temporal and spectral multimode storage capacity, as experimentally demonstrated in Chapter 6 and 10, respectively. In the temporal multimode storage scheme, a train of N pulses is sent into an AFC medium. The pulses are retrieved such that the first pulse does not leave the medium before the last pulse is stored. For this to work, the total duration of the pulse train needs to be equal to or smaller than the storage time. Therefore, the maximum number of temporal modes that can be simultaneously stored in a given AFC is roughly determined by $N = T/\tau$, where T is the storage time and τ is the duration of each pulse. Normally, each pulse's bandwidth needs to be less than or equal to the AFC bandwidth, which is $m\Delta$, where m is the number of the peaks in the AFC. Recall that the storage time equals $T = 1/\Delta$. If these definitions are plugged into the above expression, it can be seen easily that the maximum number of temporal modes that can be stored is equal to the number of the peaks in the AFC. Adding more peaks to AFC is thus sufficient to increase the multimode capacity, unlike other quantum memory protocols, which require more optical depth for larger multimode capacity, as explained in Chapter 3.

Similarly, the large frequency mode capacity of AFC is due to the large bandwidth capacity. A broadband AFC can be divided into many small frequency intervals, each one defining a frequency mode. In this way, many frequency modes that occupy a single temporal mode can be stored simultaneously using a broadband AFC approach. This is demonstrated in Chapter 10.

Chapter 5

A novel material for Quantum Memory: Tm:LiNbO$_3$ Waveguide

Developing an optical quantum memory device requires implementing a quantum memory protocol in a suitable material. There are various material candidates such as warm and ultracold gas ensembles, single atoms in high-finesse cavities, NV centers and RE-ion doped crystals. One of the key criteria for a suitable quantum memory material is a long coherence time, which directly determines quantum state storage capabilities of a quantum memory. From this aspect, cryogenically cooled RE-ion doped crystals are very attractive, since they usually posses long coherence times on optical and spin transitions. Moreover, their large inhomogeneously broadened absorption lines on various optical transitions, in conjunction with the photon-echo based quantum memory protocols, allow for a broadband solid-state quantum memory. On the other hand, the spectroscopic properties of these materials strongly depend on the physical environment to which they are exposed; such as temperature, magnetic fields, electric fields, dopant concentration as well as the structure and the type of host crystals. Therefore, establishing a suitable RE-ion doped crystal for quantum memories requires extensive spectroscopic study and characterization. Consequently in the beginning of this thesis, we investigated spectroscopic properties of promising quantum memory material, a Tm^{3+}:LiNbO$_3$ waveguide, in view of photon-echo quantum memory protocols. This study underpins all other quantum memory implementations covered in the rest of this thesis.

In this study, the fabrication and room temperature characterization of the material was performed by Prof. Sohler's group at the University of Paderborn in Germany. The rest of the experiments and all cold temperature analysis were carried out by our group in Calgary. I contributed to this study at the following stages: Building the experimental

setups, performing the measurements, analyzing and interpreting the results, writing some of the sections and editing the manuscript. Our findings from this investigation were published in the September 2010 issue of the Journal of Luminescence. The following section is the published version of this article that has been re-formatted to be consistent with the structure of this thesis.

5.1   Paper I

Spectroscopic investigations of a Ti:Tm:LiNbO$_3$ waveguide for photon-echo quantum memory

Neil Sinclair[a,1], Erhan Saglamyurek[a,1], Mathew George[b], Raimund Ricken[b], Cecilia La Mela[a], Wolfgang Sohler[b], and Wolfgang Tittel[a]

[a]*Institute for Quantum Information Science, and Department of Physics and Astronomy, University of Calgary, 2500 University Drive NW, Calgary, Alberta T2N 1N4, Canada*

[b]*Department of Physics - Applied Physics, University of Paderborn, Warburger Str. 100, 33095 Paderborn, Germany*

[1] *These authors contributed equally to this work*

Abstract

We report the fabrication and characterization of a Ti^{4+}:Tm^{3+}:LiNbO$_3$ optical waveguide in view of photon-echo quantum memory applications. Specifically, we investigated room- and cryogenic-temperature properties of the waveguide, and the Tm^{3+} ions, via absorption, spectral hole burning, photon echo, and Stark spectroscopy. For the Tm^{3+} ions, we found

45

radiative lifetimes of 82 μs and 2.4 ms for the $^3H_4$ and $^3F_4$ levels, respectively, and a 44% branching ratio from the $^3H_4$ to the $^3F_4$ level. We also measured an optical coherence time of 1.6 μs for the $^3H_6 \leftrightarrow {}^3H_4$, 795 nm wavelength transition, and investigated the limitation of spectral diffusion to spectral hole burning. Upon application of magnetic fields of a few hundred Gauss, we observed persistent spectral holes with lifetimes up to seconds. Furthermore, we measured a linear Stark shift of 25 kHz·cm/V. Our results are promising for integrated, electro-optical, waveguide quantum memory for photons.

5.1.1 Introduction

Quantum memory constitutes a key element for quantum repeaters [1], as well as linear optical quantum computing [2]. Impressive experimental and theoretical progress has been reported over the past few years [3,4], and gives hope that a workable quantum memory can eventually be built.

The *photon-echo quantum memory* [5] is based on all-optical storage of classical data, investigated already thirty years ago [6-9]. It relies on the interaction of light with a large ensemble of atoms with a suitably prepared, inhomogeneously broadened absorption line. In materials with natural broadening, this tailoring can be achieved by frequency-selectively removing absorbers from the ground to an auxiliary state using optical pumping techniques [10-13], possibly followed by controlled broadening of the resulting absorption lines, e.g. through position dependent Stark shifts.

The absorption of light in photon-echo quantum memory leads to mapping of its quantum state onto atomic coherence, which rapidly decays as the absorbers have different resonance frequencies. To recall the light, i.e. map the quantum state back onto light, the initial coherence has to be re-established. Two possibilities have been identified: In *Controlled Reversible Inhomogeneous Broadening* (CRIB), the detuning of each absorber with respect to the light carrier frequency has to be inverted [14-17]. Another possibility is to tailor the initial absorption line into an *Atomic Frequency Comb* (AFC), resulting in re-emission

of the stored light after a time that depends on the periodicity of the comb [6,18,19]. In both approaches, the memory efficiency can theoretically reach 100% [14,17,18,20]. For extended storage in CRIB or AFC (then also allowing for on-demand recall), the excited atomic coherence can be transferred temporarily to longer lived coherence, e.g. between hyperfine ground states. This reversible mapping of coherence can be achieved by means of two π-pulses [21], or via a direct Raman transfer [22-25].

Rare-earth-ion doped crystals (RE crystals) are promising material candidates for photon-echo quantum memories [5]. Key findings include the storage of qubit states encoded into attenuated laser pulses [19], light storage with up to 66% efficiency [20,26-28], mapping of photonic quantum states onto collective atomic spin states [21], and simultaneous storage of 64 photon modes [29]. Furthermore, observation of more than 30 s coherence time of a ground state hyperfine transition in $Pr:Y_2SiO_5$ [30] is highly promising for long-term storage in this crystal, as well as other RE crystals.

In this article we investigate a novel storage medium, a $Ti^{4+}:Tm^{3+}:LiNbO_3$ optical waveguide, in view of the requirements for photon-echo quantum memory. This material combines interesting features arising from the specific RE dopant, the host material, as well as the waveguide structure.

As depicted in Fig. 5.1, the thulium (Tm) $^3H_6 \leftrightarrow {}^3H_4$ transition features absorption at $\sim$795 nm, which is a wavelength where air has minimal transmission loss, where photon pairs or entangled photon pairs are conveniently created [31-34], and where high-efficiency and simple-to-operate single photon detectors based on Silicon Avalanche Photodiodes are commercially available [35]. This makes thulium-based quantum memory interesting for applications in quantum communication and linear optical quantum computing. Furthermore, the $^3F_4$ bottleneck state, whose energy is situated roughly half way between the $^3H_6$ and $^3H_4$ levels [36], allows for efficient and broadband spectral tailoring [37]. In addition, the application of suitably oriented magnetic fields has been reported to result in long-lived nuclear

spin levels forming Λ systems (e.g. in Tm:YAG), which may be used for optical pumping or long-term storage [38-43].

Low-temperature spectroscopic investigations of Tm doped crystals have so far mostly concentrated on Tm:YAG (see also [44]), and, very recently, Tm:LiNbO$_3$ [45-48]. For Tm:YAG, they have already led to implementations of the AFC protocol [26,49].

Due to lack of inversion symmetry, lithium niobate (LiNbO$_3$) crystals feature non-linear effects [50]. The crystal symmetry also results in permanent electric dipole moments for RE states, i.e. the possibility to externally control resonance frequencies via Stark shifts [51-52], as required for CRIB. Low-temperature properties of RE doped LiNbO$_3$ have been characterized in Refs [46,47,52-54] e.g. for the development of radio-frequency analyzers [55].

Given its non-linear properties, LiNbO$_3$ has become an import material for the telecommunication industry. Procedures to implement waveguides, either through proton exchange [56], or Titanium indiffusion [57], have been developed, allowing for simple integration with fibre-optics components. In addition, given their small transverse dimensions of 5-10 μm (depending on the light wavelength), traveling wave electrodes can be spaced closely, resulting in commercial intensity and phase modulators with switching (π) voltages of only a few volts, and switching times below 100 picoseconds [58]. Furthermore, as light intensities inside these waveguides can be very large, strong non-linear interactions are possible, including frequency up-conversion of photons [59]. For photon-echo quantum memory, these properties promise simple integration with fibre quantum networks, sub-ns Stark shifting, and large Rabi frequencies. LiNbO$_3$ waveguides have been used for studies relevant to quantum memory in [52,60-62].

The remainder of this article is structured as follows: In Sec. 5.1.2, we describe and characterize the fabrication process of the waveguide. Next, in Sec. 5.1.3, we discuss polarization dependent absorption profiles measured at room and cryogenic temperatures. After a description of the experimental setup used for all following low-temperature measurements in
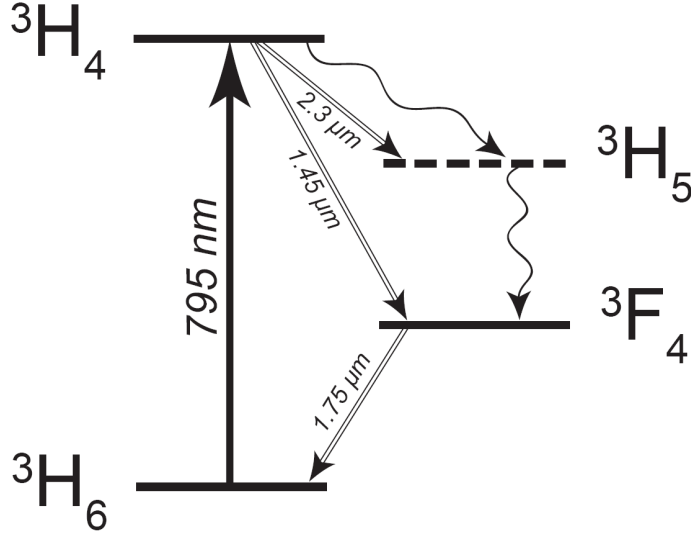
Figure 5.1: **S**implified energy level diagram of Tm:LiNbO$_3$ showing the electronic levels relevant to this work.

Sec. 5.1.4, Sec. 5.1.4 focuses on relevant radiative lifetimes and branching ratios. Our investigations of optical coherence times, and the limitation of spectral hole burning imposed by spectral diffusion are presented in Sec. 5.1.4, followed by Stark-effect-based modification of narrow absorption lines. Finally, in Sec. 5.1.5, we discuss our results in view of photon-echo quantum memory. This concludes the article.

5.1.2 Waveguide fabrication and characterization

Tm-diffusion doping of LiNbO$_3$[1]– Commercially available 0.5 mm thick Z-cut wafers of un-doped optical grade congruent lithium niobate (CLN) were used as starting material. Samples of 12 mm x 30 mm size were cut from these wafers and doped by thulium near the +Z-surface before waveguide fabrication. The doping was achieved by in-diffusing a vacuum deposited (electron-beam evaporated) Tm layer of 19.6 nm thickness. The diffusion was performed at 1130°C during 150 h in an argon-atmosphere followed by a post treatment in oxygen (1 h) to get a full re-oxidization of the crystal.

   To determine the diffusion coefficient of Tm into Z-cut CLN, secondary neutral mass

---

[1]See Appendix-A for the details of the structure of a Tm:LiNbO$_3$ crystal
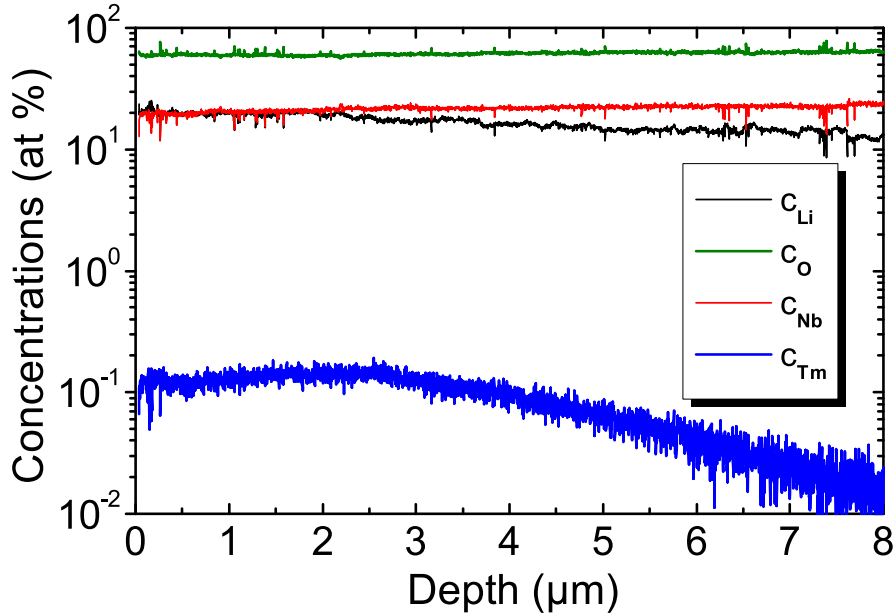
Figure 5.2: **Measured concentrations of Tm, Li, Nb, and O versus depth, using SNMS with 700 eV Ar-ions.**

spectroscopy (SNMS) was performed using 700 eV Argon-ions for ion milling. Ions and electrons were extracted from the plasma source with a duty cycle of 4:1 at a rate of 320 kHz to avoid charging of the insulating CLN-substrate. SNMS was chosen instead of secondary ion mass spectroscopy (SIMS) to significantly reduce matrix effects (see e.g. [63]). In Fig. 5.2, the concentration profiles versus depth have been recorded for thulium (Tm), lithium (Li), niobium (Nb) and oxygen (O). Interestingly, the Li-concentration slightly increases towards the surface, although it is expected that Tm occupies regular Li-sites similar to Er-ions when incorporated in CLN by diffusion [64].

In Fig. 5.3, the Tm concentration is plotted on a linear scale versus the depth. The slight dip close to the surface is unexpected and needs further investigations. Fitting a Gaussian profile to the concentration curve leads to a 1/e-penetration depth $d_{1/e}$ of about 6.5 μm. Together with the diffusion parameters, a diffusion coefficient $D = d_{1/e}^2/(4t) = 0.07 \mu m^2/h$, where t denotes the diffusion time, was evaluated for 1130°C. At this temperature, this is
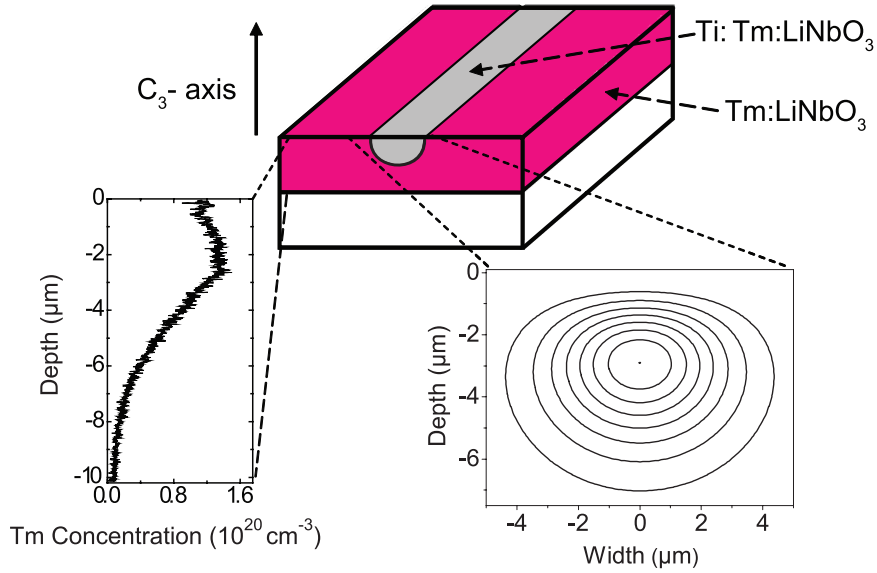
Figure 5.3: Scheme of the waveguide geometry with the measured Tm concentration profile on the left and the calculated intensity distribution of the fundamental TM-mode at 795 nm wavelength on the right. Iso-intensity lines are plotted corresponding to 100%, 87.5%, 75% etc. of the maximum intensity.

seven times larger than the corresponding coefficient for Erbium-diffusion into CLN [65]. The maximum Tm concentration of about $1.35 \cdot 10^{20}$ cm^{-3} corresponds to a concentration 0.74 mole %, which - according to Ref. [64] - is considerably below the solid solubility of Tm in CLN.

Ti-indiffused waveguides in Tm:LiNbO$_3$– On the Tm-diffusion doped surface of the substrate, a 40 nm thick titanium (Ti) layer was deposited using electron-beam evaporation. From this layer, 3.0 μm wide Ti stripes were photolithographically defined and subsequently in-diffused at 1060°C for 5 h to form 30 mm long optical strip waveguides. In the wavelength range around 775 nm, the waveguides are single mode for TE- and TM-polarization (see Fig. 5.3).

The waveguide end faces were carefully polished normal to the waveguide axis, forming a low-finesse resonator. This allows to determine the total waveguide propagation loss at room temperature, including absorption and scattering loss, by the Fabry-Perot method [66]. A

stabilized, single frequency Ti:Sapphire laser was used to measure the transmission of the low-finesse waveguide resonator as function of a small temperature change at a number of fixed wavelengths in the range between 750 nm and 807 nm. From the contrast of the measured Fabry-Perot response, the propagation loss was deduced for all wavelengths [66]. The results are presented in Fig. 5.4 for TM-polarization.

In addition, the waveguide propagation loss was determined at room temperature and 729 nm wavelength, where negligible absorption by the Tm-ions can be expected. Therefore, the measured loss coefficients reflect the scattering loss alone; they are 0.2 dB/cm for TE- as well as for TM-polarization. As the scattering loss is only weakly dependent on the wavelength, it can be regarded as a background for the Tm-induced absorption loss.

We repeated the off-resonant, polarization dependent loss measurement at 3.5 K, leading to strongly polarization dependent transmission. The exact origin of this difference compared to the room-temperature measurement requires further investigation. For this as well as all subsequent low-temperature measurements, the sample was cut to 15.7 mm and repolished. All room temperature measurements have been performed using a 30 mm long waveguide.

5.1.3   Spectroscopy of inhomogeneous broadening

Reversible atom-light interaction requires absorption on the transition between the lowest lying Stark levels in the ground and excited electronic states. To gain information about $^3H_4$ and $^3H_6$ Stark splittings, we injected weak, broadband, polarized light into the waveguide. Using wave plates, we set the polarization to TE or TM, and measured power spectra of transmitted light using an optical spectrum analyzer.

Room temperature characterization– The transmission through a 30 mm long waveguide for TE and TM-polarized light is shown in Fig. 5.5. It has been normalized to the incident spectral power density of the broadband tungsten lamp used in this experiment. We observe broad absorption, reflecting different transitions between Stark levels in the $^3H_6$ and $^3H_4$ multiplets (superimposed with inhomogeneous broadening), and the thermal distribution of
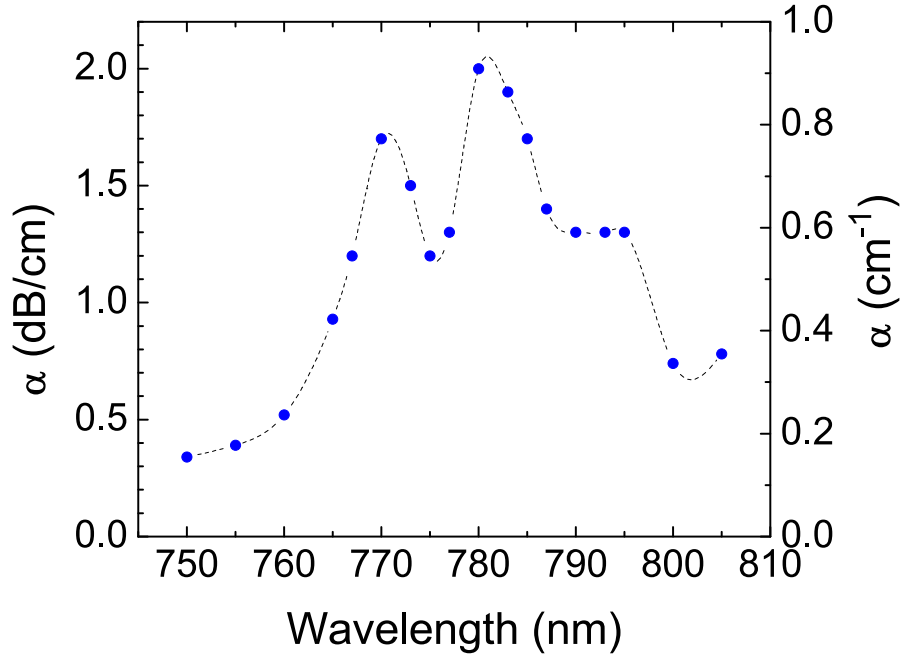
Figure 5.4: **Measured loss coefficient (α) for TM-polarization as a function of wavelength.** Data points are connected by spline fitting as a guide for the eye.

the population in the electronic ground state. In addition, a strong polarization dependence of absorption is observed, confirming previous studies performed on bulk crystals [45,67].

Low temperature characterization- A similar measurement at 3.5 K resulted, for close-to TM polarization, in the absorption profile shown in the inset of Fig. 5.6. Due to the large optical depth of our sample, reflecting redistribution of population in the ground state Stark levels, we observe an almost flat-lined spectrum.

To resolve the Stark splittings, coherent laser light was coupled into the waveguide, and its frequency was swept between 791 and 796 nm in 0.1 nm steps. The laser intensity was optimized to resolve different Stark transitions after having partially bleached the absorption line. The resulting optical depth, shown in the main plot of Fig. 5.6, was determined at each measured wavelength upon normalization to the probe light. Using results from [48,68], we can identify four transitions between the ground and excited state Stark multiplets, with splittings of 0.48 ± 0.05 nm and 0.93 ± 0.05 nm, respectively (i.e. 7.6 ± 0.8 cm^{-1} and 14.7
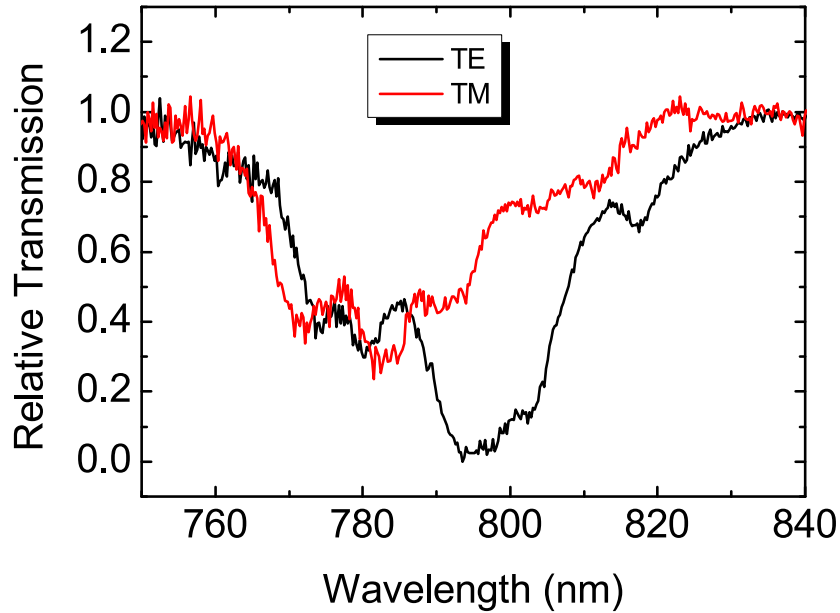
Figure 5.5: (Color online) **Relative transmission through the Ti:Tm:LiNbO$_3$ waveguide for TM- and TE-polarization, respectively, as a function of wavelength.** The resolution bandwidth of the optical spectrum analyzer used in this experiment was 2 nm due to the low spectral power density of the thermal radiator.

$\pm$ 0.8 cm^{-1}, respectively). This indicates the presence of a zero-phonon line in the high wavelength region. According to calculations taking into account the observed splittings, only a small fraction of atomic population $\sim$1% occupies higher energy Stark levels of the ground state multiplet.

5.1.4 Narrow-band spectroscopic investigations

Experimental setup

A schematic of the experimental setup used for the low-temperature spectroscopic measurements described hereafter is depicted in Fig. 5.7.

A continuous wave, external cavity diode laser was tuned to 795.520 nm wavelength, where we found optical coherence properties of our sample in the absence of a magnetic field to be promising. The laser's linearly polarized output was amplified, and frequency and intensity modulated using a 400 MHz acousto-optic modulator in double-pass configuration,
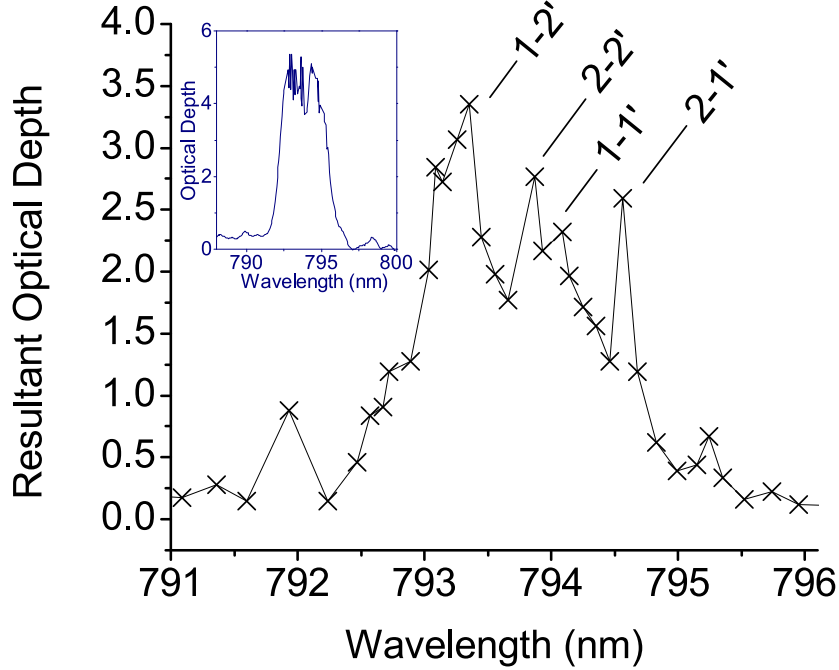
Figure 5.6: **Main figure: Absorption profile (after partial bleaching) at 3.5 K obtained using a single frequency laser:** Indicated are transitions between different Stark levels: 1 and 2 denotes the lowest energy levels within the $^3H_6$ multiplet, primed labels represent the lowest $^3H_4$ levels. **Inset: The same inhomogeneous broadening probed using weak broadband light.**

driven by a 10 GS/s arbitrary waveform generator and an amplifier. This allowed the creation of optical pulses with peak powers up to $\sim$4 mW and durations between 20 ns and 500 ms for photon-echo sequences and spectral hole burning. Here and henceforth, all pulse powers are specified at the input of the cryostat. After passing a $\lambda/2$ wave plate, the light was coupled into a single-mode optical fiber, and sent into the 3.5 μm wide, single mode Ti:Tm:LiNbO$_3$ waveguide. The light's polarization, which could be partially controlled using the wave plate, was set as to maximize the transmission, i.e. as to minimize the distance to TM. To inject and retrieve the light from the waveguide, optical fibres were butt-coupled against its front and end face using high precision translation stages, resulting in fibre-to-fibre coupling loss around 15 dB. The waveguide was placed in a pulse tube cooler and cooled to 3 K. A superconducting coil allowed the generation of magnetic fields along the crystal's C$_3$-axis, and electric fields could be generated along the same direction using aluminum electrodes
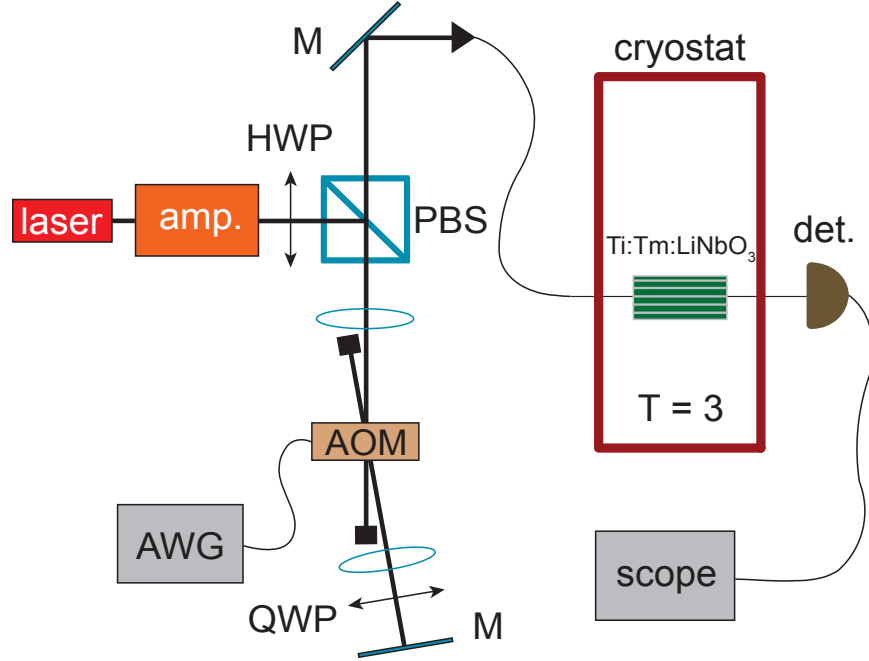
Figure 5.7: **Schematics of the experimental setup used for the narrow-band measurements at cryogenic temperature:** HWP: half-wave plate; QWP: quarter-wave plate; PBS: polarization beam splitter; AOM: acousto-optic modulator; AWG: arbitrary waveform generator; M: mirror; amp.: optical amplifier; det.: detector; scope: oscilloscope.

that were firmly pressed against the crystal. Transmitted pulses and echoes were detected using either a sensitive 10 MHz, or a fast 125 MHz photodetector, which was then connected to a 3 GHz bandwidth oscilloscope with 10 GS/s sampling rate. All measurements conducted at zero magnetic field were repeated every 100 ms, and generally averaged 300 times. Upon magnetic field application, the repetition period was set to 60 s, which was required to avoid accumulation effects, and the number of averages was reduced to 25.

Population relaxation dynamics

To optimize optical pumping strategies, and determine possibilities for long-term storage, it is important to examine the relaxation avenues and dynamics of population in atomic levels involved in the light-atom interaction. The level scheme for thulium doped crystals in the case of zero magnetic field is depicted in Fig. 5.1. Upon excitation of the lowest lying Stark level within the $^3H_4$ manifold, atoms will eventually decay back to the ground state,

either directly, or via the $^3H_5$ and $^3F_4$ levels. As the radiative lifetime of the $^3H_5$ level is short compared to the lifetimes of the $^3H_4$ and $^3F_4$ levels [45], we model atomic decay, i.e. radiative lifetimes and branching ratio (given by the rate of decay from $^3H_4$ to $^3F_4$ relative to the overall decay from $^3H_4$), using a simplified three-level scheme comprising only the $^3H_6$ ground state, the $^3F_4$ bottleneck state, and the $^3H_4$ excited state.

As material absorption is dependent upon population differences between the states coupled by the probe light, we can assess population dynamics through time-resolved spectral hole burning. To this end, we first transfer population to the excited state using a 5-10 μs long *burning* pulse with peak power of 7 μW, and then probed the shape and depth of the created spectral hole after a *waiting time* ranging from 10 μs to 15 ms using a chirped *reading* pulse. The power of the reading pulse, around 1 μW, was chosen as to not alter the population distribution created by the burning pulse. Fig. 5.8 depicts the time dependent depth of the spectral hole, which we found to be proportional to the hole area (i.e. the effect of spectral diffusion, leading to a waiting-time-dependent hole width, was not visible in this measurement).

We model the decay using three-level rate equations, leading to

$$\frac{\Delta d(t)}{\Delta d(0)} = (1 - B)e^{-t/T_{1e}} + Be^{-t/T_{1b}} \tag{5.1}$$

where $\Delta d(t)$ denotes the reduction of optical depth $d = \alpha L$ at the centre of the spectral hole at time t after burning, α is the absorption coefficient, L the sample length, T_{1e} and T_{1b} are the T_1 lifetimes of the excited and bottleneck states, respectively, and $B = \frac{\beta}{2}\frac{T_b}{T_b - T_e}$ identifies the branching ratio β. We find the time-dependent population difference to be characterized by a fast exponential decay with a lifetime of $T_{1e} = 82 \pm 2$ μs, and a slower exponential decay from $^3F_4$, characterized by $T_{1b} = 2.364 \pm 0.198$ ms. Both decay constants agree with previous measurements [69]. Furthermore, we find a branching ratio of 0.436 ± 0.017.

We also performed hole burning studies under application of magnetic fields between
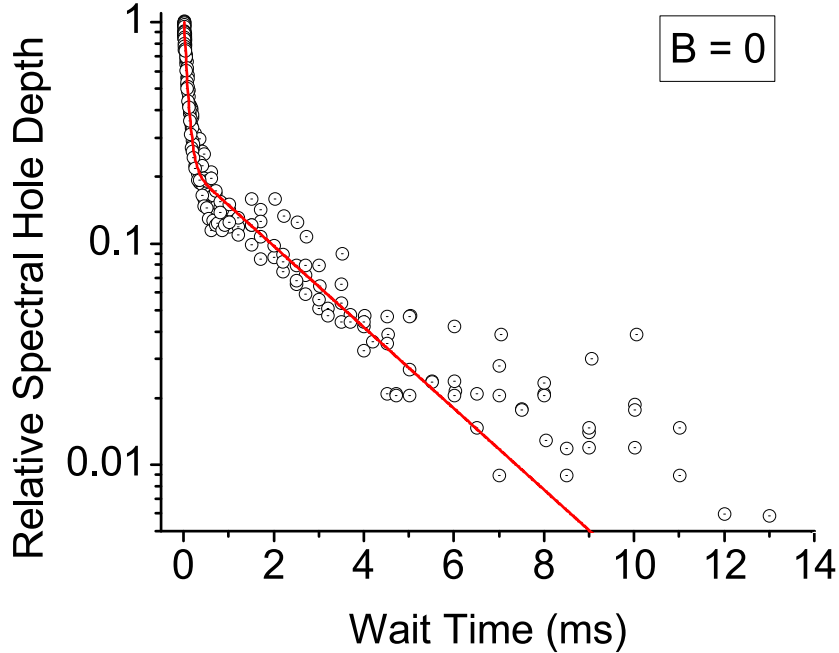
Figure 5.8: **Spectral hole decay under zero magnetic field:** Plotted circles denote the normalized spectral hole depth as a function of the waiting time between burning and reading pulses. Two exponential decays are easily identified, yielding radiative lifetimes of 82 μs and 2.4 ms for the ^{3}H$_4$ and ^{3}F$_4$ levels, respectively. The branching ratio into the ^{3}F$_4$ level is approximately 44%.

100 and 1250 Gauss, oriented parallel to the crystal C$_3$-axis. For these measurements, we increased the burning time to 500 ms, and varied the waiting time between 100 ms and 6 s so that population in the ^{3}H$_4$ and ^{3}F$_4$ levels could be ignored. As depicted in Fig. 5.9, this allowed the observation of spectral holes persisting during waiting times of up to seconds, with the decay of the hole depth being again well described by the sum of two exponentials. Furthermore, the two decay times change with magnetic field, as depicted in Fig. 5.10. This indicates the appearance of two, magnetic field dependent atomic levels with long lifetimes, and suggests maximum lifetimes at magnetic fields around 600 G.

While we have not been able to identify the levels involved in the long-term storage, e.g. through the observation of additional holes or anti-holes that indicate field-induced level splitting [70], we believe that ^{3}H$_6$ nuclear hyperfine plays a role. Note that 90 MHz splitting has been reported at 700 G [47]. We point out that the direct relaxation between different
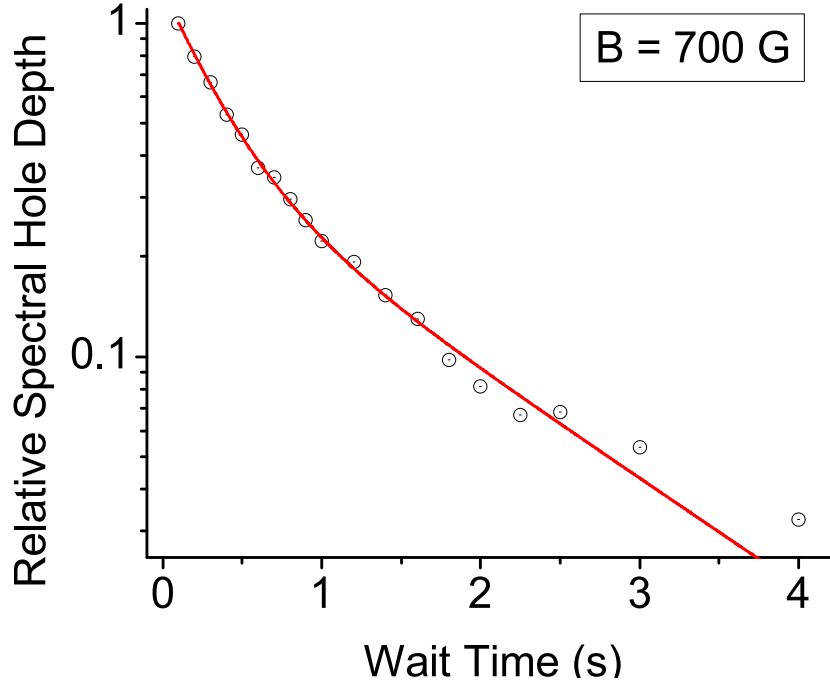
Figure 5.9: **Spectral hole depth as a function of the waiting time for a magnetic field of 700 G:** The observation of two exponential decays indicates the existence of long-lived, ground state sub-levels.

nuclear spin states in the excited and ground state multiplets is likely to be forbidden in the case where the magnetic field is parallel to the crystal C_3-axis [39]. The observed long-lived storage thus probably involves a (spin mixing) relaxation pathway including the $^3H_5$ level. The role of superhyperfine interaction of thulium ions with neighboring lithium or niobium ions, leading to level splitting of $\sim$ 1 MHz at 700 G [47], cannot be assessed from our measurements and requires more investigations.

Furthermore, relaxation between different ground states, which gives rise to the curves shown in Figs. 5.9 and 5.10, is likely to involve several contributions, including spin-lattice relaxation, spin-spin flip flops between neighboring Tm ions, or interactions of Tm ions with other magnetic impurities [71-76]. Further studies at different temperatures and with crystals with smaller Tm ion concentration are in progress.

To summarize this section, we have observed a short lifetime of the $^3H_6$ level compared to the $^3F_4$, and the $^3H_4$ sub-levels. We have also identified a large branching ratio from
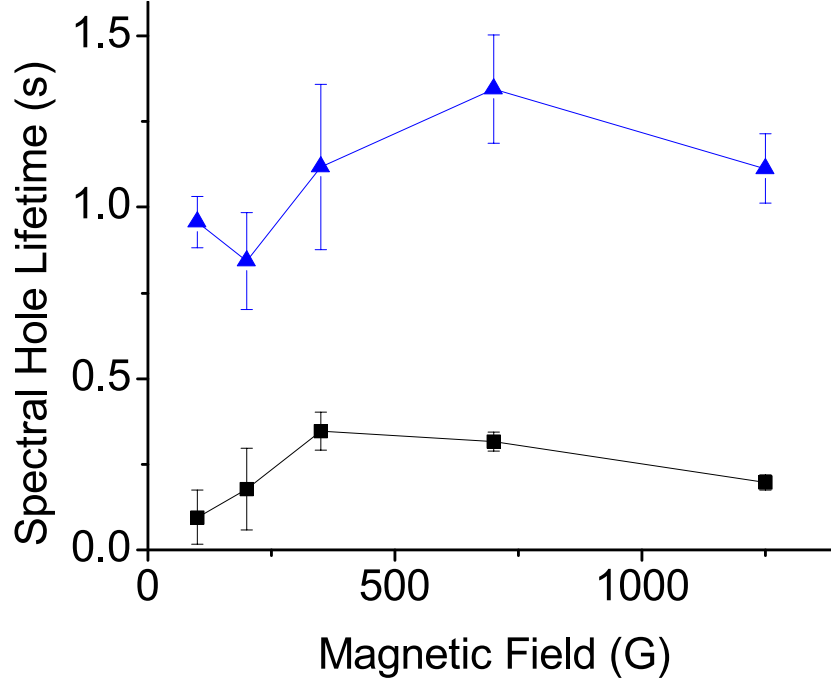
Figure 5.10: **Magnetic field dependence of the two decay times extracted from measurements of the spectral hole depth as a function of the waiting time.** The case B = 700 G is shown in Fig. 5.9.

$^3H_4$ to $^3F_4$. These observations identify two potential approaches to spectral tailoring, either involving the bottleneck state (maybe taking advantage of stimulated emission [13,77]), or the magnetic field dependent ground states as an auxiliary state. In this context, the existence of the bottleneck state is of particular interest. Indeed, due to the large energy gap relative to the $^3H_6$ and $^3H_4$ electronic levels, population pumped into this state during spectral tailoring does not interact with light coupling the ground and excited states. This allows tailoring of the initial absorption line over a spectral interval that is in principle only limited by the inhomogeneous broadening of the $^3H_6 \leftrightarrow {}^3H_4$ transition, and not by energy spacings in the ground or excited levels [11]. In other words, use of the bottleneck state for optical pumping could allow storage of short pulses of light with spectral width exceeding GHz.

Furthermore, it may be possible to reversibly map optically excited coherence ($^3H_6 \leftrightarrow {}^3H_4$ transition) onto $^3H_6 \leftrightarrow {}^3F_4$ coherence, or long-lived ground state coherence. However, more investigations are required, for instance concerning the nature of the coupling between the

60

^{3}H$_4$ and ^{3}F$_4$ states, or the possibilities for a Raman transfer into ^{3}H$_6$ ground states.

Optical coherence and spectral diffusion

For photon-echo quantum memory, the initial inhomogeneous absorption line must be tailored into one or more narrow lines using frequency selective optical pumping. In the case of CRIB, the width of the resulting spectral feature determines the time quantum information can be stored in optical coherence [78]. For AFC, it determines the spacing of the teeth in the comb structure, which, in turn, sets the storage time in optical coherence [18]. Material dependent constraints to this time arise from non-zero homogeneous line width Γ_{hom}, which is limited by natural broadening: $\Gamma_{hom}^{nat} = 1/(2\pi T_{1e}) \approx 1.9$ kHz, phonon broadening [79], as well as long-term spectral diffusion [74,80,81].

To assess the short-term homogeneous line width, we employed two-pulse photon-echoes. Two 20 ns long pulses, with peak powers ~ 3 mW that maximized the observed echo, were sent into the thulium waveguide, and the relative *delay* was varied from 100 ns to 1.8 μs in steps of 25 ns. Fig. 5.11 depicts the resulting peak echo powers for the case of zero magnetic field. We fit the decay of the peak echo intensity I (which is proportional to power) with the Mims expression [82]:

$$I = I_0 \exp(-4t/T_2)^x \tag{5.2}$$

where I_0 denotes the maximum echo intensity, T_2 is the phase memory (coherence) time and x characterizes spectral diffusion. The fit revealed a phase memory time of 1.580 ± 0.008 μs, equivalent to a homogeneous line width of ~ 200 kHz, and a spectral diffusion parameter x of 1.072 ± 0.009. We obtained similar results for non-zero fields up to 250 Gauss. This indicates that the short-term homogeneous line width at 3 K is dominated by phonon scattering.

Beyond the short-term homogeneous line width, the narrowest spectral feature that can be generated through optical pumping is limited by spectral diffusion. Spectral diffusion is caused by fluctuations of each ion's transition frequency due to the dynamic nature of the ion's environment. This causes broadening of the homogeneous line width over time. The
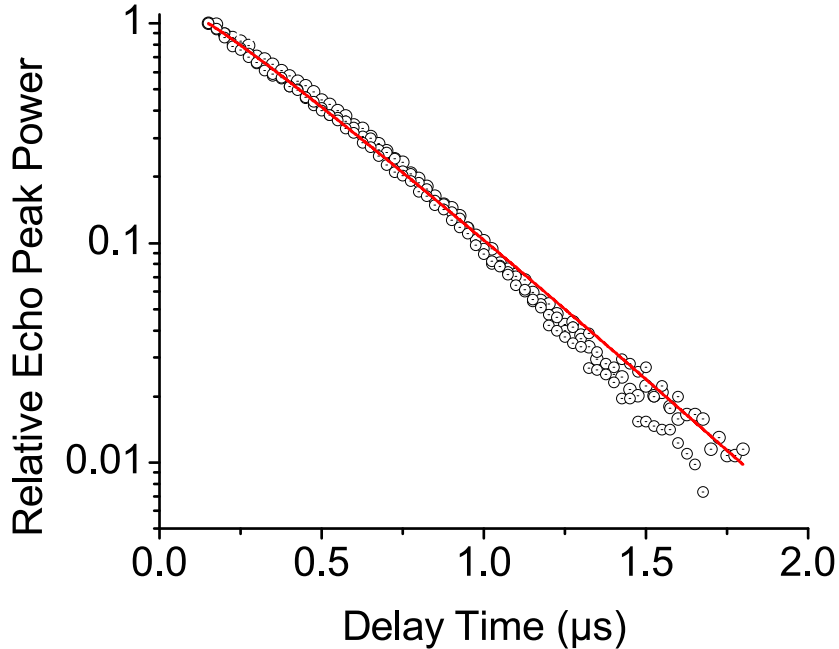
Figure 5.11: **Two pulse photon-echo peak powers measured under zero magnetic field:** Plotted circles are normalized echo powers as a function of the delay time between the two pulses. Fitted is the Mims expression giving a coherence time of 1.6 μ with nearly absent spectral diffusion.

three pulse photon-echo (3PPE), or stimulated photon-echo, is a useful tool to investigate spectral diffusion [74].

We performed a series of 3PPE experiments to probe spectral diffusion in our sample. All experiments were carried out at zero magnetic field. In the measurements, for three different *delay* settings between the first two pulses, we varied the *waiting* time, i.e. the time between the second and the third pulse, from 1 μs to 400 μs with 5-10 μs increments. The echo peak power was measured for each delay and waiting time, and each set of measurements (i.e. measurements with a specific delay time) was normalized to the echo peak power at 1 μs waiting time. The results are illustrated in Fig. 5.12.

To interpret the data, we employed the spectral diffusion model discussed in Ref. [74]. In this model, the peak intensity I of the stimulated echo is determined by the relative dephasing during the delay time t_D, the decay of the excited level population during the waiting time t_W, and diffusion mechanisms which broaden the line into the time-dependent
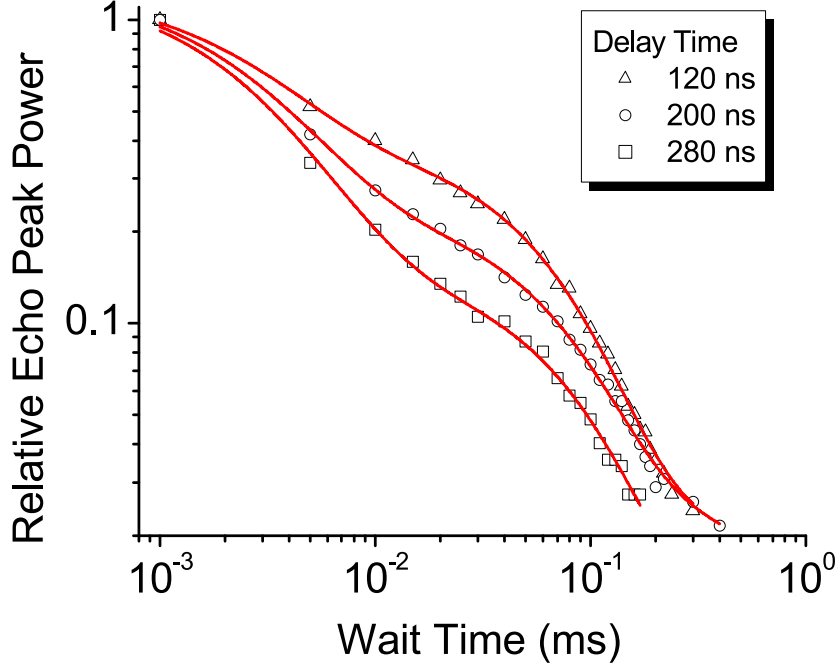
Figure 5.12: **Decay of stimulated echo with waiting time for delay times of 120 ns (triangle), 200 ns (circle) and 280 ns (square), respectively.**

effective line width Γ_{eff}. In its general form, the 3PPE intensity can be written as:

$$I(t_W, t_D) = I_0 F(t_W) \exp\left\{ -4\pi t_D \Gamma_{eff}(t_D, t_W) \right\} \tag{5.3}$$

where I_0 denotes the maximum echo intensity, $F(t_W) = (1-B)e^{-2t_W/T_{1e}} + Be^{-2t_W/T_{1b}}$ describes the population decay during t_W, and B is defined as in Eq. 5.1. The effective line width describes spectral diffusion during both the delay and waiting time, and is given by:

$$\Gamma_{eff}(t_D, t_W) = \Gamma_0 + \frac{1}{2}\Gamma_{SD}\left[Rt_D + (1 - \exp(-Rt_W))\right] \tag{5.4}$$

where Γ_0 is the short-term line width in absence of spectral diffusion, and Γ_{SD} denotes the maximum additional line width due to spectral diffusion, which occurs at rate R.

To fit our data, we fixed the bottleneck level lifetime to 2.4 ms, obtained through the spectral hole burning measurements discussed above. This was required due to the echo intensity reaching noise level after 200 μs, which is too short for the fit to generate a reliable lifetime. We also used the data obtained from the 2PPE measurements to extract an intrinsic

63

homogeneous line width of $\Gamma_0 = 152 \pm 2$ kHz via Eq. 5.3, in reasonable agreement with the result of ~ 200 kHz found via Eq. 5.2. Fitting all delay settings yielded an average excited level lifetime and branching ratio of 83 ± 8 μs and 0.23 ± 0.03, respectively, in reasonably good agreement with the more reliable values obtained from the spectral hole burning measurements.

Furthermore, the fit yielded $\Gamma_{SD} = 930 \pm 51$ kHz and a spectral diffusion rate of 227 ± 24 kHz, and the diffusion model thus predicts that the effective line width

$$\Gamma_{eff}(t_W) = \Gamma_0 + \frac{\Gamma_{SD}}{2}\big[1 - \exp\{-Rt_W\}\big] \tag{5.5}$$

saturates at around 630 kHz after a waiting time of $\sim$50 μs. When assessed through spectral hole burning, this leads to a homogeneous line width of $\Gamma_0 + \Gamma_{SD}$=1082 kHz [83].

To verify this prediction, we performed another series of spectral hole burning measurements with burning and waiting times of 5 μs and 50 μs, respectively. Varying the power of the burning pulse from 400 to 4 μW, and extrapolating the hole width to zero burning power [84], we find a homogeneous line width of 1.5 ± 0.1 MHz. Taking into account laser frequency jitter of ~ 1 MHz, this is consistent with the prediction from the spectral diffusion model.

Summarizing these results, we have identified spectral diffusion as the limiting factor for Ti:Tm:LiNbO$_3$ to storage of quantum information in optical coherence. For instance, assuming an AFC with 3 MHz teeth spacing, the storage time in optical coherence would be limited to ~ 300 ns. We expect that the application of a magnetic field and the decrease of temperature will lead to an improvement of the short-term line-width along with a reduction of spectral diffusion, similar to what has been observed for Tm:LiNbO$_3$ bulk crystals [48].

Stark effect

Electric field control can constitute a key ingredient in photon-echo quantum memory and quantum information processing. It enables controlled manipulation of resonance frequencies of absorbers for storage and recall, e.g. for controlled reversible inhomogeneous broadening

of narrow absorption lines in CRIB, and quantum state engineering such as pulse compression/decompression [85]. This control is governed by the interaction of applied external fields with permanent electric dipole moments. Provided the dipole moment is different for the ground and excited state, a shift in the resonance frequency $\Delta\omega$ occurs:

$$\Delta\omega = \frac{\chi}{\hbar}\Delta\overrightarrow{\mu_e} \cdot \overrightarrow{E} \tag{5.6}$$

where $\Delta\overrightarrow{\mu_e}$ denotes the difference in electric dipole moments for the states connected by the probe light, $\overrightarrow{E}$ is the applied electric field, and χ is the Lorentz correction factor. This is also known as the DC Stark effect [51].

To observe the frequency shift for different electric fields, we first burned a spectral hole, then applied a variable voltage parallel to the crystal C_3 axis, and assessed the displacement of the hole using a weak, chirped, read pulse, as detailed in Ref. [52].

As shown in Figs. 5.13 and 5.14, we observe a linear frequency shift of 24.6 ± 0.7 kHz·cm/V. For example, an electric field of 100 V/mm leads to a displacement of the resonance frequency by 25 MHz. In the case of a Tm waveguide, where electrodes can be spaced as closely as 10 μm, this requires the application of 1 Volt. Since low voltages can be switched rapidly with ease, waveguides provide the ability to reversibly broaden and manipulate absorbers within hundreds of picoseconds [2].

5.1.5 Discussion and conclusion

To conclude, our findings demonstrate the suitability of Ti:Tm:LiNbO$_3$ waveguides cooled to 3 K for implementations of photon-echo quantum memory protocols. Level structure, lifetimes, and branching ratios allow tailoring of the natural, inhomogeneously broadened absorption profile – either via optical pumping into the $^3F_4$ bottleneck state (then possibly

---

[2]The action of switching the electric field on a 100 ps time scale will result in about 10 GHz resolution in the frequency domain. If this switching is used to reversibly broaden an absorption feature with a linewidth that is, for example, on the MHz scale, the frequency resolution imposed by the switching time needs to be taken into account. In a recent study [72], a similar scenario was investigated in view of the CRIB protocol.
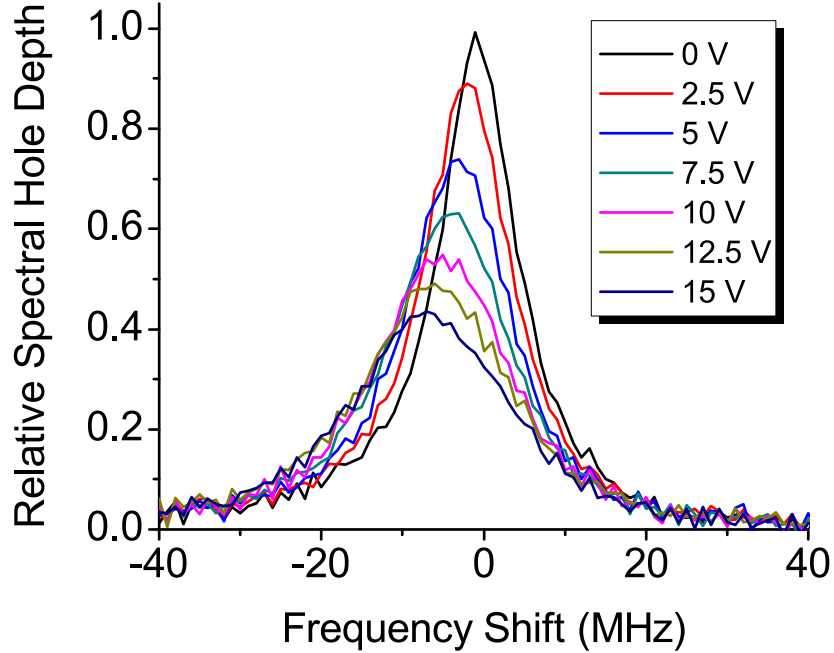
Figure 5.13: **Change of a spectral hole under application of different voltages:** We attribute the broadening of the spectral hole with increased voltage to the large inhomogeneity of the electric field at the beginning and end of the LiNbO$_3$ waveguide.

allowing storage of nanosecond pulses), or into one of the long-lived ground states that appear under the application of magnetic fields. The minimum width of spectral holes of around one MHz, as determined by spectral diffusion, will limit storage of quantum information in optical coherence to a few hundred nanoseconds. While longer times may be achievable at lower temperature, this is still sufficient for mapping coherence onto long-lived ground state coherence, as Rabi frequencies exceeding hundred MHz can be obtained, due to the high power densities achievable inside waveguiding structures. We point out that ground state coherence of 300 μs have been reported for Tm:YAG [43], but investigations for Ti:Tm:LiNbO$_3$ remain to be done. Finally, the existence of a linear Stark shift, together with the possibility to space electrodes closely, allows shifting of resonance frequencies by more than 100 MHz within sub-nanosecond times, thus enabling novel phase control techniques.

Interestingly, the lifetimes and branching ratio found in our study differ from those reported for Tm:LiNbO$_3$ bulk crystals probed at 794.22 nm wavelength and 1.7 K [47,48]. The
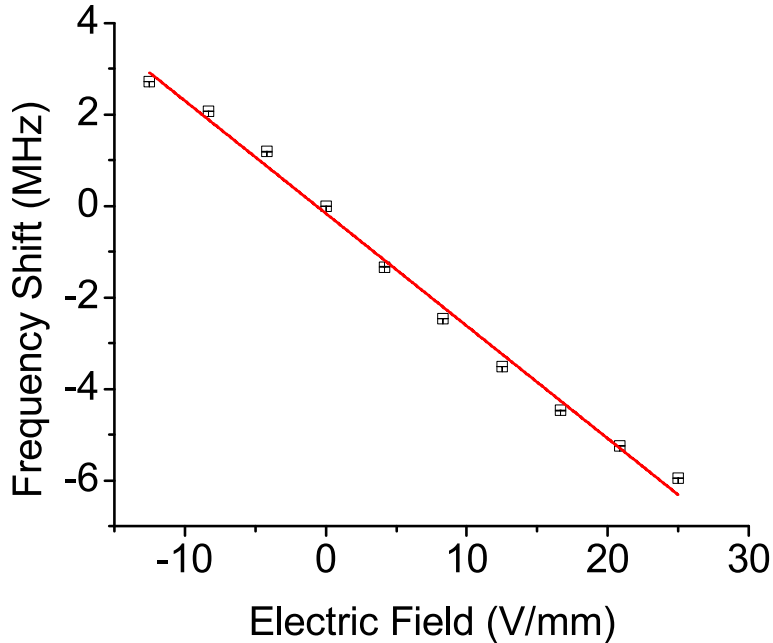
Figure 5.14: **Shift of transition frequency of the center of a spectral hole as a function of applied electric field, yielding a shift of 24.6 $\pm$ 0.7 kHz·cm/V.**

difference could be due to the addition of Titanium to our sample, which may alter radiative or non-radiative decay channels [53], to wavelength-dependent spectroscopic properties as suggested in [48], or to concentration dependence [86].

Finally, we point out that RE doped waveguides, here Ti:Tm:LiNbO$_3$, are not only interesting for quantum state storage using a photon-echo approach, but also for other approaches, e.g. based on electromagnetically induced transparency and slow light [4].

5.1.6 References

1. N. Sangouard et al., arXiv:0906.2699.

2. P. Kok et al. Rev. Mod. Phys. 79 (2007) 135.

3. K. Hammerer, A. S. Sorensen, E. S. Polzik, arxiv:0807.3358, Rev. Mod. Phys., accepted for publication.

4. A. I. Lvovsky, B. C. Sanders, W. Tittel, Nat. Photon. 3 (2009) 706.

5. W. Tittel et al., Laser and Phot. Rev. DOI 10.1002/ lpor. 200810056.

6. W. H. Hesselink, D. A. Wiersma, Phys. Rev. Lett. 43 (1979) 1991.

7. T. Mossberg, Opt. Lett. 7 (1982) p.77.

8. M. Mitsunaga, R. Yano, N. Uesugi, Opt. Lett. 16 (4) (1991) p.264.

9. M. Mitsunaga, Opt. Quant. Elect. 24 (1992) p. 1137.

10. G. J. Pryde, M. J. Sellars, N. B. Manson, Phys. Rev. Lett. 84 (2000) p.1152.

11. M. Nilsson et al., Phys. Rev. B70 (2004) 214116.

12. V. Crozatier et al., Opt. Comm. 241 (2004) 203.

13. B. Lauritzen et al., Phys. Rev. A78 (2008) 043402.

14. S. A Moiseev, S. Kröll, Phys. Rev. Lett. 87 (2001) 173601.

15. M. Nilsson, S. Kröll, Opt. Comm. 247 (2005) 292.

16. A. L. Alexander et al., Phys. Rev. Lett. 96 (2006) 043602.

17. B. Kraus et al., Phys. Rev. A. 73 (2006) 020302(R).

18. M. Afzelius et al., Phys. Rev. A 79 (2009) 052329.

19. H. de Riedmatten et al., Nature 456 (2008) 773.

20. G. Hétet et al., Phys. Rev. Lett. 100 (2008) 023601.

21. M. Afzelius et al., arXiv:0908.2309.

22. G. Hétet et al. Opt. Lett. 33 (2008) 2323.

23. S. A. Moiseev, W. Tittel, arXiv:0812.1730.

24. J. L. Le Gouët and P. R. Berman, arXiv:0904.0667.

25. M. Hosseini et al., Nature 461 (2009) 241.

26. T. Chanelière et al., arXiv:0902.2048.

27. A. Amari et al., arXiv:0911.2145.

28. M. Hedges et al., Poster presentation at the International Conference on Hole Burning, Single Molecule, and Related Spectroscopies: Science Applications (HBSM 2009), Palm-Cove, Australia, June 2009.

29. I. Usmani et al., unpublished.

30. E. Fraval, M. J. Sellars, J. J. Longdell, Phys. Rev. Lett. 95 (2005) 030506.

31. P. J. Kwiat et al., Phys. Rev. Lett. 75 (1995) 4337.

32. G. Ribordy et al., Phys. Rev. A63 (2001) 012309.

33. M. Halder et al., Opt. Express 17 (2009) 4670.

34. J. Slater et al., arXiv:0908.3516.

35. See Perkin Elmer single photon counting modules http://optoelectronics.perkinelmer.com

36. J. Gruber et al., Phys. Rev. B40 (1989) 9464.

37. M. Tian et al., J. Opt. Soc. Amer. B18 (2001) 673.

38. M. Ohlsson et al., Opt. Lett. 28 (2003) 450.

39. O. Guillot et al., Phys. Rev.B 71 (2005) 174409.

40. P. Goldner et al., Opt. Mater. 28 (2006) 649.

41. F. de Seze et al., Phys. Rev. B73 (2006) 85112.

42. A. Louchet et al., Phys. Rev. B75 (2007) 35131.

43. A. Louchet et al., Phys. Rev. B77 (2008) 195110.

44. R. Macfarlane, Opt. Lett. 18 (22) (1993) 1958.

45. L. Nunez et al., J. Lumin. 55 (1993) 253.

46. R. K. Mohan et al., J. Lumin. 127 (2007) 116.

47. C. W. Thiel et al., Workshop on the Storage and Manipulation of Quantum Information

in Optically-Addressed Solids, Bozeman, Montana, January 2008.

48. C. W. Thiel et al., J. Lumin., this issue.

49. T. Chanelière et al., arXiv:0911.3328.

50. D. N. Nikogosyan, Nonlinear Optical Crystals: A Complete Survey, Springer, Berlin, 2005.

51. R. Macfarlane, J. Lumin. 125 (2007) 156.

52. S. R. Hastings-Simon et al., Opt. Comm. 266 (2006) 716.

53. V. Dierolf et al., Appl. Phys. B72 (2001) 803.

54. Y. Sun, et al.,J. Lumin. 98 (2002) 281.

55. M. Colice, F. Schlottau, K. H. Wagner, Appl. Opt. 45 (2006) 6393.

56. Y. N. Korkishko et al., Appl. Opt. 35 (1996) 7056.

57. R. V. Schmidt, I. P. Kaminov, Appl. Phys. Lett. 25 (1974) 458.

58. E. L. Wooten, et al., IEEEJ. Sel. Top. Quant. Electron. (2000) 1.

59. S. Tanzilli et al., Nature 437 (2005) 116.

60. M. Staudt et al., Phys. Rev. Lett. 98 (2007) 113601.

61. M. Staudt et al., Phys. Rev. Lett. 99 (2007) 173602.

62. A. Delfan-Abazari et al., arXiv:0910.2457.

63. H. Bubert, H.Jenett, Surface and Thin Film Analysis, Wiley-VCH, 2002 ISBN: 9783527304585.

64. M. Quintanilla, et al., Opt. Mater. 30 (2008) 1098-1102.

65. Baumann et al., Appl. Phys. A64 (1997) 33-44.

66. R. Regener, W. Sohler, Appl. Phys. B36 (1985) 143-147.

67. E. Cantelar, et al., J. Lumin. 128 (2008) 988.

68. L. F. Johnston, A. A. Ballman, J. Appl. Phys. 40 (1969) 297.

69. E. Cantelar et al., Phys. Scripta T118 (2005) 69.

70. R. M. Macfarlane, R. M. Shelby, in W.E. Moerner (Ed.), Persistent Spectral Hole Burning: Science and Applications, Springer, Berlin, 1988.

71. D. A. Davids, P. E. Wagner, Phys. Rev. Lett. 12 (1964) 141.

72. G. H. Larson, C. D. Jeffries, Phys. Rev. 141 (1966) 461.

73. I. N. Kurkin, K. P. Chernov, Physica B C233 (1980) 101.

74. T. Böttger et al., Phys. Rev. B73 (2006) 075101.

75. S. R. Hastings-Simon et al., Phys. Rev. B77 (2008) 125111.

76. S. R. Hastings-Simon et al., Phys. Rev. B78 (2008) 085410.

77. G. Gorju et al., J. Phys. Condens. Matter 19 (2007) 386226.

78. N. Sangouard, et al., Phys. Rev. A75 (2007) 032327.

79. R. S. Meltzer, in: G. Liu, B. Jacquier (Eds.), Spectroscopic Properties of Rare Earths Optical Materials, Springer, Berlin, 2005.

80. W. B. Mims, K. Nassau, J. D. Mc Gee, Phys. Rev. 123 (1961) 2059.

81. Y. S. Bai, M. D. Fayer, Phys. Rev. B39 (1989) 11066.

82. W. Mims Phys. Rev. 168 (1968) 370.

83. M. Staudt et al., Opt. Comm. 266 (2006) 720.

84. E. S. Maniloff et al., Chem. Phys. 193 (1995) 173.

85. S. A. Moiseev, W. Tittel, in preparation.

86. M. Quintanilla et al., J. Lumin. 128 (2008) 927.

Chapter 6

Implementations of Atomic Frequency Comb Protocol in Tm:LiNbO$_3$ waveguide

In the previous chapter, I reported the investigation of the main properties of a Tm:LiNbO$_3$ waveguide in the view of photon-echo quantum memory. In this chapter, I present how we implemented the AFC protocol in this material. First, I explain the optical pumping strategies and the tools that we employ for the preparation of a broadband AFC. Next, I present some basic storage experiments including multimode storage and double AFC schemes. More sophisticated experiments that directly address the needs of a quantum repeater will be discussed in subsequent chapters. Finally, I discuss the limitations and potential improvements of our current implementations.

6.1 Frequency-Selective Optical Pumping

Implementing an AFC in a rare-earth crystal requires frequency-selective optical pumping using spectral hole burning techniques. These techniques have been studied extensively for several years [73, 74]. In this section, my goal is first to give a brief introduction to a typical optical pumping process for preparing an AFC and next, to show how this procedure can be performed in a Tm:LiNbO$_3$ waveguide.

As briefly described in Section 4.6, in order to perform optical pumping for the preparation of an AFC, the existence of a long-lived shelving level is required in addition to the ground and excited level. In this procedure, the atoms within the inhomogeneous line that are resonant with the laser light are pumped to the excited level $|e\rangle$, as represented on the left hand side of Fig. 6.1. The excited atoms decay either back to the original ground level
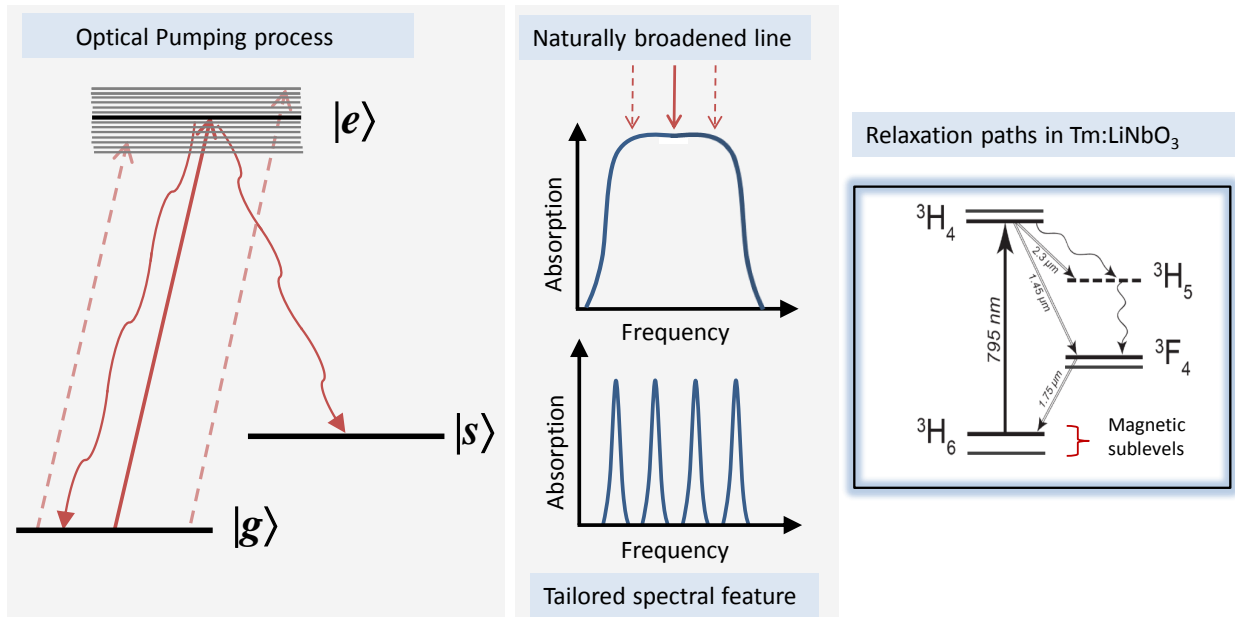
Figure 6.1: **Frequency selective optical pumping process to prepare an AFC:** The procedure starts with a naturally broadened absorption profile. The atoms at the selected transitions frequencies (shown by straight arrows) are transferred from ground level $|g\rangle$ to shelving level $|s\rangle$ via optical excitation to level $|e\rangle$. Sufficiently long interaction allows for transferring all these atoms to populate in the shelving state, resulting in the tailored spectral feature illustrated at the bottom of the middle figure. The figure on the right shows the energy level structure of the Tm:LiNbO$_3$ waveguide and the relevant relaxation paths for optical pumping.

$|g\rangle$ or to the long-lived shelving level $|s\rangle$. Depending on the relaxation dynamics, in principle all atomic population at the selected transition frequencies can be transferred to the shelving level, forming the troughs of the AFC. The atoms left in the ground states form the comb teeth, as illustrated in the middle of Fig. 6.1.

A requirement for efficient optical pumping is that the lifetime of the shelving level has to be much longer than that of the excited level. The other requirement is that the probability of excited atoms to decay to the shelving level must be significantly high, which is stated in the previous chapter as the need for large branching ratio. As explained therein, there are two possible shelving levels in Tm:LiNbO$_3$: the $^3F_4$ state, which has a lifetime of about 2.4 ms, and the nuclear magnetic Zeeman levels, which can have lifetimes up to 1 second,
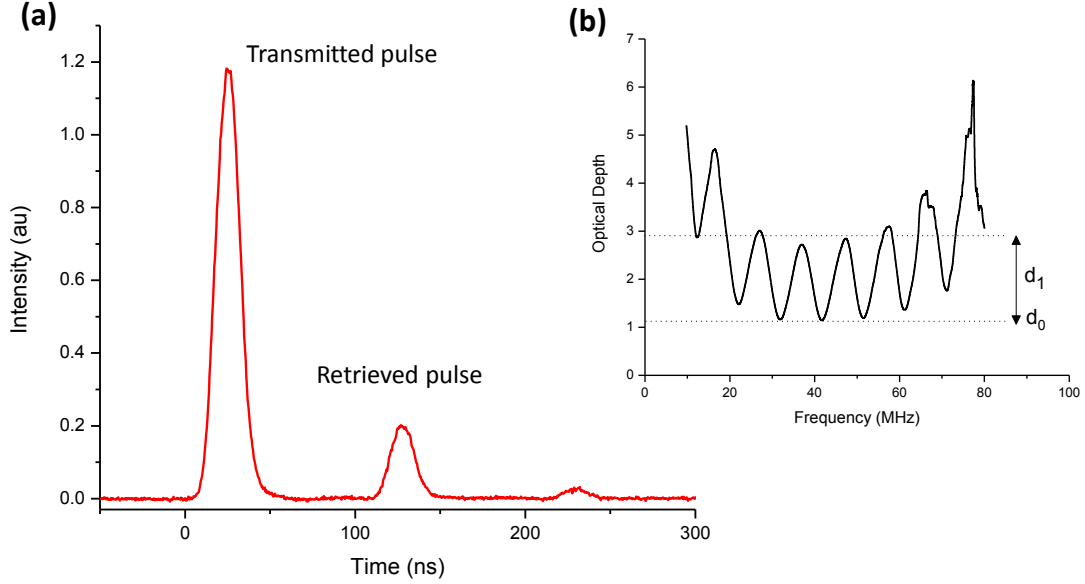
Figure 6.2: **Initial implementation of the AFC protocol in a Tm:LiNbO$_3$ waveguide.** Spectral tailoring was performed by sending a train of strong pump pulses with 20 ns duration and 100 ns separations into the crystal at 3 K temperature and exposed to a few hundred Gauss magnetic field. Following a wait time of about 10 times the excited level lifetime, the process yielded the AFC shown in Figure **(b)**. Next, to demonstrate light storage in the prepared AFC, a strong probe pulse with 20 ns duration was sent into the crystal. This pulse was retrieved after 100 ns storage time from the AFC medium as shown in **(a)**. In addition to the AFC echo, a partially transmitted pulse, stemming from low absorption was detected.

depending on the applied magnetic field (see the right hand side of Fig. 6.1). The $^3F_4$ level possesses some beneficial properties such as a large branching ratio from the excited level $^3H_4$ and very large separation from the ground state $^3H_6$. However, we are unable to take advantage of this level, the main reason being that we have to set a wait time of at least 2 ms between the optical pumping and photon storage stages to ensure that $^3H_4$ is minimally populated. Without this step, the excited atoms contaminate the signal with noise photons. Since this wait time is comparable to the lifetime of $^3F_4$, a significant fraction of the atoms decay back to the ground level. Thus we are unable to use the $^3F_4$ as a shelving level.

The other option is to use the nuclear Zeeman levels for long-lived population storage. The lifetime of these levels under certain magnetic fields is substantially longer than that of

the excited level. However, the probability of atoms to decay to this level with the opposite spin orientation after excitation is very small, which is a consequence of the spin-selection rules. According to Ref. [75], only a few percent of the excited state population decays into the oppositely oriented spin state during the optical pumping in a bulk $Tm:LiNbO_3$, which confirms our observation with a $Tm:LiNbO_3$ waveguide. This leads to an inefficient preparation of the AFC in the following way. In order to efficiently populate the nuclear Zeeman level with the opposite spin, one must perform the optical pumping with high intensity light and/or for a longer duration. These steps result in two competing effects. On the one hand, more atoms are pumped to the shelving level, which results in better transparency in the troughs of the AFC, yielding reduced d_0. On the other hand, off-resonant interactions become more significant. This effect, known as power broadening, causes some of the atoms in the peaks of AFC to be transferred to the excited level whereby they may end up in the oppositely oriented spin state, reducing the optical depth of the AFC (yielding a reduction of d_1). In this situation, optimizing the ratio of d_1 and d_0 is required.

The experimental procedure to find the optimum AFC parameters including d_0 and d_1 is to vary one of the optical pumping parameters such as the pump power, pump duration and magnetic field while keeping the others fixed until the most efficient AFC echo is obtained. Fig. 6.2 shows our first AFC-based light storage implementation in a $Tm:LiNbO_3$ waveguide. In this implementation, the AFC peak separation was set to 10 MHz, leading to 100 ns storage time. The width of each AFC peak is about 5 MHz yielding a finesse of nearly 2. The effective AFC bandwidth is nearly 60 MHz. The resulting d_1 is 2 and d_0 is around 1, which is the consequence of the imperfect optical pumping explained above. The retrieval efficiency of this AFC memory can be estimated by plugging these numbers into Eq. 4.4. It is found to be around 1.7%, which is close to the directly measured efficiency of %1.5.

6.2   Preparing a Broadband AFC

The large bandwidth of our AFC memory is one of the most important features in our experimental demonstrations; it allows us to store broadband single photons (Chapter 7 and 8), to implement a highly multimode quantum memory (Chapter 10) and to use our memory as a processor for quantum optical signals (Chapter 11). Because of its importance, in this section I will describe in some detail how we can prepare a broadband AFC in the Tm:LiNbO$_3$ waveguide. Certainly, the large inhomogeneous broadening of this material, which is hundreds of GHz, is a necessary element to achieve memory bandwidths on the order of GHz. However, as briefly discussed in Section 4.6, the bandwidth of an AFC is limited by the energy level structure of RE materials. Therefore, we need to know how this limitation applies in our material, which requires detailed understanding of the nature of the magnetic sub-levels and the population re-distribution between these levels during the optical pumping. This is the first topic I will cover. Secondly, I will show how, under certain conditions, the bandwidth limit imposed by the energy level structure can be alleviated. Finally, I will discuss the optical pulse sequence, we employed for the preparation of the broadband AFC.

6.2.1   Spectral Hole Burning and Magnetic Sublevel Splitting

Upon application of a magnetic field along the C$_3$ axis of the Tm:LiNbO$_3$ crystal[1], the ground and excited levels split into two magnetic sub-levels corresponding to the orientation of the Tm^{+3} nuclear spin ($\pm 1/2$). The amount of splitting is proportional to the magnetic field strength and, in a RE material, is typically different for the ground and excited states as shown in Fig. 6.3a. When narrow bandwidth laser light at ω_0 is applied to the inhomogeneously broadened absorption line, there are four classes of transitions that may be excited by the laser light: $|g\rangle_+ \rightarrow |e\rangle_-$, $|g\rangle_+ \rightarrow |e\rangle_+$, $|g\rangle_- \rightarrow |e\rangle_-$ and $|g\rangle_- \rightarrow |e\rangle_+$. Assuming that

---

[1]See Appendix-A for the details of the C$_3$ symmetry in a Tm:LiNbO$_3$ crystal
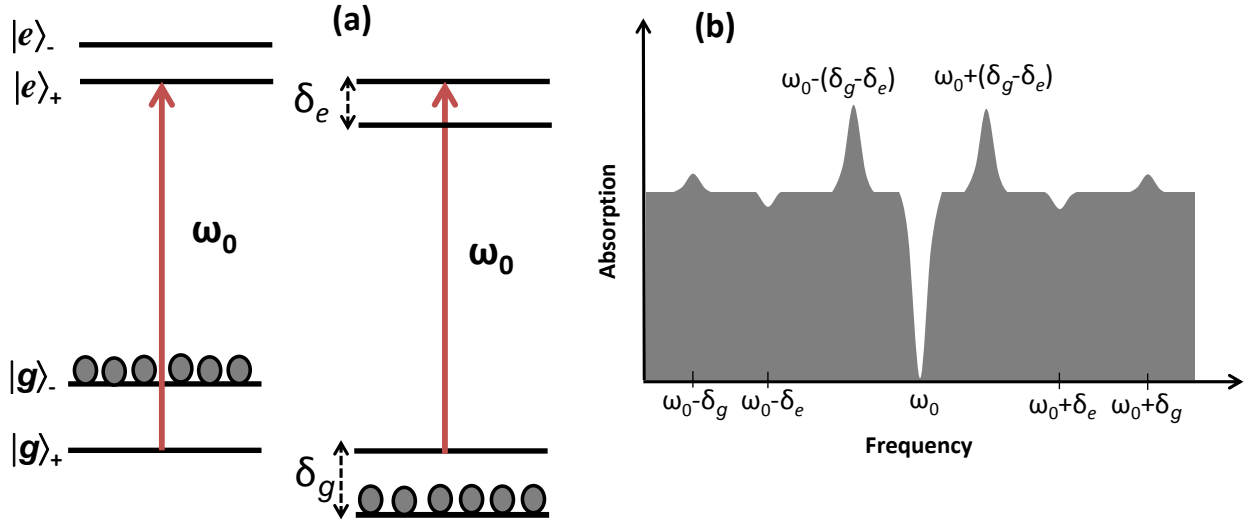
Figure 6.3: **Population re-distribution of the atoms between two-level spin states after excitation of an inhomogeneously broadened optical transition.** Figure **(a)** shows the two classes of transitions with the highest probability out of the four possible classes. Sufficiently long and intense excitation leads to the transfer of population to the other spin level. Figure **(b)** represents the expected spectral hole burning pattern after the population re-distribution. The hole and anti-hole depths were arbitrarily chosen for illustration. See text for details.

transitions to opposite polarity spin-levels, (i.e. those involving an optically induced spin-flip) are quite low, then only the transitions $|g\rangle_+ \to |e\rangle_+$ and $|g\rangle_- \to |e\rangle_-$ may be excited by the laser light, as represented in Fig. 6.3a. The excited ions may then spontaneously decay through a variety of mechanisms back to the ground state, with some chance of a spin-flip in the process. After a sufficiently long and intense excitation at ω_0, the population is re-distributed as shown in Fig. 6.3a, in principle yielding empty magnetic sublevels [76]. If one probes this distribution by scanning a laser over a frequency range that covers all possible transitions, an absorption spectrum similar to the one in Fig. 6.3b is obtained [2]. As seen from the figure, there are regions of decreased and increased absorption, which are called holes and anti-holes, respectively. Depending on the coupling strength of the transitions

---

[2] We should note that if the spin-selection rules are relaxed, all possible transitions would be excited and a more complicated spectrum than that represented in the figure would result. However, in our own experiments and those reported in the literature [75] with a Tm:LiNbO$_3$ crystal, only one pair of anti-holes (at the magnetic fields oriented to the C$_3$ axis) is observed. This indicates that our assumption is valid.

and the population difference between the levels after the re-distribution, the relative depth of the holes and anti-holes differ. The main spectral features in the modified absorption spectrum are the hole at excitation frequency ω_0 and the two anti-holes at a detuning given by the difference of the excited and ground level splittings $(\delta_g - \delta_e)$.

A crucial point in the AFC preparation is how to choose the magnetic field, which determines the hole and the anti-hole structure, for a given teeth spacing, i.e. storage time. For example, if the separation between the main hole and the anti-holes equals the teeth spacing, pumping and de-pumping would cancel each other, and, in the worst case, result in no AFC structure. Consequently, we need to develop optical pumping strategies for preparing a broadband AFC, which requires knowledge about the frequency shift of anti-holes with respect to magnetic field.

In our initial attempts to gain this knowledge, we were unable to observe a resolvable hole and anti-hole pattern arising from a single frequency excitation as shown in Fig. 6.3b. Hence, we developed the method illustrated in Fig. 6.4a. to observe this pattern indirectly. We applied laser light at two different frequencies referred to as reference (ω_r) and control (ω_c) and measured the resulting holes at these frequencies at zero magnetic field. We then scanned the magnitude of the magnetic field starting from zero, while monitoring the shape of the hole at ω_r. When the anti-hole generated by the light at ω_c started overlapping with the hole generated at ω_r, the reference hole depth decreased. This is shown in Fig. 6.4b and c. When the minimum hole depth was reached at a certain magnetic field, the frequency difference of the two laser beams gave the value of the separation between the hole and anti-hole for that magnetic field. Repeating this process for various frequency differences $(\omega_r - \omega_c)$ (Fig. 6.4d), we found that the separation of the main anti-hole from the main hole is nearly 12.5 MHz per 100 Gauss, which is very close to the value found in Ref. [75] for a Tm:LiNbO$_3$ bulk crystal.
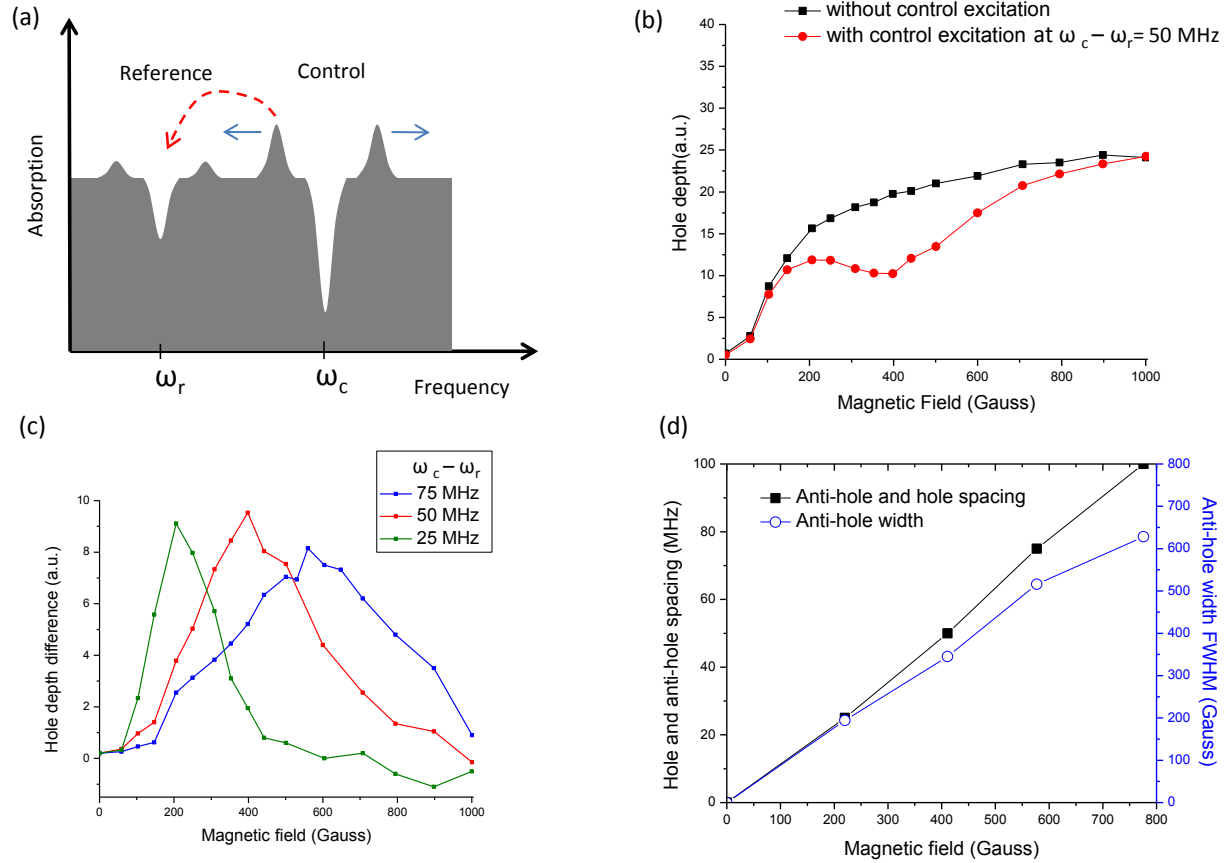
Figure 6.4: **Determination of magnetic level splittings using a hole-burning technique.** **(a)** The crystal was excited at two frequencies, referred to as reference (ω_r) and control (ω_c), such that at a certain magnetic field the hole at ω_r (reference hole) was significantly "filled" by the anti-hole generated by the excitation at ω_c. **(b)** The plot shows the measured depth of the reference hole with respect to the applied field with and without the control excitation at $\omega_c - \omega_r = 50$ MHz. The measurement point that belongs to the maximum decrease in the hole depth determines the magnetic field value that generates 50 MHz separation between the main hole and the anti-hole. **(c)** The difference between the hole depths with and without control excitations as a function of the magnetic field, for various frequency differences ($\omega_c - \omega_r$). **(d)** Hole and anti-hole spacing and anti-hole width with respect to the applied magnetic field.

79

6.2.2 Generation of AFC with Bandwidth Limit Imposed by Atomic Level Structure

Two different optical pumping strategies can be applied for preparing a broadband AFC. The first strategy, explained in this section, is to operate in a high magnetic field regime in which the anti-holes (the regions with increased absorption) are moved out of the AFC to avoid any overlap with the troughs. In this case, the achievable bandwidth is limited by the maximum applied magnetic field, which was around 5000 G. Fig. 6.5a shows a 600 MHz-wide AFC prepared with this method. As seen from the figure, the anti-holes, which correspond to increased absorption regions, appear at each side of the AFC. The major advantage of this scheme is that, in principle, any AFC with arbitrary finesse can be prepared. In addition, with high magnetic fields, longer nuclear Zeeman lifetimes are obtained as shown in Chapter 5. This gives rise to more efficient optical pumping with smaller absorption background (d_0) in the prepared AFC. However, the broadening of the anti-holes with higher magnetic fields, as can be observed from Fig. 6.3d, sets limits to high quality AFCs; the anti-holes eventually overlap with the prepared comb structure, leading to increased absorption background. The broadening could arise from inhomogenity in the applied field or some specific structural deformation in the LiNbO$_3$ host crystal as discussed in Ref. [77]. If this issue can be resolved, the application of higher magnetic fields will allow us to obtain GHz bandwidth AFCs.

6.2.3 Generation of Broadband AFC without Bandwidth Limit Imposed by Atomic Level Structure

The other optical pumping strategy is based on adjusting the magnetic field for a given storage time in such a way that the position of anti-holes and holes match the peaks and troughs of the AFC, respectively. This means that the separation between anti-hole and hole needs to be half of the peak spacing of the AFC.

Fig. 6.5b shows a 600 MHz-wide AFC generated using this method. In this implemen-
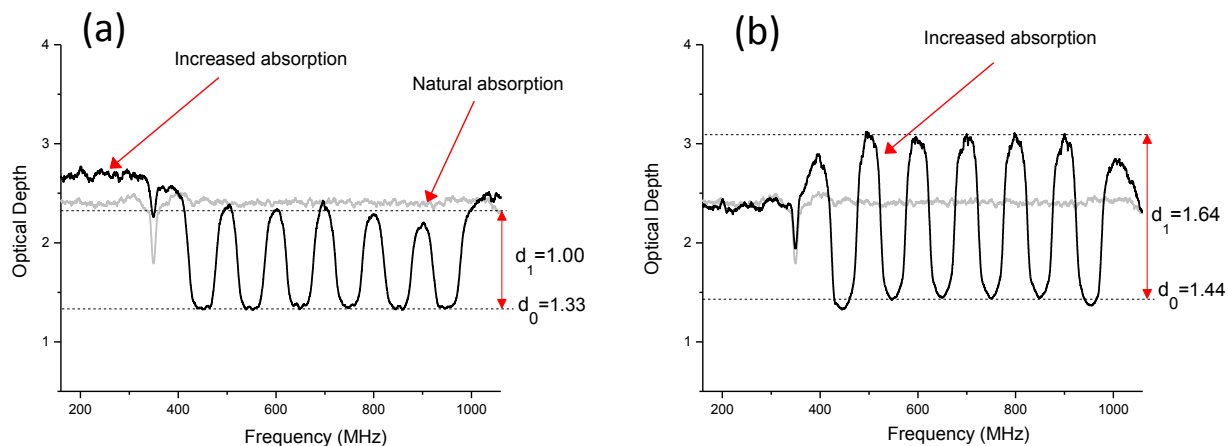
Figure 6.5: **Optical pumping strategies for preparing a broadband AFC based on high magnetic field (a) and low magnetic field (b) applications.** In the high magnetic field regime **(a)**, the population from the AFC troughs is moved completely out of the AFC region. Therefore, in practice, the AFC bandwidth is only limited by the strength of the applied field (considering the fact that inhomogeneous broadening in our material is hundreds of GHz). In the low magnetic field regime **(b)**, the magnetic field is adjusted according to the peak spacing of the AFC such that the population from the troughs is moved to the peaks of the AFC. In this scheme, the width of the inhomogeneous broadening is the ultimate limit of the AFC bandwidth. However the finesse of the comb can only be 2 or less.

tation, the peak separation of the AFC was set to 100 MHz leading to 10 ns storage time. Accordingly, the applied magnetic field was about 400 G, yielding about 50 MHz hole–anti-hole separation. The main advantage of this strategy is that it allows for preparing an AFC whose bandwidth not limited by the magnetic sublevel splitting. Another advantage is that the optical depth of the peaks can be higher than the natural optical depth because of the described population shuffling as seen from the AFC spectrum in Fig. 6.5b.

On the other hand, the major drawback in this scheme is that the finesse of the AFC (Δ/γ) cannot exceed 2, which prevents one from reaching high efficiencies. Another problem with this strategy arises when an AFC leading to relatively long storage time (≥ 100 ns) is prepared. In this situation, the magnetic field strength is relatively low (≤ 40 G), which results in a relatively short lifetime of the nuclear Zeeman levels, as shown in the previous chapter. Hence, the absorption background (d_0) is typically higher than in the case of AFC

preparation with high magnetic field. If the AFCs resulting from each of the strategies are compared by inspecting Fig. 6.5a and b, it can be seen that d_0 and d_1 are higher in the low magnetic field implementation, as expected.

Throughout this thesis, we used the technique described in this section to prepare all AFCs with more than 1 GHz bandwidth.

6.2.4 Broadband AFC Preparation with Various Pulse Sequences

In the discussion of the AFC preparation, so far there hasn't been any explicit description of the actual optical pumping pulse-sequences used. In this section, I will explain the optical pumping pulse sequences that were employed to generate broadband AFCs in our experiments. Also based on our observations, I will discuss the advantages and limitations of each implementation. Although this section involves some extra technical details, it is the basis of all experimental demonstrations and implementations carried out during my thesis.

In an optical pumping scheme, the main process is the frequency selective excitation of atoms by optical pulses. The spectrum of the excited atoms is determined by the power spectrum of the incident light, as determined by it's Fourier transform. By tailoring the input light's power spectrum, any spectral distribution of atoms can in principle be obtained. This assumes that the intensity of the optical pulses are sufficiently low not to cause saturation effects.

Based on the type of optical pulse sequences, we can define two main approaches for the frequency selective pumping, which we refer as to the time-domain and the frequency domain approaches. The former one is based on the use of Fourier-limited short laser pulses, while the latter is based on frequency swept continuous wave (CW) laser light. In the next two sections, I will describe these approaches.
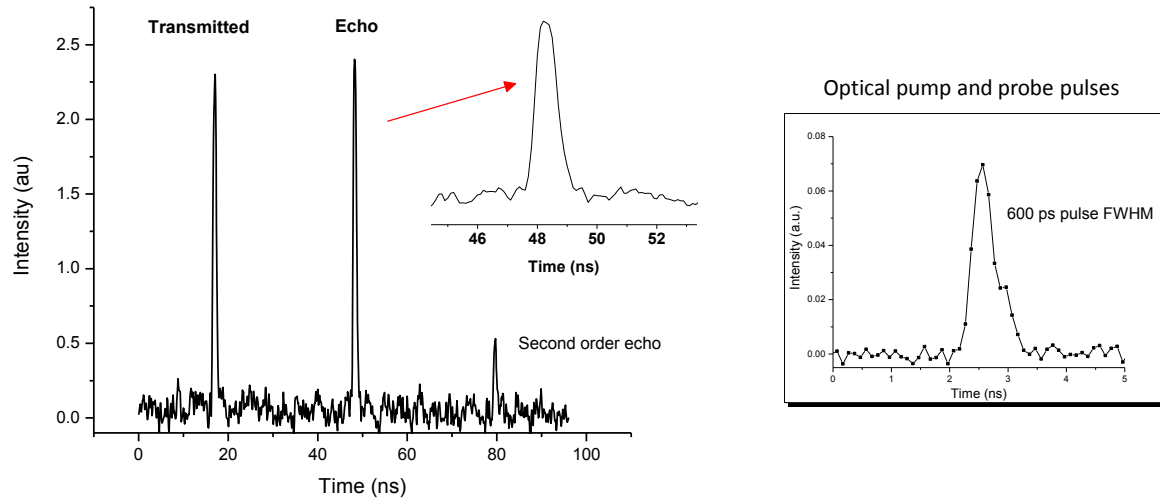
Figure 6.6: **Storage of sub-ns optical pulses in a broadband AFC memory prepared by pulse pairs.** A train of short pulse pairs, with a duration of 600 ps per pulse, shown on the right side of the figure, were produced using an intensity modulator and sent to the crystal to generate a broadband AFC. The separation between the pulses in each pair and between subsequent pairs were 31 ns and 4 μs, respectively. To accumulate a persistent population grating, this cycle was repeated several times during 2 ms, resulting in an AFC memory with 31 ns storage time. Following 1.5 ms wait time, a strong probe pulse with 600 ps duration was stored and retrieved in the prepared AFC memory, as shown in the figure. The measured pulse width of the echo was approximately 700 ps, confirming the over GHz bandwidth of the AFC. In the experiment, the crystal was maintained at 3 K under at 133 G magnetic field oriented along the c-axis and the peak power of the pumping pulses was about 1 mW

Time Domain approach

In the time-domain approach, multiple short pulses interact with the RE medium for spectral tailoring. To generate an AFC, sending pulse pairs is one of the common techniques. A pulse pair yields a sinusoidally modulated spectrum. When interacting with the atoms in a RE material, thus it imprints a sinusoidally varying frequency dependent population grating. Sending several pulse pairs, which are separated by more than the coherence time of the optical transition, leads to the accumulation of a grating by transferring atomic population into the shelving level. As a result of this procedure, an AFC is generated.

The spacing between the peaks of the AFC is given by the inverse of the separation of the pulses in a pair. The bandwidth of the AFC is determined by the inverse of the duration of each pulse. Therefore, broad AFC bandwidths require short pulses. The AFC shown in Fig. 6.2 was prepared using 10 ns pulses generated by an AOM, resulting in effectively a 60 MHz-wide AFC.

To extend the bandwidth of the AFC into the GHz regime, sub-nanosecond pulses need to be produced, which is impossible using a standard AOM. In this situation, one option is to use a fast electro-optic intensity modulator. Fig. 6.6 shows an example of the storage of a sub-ns pulse in a 1.5 GHz broad AFC prepared by 600 ps–long pair of pulses using an intensity modulator.

One of the main problems of the optical pumping techniques based on short pulses is the high peak power required to transfer the same energy per frequency interval. Optical amplifiers can help reaching high optical powers, however amplified spontaneous emission is a considerable problem in single-photon level storage experiments. Another issue is the limited finesse of the prepared AFC due to the sinusoidal pulse pair spectrum.

It is possible to use a different pulse pattern in order to get around some of these limitations. For instance, sending a pulse train composed of N equally spaced pulses relaxes the requirement of high peak power for large bandwidths, because no waiting time needs to be added between the pulse pairs. Fig. 6.7 shows an example of the preparation of a broadband AFC using this technique as well as the storage of sub-ns pulses in the resulting AFC.

When working with large optical depths ($d \geq 3$), this method yielded higher retrieval efficiency compared to the pulse pair scheme. However in general, this technique is not suitable for preparing an efficient AFC. First, the spectrum of a pulse train is a comb in the frequency domain, which results in the width of AFC peaks being wider than the width of the transmission windows. Thus the finesse of the comb prepared in this way is less than 2, which limits to get the recall with arbitrarily high efficiency. The other issue in our
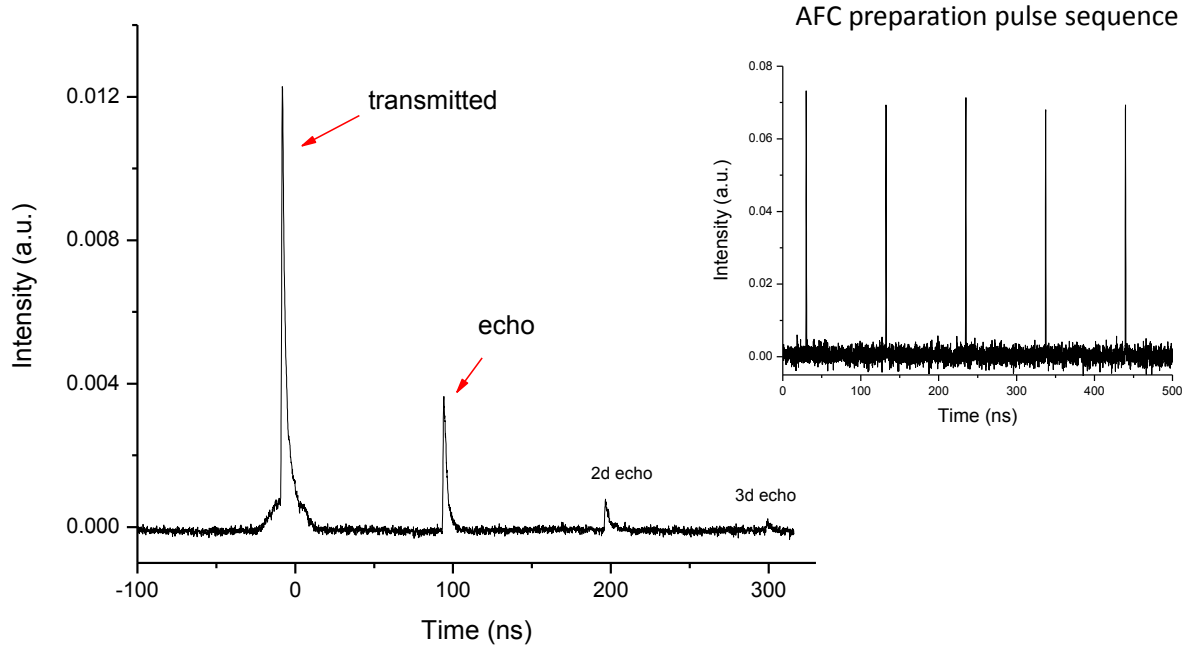
Figure 6.7: **Storage of sub-ns optical pulses in a broadband AFC memory prepared by a pulse train composed of equally spaced short pulses.** In the optical pumping stage, shown in the inset figure, the duration of each pulse was 600 ps and the separation between the pulses was set to 100 ns. This pulse pattern was repeated 10^5 times during 10 ms, resulting in a nearly 1.5 GHz wide AFC with 10 MHz peak spacing. After a 1.5 ms wait time, a strong pulse with 0.6 ns duration was sent to the AFC medium and retrieved after 100 ns storage as shown in the figure.

implementations is that generating a large effective optical depth (d_1/F) by reducing the finesse increases the re-absorption probability of the emitted echoes. This in turn results in several high order echo re-emissions, which takes energy from the primary (first) echo. Fig. 6.8 shows an example of this situation. As seen from the figure, the low finesse AFC (6.8a) causes many higher order echoes.

In order to solve the limited finesse issue, one can produce more complicated pulse patterns with carefully tailored amplitude and phase modulation. Additionally, engineering a pulse sequence in this way can allow for generating squared-shaped AFC peaks, which is known to optimize the AFC efficiency [78]. However, the necessity to find and produce an
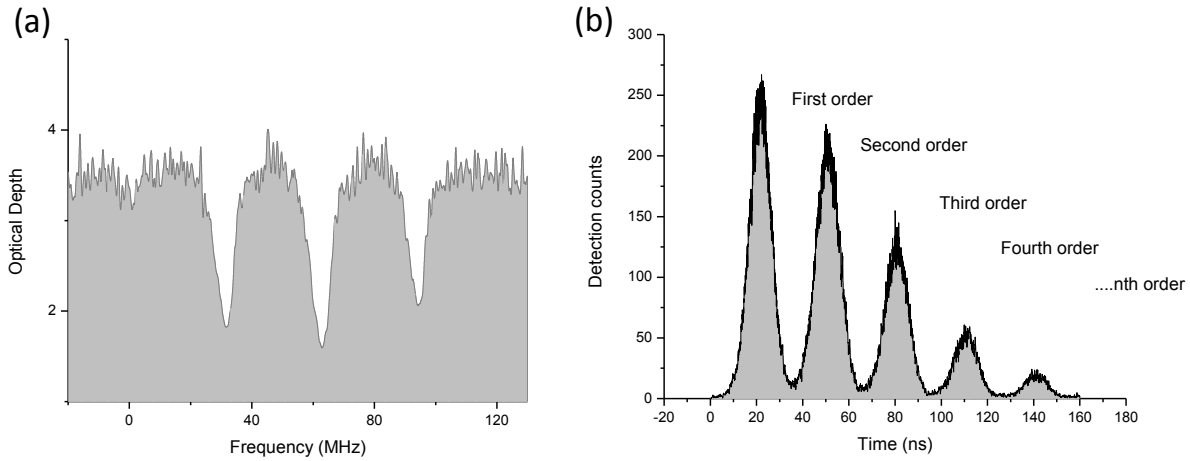
Figure 6.8: **Emission of high order echoes due to the limited finesse.** An AFC with finesse 1.4 and nearly 80 MHz bandwidth, shown in Figure **(a)**, was generated by performing optical pumping with a train of pulses separated by 30 ns. Probe pulses containing approximately 50 photon on average were sent to the AFC medium and re-emitted in the form of up to 6 high order echoes (only first four orders are displayed) as seen in Figure **(b)**

optimal pulse sequence with the precise phase and amplitude control, along with the high peak power requirement, makes this approach impractical for flexible and broadband AFC preparation.

Frequency Domain Approach

The frequency domain approach for spectral tailoring can alleviate some of the limitations of the time-domain technique that is based on short-pulses. In this approach, the ability to sweep the frequency of CW laser light and to modulate its amplitude simultaneously is in principle sufficient for frequency selective optical pumping. The use of CW laser light reduces the required optical peak power substantially. In our experiments, with the short-pulse technique the applied peak optical power typically ranged from 1 mW to 15 mW, whereas with the frequency sweep technique, the power values were around tens of μW.

The other advantage of this approach is that it allows for preparation of any desired AFC structure with great flexibility. For instance, combs with high finesse and/or square-shaped
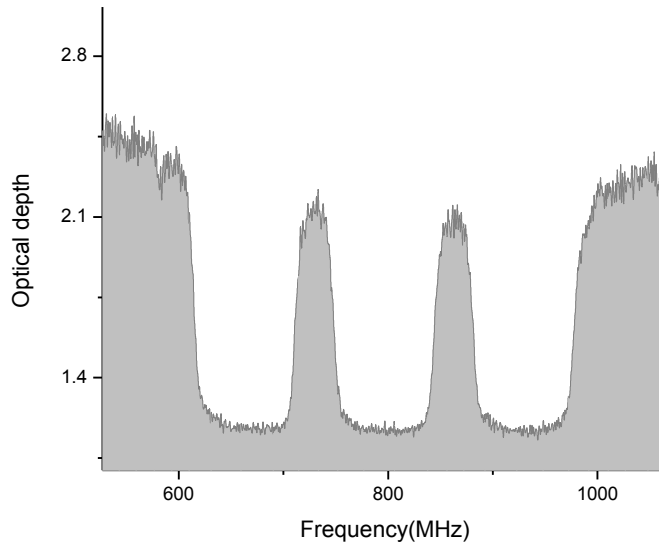
Figure 6.9: **A high finesse AFC with sharp spectral features generated by a frequency sweep technique.** To prepare this AFC, the frequency of the laser light was linearly scanned in selected frequency intervals during optical pumping by means of a phase modulator. The resulting finesse of the comb is about 3.7

peaks can be generated much more conveniently using appropriate frequency and amplitude control, as demonstrated in Fig. 6.9.

In the frequency domain approach, the maximum bandwidth is determined by the achievable frequency shifting capacity. Therefore, for a large frequency shifts ($\geq 500 MHz$), a standard AOM is not suitable, due to its limited bandwidth of a few hundred MHz. Controlling the laser frequency directly from a laser can be more advantageous. For example, frequency sweeps can be obtained by modulating the laser current. However, in a typical solid-state laser, this method does not allow a controlled frequency shift of more than 500 MHz. On top of this, it leads to frequency instability problems in the laser. Controlling the diffraction grating of an extended cavity laser is also an option. But the slow operation of the piezo systems and non-linearities in the frequency sweep are some of the problems with this option.
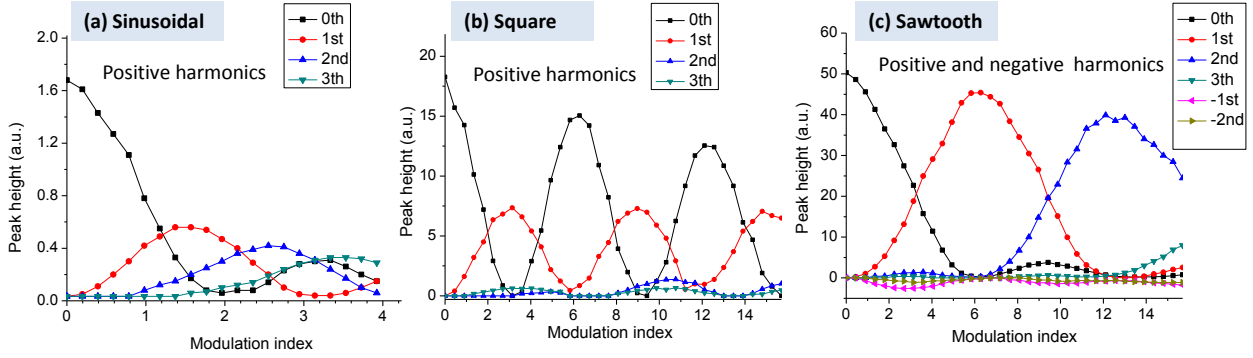
Figure 6.10: **Comparison of (a) sinusoidal, (b) square and (c) sawtooth waveforms for phase modulations.** In the measurements, single mode laser light was sent through a commercial $LiNbO_3$ waveguide phase modulator. An arbitrary waveform generator applied periodic voltages to the modulator at 100 MHz via a high-speed amplifier. The resulting side-bands at 100 MHz and their harmonics for several driving voltage amplitudes were analyzed by slowly scanning the laser carrier frequency and simultaneously measuring the transmission of the phase modulated light through a high finesse Fabry-Perot cavity (with 5 GHz free spectral range). For **(a)** sinusoidal and **(b)** square type phase modulations, only the positive harmonic were measured since the negative harmonics were identical. For **(c)** sawtooth (serrodyne) phase modulation, the positive and negative harmonics are shown.

One of the best approaches to accomplish fast, robust and large bandwidth frequency shifting is to use electro-optic phase modulators, which was initially proposed and implemented in various experiments by W. R. Babbitt and co-workers for broadband optical signal processing [79, 80].

As is well-known, the periodic modulation of the light's phase produces frequency modes (harmonics) at multiples of the modulation frequency. This concept can be understood from the simple relation between the phase and frequency of light. The phase of light is given by $\phi(t) = \omega_0 t + \phi(t)$, where ω_0 is the carrier frequency of the light. If no modulation is applied to the phase, the second term on the right hand side is zero, and the frequency of the light is $d\phi(t)/dt = \omega_0$. If there is a periodic phase modulation at frequency ω_m, the frequency of the light becomes $d\phi(t)/dt = \omega_0 + d\phi(t)/dt$, which results in $\omega = \omega_0 \pm n\omega_m$ where n is an integer. The generated frequency modes can be swept by varying the modulation frequency (ω_m) with time, which is the basic idea behind preparing an AFC using phase modulated

light.

The crucial point is to control the weight of all harmonics, i.e. to control the spectral distribution of the phase modulated light, which depends on the form of the phase modulation $\phi(t)$. Therefore it is necessary to engineer the phase modulation when employing this approach in the optical pumping process. We extensively used three type of phase modulations, sinusoidal, square and sawtooth, in our experiments. The observed spectral distributions of light with respect to modulation index for each phase modulation pattern are shown in Fig. 6.10. The modulation index is essentially determined by the peak voltage (V) applied to the phase modulator and given by $\pi V/V_\pi$ where V_π is the peak voltage required to introduce a π phase shift. In the following, the main characteristics of each phase modulation scheme will be briefly described.

First, inspecting the sinusoidal phase modulation in Fig. 6.10a, one notices that as the modulation index increases, more higher order harmonics appear. However, this is not desirable when the modulation frequency is swept for optical pumping to prepare an AFC, as each harmonic imprints its own population grating, which may lead to overlapping AFCs.

One general strategy to overcome this problem is to set the modulation index to a sufficiently small value so that harmonics higher than the second order can be ignored. In this situation, the overlap between the population gratings generated by the first and second order side peaks can be eliminated by choosing the start modulation frequency equal to the scan range. For example, to generate a 5 GHz AFC, the first harmonic could be swept from 5 GHz to 10 GHz. By employing such a frequency sweep and simultaneously modulating the intensity of the pump light to set the peak spacing, we were able to produce up to 5 GHz-wide AFCs. This value was limited by the sampling rate of the arbitrary waveform generator, used to generate the sweep. Fig. 6.11 shows an example of the storage of photons with 6 GHz bandwidth (FWHM) in an AFC prepared by this technique.

Despite the advantages, there are also a few technical issues with the sinusoidal phase

modulation scheme. First of all, due to the unavoidable existence of the zeroth order light, the medium is exposed to extra optical power, causing spontaneously emitted light from excited atomic levels and heating issues. In addition, the frequency scan with the sinusoidal phase modulation makes it difficult to appropriately probe and analyze the generated AFC.

Finally the necessity of setting the start frequency high makes this approach quite demanding in terms of fast electronics. To prepare the 5 GHz AFC, we had to generate a sine wave up to 10 GHz with the AWG, which has 20 G/s sampling rate. Aliasing at higher frequencies reduced the AFC quality at the high frequency end. As a result, the retrieval efficiency is not uniform over the entire AFC. This effect was characterized by comparing the retrieval efficiency of echoes produced from the high frequency and the low frequency end of the prepared AFC. For an AFC optimized for maximum recall efficiency, we found that the efficiency of its upper frequency half was 20-30 % less than that of its lower frequency half.

The second type of the phase modulation we studied is the square phase modulation. As seen from Fig. 6.10b, when the modulation index matches the π-voltage of the modulator, the zeroth order is completely suppressed and principally only the first negative and positive (± 1) orders are present. In this situation, the problem with the zeroth order light and the high start frequency problem is solved. However in practice, the bandwidth limitation of the AWG and the modulator causes an imperfect square waveform generation. This results in spurious higher order harmonics, as seen from the figure.

The final scheme is the sawtooth phase modulation, which is also known as Serrodyne technique [81]. Theoretically this scheme allows shifting the frequency of light to a single frequency without any harmonics at higher or negative frequency sidebands. As can be seen from our characterization in Fig. 6.10c, at the 2π-voltage, 90% of the energy of the laser light is shifted to the $+100$ MHz mode. The rest of the energy is, as a consequence of the imperfection in the sawtooth waveform, distributed among a number of negligible higher order harmonics, which renders issues with overlap in the AFC preparation.
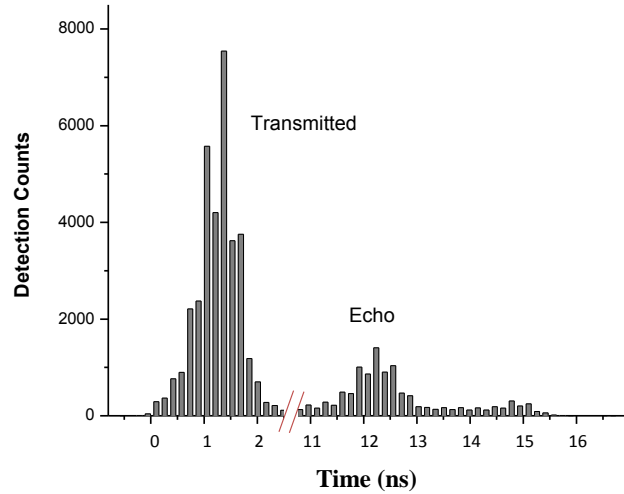
Figure 6.11: **AFC prepared by sinusoidal phase modulated light: Storage and retrieval of broadband photons from an SPDC source.** Optical pumping was performed using sidebands generated by a sinusoidal phase modulation. The first order sides peaks were swept in 5 GHz range by linearly varying the frequency of the modulation as described in the main text. During the frequency scan, the intensity of the light was modulated at certain rate as detailed in Chapter 7 and 8 to obtain an AFC with 90 MHz peak spacing and 5 GHz bandwidth. A stream of single photons with 80 ps pulse duration, derived from a spontaneous parameteric down conversion source (see Chapter 7), were sent to the prepared memory and retrieved after 11 ns. The detection counts were obtained over 2 minutes. The echo and transmitted pulses were measured to be longer than 80 ps due to the timing jitter of the electronics. Also we were not able to appropriately probe the full AFC in the frequency domain, due to the zeroth order light and a distortion in the generated sinus waveform over 8 GHz

Fig. 6.12 shows the example of the storage of 6 GHz bandwidth photons, derived from an SPDC source, in a 10 GHz-wide AFC memory generated by the Serrodyne chirping technique. As seen from the figure, this technique also allows probing for broadband AFCs in the frequency domain. Furthermore as we will show in Chapter 10 and 11, it is an important tool for developing new ideas such as frequency selective on-demand recall and pulse manipulation.

The final point is that when the chirping technique is employed for preparing an AFC, instead of directly modulating the intensity of the pump light it is possible to skip certain

frequency intervals to form the peaks as implemented in the last example (Fig. 6.12). Care needs to be taken in certain limits. The action of rapidly switching the phase modulation on and off (skipping certain frequency intervals) can broaden the pump light's spectrum depending on the relation between the switching rate and the bandwidth of the light in combination with the chirp rate. If the AFC's peak separation (or the width of the peaks) is comparable to this broadening, this effect can lead to the excitation of the atoms that forms the peaks, resulting in an inefficient AFC. In the experiment described above, the peak separations of the AFC was about 140 MHz, while the switching rate was nearly 1.4 μs which corresponds to better than 1 MHz frequency resolution. Due to almost two-orders of magnitude difference between the peak separation and the frequency resolution imposed by the switching rate, the switching of the phase modulation does not introduce any limitation in this implementation.
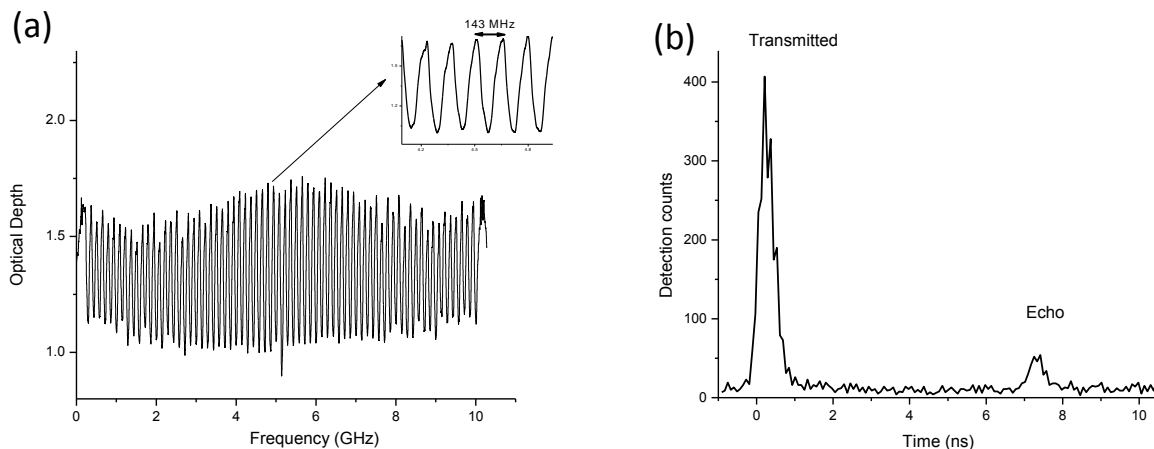
Figure 6.12: **AFC prepared by Serrodyne phase-modulated light: Storage of broadband photons from an SPDC source.** In the memory preparation stage, the frequency of the laser was linearly scanned over ± 5 GHz range, skipping every other 143 MHz interval within a 100 μs duration. This cycle was repeated 50 times to accumulate the population grating. After a wait time of 2.2 ms, a 10 GHz-wide AFC with 143 MHz peak spacing, shown in Figure **(a)**, was obtained. To demonstrate storage, photons with 6 GHz bandwidth, derived from a spontaneous parametric down conversion source (see Chapter 7) were sent the AFC memory and detected after storage of 7 ns as shown in Figure **(b)**.
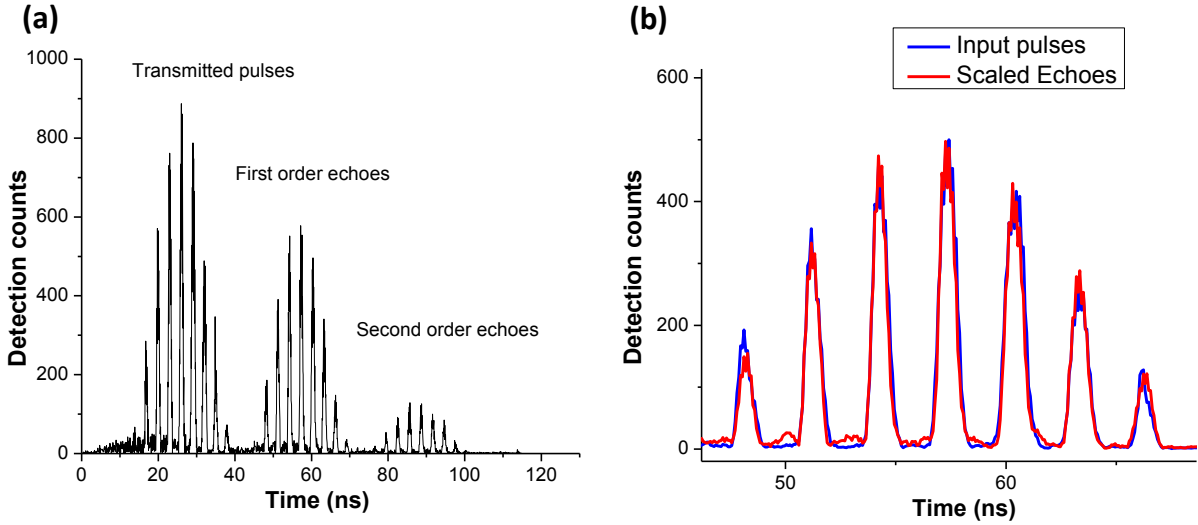
Figure 6.13: **Storage and retrieval of multiple temporal modes with different mean photon numbers.** The AFC medium was prepared with strong pulse pairs, as explained in Section 6.2.4. Each pulse was 600 ps long, resulting in nearly 1.5 GHz bandwidth. The peak spacing of the AFC was set to 32.2 MHz, corresponding to pulses separated by 31 ns. To demonstrate the multiple temporal mode storage in the prepared memory, a train of 8-short pulses, each with 1 ns duration was generated. These pulses were attenuated down to the single photon level– the tallest pulse containing on average 0.8 photons. All pulses were simultaneously stored, and were retrieved in the same order after 31 ns storage, as shown in Figure **(a)**. To assess the preservation of amplitude during storage, the measured echoes were scaled with respect to the input pulse train, as shown in Figure **(b)**. The good agreement between input and retrieved pulse train demonstrates the linearity of the AFC memory

6.3   Storage of Multiple Temporal Modes

As discussed in Section 4.7, the temporal multimode storage capacity of the AFC scales with the number of prepared absorption peaks. This number can be increased by extending the bandwidth and/or increasing the storage time (thus decreasing the peak spacing). Here, we take advantage of our large bandwidth AFC to demonstrate the high multimode storage capacity of our implementation. First, we demonstrate the storage of multiple temporal modes with attenuated laser pulses, each having different mean photon numbers as shown in Fig. 6.13a. As seen from Fig. 6.13b, the amplitudes of the retrieved pulses is preserved during

the storage. Fig. 6.14a illustrates the simultaneous storage of 128 modes with attenuated laser pulses, each containing one photon on average. In this demonstration, the AFC medium was again prepared with pulse pairs having 600 ps duration, resulting in nearly 1.5 GHz bandwidth. The storage time was set to 265 ns, which approaches the upper limit of our current storage medium. We also demonstrate the storage of 8-bit classical data using temporal modes occupied by single-photon level pulses, as shown in Fig 6.14b.

To finish this section, let me remind you that our memory also possesses large spectral multimode capacity. This will be further discussed in Chapter 10.
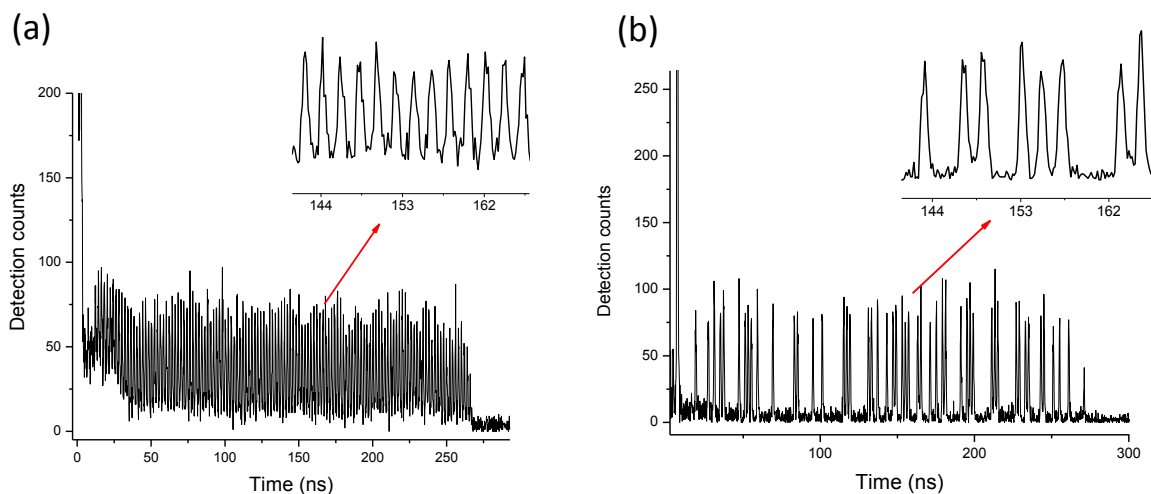
Figure 6.14: **Demonstration of simultaneous storage of 128 temporal modes.** An AFC memory with 1.5 GHz bandwidth and 2.77 MHz peak spacing, which yields 265 ns storage time, was prepared by short pair of pulses. To demonstrate the high multimode capacity of the memory, a pulse train, composed of 128 temporal modes with 600 ps duration and 2 ns separation was produced using an intensity modulator. Each pulse was attenuated down to the few photon level and directed to the prepared memory. All the temporal modes of the input pulse train were simultaneously stored for 265 ns such that the first mode did not come out until the last mode had entered the AFC medium as shown in Fig. **(a)**. 8-bit classical data was encoded into pulse trains and stored in the memory. The data was faithfully retrieved from the memory after 265 ns, as shown in Fig. **(b)**. In the figures, only echoes are displayed.

6.4   Double AFC scheme for Time-bin Qubit Manipulation

An AFC based quantum memory can be used as a robust tool to generate and analyze time-bin qubit states of photons. The idea behind this implementation is to superimpose two AFCs, referred to as double AFC, with different peak spacings such that each leads to different re-emission times, as illustrated in Fig. 6.15a.

First, to understand how this scheme can be used to produce a general time-bin qubit state, let us imagine that a photon occupying a well-defined temporal mode is mapped to a memory prepared with the double AFC shown in Fig. 6.15a. There is a certain probability for this photon to be absorbed by each AFC structure, but it is in principal impossible to know by which one. Hence the photon comes out in a superposition of two temporal modes (early and late), determined by the re-emission times of the superimposed AFCs, as shown in Fig. 6.15b. The phase of each output temporal mode is set by the frequency of the central of each AFC, as follows :

$$e^{2\pi i \frac{\Delta_{0i}}{\Delta_i}} \tag{6.1}$$

where Δ_{0i} is the difference between the input photon carrier frequency and the center peak of each AFC, and Δ_i is the peak separation within each AFC ($i = 1, 2$). This means that by shifting the centers of the AFCs, we can set any relative phase for re-emitted temporal modes, which allows the generation of arbitrary time-bin qubit states,

$$|\psi\rangle = \frac{1}{\sqrt{2}} \left(|e\rangle + e^{i\phi} |l\rangle \right) \tag{6.2}$$

where $|e\rangle$ and $|l\rangle$ denote early and late time-bin states and ϕ is the relative phase.

To see how a time-bin qubit is analyzed using the same AFC configuration, imagine that a photon is prepared in an equal superposition of early and late temporal modes such that the time separation between the modes is equal to the difference between re-emission times of the AFCs. When this photon is mapped to the double AFC memory, it has a certain probability of being absorbed and re-emitted by each AFC. This results in the observation
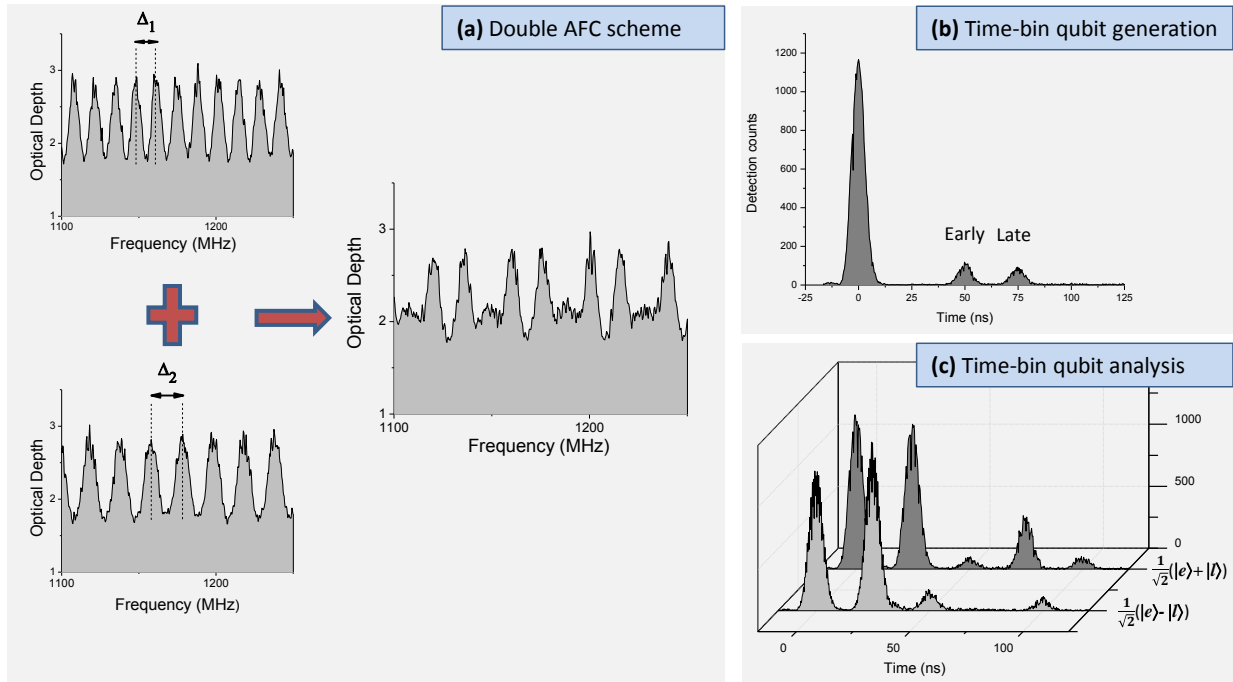
Figure 6.15: **A "double AFC" interferometer: (a)** Preparation of two superimposed AFCs with Δ_1 =13.3 MHz and Δ_2 =20 MHz peak spacings, yielding 75 ns and 50 ns storage times, respectively.**(b)** Generation of time-bin qubit states by the double-AFC scheme: When a single photon that occupies a well-defined temporal mode is stored in the prepared double-AFC, it is retrieved in a superposition of two temporal modes. Here the separation is 25 ns. **(c)** Projection measurement of a time-bin qubit using a double AFC. When a qubit, generated in a superposition of early and late temporal modes separated by 25 ns, is stored in the prepared double AFC, it is retrieved in a superposition of three temporal modes. The middle one arises from the overlap between early and late qubit modes, which allows analyzing the input superposition quantum states as shown in the figure. In the double-AFC, the center peak of each AFC was set to match the center frequency of the input photon, leading to a projection onto $|\psi\rangle = \frac{1}{\sqrt{2}}(|e\rangle + |l\rangle)$. If the input state is $|\psi\rangle = \frac{1}{\sqrt{2}}(|e\rangle - |l\rangle)$, practically no detection is observed in the middle temporal mode, as seen in the front curve. However, if the input state is $|\psi\rangle = \frac{1}{\sqrt{2}}(|e\rangle + |l\rangle)$, number of the detections in the middle temporal mode is nearly four times higher than the side modes as shown in the back figure. In the experiments, the double AFC was generated using the serrodyne frequency shifting technique. The applied magnetic field was adjusted so that the retrieval efficiency was the same for each AFC. Each probe pulse was generated by carving CW laser light using an AOM, and attenuated down to 20-30 photons on average before the cryostat. The size of the echoes was increased by a factor of three for illustration purpose.

of three temporal modes at the output of the memory as shown in Fig 6.15c. The middle temporal mode arises from the overlap between the early and late qubit modes. The detection of a photon in this mode corresponds to a projection of its state onto a superposition state, with phase given by the relative frequency between the center peaks of each AFC.

In this way, the double AFC scheme can be used as an alternative to imbalanced Mach-Zehnder interferometers for the manipulation of time-bin qubits. To demonstrate this capability, we prepare various time-bin qubits and project them onto a fixed state using a double AFC, as shown in Fig. 6.16a. Alternatively, we project a fixed quantum state onto varying bases using appropriately prepared double AFC configurations. From the latter measurement set, we also obtain the visibility curve, shown in Fig. 6.16b, and determine a visibility of about 96%. This is reasonably close to the theoretical maximum of 100%, demonstrating that our memory works as anticipated.

Furthermore, the double AFC can be employed to determine how faithfully quantum states can be stored in our memory. As will be shown in the next chapter, we used this approach to assess the quantum nature of our memory device by storing and analyzing retrieved time-qubits encoded into photons generated by SPDC.

The preparation of a double AFC can be done in different ways. One approach is to imprint the two AFCs one after the other in each optical pumping cycle, using one of the time-domain or frequency domain optical pumping approaches discussed in Section 6.2.4. The other approach is to imprint both population gratings simultaneously with an appropriate modulation of the intensity of the pumping light during each frequency sweep. Regardless the chosen method, one difficulty was to prepare each AFC with the same retrieval efficiency, in particular due to the fact that each AFC requires a different magnetic field to work optimally, i.e. to appropriately set the positions of holes and anti-holes. Therefore, the requirement for equal recall efficiencies leads to a reduction of the overall efficiency. In the experiments, the typical efficiency drop was about 10-40 % compared to that for the single AFC scheme,
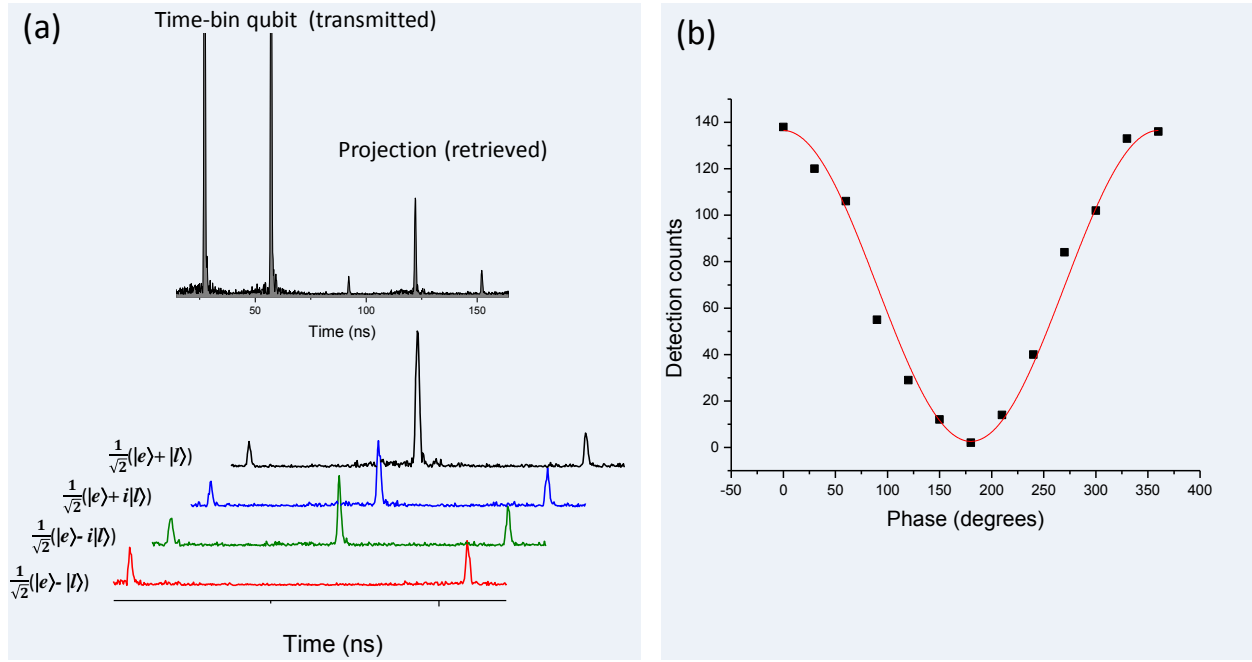
Figure 6.16: **Demonstration of manipulation of time-bin qubit states using double AFC interferometer: (a)** Time-bin qubits with different phase setting (ϕ), containing on average 0.4 photon per temporal mode, were stored in a double-AFC memory prepared for a projection onto $|\psi\rangle = \frac{1}{\sqrt{2}}(|e\rangle + |l\rangle)$. The lower part of the figure shows the results of the projection measurements for the input states $|\psi\rangle \in [\frac{1}{\sqrt{2}}(|e\rangle \pm |l\rangle), \frac{1}{\sqrt{2}}(|e\rangle \pm i|l\rangle)$. **(b)** Time-bin qubits in state $|\psi\rangle = \frac{1}{\sqrt{2}}(|e\rangle + |l\rangle)$ were stored in various double-AFCs with different phase setting. The phase setting (ϕ) for each measurement was changed by 30 degrees by appropriately shifting one of the AFC's center frequency, allowing projections onto $|\psi\rangle = \frac{1}{\sqrt{2}}(|e\rangle + e^{i\phi}|l\rangle)$. The figure shows the detection counts in the middle temporal mode for each phase. From these measurements, the visibility was established to be $96 \pm 2\%$, which is reasonably close to the theoretical maximum of $\%100$. In the experiments, time-bin qubits were produced by carving CW laser light into two temporally separated sub-ns pulses with relative phase and amplitude controlled by an AOM, and attenuating down to the single-photon level using neutral density filters. The storage time for each AFCs was set to 65 and 95 ns and, accordingly, the separation between the temporal early and late modes was 30 ns.

depending on selected storage times.

6.5 Limitations and Potential Improvements

The main limitations of our current AFC implementation with a Tm:LiNbO$_3$ waveguide are low retrieval efficiency, typically 0.5-3%, short storage time, up to 0.3 μs, and the small coupling efficiency of photons into the waveguide of around 20%. As discussed in Section 6.1, imperfect optical pumping in the preparation of the AFC, which arises from our material-specific relaxation dynamics is the main reason for the small efficiency. Specifically, the low transition probability between the oppositely oriented nuclear spin states that are used to shelve atomic populations leads to non-zero absorption background (d_0). For example, d_0 of 1 causes the loss of nearly 90% of the input photons due to irreversible absorption.

One way to overcome this problem in our material could be changing the orientation of the applied magnetic field, which, in all our experiments, was always oriented parallel to C_3 axis of the crystal. Experiments with bulk Tm:LiNbO$_3$ have shown that the application of a magnetic field perpendicular to the C_3 axis significantly improves the branching ratio between the oppositely oriented spin states by relaxing the spin selection rules [75]. This may also be valid in our waveguide material and could potentially help solving the problem. Spin mixing could be another approach to increase the decay probability to the oppositely oriented spin states. In this case, the application of an RF field that is on resonance with the excited level spin transition flips the spin states during optical pumping, speeding up the decay process to the oppositely oriented spin states [82]. Finally, stimulated emission through a fast decaying auxiliary optical level, e.g. the Stark levels or the ^{3}H$_5$ level in our material, could be another potential technique to improve the relaxation dynamics during optical pumping [83, 82]. Employing any of these techniques requires more spectroscopic investigations and additional elements such as RF field application.

As discussed in Section 4.4, the storage time of photons in an AFC in a RE material
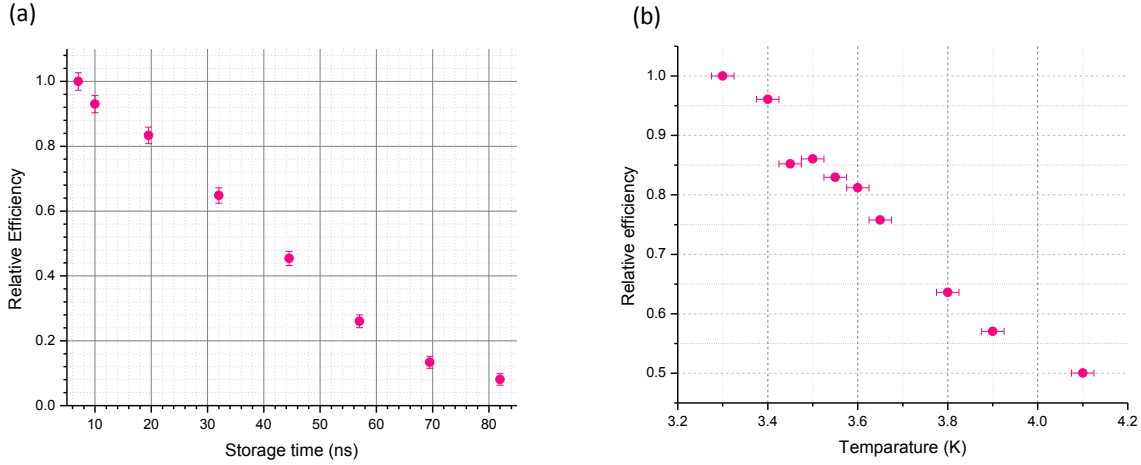
Figure 6.17: **Variation of AFC memory efficiency with respect to (a) storage time and (b) temperature.** The experiments were carried out with single photons provided from an SPDC source. The retrieval efficiency of the AFC memory was optimized for each configuration by adjusting the optical pumping power and magnetic field.

is upper bounded by the coherence time of the corresponding optical transition, which is nearly 1.5 μs in our material. This value is already quite small compared to the optical transitions in other RE systems. Furthermore this value cannot be achieved without excessively compromising the storage efficiency, and more reasonable limit is thus a few hundred ns as discussed in previous chapter. Fig. 6.17a shows the results of the experiment that characterizes relative retrieval efficiency versus storage time. As seen from the figure, increasing the storage time from 7 ns to 60 ns dramatically reduces the efficiency. This observation is the reason that in many of the proof-of-principle experiments we have selected small storage time settings to increase the signal to noise ratio in the detection of retrieved photons.

In RE materials, temperature is an important parameter that affects the coherence time of an optical transition and the lifetime of the long-lived magnetic levels as discussed in Chapter 5. In general, lowering the temperature reduces the energy perturbations of electronic levels and magnetic levels arising from the interaction with the crystal lattice, i.e. with phonons. Thus lowering temperature gives rise to increase of coherence time of the optical transition

and lifetime of magnetic levels. Therefore, maintaining the material temperatures at lower values allows preparing better AFCs.

Fig. 6.17b shows the characterization of the relative AFC retrieval efficiency with respect to the temperature, varied between 3.3 K and 4.2 K. As the temperature decreases, there is a significant increase in the retrieval efficiency. Consequently, lowering the temperature also allows for extending the storage time, while keeping the retrieval efficiency constant. With our current cryostat, the minimum temperature we can have is around 3 K. However, we are in the process of upgrading our cryostat so that we are able to lower the temperature down a few hundred mK. Based on the experiments with a bulk $Tm:LiNbO_3$ at about 1.5 K as shown in ref. [75], we anticipate that a temperature less than 1 K will have significant impact on the storage time and the efficiency.

The comparison of the spectroscopic properties of the waveguide $Tm:LiNbO_3$ crystals with bulk $Tm:LiNbO_3$ crystal can also give some understanding of the limits of our current quantum memory implementation. In ref. [75], a detailed study of the spectroscopic properties of the Tm atoms in a $LiNbO_3$ bulk crystal was reported. It can be seen that the Tm atoms in the bulk crystal have significantly longer coherence times and longer nuclear Zeeman lifetimes than in the waveguide structure at the same temperature. This may suggest that Ti ions, which cause the waveguiding property by introducing a refractive index change, could negatively affect the spectroscopic properties of the Tm atoms.

Furthermore, in ref. [84] a systematic comparison is made between the bulk and waveguide form of the different RE crystals in view of quantum memories. The conclusion of that study is that typically the bulk form of RE doped crystals have better properties for quantum memory applications, but careful waveguide fabrication can reduce the gap. In that study, a heating effect in the waveguide was also addressed as a potential cause of performance degradation in waveguide quantum memories. In fact, our observations and measurements support the existence of heating. We observed in some experimental configurations that

increasing the optical pumping power results in an increase in the absorption background (d_0) of the prepared AFC, contrary to the expectations. Our further characterizations have shown that the effect of having less deep holes with higher pump power is associated with the application of a magnetic field. As a result, this effect could be attributed to a decrease in the lifetime of nuclear Zeeman levels due to temperature increase inside the waveguide, although there has been no observation of temperature rise at the crystal in the course of experiments. Understanding the nature of such an effect requires more investigations.

The last limitation is the low coupling efficiency of light into the single mode waveguide. Our characterizations have shown that this problem stems from optical mode mismatch between the fibers and the waveguide. Tapered fibers, which can be tailored for matching the waveguide mode, should substantially increase the coupling efficiency beyond the current maximum of 0.2

In this thesis, for the first time, a quantum memory for light based on a rare earth element in a waveguide was developed. Improving its performance to the level required for use in a quantum repeater necessities extensive further material development and spectroscopic investigations. This includes the fabrication of waveguides with different techniques, in different host crystals doped with different RE ions in different concentrations, and the characterization of the spectroscopic properties of each material.

Chapter 7

Storage of Quantum Information

A quantum memory must be capable to faithfully store quantum information, as discussed in Chapter 3. Towards the development of a quantum memory with high fidelity storage capability, first, the spectral properties of a material candidate must be investigated, as we did for our Tm:LiNbO$_3$ waveguide (Chapter 5). Secondly, using the results of that and other investigations, a quantum memory protocol must be implemented, as we did with the AFC protocol (Chapter 6). The next step is to assess the quantum nature of the developed memory device, which requires storing quantum states encoded into photons, and verifying that the retrieved photons carry the originally encoded quantum state. In addition, quantum repeaters require a mechanism that heralds the storage of quantum information, which can be done, for example, by taking advantage of the generation of photons in pairs, as explained in Section 3.2.3. Hence, we interfaced our memory device with a photon pair source based on parametric down conversion and then we demonstrated the faithful storage of time-bin qubit states, encoded into one member of a photon pair. Also, the detection of the other photon member was used to conditionally accept a detection after retrieval from the quantum memory, which is closely related to heralded quantum state storage. This study is an important step towards the implementation of quantum repeaters. I contributed to this study at the following stages: Developing the broadband quantum memory, performing the measurements, analyzing and interpreting the main results and writing the most part of the manuscript. Our findings from this investigation were published in Physical Review Letters. The following section is the published version of this article, which has been re-formatted for the consistency with the other chapters of this thesis.

7.1 Paper II

Conditional Detection of Pure Quantum States of Light after Storage in a Tm-Doped Waveguide

Erhan Saglamyurek[1], Neil Sinclair[1], Jeongwan Jin[1], Joshua A. Slater[1], Daniel Oblak[1], Félix Bussières[1], Mathew George[2], Raimund Ricken[2], Wolfgang Sohler[2], and Wolfgang Tittel[1]

[1]*Institute for Quantum Information Science, and Department of Physics and Astronomy, University of Calgary, 2500 University Drive NW, Calgary, Alberta T2N 1N4, Canada*

[2]*Department of Physics - Applied Physics, University of Paderborn, Warburger Str. 100, 33095 Paderborn, Germany*

Abstract

We demonstrate the conditional detection of time-bin qubits after storage in and retrieval from a photon-echo based waveguide quantum memory. Each qubit is encoded into one member of a photon-pair produced via spontaneous parametric down conversion, and the conditioning is achieved by the detection of the other member of the pair. By performing projection measurements with the stored and retrieved photons onto different bases, we obtain an average storage fidelity of 0.885±0.020, which exceeds the relevant classical bounds and shows the suitability of our integrated light-matter interface for future applications of quantum information processing.

7.1.1 Introduction

Quantum memories are key elements for future applications of quantum information science such as long-distance quantum communication via quantum repeaters [1,2] and, more generally, distributed quantum information processing in quantum networks [3]. They enable

reversible mapping of arbitrary quantum states between travelling and stationary carriers (i.e. light and matter). This reduces the impact of loss on the time required to establish entanglement between distant locations [1], and allows the implementation of local quantum computers based on linear optics [3]. However, towards these ends, the successful transfer of a quantum state into the memory must be announced by a heralding signal. When using an individual absorber, such a signal can be derived through the detection of a change of atomic level population [5]. In atomic ensembles, this approach is infeasible. Instead, storage is derived from the detection of a second photon that indicates either the absorption [6], or the presence of the first at the input of the memory [7] (the first approach relies on spontaneous Raman scattering, the second on using pairs of photons). Furthermore, quantum memories must have large acceptance bandwidths and multi-mode capacities, and allow on-demand read-out after second-long storage with high efficiency [7,8]. In addition, for viable quantum technology, quantum memories should be robust and simple to operate (e.g. be based on integrated optics).

A lot of progress towards these figures of merit has been reported over the past few years, including work that explores electromagnetically induced transparency (EIT), as well as photon-echo and cavity QED-based approaches (see [2,5,7-16] for reviews and latest achievements). For instance, quantum memories employing Rb vapour have demonstrated efficiencies up to 87% [9] and storage times in excess of 0.1 s [10], while GHz bandwidths [11] and storage of 64 modes [14] have been shown in rare-earth materials. However, having a quantum memory that simultaneously satisfies all figures of merit currently remains an outstanding challenge.

Yet, strictly, most of these experiments did not report true heralding – either heralding was not actually implemented, the "heralding" signal was generated only after the stored photon left the memory, or the signal could, due to technical issues, only be derived once the stored photon was detected. Nevertheless, experiments that employ photon pairs [11-13,17]

do gain from conditioning the detection of the stored photon on that of the auxiliary photon (i.e. *a posteriori* "heralding"): By reducing the effects of loss and detector noise, conditioning generally increases the fidelity between the quantum state of the original and the retrieved photon.

Supplementing the experiments on storage of entangled photons [11-13,17], we now report another step towards the goal of building universal, viable, and heralded quantum memory devices – the storage of photons in pure quantum states in a solid state waveguide, their retrieval, and their conditional detection by means of temporal correlations with auxiliary photons. We point out that the step to true heralding is minor and of purely technical nature; it simply requires using different, existing, single-photon detectors (see [18,19]).

7.1.2 Experiment

Our experimental setup consists of two main blocks, see Fig. 7.1: a spontaneous parametric down-conversion (SPDC) photon-pair source, and a Ti:Tm:LiNbO$_3$ single mode waveguide fabricated by indiffusion processes [20]. When cooled to 3 K, and by using a photon-echo quantum memory protocol [7,8,21], the Tm-doped waveguide allows storage and retrieval of quantum states encoded into one member of each photon pair, while the detection of the other member provides the conditioning signal.

In the photon-pair source a mode-locked pump laser generates 6 ps long pulses at a rate of 80 MHz and 1047.328 nm central wavelength. They are subsequently frequency-doubled (FD) in a periodically poled LiNbO$_3$ (PPLN) crystal, yielding pulses with 523.664 nm central wavelength, 16 ps duration, and 90 mW average power. The FD pulses are sent to a second PPLN crystal that, via SPDC, produces pairs of photons centred at 795.506 nm and 1532.426 nm. Frequency filtering the 795 nm photons with a 6 GHz-bandwidth Fabry-Perot filter (FPF) and the 1532 nm photons with a 9 GHz-bandwidth fiber-Bragg grating (FBG) we obtain frequency uncorrelated pairs. Each 795 nm photon travels through an imbalanced, temperature-stabilized Mach-Zehnder interferometer with 42 cm path-length
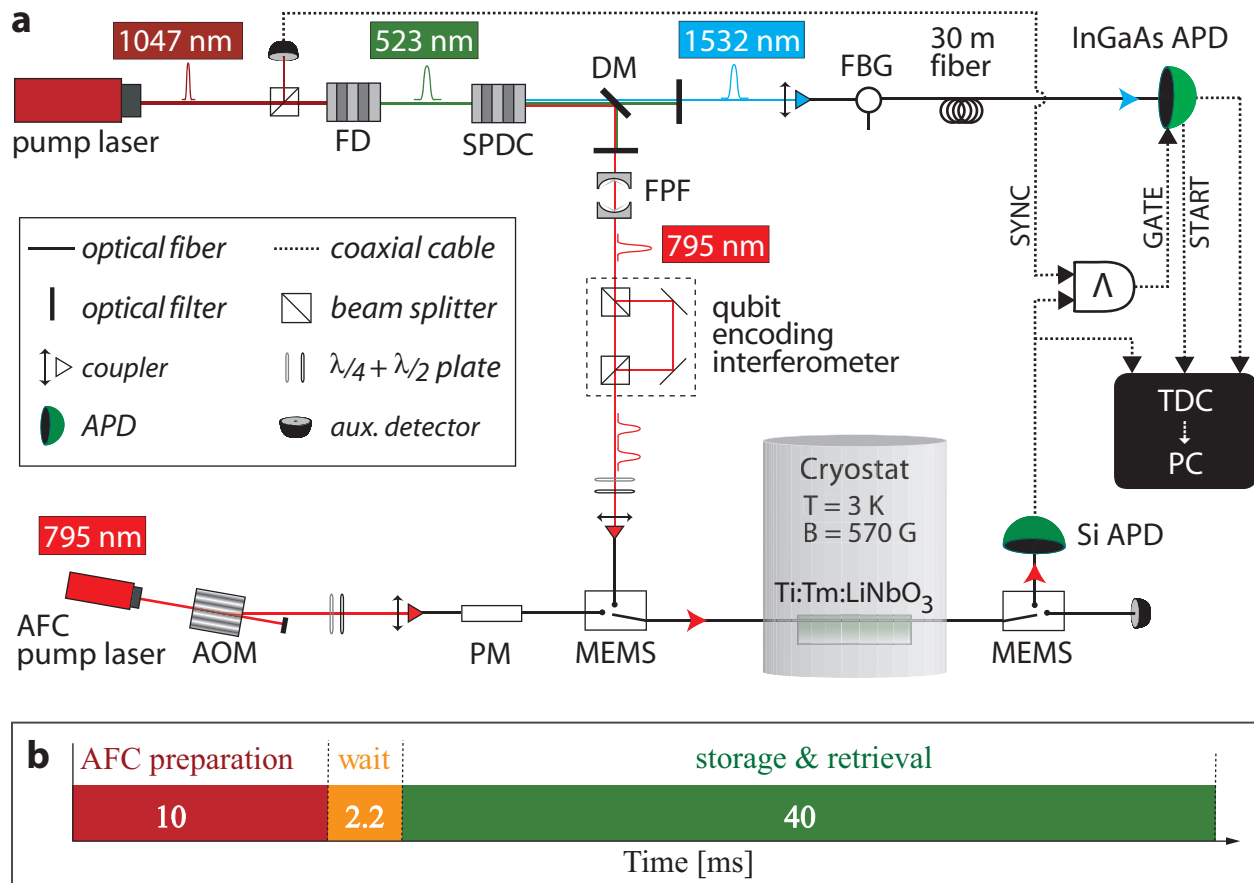
Figure 7.1: (color online) **a. Photon pair source and quantum memory setup (see text for details):** Wave-plates align light polarization along the LiNbO$_3$'s C$_3$-axis. The waveguide is held at 3 K, and a 570 G magnetic field is applied along the crystal's C$_3$-axis (see Fig. 7.1 2a). **b.** Timing sequence containing three repeated phases: 10 ms *AFC preparation* for optical pumping, 2.2 ms *wait* to allow excited population to decay, and 40 ms *storage and retrieval*, during which 795 nm photons are successively stored for $t_{st} = 6$ ns and then recalled.

107

difference, corresponding to 1.4 ns relative delay. Thus, each photon emerges in a super-position of two temporal modes (early and late), i.e., in a time-bin qubit state [22]. They are then directed into the quantum memory, stored, retrieved, and finally detected by a Si avalanche-photo-diode (APD)-based single-photon detector.

All 1532 nm photons are sent through 30 m standard telecommunication fiber to an InGaAs APD-based single-photon detector. As is typically done, the detector is gated to reduce noise. The gate signal could in principle be the SYNC signal derived from each pulse emitted by the pump laser. However, as its repetition rate of 80 MHz by far exceeds the maximum gate frequency of our detector, around 1 MHz, we first AND the SYNC pulses with pulses generated by each Si-APD detection, and then use this low-rate signal to gate the InGaAs-APD. Provided the latter is ready for photon detection (i.e. not deadtime-blocked due to a previous detection), this signal also starts a time-to-digital converter (TDC), which then records the time-difference between the detection events produced by the Si-APD and the InGaAs-APD. These data are used to obtain statistics for single detections of the retrieved 795 nm photons, as well as for detections conditioned on the existence of 1532 nm photons. We emphasize that if an InGaAs APD supporting 80 MHz gate rate had been available [18,19], then 1532 nm photons could have been detected without the need for *a priori* detection of a 795 nm photon. This simple modification of our setup would have turned the conditional detection of 795 nm photons into detections that are heralded by clicks of the InGaAs APD.

The other main block of our setup is a Ti:Tm:LiNbO$_3$ waveguide that allows storage and retrieval of the 795 nm photons via the atomic frequency comb (AFC) quantum memory protocol [21]. This approach to quantum state storage requires the spectral absorption of an atomic ensemble to be constituted of a series of equally spaced lines with frequency spacing Δ_ν. The interaction between such an AFC and a photon with wavevector k leads to the absorption of the photon and generates a collective excitation in the atomic medium that is

described by

$$|\Psi\rangle = \frac{1}{\sqrt{N}} \sum_{j=1}^{N} c_j e^{i2\pi m_j \Delta_\nu t} e^{-ikz_j} |g_1, \cdots e_j, \cdots g_N\rangle . \qquad (7.1)$$

Here, $|g_j\rangle$ ($|e_j\rangle$) denotes the ground (excited) state of atom j, $m_j\Delta_\nu$ is the detuning of the atom's transition frequency from the photon carrier frequency, z_j its position measured along the propagation direction of the light, and the factor c_j depends on the atom's resonance frequency and position. Because of the presence of different atomic transition frequencies, the excited collective coherence dephases rapidly. However, the particular shape of the absorption line results in the recovery of the collective coherence after storage time $t_{st} = 1/\Delta_\nu$. This can easily be seen from Eq. (7.1): for $t = 1/\Delta_\nu$ all frequency dependent phase factors are zero (mod 2π). This leads to re-emission of the photon into the original mode and quantum state with maximally 54% efficiency for an optimally implemented AFC. Modifications to the procedure enable recall on demand and up to 100% efficiency [21].

Suitable media in which to implement the AFC protocol are cryogenically cooled rare-earth ion doped crystals [7,23]. They feature inhomogeneously broadened absorption profiles, often posses long-lived atomic sub-levels that can serve as shelving levels for tailoring the AFC through persistent spectral hole burning, and generally have long coherence times on optical and spin transitions. We use the $^3H_6$-$^3H_4$ transition of Tm ions in a single-mode channel waveguide fabricated by Ti indiffusion into the Tm doped surface of a Z-cut LiNbO$_3$ crystal, see Fig. 7.2a [20]. To tailor the desired AFC into the inhomogeneously broadened absorption profile, Tm ions with transition frequencies within the comb's troughs are optically pumped via the excited level into long-lived nuclear Zeeman levels, see Fig. 7.2b [20,24]. To achieve frequency selective optical pumping we employed a linear side-band chirp technique [11,25] that allowed us to create a 5 GHz broad grating (matching the spectral width of the 795 nm photons) with tooth spacing of 167 MHz, see Fig. 7.2c. This corresponds to a storage time of 6 ns. After each 10 ms-long AFC preparation a 2.2 ms-long wait time allows atoms excited by the optical pumping to decay before photon storage (see Fig. 7.1b for the
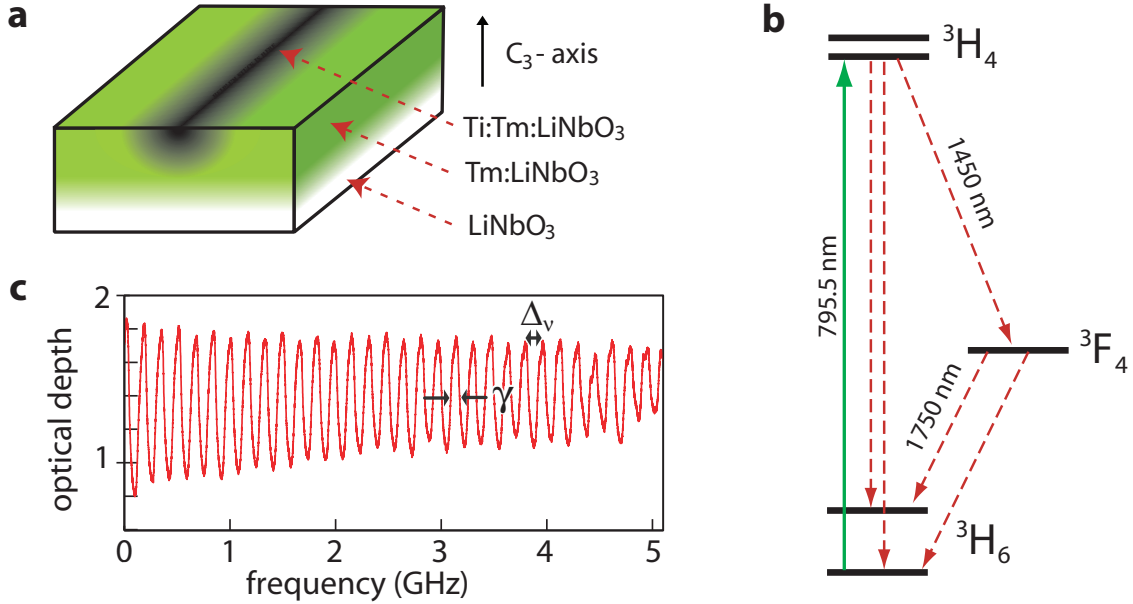
Figure 7.2: (color online) **a. Waveguide geometry:** The sample surface is first doped by indiffusing a ≈ 20 nm thick Tm layer yielding a concentration profile of ≈ 6 μm depth with $\approx 10^{20}$ ions per cm^3 surface concentration. Subsequently a 3 μm wide channel waveguide is fabricated by indiffusion of a 40 nm thick vacuum-deposited Ti stripe. AFC preparation light and single photons are coupled in and out of the waveguide with 10% total efficiency by butt-coupling single mode fibers. **b. Simplified energy level diagram of Tm ions:** The optical coherence time of the $^3H_6$-$^3H_4$ transition at 3 K is 1.6 μs, and the radiative lifetimes of the $^3H_4$ and $^3F_4$ levels are 82 μs and 2.4 ms, respectively. A 570 G magnetic field splits the ground and excited levels into Zeeman sub-levels. The ground Zeeman level splitting is $\sim$ 83 MHz, and the lifetime of the upper ground level exceeds one second. **c. 5 GHz-bandwidth AFC:** The tooth separation is $\Delta_\nu = 167$ MHz, corresponding to 6 ns storage time. The line-width of the teeth is $\gamma = 83$ MHz.

timing per experimental cycle). A set of micro electro-mechanical switches (MEMS) then open the channel for qubits to enter the memory, and, after recall, direct them towards the Si-APD. We assessed our memory's retrieval efficiency to be $(2 \pm 0.5)\%$. Taking the 10 dB fibre-to-fibre coupling loss in and out of the waveguide into account, this yields an overall system efficiency of approximately 0.2% [11].

An interesting and useful aspect of photon-echo quantum memory protocols is that they provide a robust tool to manipulate time-bin qubits [26-29]. For example, by using the

110

AFC approach, any projection measurement on time-bin qubit states can be performed by superimposing two combs (double AFC) with appropriately chosen relative center frequencies and amplitudes [27]. This leads to two re-emission times that can be set to differ by the temporal mode separation of the qubit to be analyzed (1.4 ns for our experiments). Hence, as a previously absorbed photon is re-emitted by the superimposed combs, early and late temporal modes interfere, allowing the qubit state to be analyzed in the same way as is typically done with an imbalanced Mach-Zehnder interferometer [27]. Double AFC recall will, however, lead to a reduction of the recall efficiency (compared to single recall).

7.1.3 Measurements

To demonstrate faithful storage and retrieval of quantum states from the memory, we performed projection measurements with various time-bin qubits onto different bases using single (standard) and double AFC schemes as explained before. In all our measurements the average photon number per qubit was 0.1 at the output of the qubit-encoding interferometer. First we generated qubit states that occupy only early $|e\rangle$ or late $|l\rangle$ temporal modes by blocking either the long or short arm of the qubit-encoding interferometer, respectively, and then stored these states in the memory for 6 ns. Fig. 7.3 (left) shows single detections (no conditioning) of the retrieved photons as a function of the time difference with respect to the START signal. The dark counts from the Si-APD reduce the signal to noise ratio (SNR) to ~ 5. For an input state $|e\rangle$, we compute the fidelity as $\mathcal{F}_e = C_{e|e}/(C_{e|e} + C_{l|e})$, where, e.g., $C_{l|e}$ denotes the number of detected counts in the late time-bin given $|e\rangle$ was encoded in the qubit at the input. Similarly, we can find $\mathcal{F}_l$, enabling us to calculate the mean fidelity: $\mathcal{F}_{el} = (\mathcal{F}_e + \mathcal{F}_l)/2 = 0.8514 \pm 0.0004$.

On the other hand, conditioning the detections of the retrieved photons on the detection of 1532 nm photons leads to a substantial increase of the SNR to ~ 22, as shown in Fig. 7.3 (right). This yields a mean fidelity of $\mathcal{F}_{el}^* = 0.9539 \pm 0.0024$.

Next, qubit states in an equal superposition of early and late temporal modes $\frac{1}{\sqrt{2}}(|e\rangle +$
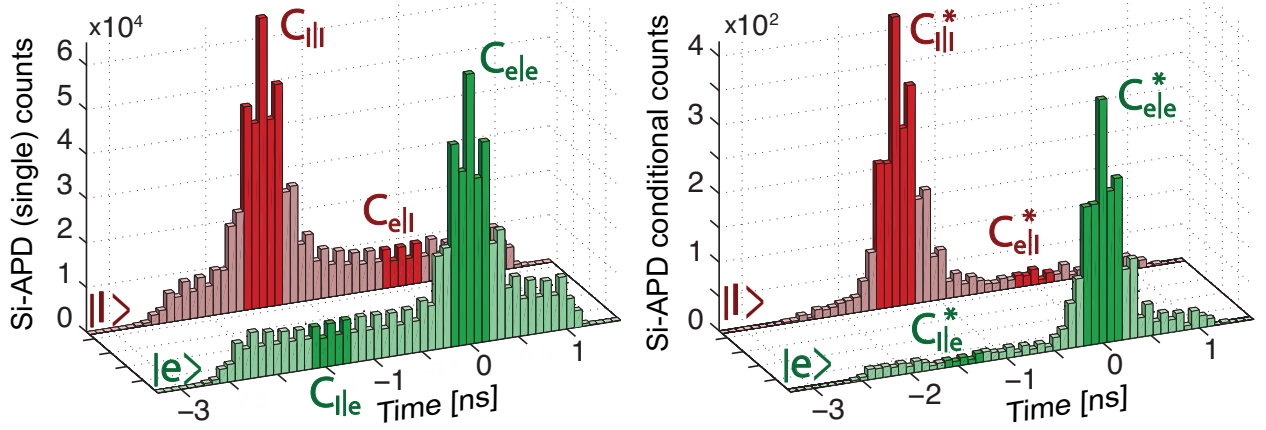
Figure 7.3: (color online) **Storage of early and late time-bin qubit states in the AFC memory:** The left-hand figure depicts the histograms from 180 min of single detections of the retrieved 795 nm photons prepared in early (red) and late (green) qubit states with the highlighted regions marking the relevant detection windows. The right-hand figure shows the detections conditioned on 1532 nm photons for the same states. Without conditioning the fidelities are $\mathcal{F}_e = 0.8652 \pm 0.0006$ and $\mathcal{F}_l = 0.8376 \pm 0.0004$ for the storage of early and late time-bin states, respectively. Correspondingly, with conditioning, the fidelities are $\mathcal{F}_e^* = 0.9505 \pm 0.0058$ and $\mathcal{F}_l^* = 0.9573 \pm 0.0033$.

$e^{i\phi}|l\rangle$) were produced with ϕ set to zero. Storage and projection measurements were performed using the double AFC scheme with the relative phase of the two combs (measured w.r.t. the phase introduced by the qubit-encoding interferometer) varied by $\pi/2$ increments. The results for single and conditional detections are given in Fig. 7.4. The histograms show the detection statistics for zero and π double AFC phase settings, from which we extract a SNR slightly above 1 for the single, and above 6 for the conditional detection. In the lower part of Fig. 7.4 we show the normalized counts for each projection setting for the single and conditional detections. Fitting sinusoidal curves to these we derive visibilities $\mathcal{V}$, which, in turn, yield a fidelity $\mathcal{F} = (1 + \mathcal{V})/2$ for single detections of $\mathcal{F}_\phi = 0.682 \pm 0.020$. For conditional detections we find a significantly larger value of $\mathcal{F}_\phi^* = 0.851 \pm 0.030$. These figures allow establishing an average, single detection fidelity: $\overline{\mathcal{F}} \equiv (\mathcal{F}_{el} + 2\mathcal{F}_\phi)/3 = 0.738 \pm 0.029$. This violates the quantum classical bound [30] of ~ 0.667, thus verifying that our memory outperforms any classical storage protocol. However, it is below the bound of ~ 0.833

for an optimal universal quantum cloner [31]. Harnessing the conditional detection we find $\overline{\mathcal{F}^*} = 0.885 \pm 0.020$. This beats the quantum-classical bound by 10 standard deviations and also violates the optimal universal quantum cloner bound by 2.5 standard deviations.
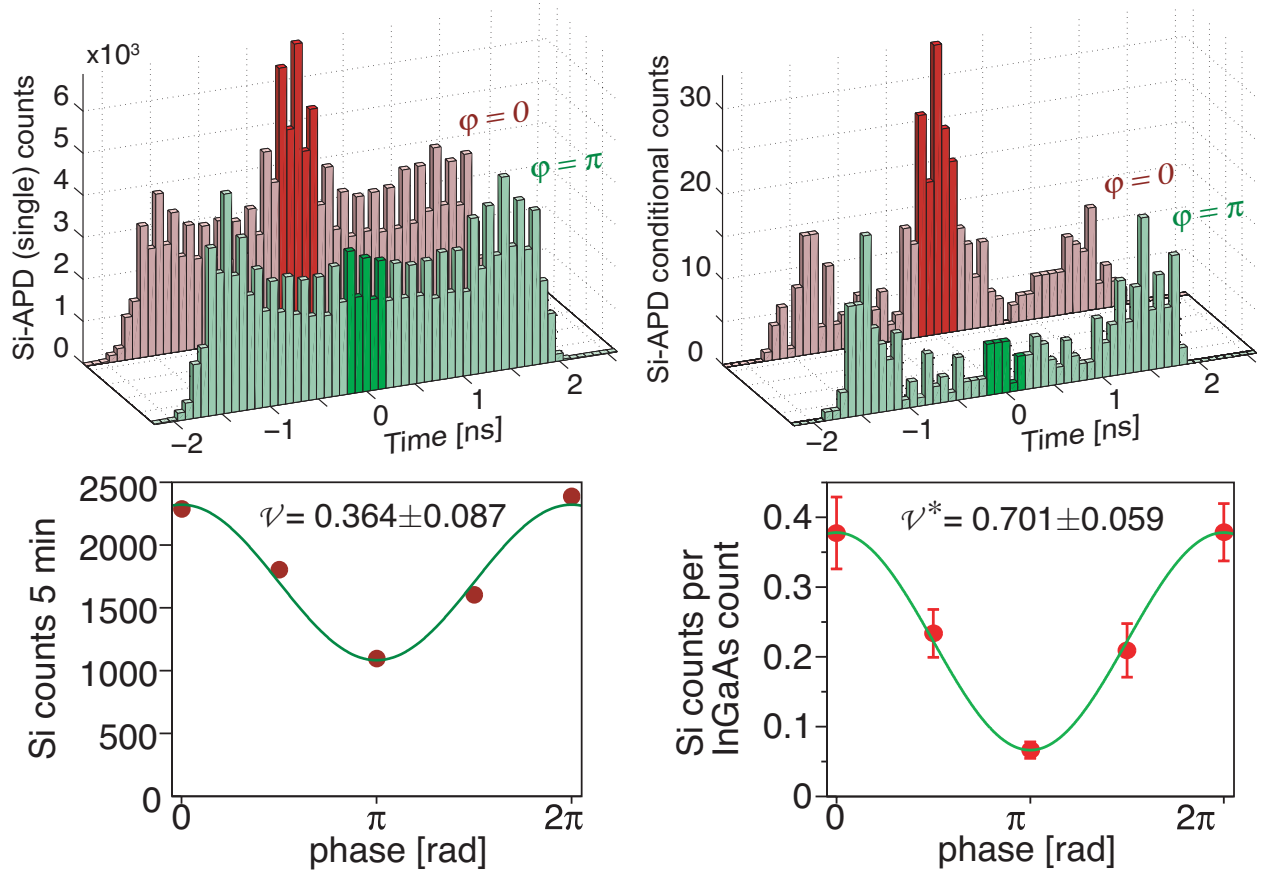
Figure 7.4: (color online) **Retrieval of qubits created in a superposition of early and late temporal modes:** The top left figure presents histograms of single detections of the retrieved 795 nm photons with AFC phase settings of zero (red) and π (green), collected during 80 min. The top right figure shows the same histograms for conditional detections. The highlighted regions mark detection windows used to derive projection probabilities required to calculate fidelities. The lower curves show single and coincidence counts obtained for all phase settings for single detections (left) and conditional detections (right), yielding visibilities of 0.364 ± 0.087 and 0.701 ± 0.059, respectively.

7.1.4 Conclusion

To conclude, we have demonstrated storage, retrieval, and conditional detection of different time-bin qubit states using a solid-state Ti:Tm:LiNbO3 waveguide quantum memory with

average fidelity $\overline{\mathcal{F}^*} = 0.885 \pm 0.020$, which exceeds the relevant classical bounds. Operating the memory in a heralded fashion is readily achievable with high-rate APDs that have recently become commercially available. Despite our memory device's current limitations, namely efficiency, storage time, and preset recall time, the high fidelity and the wide spectral acceptance makes our approach promising for future quantum communication schemes and quantum networks. The LiNbO$_3$ host crystal and the waveguide structure have potential advantages in quantum memory applications such as fast electric field control of collective atomic phase evolution and, due to the resemblance with building blocks of classical integrated optical devices [32], it holds promise for simple integration with existing information technology. Furthermore, the ability to perform projection measurements using a photon-echo memory provides a simple and robust tool that might find use in other applications of quantum information processing.

Acknowledgments

7.1.5   References

1. H.-J. Briegel et al., Phys. Rev. Lett. 81, 5932 (1998).

2. N. Sangouard et al., Rev. Mod. Phys. 83, 33 (2011).

3. J. Kimble, Nature (London) 453, 1023 (2008).

4. P. Kok et al., Rev. Mod. Phys. 79, 135 (2007).

5. H.P. Specht et al., Nature (London) 473, 190 (2011).

6. H. Tanji et al., Phys. Rev. Lett. 103, 043601 (2009).

7. W. Tittel et al., Laser Photon. Rev. 4, 244 (2010).

8. A.I. Lvovsky, B.C. Sanders and W. Tittel, Nature Photon. 3, 706 (2009).

9. M. Hosseini et al., Nature Phys. 7, 794 (2011).

10. A.G. Radnaev et al., Nature Phys. 6, 894 (2010).

11. E. Saglamyurek et al., Nature (London) 469, 512 (2011).

12. C. Clausen et al., Nature (London) 469, 508 (2011).

13. H. Zhang et al., Nature Photon. 5, 628 (2011).

14. I. Usmani et al., Nature Commun. 1, 12 (2010).

15. K.F. Reim et al., Phys. Rev. Lett. 107, 053603 (2011).

16. M. Hedges et al., Nature (London) 465, 1052 (2010).

17. K. Akiba et al., New J. Phys. 11, 013049 (2009).

18. M.D. Eisaman et al., Rev. Sci. Instrum. 82, 071101 (2011).

19. ID Quantique SA, Phys. Today 64, 59 (2011).

20. N. Sinclair et al., J. Lumin. 130, 1586 (2010).

21. M. Afzelius et al., Phys. Rev. A 79, 052329 (2009).

22. W. Tittel and G. Weihs, Quantum Inf. Comput. 1, No. 2, 3 (2001).

23. C. Thiel, T. Böttger, and R. Cone, J. Lumin. 131, 353 (2011).

24. C.W. Thiel et al., J. Lumin. 130, 1598 (2010).

25. R.R. Reibel et al., J. Lumin. 107, 103 (2004).

26. S.A. Moiseev and B.S. Ham, Phys. Rev. A 70, 063809 (2004).

27. H. de Riedmatten et al., Nature (London) 456, 773 (2008).

28. M. Hosseini et al., Nature (London) 461, 241 (2009).

29. S.A. Moiseev and W. Tittel, Phys. Rev. A 82, 012309 (2010).

30. S. Massar and S. Popescu, Phys. Rev. Lett. 74, 1259 (1995).

31. V. Buzek and M. Hillery, Phys. Rev. A 54, 1844 (1996).

32. W. Sohler et al., Opt. Photonics News 19, 24 (2008).

Chapter 8

Storage and Retrieval of Photonic Entanglement

Entanglement is one of the fundamental and most surprising concepts in quantum mechanics. It can give rise to certain correlations between separate quantum mechanical systems that cannot be explained by classical physics (see Sect. 2.2 and 2.3). The most astonishing feature of these correlations is their non-local character. The interpretation of this counter-intuitive phenomenon is so important that it has occupied philosophers, physicists, other scientists and the general populace since the early days of quantum theory.

Beyond this fundamental aspect, quantum entanglement is a basic resource for long distance quantum communications, as discussed in Chapter 2. Entanglement allows for the distribution of quantum information between remote locations without direct transmission of that information. As further explained in Sect. 3.1, for achieving this task over large distances, one also requires quantum memories that store entanglement until needed. Consequently, a quantum memory that is suitable for quantum communication must preserve entanglement during storage. Following our demonstration of faithful quantum information storage, our next goal thus was to demonstrate the storage and retrieval of entangled states of light. To do this, we reversibly mapped one member of time-bin entangled photon pairs into and out of our waveguide quantum memory. By performing correlations measurements, we demonstrated that the retrieved photon remains entangled with the other member of the pair, without degradation in the amount of entanglement. This experiment is a very important step towards the realization of long distance quantum communication. My contributions to this study were the following : Developing the broadband quantum memory, performing measurements, analysis and interpretation of the main results, editing the manuscript. Our study was published in the January 2011 issue of Nature. The following section is the pub-

lished version of this article which has been re-formatted for the consistency with the other chapters of this thesis.

8.1   Paper III

Broadband Waveguide Quantum Memory for Entangled Photons

Erhan Saglamyurek[1], Neil Sinclair[1], Jeongwan Jin[1], Joshua A. Slater[1], Daniel Oblak[1], Félix Bussières[1], Mathew George[2], Raimund Ricken[2], Wolfgang Sohler[2], and Wolfgang Tittel[1]

[1]*Institute for Quantum Information Science, and Department of Physics and Astronomy, University of Calgary, 2500 University Drive NW, Calgary, Alberta T2N 1N4, Canada*
[2]*Department of Physics - Applied Physics, University of Paderborn, Warburger Str. 100, 33095 Paderborn, Germany*

Abstract

The reversible transfer of quantum states of light into and out of matter constitutes an important building block for future applications of quantum communication: it will allow the synchronization of quantum information [1], and the construction of quantum repeaters [2] and quantum networks [3]. Much effort has been devoted to the development of such quantum memories [1], the key property of which is the preservation of entanglement during storage. Here we report the reversible transfer of photon–photon entanglement into entanglement between a photon and a collective atomic excitation in a solid–state device. Towards this end, we employ a thulium-doped lithium niobate waveguide in conjunction with a photon-echo quantum memory protocol [4], and increase the spectral acceptance from the current maximum [5] of 100 Megahertz to 5 Gigahertz. We assess the entanglement-preserving

117

nature of our storage device through Bell inequality violations [6] and by comparing the amount of entanglement contained in the detected photon pairs before and after the reversible transfer. These measurements show, within statistical error, a perfect mapping process. Our broadband quantum memory complements the family of robust, integrated lithium niobate devices [7]. It simplifies frequency-matching of light with matter interfaces in advanced applications of quantum communication, bringing fully quantum-enabled networks a step closer.

8.1.1 Introduction

Quantum communication is founded on the encoding of information, generally referred to as quantum information, into quantum states of light [6]. The resulting applications of quantum physics at its fundamental level offer cryptographic security through quantum key distribution without relying on unproved mathematical assumptions [8] and allow for the disembodied transfer of quantum states between distant places by means of quantum teleportation [6]. Reversible mapping of quantum states between light and matter is central to advanced applications of quantum communication such as quantum repeaters [2] and quantum networks [3], in which matter constitutes nodes that hold quantum information until needed, and thereby synchronize the information flow through the communication channel or network. Furthermore, such a quantum interface allows the generation of light–matter entanglement through the mapping of one of two entangled photons into matter. To determine whether and how different physical systems can be entangled, and to localize the fundamental or technological boundaries where this fascinating quantum link breaks down, are central goals in quantum physics and have received much attention over the past decades [6].

The reversible light–matter interface can be realized through the direct transfer of quantum states from light onto matter and back, or through the generation of light–matter entanglement followed by teleportation of quantum information from an externally provided

photon into matter, and eventually back. Experimental capabilities have advanced rapidly over the past years and quantum state transfer between light and atomic vapour [9–13], solid–state ensembles [4,14], or single absorbers [15], as well as the generation of light–matter entanglement through the absorption of photons [16–18], or the emission of photons from atomic ensembles [19–21] or single emitters [22, 23] have all been reported.

For quantum memory to become practical, it is important to reduce the complexity of experimental implementations, and the recent addition of rare-earth-ion-doped crystals [4,14] to the set of storage materials has been a valuable step towards this goal. The promise of such crystals is further enhanced through potentially long storage times–up to several seconds in Pr:Y_2SiO_5 [24]. In addition, given the large inhomogeneous broadening of optical zero-phonon lines, up to 100 Gigahertz (GHz), rare-earth-ion-doped crystals in principle offer storage of photons with less than 100-picosecond duration when being used in conjunction with a suitable quantum memory protocol [4]. Yet, the reversible state transfer between light and solid–state devices has so far not been shown to preserve entanglement. This is largely due to the limited spectral bandwidth of current implementations, 100 Megahertz (MHz) at most [5], which is orders of magnitude smaller than that of entangled photon pairs generated in the widely used process of spontaneous parametric down-conversion [6]. In this work, we approach the problem from both ends: we increase the acceptance bandwidth of our storage device to 5 GHz and narrow the bandwidths of our entangled photons to similar values. Furthermore, by using a wave-guiding storage medium, we move fundamental quantum memory research further towards application.

8.1.2 Experiment

The layout of our experiment is depicted in Fig. 8.1. Short pulses of 523-nm wavelength light travel through an unbalanced interferometer. For sufficiently small pulse energies, subsequent spontaneous parametric down-conversion yields, to a good approximation, individual pairs of photons, centred at wavelengths around 795 nm and 1,532 nm, in the time-bin entangled

qubit state [25]:

$$\left|\phi^+\right\rangle = \frac{1}{\sqrt{2}}\left(|e,e\rangle + |l,l\rangle\right) \tag{8.1}$$

Here, $|e\rangle$ and $|l\rangle$ denote early and late temporal modes and replace the usual spin-down and spin-up notation for spin-half particles. More specifically, $|i,j\rangle$ denotes a quantum state in which the 795-nm photon has been created in the temporal mode i, and the 1,532-nm photon has been created in the temporal mode j. We point out that, owing to the spectral filtering, our source generates frequency-uncorrelated entangled photons at wavelengths that match the low-loss windows of free-space and standard telecommunication fibre. It can thus be readily used in real-world applications of quantum communication that involve quantum teleportation and entanglement swapping.

The 1,532-nm photon is directed to a qubit analyser. It consists of either a fibre delay line followed by a single-photon detector that monitors the photons arrival time, or a fibre-optical interferometer that is unbalanced in the same way as the pump interferometer, followed by single-photon detectors. The role of the delay line is to perform projection measurements of the photons state onto early and late qubit states. Alternatively, the interferometer enables projections onto equal superpositions of early and late modes [25]. Using the language of spin-half systems, this corresponds to projections onto σ_z and, for appropriately chosen phases, σ_x and σ_y, respectively.

The 795-nm photon is transmitted to the quantum memory where its state –specifically that it is entangled with the 1,532-nm photon– is mapped onto a collective excitation of millions of thulium ions. Some time later, the state is mapped back onto a photon that exits the memory through a fibre in well-defined spatio-temporal modes and is probed by a second qubit analyser.

To reversibly map the 795-nm photon onto matter, we use a photon-echo quantum memory protocol based on atomic frequency combs (AFC) [4]. It is rooted in the interaction of light with an ensemble of atomic absorbers (so far rare-earth-ion-doped crystals cooled to
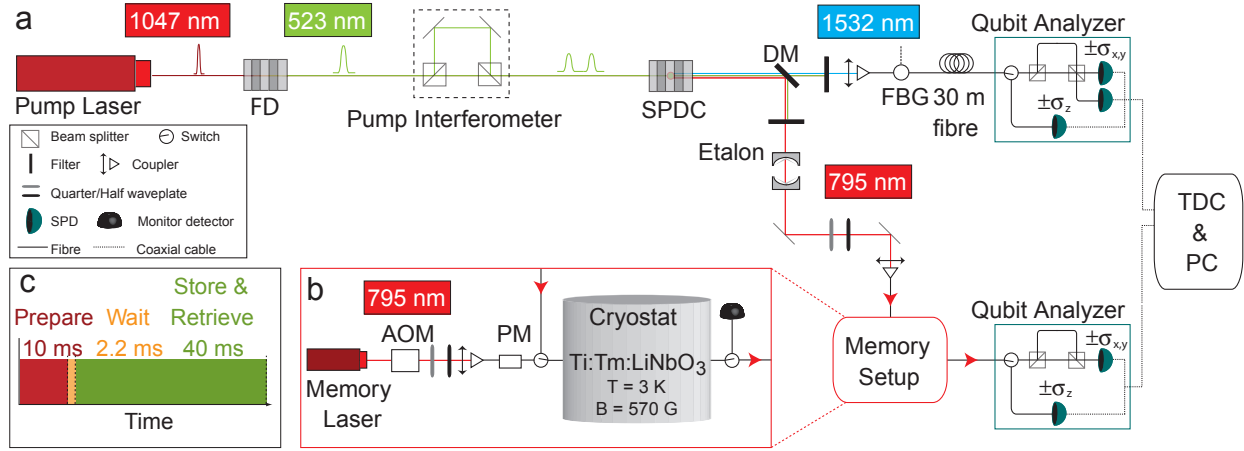
Figure 8.1: **Schematics of the experimental set-up: a**. Generating and measuring entanglement. Six-picosecond-long pump laser pulses (1,047.328nm wavelength, 80MHz repetition rate) are frequency doubled (FD) in a periodically poled lithium niobate (PPLN) crystal. Each resulting 16-ps-long pulse (523.664-nm wavelength, 90mW average power) is coherently split into two by the unbalanced pump interferometer, featuring a 1.4-ns travel-time difference. Spontaneous parametric down-conversion (SPDC) in a second PPLN crystal followed by frequency filtering using an etalon and a fibre Bragg grating (FBG) (bandwidths of 6 GHz and 9 GHz, respectively), yields maximally entangled pairs of photons centred at 795.506-nm and 1,532.426-nm wavelength (DM, dichroic mirror). The 1,532-nm photon travels through a 30-m telecommunication fibre, and the 795-nm photon is either stored in the memory or sent through a fibre delay line (not pictured). To characterize the bi-photon state, we use qubit analysers consisting of delay lines or unbalanced interferometers connected to single-photon detectors. Detection events are collected with a time-to-digital converter (TDC) connected to a personal computer (PC). All interferometers are phase-locked to stable reference lasers (not shown). **b**. Memory set-up. The 795.506-nm continuous-wave memory laser beam is intensity- and phase/frequency-modulated using an acousto-optic modulator (AOM) and a phase modulator (PM). The waveguide is cooled to 3 K and exposed to a 570-G magnetic field aligned with the crystals C_3-axis. Waveplates allow adjusting the polarization of the beam to the waveguides transverse magnetic (TM) mode, and optical switches combine and separate the optical pump beam and the 795-nm photons. **c**. Timing sequence. We use three continuously repeated phases: the 10ms "prepare" phase for optical pumping, the 2.2-ms "wait" phase, which ensures stored photons are not polluted by fluorescence from the excited state, and the 40-ms "store and retrieve" phase, during which many 795-nm photons are successively stored in the waveguide and recalled after 7 ns.

cryogenic temperatures) with an inhomogeneously broadened absorption line that has been tailored into a series of equally spaced absorption peaks (see Fig. 8.2). The absorption of a single photon leads to a collective excitation shared by many atoms. Owing to the particular shape of the tailored absorption line, the excited collective coherence rapidly dephases and repeatedly recovers after multiples of the storage time T_s. This results in the re-emission of a photon in the state encoded into the original photon.

In our implementation the moment of photon re-emission is predetermined by the spacing of the teeth in the comb, $T_s = 1/\Delta$, and the storage process can be described as arising from the linear response of an optical filter made by spectral hole burning. Yet, readout on demand can be achieved by temporarily mapping the optically excited coherence onto ground-state coherence where the comb spacing is smaller or the comb structure is washed out [4], or by combining the AFC protocol with controlled reversible inhomogeneous broadening of each absorption line, similar to the storage mechanism used in another photon-echo quantum memory protocol [1].

Our storage device, a Ti:Tm:LiNbO$_3$ optical waveguide cooled to 3 K, is detailed in Fig. 8.2. It was previously characterized to establish its suitability as a photon-echo quantum memory material [26]. It combines interesting properties from the specific rare-earth element (795-nm storage wavelength), the host crystal (allowing for controlled dephasing and rephasing by means of electric fields), and from the wave-guiding structure (ease-of-use). Lithium niobate waveguides have also been doped with neodymium, praseodymium and erbium [7], and we conjecture that other rare-earth ions could also be used. This could extend the properties of LiNbO$_3$ and allow an integrated approach to other storage wavelengths, ions with different level structures, and so on.

To generate the AFC, we use a sideband-chirping technique (see Supplementary Information) to transfer atomic population between magnetic sublevels and create troughs and peaks in the inhomogeneously broadened absorption line. They form a 5-GHz-wide comb
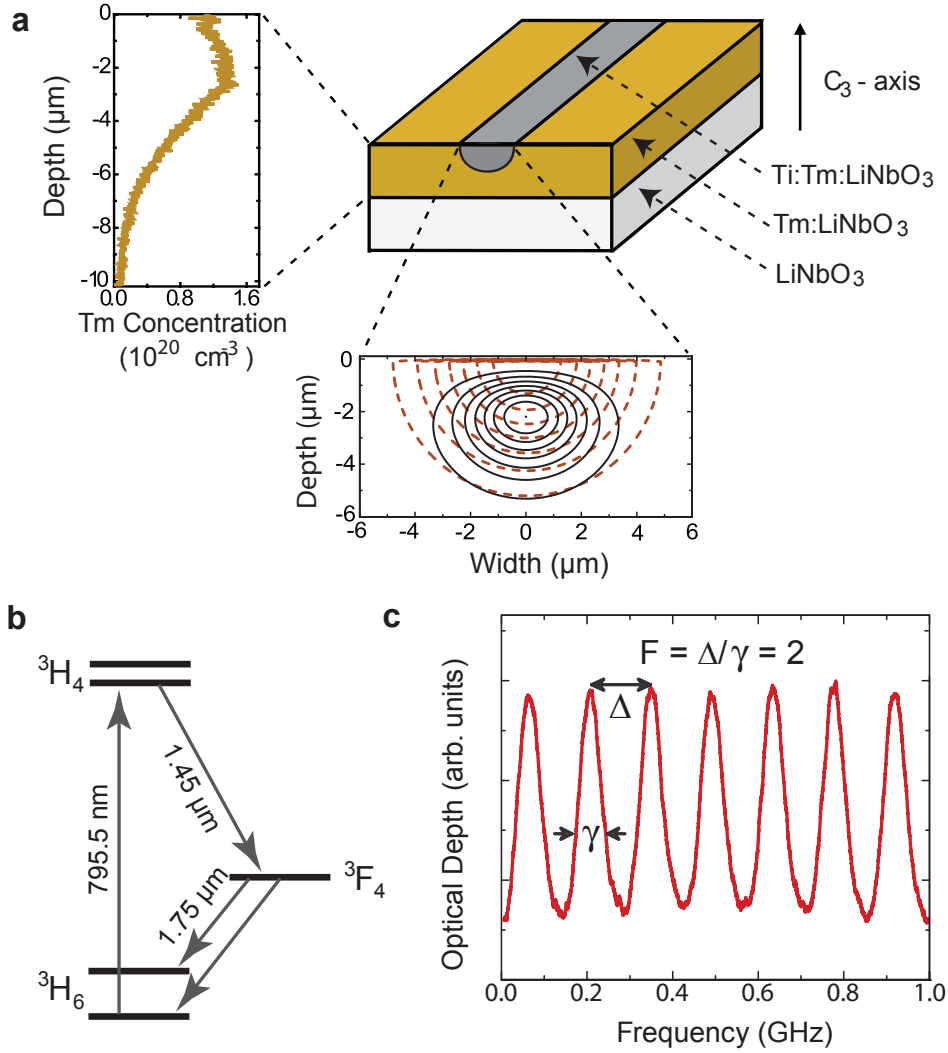
Figure 8.2: **The storage medium: a**. Waveguide geometry. The measured thulium (Tm) concentration profile is given on the left and the calculated intensity distribution of the fundamental TM-mode at the 795-nm wavelength is shown below. Iso-intensity lines are plotted corresponding to 90%, 87.5%, 75% and so on of the maximum intensity. **b**. Simplified energy level diagram of thulium ions. The optical coherence time of the $^3H_6 \leftrightarrow ^3H_4$ transition at 3 K is 1.6 μs, the radiative lifetimes of the $^3H_4$ and $^3F_4$ levels are 82 μs and 2.4 ms, respectively, and the branching ratio from the $^3H_4$ to the $^3F_4$ level is 44%. Upon application of a magnetic field of 570 G, the ground and excited levels split into magnetic sublevels with lifetimes exceeding one second [27].**c**. Atomic frequency comb. The bandwidth of our AFC is 5 GHz (shown here is a 1-GHz broad section). The separation between the teeth is $\Delta \approx 143$ MHz, resulting in 7 ns storage time. The line width of the peaks is $\gamma \approx 75$ MHz, yielding a finesse $F = 2$, as expected for the sinus-type comb.

with tooth spacing of 143 MHz, setting the storage time to 7 ns. The system efficiency in our implementation is currently about 0.2%. This is in part due to the 90% fibre-to-waveguide input and output coupling loss, which we attribute to imperfect mode overlap. In addition, owing to the specific level structure of thulium under current experimental conditions, the finesse of the comb in the broadband approach is two, which limits the memory efficiency to about 10%. However, imperfections in the creation of the comb decrease this efficiency to around 2%. The system efficiency can be increased by improving the spectral tailoring of the AFC, and triggering photon re-emission in the backward direction. By also optimizing the mode overlap, we anticipate that it could reach approximately 15%. Furthermore, if the two long-lived atomic levels between which population is transferred during the optical pumping procedure (in our case the two magnetic ground states; see Fig. 8.2) are spaced by more than the storage bandwidth, the memory efficiency can theoretically reach unity (see Supplementary Information).

8.1.3 Measurements

To assess the quantum nature of our light–matter interface, we first make projection measurements with the 795 nm photons and the 1532 nm photons onto time-bin qubit states characterized by Bloch vectors aligned along $\boldsymbol{a}$, $\boldsymbol{b}$, respectively, where $\boldsymbol{a}, \boldsymbol{b} \in [\pm\sigma_x, \pm\sigma_y, \pm\sigma_z]$ (see Fig. 8.3). Experimentally, this is done by means of suitably adjusted qubit analyzers, and by counting the number $C(\boldsymbol{a}, \boldsymbol{b})$ of detected photon pairs. From two such spin-measurements, we calculate the normalized *joint-detection probability*

$$P(\boldsymbol{a}, \boldsymbol{b}) = \frac{C(\boldsymbol{a}, \boldsymbol{b})}{C(\boldsymbol{a}, \boldsymbol{b}) + C(\boldsymbol{a}, -\boldsymbol{b})} \tag{8.2}$$

The measurement and the results with the fibre delay line, as well as the memory, are detailed in Fig. 8.3 and the Supplementary Information. From this data, we reconstruct the bi-photon states before and after storage in terms of their density matrices ρ_{in} and ρ_{out}, depicted in Fig. 8.3, using a maximum likelihood estimation [27]. This, in turn, allows us
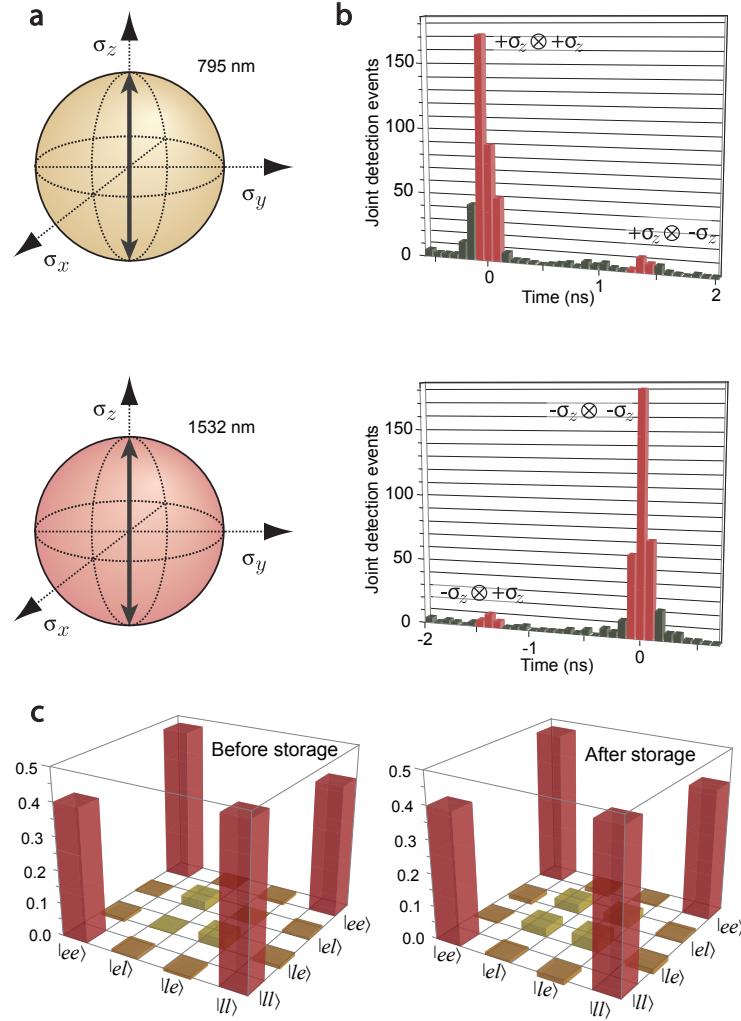
Figure 8.3: **Measurement of density matrices: a**. Visualization of projection measurements. The measurement settings for the 795-nm (or 1,532-nm) qubit analyser are depicted on the upper (or lower) Bloch sphere. The example shows joint settings that enable calculating normalized probabilities for projections onto $\sigma_z \otimes \sigma_z$ $\sigma_z \otimes -\sigma_z$. **b**. Results for joint projection measurement after storage. The top (bottom) histogram displays joint detection events for the projection onto $\sigma_z \otimes \sigma_z$ and $\sigma_z \otimes -\sigma_z$ ($-\sigma_z \otimes \sigma_z$ and $-\sigma_z \otimes -\sigma_z$) as a function of the time difference between detections of the 795-nm and the 1,532-nm photons. The desired events are those within the red-highlighted time windows. This allows us to calculate the joint-detection probabilities for projections onto $\sigma_z \otimes \sigma_z$ and $\sigma_z \otimes -\sigma_z$ (for results with other joint settings see the Supplementary Information). **c**. Density matrices. Density matrices were calculated using a maximum-likelihood estimation for the bi-photon states before and after storage. Only the real parts are shown the absolute values of all imaginary components are below 0.04.

	Entanglement of formation (%)	Purity (%)	Fidelity with $|\phi^+\rangle$	Input/output fidelity (%)	Expected S_{th}	Measured S
ρ_{in}	64.4 ±4.2	75.7± 2.4	86.2±1.5		2.235±0.085	2.379±0.034
ρ_{out}	65 ±11	76.3±5.9	86.6±3.9	95.4 ±2.9	2.2 ±0.22	2.25±0.060.22

Table 8.1: **Entanglement measures, purities and fidelities:** Entanglement of formation (normalized with respect to the entanglement of formation of $|\phi^+\rangle$, purity $P=\text{tr}(\rho^2)$), fidelity with $|\phi^+\rangle$, input–output fidelity $\mathcal{F} = \left(\text{tr}\sqrt{\sqrt{\rho_{out}}\rho_{in}\sqrt{\rho_{out}}}\right)^2$ (referring to the fidelity of ρ_{out} with respect to ρ_{in}), and expected and experimentally obtained S values for tests of the CHSH Bell inequality (measured for $\boldsymbol{a} = \sigma_x$, $\boldsymbol{a'} = \sigma_y$, $\boldsymbol{b} = \sigma_x + \sigma_y$ and $\boldsymbol{b'} = \sigma_x - \sigma_y$). The correlation coefficients used to compute S and the calculation of S_{th} are detailed in the Supplementary Information. We note that the original state (and hence the recalled state) has limited purity and fidelity with $|\phi^+\rangle$. This is due to the probabilistic nature of our spontaneous parametric down-conversion source, which features a non-negligible probability of generating more than two photons simultaneously [26]. Uncertainties indicate one-sigma standard deviations and are estimated from Poissonian detection statistics and using a Monte Carlo simulation

to examine the entanglement of formation [28], a measure that indicates entanglement if it exceeds zero; it is upper-bounded by one. The results, listed in Table 8.1, clearly show the presence of entanglement in ρ_{in} and ρ_{out} and, within experimental uncertainty, establish that the storage process preserves entanglement without measurable degradation. Furthermore, we note that the fidelity $\mathcal{F}$ between ρ_{in} and ρ_{out} is close to one, and hence the unitary transformation introduced by the storage process is almost the identity transformation.

In addition, as a second entanglement measure, we perform tests of the Clauser–Horne–Shimony–Holt (CHSH) Bell inequality [6]. This test indicates non-local correlations and thus the possibility of using the bi-photons for entanglement-based quantum key distribution [8] if the sum:

$$S = |E(\boldsymbol{a},\boldsymbol{b}) + E(\boldsymbol{a'},\boldsymbol{b}) + E(\boldsymbol{a},\boldsymbol{b'}) - E(\boldsymbol{a'},\boldsymbol{b'})| \tag{8.3}$$

of four correlation coefficients

$$E(\boldsymbol{a},\boldsymbol{b}) = \frac{C(\boldsymbol{a},\boldsymbol{b}) - C(\boldsymbol{a},-\boldsymbol{b}) - C(-\boldsymbol{a},\boldsymbol{b}) + C(-\boldsymbol{a},-\boldsymbol{b})}{C(\boldsymbol{a},\boldsymbol{b}) + C(\boldsymbol{a},-\boldsymbol{b}) + C(-\boldsymbol{a},\boldsymbol{b}) + C(-\boldsymbol{a},-\boldsymbol{b})} \tag{8.4}$$

with appropriately chosen settings $\boldsymbol{a}$, $\boldsymbol{a'}$ and $\boldsymbol{b}$, $\boldsymbol{b'}$ exceeds the classical bound of two; quantum mechanically it is upper-bounded by $2\sqrt{2}$. As detailed in Table 8.1, we find $S_{in} = 2.379 \pm$

$0.034 > 2$ before the memory and, crucially, $S_{out} = 2.25 \pm 0.06 > 2$, which is in agreement with the value $S_{th} = 2.2 \pm 0.22$ predicted from the reconstructed density matrix ρ_{out}. This validates the suitability of our set-up for quantum communication.

8.1.4 Conclusions

Our investigation provides an example of entanglement being transferred between physical systems of different nature, thereby adding evidence that this fundamental quantum property is not as fragile as is often believed. Furthermore, our broadband integrated approach permits the linkage of a promising quantum storage device with extensively used, high-performance sources of photons in bi- and multi-partite entangled states [6]. Although the storage efficiency and the storage time need to be significantly increased, and the moment of recall was pre-set, this study opens the way to new investigations of fundamental and applied aspects of quantum physics. Having increased the storage bandwidth also significantly facilitates the building of future quantum networks, because mutual frequency matching of photons and distant quantum memories will be simple. In addition, a large storage bandwidth –that is, the possibility to encode quantum information into short optical pulses– allows us to increase the number of temporal modes that can be stored during a given time. This enhances the flow of quantum information through a network and decreases the time needed to establish entanglement over a large distance using a quantum repeater [1,2].

We note that, parallel to this work, Clausen et al. have demonstrated the storage of an entangled photon using a neodymium-doped crystal [29].

8.1.5 References

1. Lvovsky, A. I., Sanders, B. C., &. Tittel, W. Optical quantum memory. Nature Photon. 3, 706–714 (2009).
2. Sangouard, N., Simon, C., de Riedmatten, H. & Gisin, N. Quantum repeaters based on atomic ensembles and linear optics. Preprint at http://arxiv.org/abs/ 0906.2699 (2009).

3. Kimble, H. J. The quantum Internet. Nature 453, 1023–1030 (2008).

4. de Riedmatten, H., Afzelius, M., Staudt, M. U., Simon, C. & Gisin, N. A solid–state lightmatter interface at the single-photon level. Nature 456, 773–777 (2008).

5. Usmani, I., Afzelius, M., de Riedmatten, H. & Gisin, N. Mapping multiple photonic qubits into and out of one solid–state atomic ensemble. Nature Commun. 1, 1–7 (2010).

6. Pan, J.-W., Chen, Z.-B., Zukowski, M., Weinfurter, H. & Zeilinger, A. Multi-photon entanglement and interferometry. Preprint at http://arxiv.org/abs/0805.2853 (2008).

7. Sohler, W. et al. Integrated optical devices in lithium niobate. Opt. Photon. News 24–31 (January 2008).

8. Gisin, N., Ribordy, G., Tittel, W. & Zbinden, H. Quantum cryptography. Rev. Mod. Phys. 74, 145–195 (2002).

9. Julsgaard, B., Sherson, J. & Cirac, J. I. J. Fiurasek, J. & Polzik, E. S. Experimental demonstration of quantum memory for light. Nature 432, 482–486 (2004).

10. Chanelière, T. et al. Storage and retrieval of single photons transmitted between remote quantum memories. Nature 438, 833–836 (2005).

11. Eisaman, M. D. et al. Electromagnetically induced transparency with tunable single-photon pulses. Nature 438, 837–841 (2005).

12. Honda, K. et al. Storage and retrieval of a squeezed vacuum. Phys. Rev. Lett. 100, 093601 (2008).

13. Appel, J., Figueroa, E., Korystov, D., Lobino, M. & Lvovsky, A. Quantum memory for squeezed light. Phys. Rev. Lett. 100, 093602 (2008).

14. Hedges, M. P., Longdell, J. J., Li, Y. & Sellars, M. J. Efficient quantum memory for light. Nature 465, 1052–1056 (2010).

15. Boozer, A. D. et al. Reversible state transfer between light and a single trapped atom. Phys. Rev. Lett. 98, 193601 (2007).

16. Choi, C. S. Deng, H. Laurat, J. & Kimble, H. J. Mapping photonic entanglement into

and out of a quantum memory. Nature 452, 67–71 (2008).

17. Akiba, K., Kashiwagi, K. Arikawa, M. & Kozuma, M. Storage and retrieval of nonclassical photon pairs and conditional single photons generated by the parametric down-conversion process. N. J. Phys. 11, 013049 (2009).

18. Jin, X.-M. et al. Quantum interface between frequency-uncorrelated down converted entanglement and atomic-ensemble quantum memory. Preprint at http://arxiv.org/abs/1004.4691 (2011).

19. Chou, C. W. et al. Measurement-induced entanglement for excitation stored in remote atomic ensembles. Nature 438, 828–832 (2005).

20. Matsukevich, D. N. et al. Entanglement of a photon and a collective atomic excitation. Phys. Rev. Lett. 95, 040405 (2005).

21. Yuan, Z.-S. et al. Experimental demonstration of a BDCZ quantum repeater node. Nature 454, 1098–1101 (2008).

22. Blinov, B. B., Moehring, D. L., Duan, L.M. & Monroe, C. Observation of entanglement between a single trapped atom and a single photon. Nature 428, 153–157 (2004).

23. Togan, E. et al. Quantum entanglement between an optical photon and a solid state spin qubit. Nature 466, 730734 (2010).

24. Longdell, J., Fraval, E., Sellars, M. & Manson, N. Stopped light with storage times greater than one second using electromagnetically induced transparency in a solid. Phys. Rev. Lett. 95, 063601 (2005).

25. Marcikic, I. et al. Time-bin entangled qubits for quantum communication created by femtosecond pulses. Phys. Rev. A 66, 062308 (2002).

26. Sinclair, N. et al. Spectroscopic investigations of a Ti:Tm:LiNbO$_3$ waveguide for photon-echo quantum memory. J. Lumin. 130, 1586–1593 (2010).

27. Altepeter, J. B., Jeffrey, E. R., &. Kwiat, P. G. Photonic state tomography. Adv. At. Mol. Opt. Phys. 52, 105–159 (2005).

28. Plenio, M. B. & Virmani, S. An introduction to entanglement measures. Quant. Inf. Comput. 7, 151 (2007).

29. Clausen, C. et al. Quantum storage of photonic entanglement in a crystal. Nature doi:10.1038/nature09662 (this issue).

8.1.6 Supplementary Information

Preparation of the Atomic Frequency Comb (AFC): The AFC amounts to a periodic modulation in frequency of the optical density of the inhomogeneously broadened $^3H_6 \leftrightarrow ^3H_4$ thulium absorption line. It can be generated by optically pumping atoms to off-resonant shelving levels - in our case nuclear Zeeman levels [27,31]. To that end, we modulate the intensity of the 795 nm memory laser while scanning its frequency [32]. The frequency sweep is implemented using a lithium niobate phase modulator driven by a 20 GS/s arbitrary waveform generator. To avoid overlap of first and higher order modulation, the sweep extends from 5 GHz to 10 GHz, thus efficiently preparing a 5 GHz-bandwidth AFC memory. The laser intensity modulation is achieved by beating two frequency components, generated in an acousto-optic modulator (AOM) placed before the phase-modulator.

The memory storage time T_s is set by the frequency spacing between the teeth of the AFC, and is determined by $T_s = \delta/\alpha$, where $\delta = 0.35$ MHz is the difference between the two frequency components and $\alpha = 50 \times 10^{12}$ MHz/s is the sweep rate. This yields 142.85 MHz spacing between the AFC teeth, which translates into 7 ns memory storage time. For a high contrast AFC, the chirp cycle is repeated 100 times leading to a 10 ms overall optical pumping duration. The 2.2 ms wait time following the preparation corresponds to 27 times the radiative lifetime of the $^3H_4$ excited level, and ensures no fluorescence masks the retrieved photons.

The optical pumping involves population transfer between ground-state sublevels. As the comb structure extends over all these levels, we carefully chose the magnetic field to make sure that those ions that initially absorb at frequencies where we desire a trough are

	$\sigma_x\otimes\sigma_x$	$\sigma_x\otimes\sigma_y$	$\sigma_x\otimes\sigma_z$	$\sigma_x\otimes\text{-}\sigma_z$	$\sigma_y\otimes\sigma_x$	$\sigma_y\otimes\sigma_y$	$\sigma_y\otimes\sigma_z$	$\sigma_y\otimes\text{-}\sigma_z$
P_{in} [%]	90±2	49±1	49±1	51±1	52±1	10±2	51±1	49±1
P_{out} [%]	89±6	49±8	48±4	52±4	49±6	14±5	49±4	51±4
	$\sigma_z\otimes\sigma_x$	$\sigma_z\otimes\sigma_y$	$\sigma_z\otimes\sigma_z$	$\sigma_z\otimes\text{-}\sigma_z$	$\text{-}\sigma_z\otimes\sigma_x$	$\text{-}\sigma_z\otimes\sigma_y$	$\text{-}\sigma_z\otimes\sigma_z$	$\text{-}\sigma_z\otimes\text{-}\sigma_z$
P_{in} [%]	46±1	46±1	94.2±0.1	5.8±0.1	46±1	45±1	7.6±0.2	93.0±0.2
P_{out} [%]	51±6	56±6	94±1	6±1	48±5	52±5	6±1	94±1

Table 8.2: **Joint-detection probabilities for density matrix reconstruction:** Measured joint-detection probabilities for all projection measurements required to calculate the density matrices for the bi-photon state emitted from the source (P_{in}), and after storage and recall of the 795 nm photon (P_{out}). Uncertainties indicate one-sigma standard deviations based on Poissonian detection statistics.

transferred to frequencies where we desire a peak.

The measurement: First, we stabilize the pump interferometer and the 1532 nm interferometer to arbitrarily chosen phase values. We define the phase introduced by the pump interferometer to be zero, i.e. we absorb it into the definition of the "early" and "late" qubit states, leading to the maximally entangled state

$$\left|\phi^+\right\rangle = \frac{1}{\sqrt{2}}\left(|e,e\rangle + |l,l\rangle\right) \tag{8.5}$$

Furthermore, we define the measurement performed by the 1532 nm qubit analyzer to be $+\sigma_x$. Next, we change the phase of the 795 nm interferometer and maximize the normalized *joint detection probability*

$$P(\boldsymbol{a},\boldsymbol{b}) = \frac{C(\boldsymbol{a},\boldsymbol{b})}{C(\boldsymbol{a},\boldsymbol{b}) + C(\boldsymbol{a},-\boldsymbol{b})} \tag{8.6}$$

with a fibre delay line in place of the memory. We define this setting to correspond to a projection onto $+\sigma_x$, and we measure $P_{in}(\sigma_x \otimes \sigma_x)$ over 5 minutes. This measurement (without the memory) is taken as being on the state ρ_{in}, i.e. the bi-photon state before storage. Next, we add the memory and similarly measure $P_{out}(\sigma_x \otimes \sigma_x)$ over approximately 5 hours. When necessary to change the setting of either qubit analyzer to σ_y, we increase the phase difference introduced by the respective interferometer by $\pi/2$. For projection measurements onto σ_z, we use the delay line in the qubit analyzer. Each joint projection

measurement is done with and without memory; the results, given in supplementary table 8.2, allow calculating the density matrices ρ_{in} and ρ_{out} describing the photon pair states before and after storage, respectively [28].

To measure the correlation coefficients

$$E(\boldsymbol{a}, \boldsymbol{b}) = \frac{C(\boldsymbol{a}, \boldsymbol{b}) - C(\boldsymbol{a}, -\boldsymbol{b}) - C(-\boldsymbol{a}, \boldsymbol{b}) + C(-\boldsymbol{a}, -\boldsymbol{b})}{C(\boldsymbol{a}, \boldsymbol{b}) + C(\boldsymbol{a}, -\boldsymbol{b}) + C(-\boldsymbol{a}, \boldsymbol{b}) + C(-\boldsymbol{a}, -\boldsymbol{b})} \tag{8.7}$$

required for testing the Clauser-Horne-Shimony-Holt (CHSH) Bell inequality [33]. we chose, $\boldsymbol{a} = \sigma_x$, $\boldsymbol{a'} = \sigma_y$, $\boldsymbol{b} = \sigma_x + \sigma_y$, and $\boldsymbol{b'} = \sigma_x - \sigma_y$. Projections onto $\sigma_x \pm \sigma_y$ require changing phase differences by $\pm\pi/4$ as compared to those defining projections onto σ_x. For this measurement we added a detector to the second output of the interferometer in the 795 nm qubit analyzer so that C(**a**,**b**), C(**-a**,**b**), C(**a**,**-b**) and C(**-a**,**-b**) could be measured simultaneously. Measurements without memory are done over 15 min, those with memory over 12-15 hours. The resulting correlation coefficients are detailed in supplementary table 8.3. From these we calculate $S_{in} = 2.379 \pm 0.034 > 2$ before storage and $S_{out} = 2.25 \pm 0.06 > 2$ after storage. Both are approximately equal, larger than 2, and hence violate the CHSH Bell inequality, proving again the presence of entanglement and, beyond that, the suitability of the bi-photon states for quantum key distribution [9]. Moreover, the measured S–values are in good agreement with the respective theoretical values of $S_{th} = 2.235 \pm 0.085$ and $S_{th} = 2.2 \pm 0.22$ calculated using the measured density matrix with uncertainties estimated from Monte-Carlo simulations.

Calculation of purity, entanglement measures [29] and fidelities: Assuming an arbitrary two-qubit input state ρ, the *concurrence* is defined as $C(\rho) = \max\{0, \lambda_1 - \lambda_2 - \lambda_3 - \lambda_4\}$, where the λ_is are, in decreasing order, the square roots of the eigenvalues of the matrix $\rho(\sigma_y \otimes \sigma_y)\rho^*(\sigma_y \otimes \sigma_y)$ and ρ^* is the element wise complex conjugate of ρ. The *entanglement of formation* is then calculated as

$$E_F(\rho) = H\left(0.5 + 0.5\sqrt{1 - C^2(\rho)}\right) \tag{8.8}$$

	$\sigma_y \otimes (\sigma_x + \sigma_y)$	$\sigma_y \otimes (\sigma_x - \sigma_y)$	$\sigma_x \otimes (\sigma_x + \sigma_y)$	$\sigma_x \otimes (\sigma_x - \sigma_y)$
E_{in} [%]	59.7 ± 1.7	-55.4 ± 1.9	52.0 ± 1.5	70.8 ± 1.8
E_{out} [%]	54 ± 3	-64 ± 4	53 ± 3	53 ± 3

Table 8.3: **Correlation coefficients for Bell-inequality tests:** Measured correlation coefficients (see Eq. 8.7) required to test the CHSH Bell inequality. Uncertainties indicate one-sigma standard deviations based on Poissonian detection statistics.

where $H(x) = -x\log_2 x - (1-x)\log_2(1-x)$. Finally, fidelity between ρ and σ is

$$F(\rho, \sigma) = \left(tr\sqrt{\sqrt{\rho}\sigma\sqrt{\rho}} \right)^2 \tag{8.9}$$

and the *purity* of a state ρ is

$$P = \mathrm{tr}(\rho^2) \tag{8.10}$$

The Ti:Tm:LiNbO$_3$ waveguide: To fabricate the Ti:Tm:LiNbO$_3$ waveguide, a commercially available 0.5 mm thick Z-cut wafer of undoped, optical grade congruent lithium niobate (CLN) was cut into samples of 12 mm x 30 mm size. Tm doping was achieved by indiffusing a vacuum-deposited (electron-beam evaporated) Tm layer of 19.6 nm thickness. The diffusion was performed at 1130 °C during 150 h in an argon-atmosphere followed by a post treatment in oxygen (1 h) to get a full re-oxidization of the crystal. Tm occupies regular Li-sites when incorporated in CLN by diffusion [34]. The Tm indiffusion leads to a 1/e penetration depth of about 6.5 μm. The maximum Tm concentration of about 1.35×10^{20} cm^{-3} corresponds to a concentration of 0.74 mole %, which is considerably below the solid solubility of Tm in CLN [35]. Subsequently, the waveguide was formed by the well-known Ti–indiffusion technique. At first, a 40 nm thick titanium layer was electron-beam deposited on the Tm-doped surface of the CLN substrate. From this layer, 3.0 μm wide Ti stripes were defined by photolithography and chemical etching and subsequently in-diffused at 1060°C for 5 h to form 30 mm long optical strip waveguides. In the wavelength range around 795 nm, the waveguides
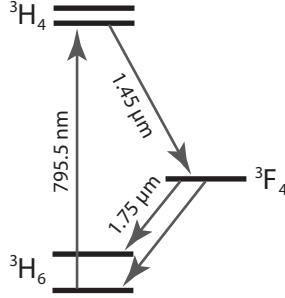
Figure 8.4: Simplified level diagram for Tm:LiNbO$_3$.

are single mode for TE- and TM-polarization. To finish the fabrication, the waveguide was cut to 15.7 mm and end faces were carefully polished normal to the waveguide axis.

Limitation to efficiency: While the current system efficiency (characterizing the probability for a photon that enters the cryostat to leave it after recall) of around 0.2% is sufficient to show the entanglement-preserving nature of the storage process, it is clear that this number has to be improved to make the memory more practical and to allow for more involved fundamental measurements.

First, we note that better optical mode matching between the fibre and the LiNbO$_3$ waveguide can be expected to improve the fibre-to-fibre transmission from 10% to 50%.

Second, assuming storage in optical coherence and Gaussian-shaped teeth, the efficiency of the first recall in the forward direction is given by

$$\epsilon = (d_1/F)^2 e^{d_1/F} e^{7/F^2} e^{-d_0} \tag{8.11}$$

where $F = \Delta/\gamma$ denotes the finesse of the comb, and d_1/F and d_0 are the reversible and irreversible optical depth [36] (see supplementary figure 8.4). As discussed above, our comb structure extends over all ground state levels. This fixes the fidelity of the comb to two, as ions can only be "shuffled around" but not removed from the spectral region covered by the SPDC photons. This impacts on the memory efficiency and sets, according to Eq. 8.11, an upper bound of $\approx 10\%$. Yet, we note that the memory efficiency can be increased when applying a phase-matching operation that results in backward emission of the stored photon. Further improvement is expected when changing the teeth shape from Gaussian to

square [37]. All options combined, it seems possible to achieve a system efficiency of around 15%, which is 75 times larger than in the current implementation. We point out that the limitation due to the comb finesse is not necessarily a consequence of generating broadband combs, but of the small Zeeman splitting of the thulium ground state levels relative to the storage bandwidth. Provided the splitting between the long-lived atomic levels involved in the optical pumping procedure exceeds the storage bandwidth, the finesse can be increased beyond two, and memory efficiencies up to 100% are possible. This may be possible when using the $^3F_4$ level as shelving level, or for other RE impurities featuring greater sensitivity to magnetic fields [38].

Longer storage time and on-demand readout : Currently, the maximum storage time of our memory is approximately 300 ns. This value is determined by the minimum tooth spacing of the AFC, which is limited by spectral diffusion [27,31]. However, spectroscopic investigation of a Tm:LiNbO$_3$ bulk crystal shows that spectral diffusion decreases when lowering the temperature, similar to the observed improvement of the optical coherence time [31]. This implies the possibility to extend the storage time.

In addition, it may be possible to further improve the storage time and achieve on-demand recall by temporarily transferring the optical excited coherence between the $^3H_6$ and $^3H_4$ levels to coherence between the $^3H_6$ and $^3F_4$ electronic levels, similar to storage of coherence in spin-waves [39]. However, the coherence properties and the suitability of the $^3F_4$ state for such a transfer remains to be investigated. Furthermore, combining the AFC protocol with a quantum memory approach based on controlled reversible inhomogeneous broadening (CRIB) [38] allows one to inhibit the pre-set rephasing of coherence by adding additional, controlled inhomogeneous broadening of each line in the AFC. Rephasing would occur only after reversing, i.e. undoing, the additionally introduced dephasing, and readout would be possible after any multiple of the AFC recall time determined by the tooth spacing.

References for Supplementary Information

1. Thiel, C.W., Sun, Y., Böttger, T., Babbitt, W.R. and Cone, R.L. Optical decoherence and persistent spectral hole burning in Tm^{3+}:$LiNbO_3$. J. Lumin, 130 (9), 1603-1609 (2010).

2. Reibel R.R., Barber, Z.W., Fischer, J.A., Tian, M. and Babbitt, W.R. Broadband demonstrations of true-time delay using linear sideband chirped programming and optical coherent transients. J. Lumin. 107, 103-113 (2004).

3. Clauser, J.F., Horne, M.A., Shimony, A. and Holt, R.A. Proposed experiment to test local hidden-variable theories. Phys. Rev. Lett. 23, 880-884 (1969).

4. Novikov, D. V. et al. Plane wave GID topography of defects in lithium niobate after diffusion doping, Nuclear Instruments and Methods in Physics Research B 97, 342-345 (1995).

5. Quintanilla, M., Cantelar, E., Sanz-Garca, J.A. Cusso, F. Growth and optical characterization of Tm^{3+}-doped $LiNbO_3$. Optical Materials 30, 1098-1102 (2008).

6. Afzelius, M., Simon, C., de Riedmatten, H. and Gisin, N. Multimode quantum memory based on atomic frequency combs. Phys. Rev. A 79, 052329 (2009).

7. Bonarota, M., Ruggiero, J., Le Gouët, J.-L. and Chanelière, T. Efficiency optimization for Atomic Frequency Comb storage. Preprint at http://arxiv.org/abs/0911.4359 (2009).

8. Tittel, W. et al. Photon-echo quantum memory in solid state systems. Laser and Photon. Rev. 4, (2), 244-267 (2010).

9. Afzelius, M. et al. Demonstration of Atomic Frequency Comb Memory for Light with Spin-Wave Storage. Phys. Rev. Lett. 104, 040503 (2010).

Acknowledgment

experiment, C. Simon, K. Rupavatharam and N. Gisin for discussions, and A. Lvovsky for lending us a single-photon detector.

Author Contributions

Chapter 9

Two-photon Interference of Pulses Recalled from Separate Quantum Memories

In the operation of quantum repeaters, which are based on entangled photon pairs and quantum memories, the distribution of entanglement between different sections of a quantum repeater network is accomplished via Bell-state projection measurements with two photons recalled from separate quantum memories, as explained in Chapter 3. The mechanism behind this measurement involves interfering the two photons on a beam splitter and detecting them in different temporal modes (assuming time-bin qubits) and separate outputs of the beam splitter. The resulting coincidence detection projects the state of the photons onto a maximally entangled Bell State (see Sec. 2.4 for the details of a Bell-state meausurement). For a successful Bell-state measurement, the photons that overlap at the beam splitter must be indistinguishable in all degrees of freedom, namely, polarization, frequency, time and spatial mode. In order to satisfy this condition in general, there must be no modification to the wavefunction of the photons during storage in the quantum memories. Therefore, to demonstrate the suitability of our quantum memories for quantum repeaters, it needs to be shown that they preserve not only quantum information (including entanglement) but also entire photonic wavefunctions. Towards this end, we performed two-photon interference experiments with weak laser pulses recalled from two, one or none of our waveguide quantum memories. From these measurements, we quantitatively assessed whether there is any modification to the wavefunction of the stored photons. Moreover, we demonstrated a Bell-State measurement on weak laser pulses, after one of them is recalled from a quantum memory. Our results verify that our quantum memories are suitable for long distance quantum communication and for photonic quantum communication protocols that require

two-photon interference. My contributions to this study were the following: Designing and setting up the experiment, performing the measurements, analysis and interpretation of the main results, editing the manuscript. Our findings will be submitted very shortly to a journal for publication. The following section is the current version of this manuscript, which has been re-formatted for the consistency with the other chapters of this thesis.

9.1 Paper IV

Two-photon Interference of Weak Coherent Laser Pulses Recalled From Separate Solid-state Quantum Memories

Jeongwan Jin[1], Erhan Saglamyurek[1], Neil Sinclair[1], Joshua A. Slater[1], Mathew George[2], Raimund Ricken[2], Daniel Oblak[1], Wolfgang Sohler[2], and Wolfgang Tittel[1]

[1]*Institute for Quantum Information Science, and Department of Physics and Astronomy, University of Calgary, 2500 University Drive NW, Calgary, Alberta T2N 1N4, Canada*

[2]*Department of Physics - Applied Physics, University of Paderborn, Warburger Str. 100, 33095 Paderborn, Germany*

Abstract

Quantum memories for light, which allow the reversible transfer of quantum states between light and matter, are central to the development of quantum repeaters [1], quantum networks [2], and linear optics quantum computing [3]. Significant progress has been reported in recent years, including the faithful transfer of quantum information from photons in pure and entangled qubit states [4–10]. However, none of these demonstrations confirm that photons stored in and recalled from quantum memories remain suitable for two-photon interference measurements, such as C-NOT gates and Bell-state measurements, which constitute another key ingredient for all aforementioned applications of quantum information processing. Using

pairs of weak laser pulses, each containing less than one photon on average, we demonstrate two-photon interference as well as a Bell-state measurement after either none, one, or both pulses have been reversibly mapped to separate thulium-doped lithium niobate waveguides. As the interference is always near the theoretical maximum, we conclude that our solid-state quantum memories, in addition to faithfully mapping quantum information, also preserves the entire photonic wavefunction. Hence we demonstrate that our memories are generally suitable for use in advanced applications of quantum information processing that require two-photon interference

9.1.1   Introduction

When two indistinguishable single photons impinge on a 50/50 beam-splitter (BS) from different input ports, they bunch and leave together by the same output port. This so-called Hong-Ou-Mandel (HOM) effect [11] is due to destructive interference between the probability amplitudes associated with both input photons being transmitted or both reflected, see Fig. 9.1. Since no such interference occurs for distinguishable input photons, the interference visibility V provides a convenient way to verify that two photons are indistinguishable in all degrees of freedom, i.e. spatial, temporal, spectral, and polarization modes. The visibility is defined as

$$V = (\mathcal{R}_{\max} - \mathcal{R}_{\min})/\mathcal{R}_{\max}, \tag{9.1}$$

where $\mathcal{R}_{\min}$ and $\mathcal{R}_{\max}$ denote the rate with which photons are detected in the two output ports in coincidence if the incoming photons are indistinguishable and distinguishable, respectively. Consequently, the HOM effect has been employed to characterize the indistinguishability of photons emitted from a variety of sources, including parametric down-conversion crystals [12], trapped neutral atoms [13], trapped ions [14], quantum dots [15-17], organic molecules [18], nitrogen-vacancy centers in diamond [19,20], and atomic vapours [21,25]. Furthermore, two-photon interference is at the heart of linear optics Bell-state measurement

$|\psi^{(in)}\rangle = |1\rangle_a \otimes |1\rangle_b$

$|\psi^{(out)}\rangle = \quad i \, |0\rangle_a|0\rangle_b \otimes |1\rangle_a|1\rangle_b \quad + \quad |0\rangle_a|1\rangle_b \otimes |1\rangle_a|0\rangle_b \quad - \quad |1\rangle_a|0\rangle_b \otimes |0\rangle_a|1\rangle_b \quad + \, i \, |1\rangle_a|1\rangle_b \otimes |0\rangle_a|0\rangle_b$
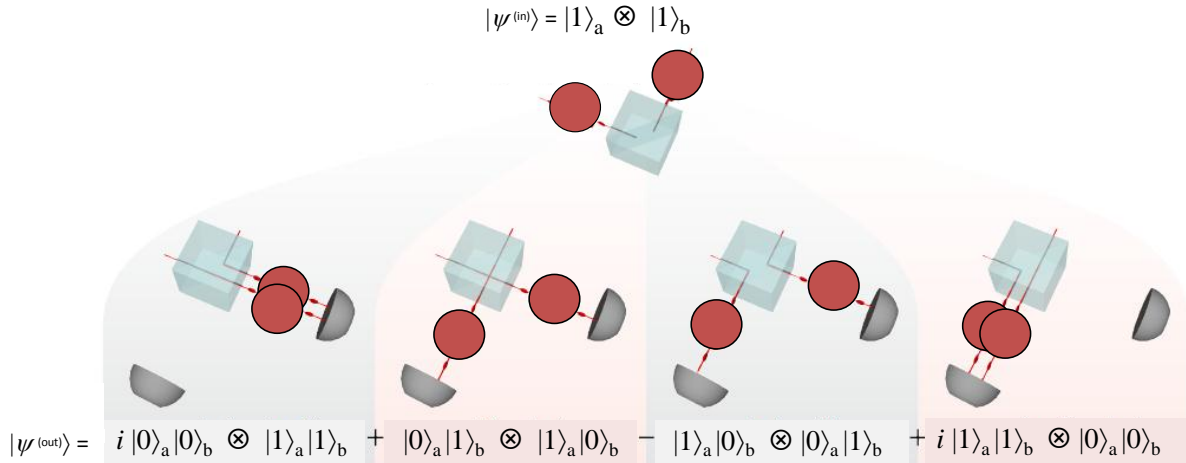
Figure 9.1: **Illustration of HOM-interference in the case of single photons at BS input $|\psi^{(in)}\rangle = |1\rangle_a \otimes |1\rangle_b$.** The four possible paths of the photons are illustrated, together with their corresponding output state. If the input photons are indistinguishable with respect to all degrees of freedom, i.e $a = b$, the paths shown in the two central pictures are indistinguishable and thus cancel, leaving in the output state $|\psi^{(out)}\rangle$ only the possibilities in which photons bunch. For distinguishable photons, e.g. having orthogonal polarizations, all paths are distinguishable and all terms remain in $|\psi^{(out)}\rangle$. In the representation, $|\psi^{(out)}\rangle$ is not normalized.

[26], and, as such, has already enabled experimental quantum dense coding [27], quantum teleportation [43], and entanglement swapping [44]. However, to date, the possibility to perform Bell-state measurements with photons that have previously been stored in a quantum memories, as required for advanced applications of quantum information processing, has not yet been established. For these measurements to succeed, photons need to remain indistinguishable in all degrees of freedom, which is more restrictive than the faithful recall of encoded quantum information. Indeed, taking into account that photons may or may not have been stored before the measurement, this criterion amounts to the requirement that a quantum memory preserves a photon's wavefunction during storage. Similar to the case of photon sources, meeting this criterion is best assessed using HOM interference, provided single-photon detectors are employed.
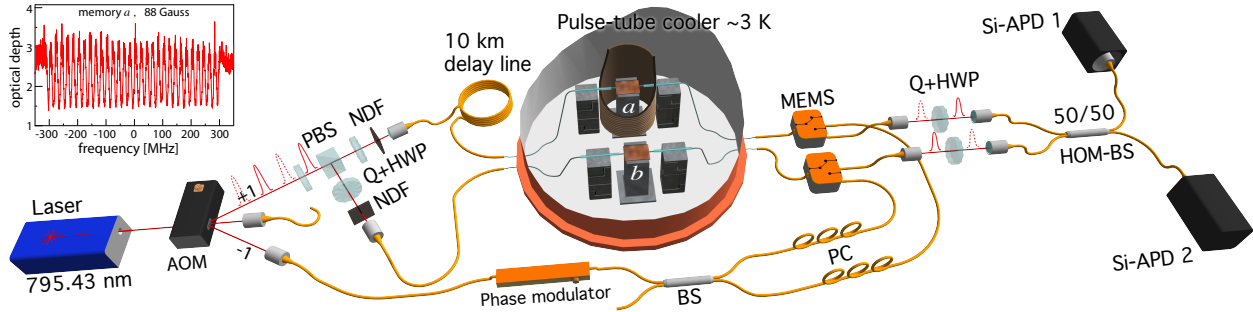
Figure 9.2: **Experimental setup:** A 795.43 nm wavelength CW laser passes through an acousto-optic modulator (AOM) driven by a sinusoidally varying signal. The first negative refraction order is fibre coupled into a phase modulator and, via a beam-splitter (BS), two polarization controllers (PCs) and two micro-electromechanical switches (MEMS), injected from the back into two thulium-doped lithium niobate waveguides (labelled a and b) cooled to 3 K [28]. Waveguide a is placed inside a superconducting solenoid. Using a linear frequency-chirping technique [29] we tailor AFCs with 600 MHz bandwidth and a few tens of MHz peak spacing, depending on the experiment, into the inhomogeneously broadened absorption spectrum of the thulium ions, as shown for crystal a in the inset. After 3 ms memory preparation time and 2 ms wait time we store and recall probe pulses during 3 ms. The 8 ns long probe pulses with $\approx$ 50 MHz Fourier limited bandwidth are derived from the first positive refraction order of the AOM output at a repetition rate of 2.8 MHz. Each pulse is divided into two spatial modes by a half-wave plate (HWP) followed by a polarizing beam-splitter (PBS). All pulses are attenuated by neutral-density filters (NDFs) and coupled into optical fibres and injected from the front into the Tm:LiNbO₃ waveguides. After exiting the memories (i.e. either after storage, or after transmission), the pulses pass quarter- and half-wave plates used to control their polarizations at the 50/50 BS (HOM-BS) where the two-photon interference occurs. Note that, to avoid first-order interference, pulses passing through memory a propagate through a 10 km fibre to delay them w.r.t. the pulses passing through memory b by more than the laser coherence length. Finally, they are detected by two single-photon detectors (actively quenched silicon avalanche photodiodes, Si-APDs) placed at the outputs of the beam-splitter, and coincidence detection events are analyzed with a time-to-digital convertor (TDC) and a computer.

9.1.2 Experiment

Our experimental setup is depicted in Fig. 9.2. We employ solid-state quantum memories, more precisely thulium-doped lithium-niobate waveguides in conjunction with the atomic frequency comb (AFC) quantum memory protocol [30], which have shown great promise for advanced applications of quantum information processing [5,7]. We then interfere various combinations of recalled and non-stored (i.e. directly transmitted) pulses on a 50/50 BS (HOM-BS). When using single photon Fock states at the memory inputs, the HOM visibility given in (9.1) theoretically reaches 100%. However, with phase incoherent laser pulses obeying Poissonian photon-number statistics, as in our demonstration, the maximally achievable visibility is 50% [31], irrespective of the mean photon number (see Supplementary Information). Nevertheless, attenuated laser pulses are perfectly suitable for assessing the effect of our quantum memories on the photonic wavefunction. Any reduction of indistinguishability due to storage causes a reduction of visibility, albeit from maximally 50%. This approach extends the characterization of quantum memories using attenuated laser pulses [32] from assessing the preservation of quantum information during storage to assessing the preservation of the entire wavefunction, and from first to second-order interference.

9.1.3 Measurements

We first deactivate both quantum memories (see Methods), to examine the interference between directly transmitted pulses, and thereby establish a reference visibility in our experimental setup. We set the mean photon number per pulse before the memories to 0.6, i.e. to the single-photon level. Using the wave plates, we rotate the polarizations of the pulses at the two HOM-BS inputs to be parallel (indistinguishable) or orthogonal (distinguishable). Employing (9.1) we find a visibility of $(47.9 \pm 3.1)\%$.

Subsequently, we activate memory a while keeping memory b off, and adjust the timing of the pulse preparation so as to interfere a recalled pulse from the active memory with a

directly transmitted pulse from the inactive memory (see Methods). Pulses are stored for 30 ns in memory a, and the mean photon number per pulse at the quantum memory input is 0.6. Taking the limited storage efficiency of $\approx 1.5\%$ and coupling loss into account, this results in 3.4×10^{-4} photons per pulse at the HOM-BS inputs. As before, changing the pulse polarizations from mutually parallel to orthogonal, we find $V = (47.7 \pm 5.4)\%$, which equals our reference value within the measurement uncertainties.

As the final step, we activate both memories to test the feasibility of two-photon interference in a quantum-repeater scenario. We note that in a real-world implementation, memories belonging to different network nodes are not necessarily identical in terms of material properties and environment. This is captured by our setup where the two Tm:LiNbO$_3$ waveguides feature different optical depths and experience different magnetic fields (see Fig. 9.2 and Supplementary Information). To balance the ensuing difference in memory efficiency we set the mean photon number per pulse before the less efficient and more efficient memories to 4.6 and 0.6, respectively, so that, as before, the mean photon numbers are 3.4×10^{-4} at both HOM-BS inputs. With the storage time of both memories set to 30 ns, we get $V = (47.2 \pm 3.4)\%$, in good agreement with the values from the previous measurements. The consistently high visibilities, compiled in the first column of Table 9.1, hence confirm that our storage devices do not introduce any degradation of photon indistinguishability during the reversible mapping process, and that two-photon interference is feasible with photons recalled from separate quantum memories, even if the memories are different.

We now investigate in greater detail the change in coincidence count rates as photons gradually change from being mutually indistinguishable to completely distinguishable w.r.t. each degree of freedom accessible for change in single-mode fibres, i.e. polarization, temporal, and spectral modes (see Methods). To acquire data more efficiently we increase the mean number of photons per pulse at the memory input to between 10 and 50 (referred to as few-photon-level measurements), however, the mean photon number at the HOM-BS remains
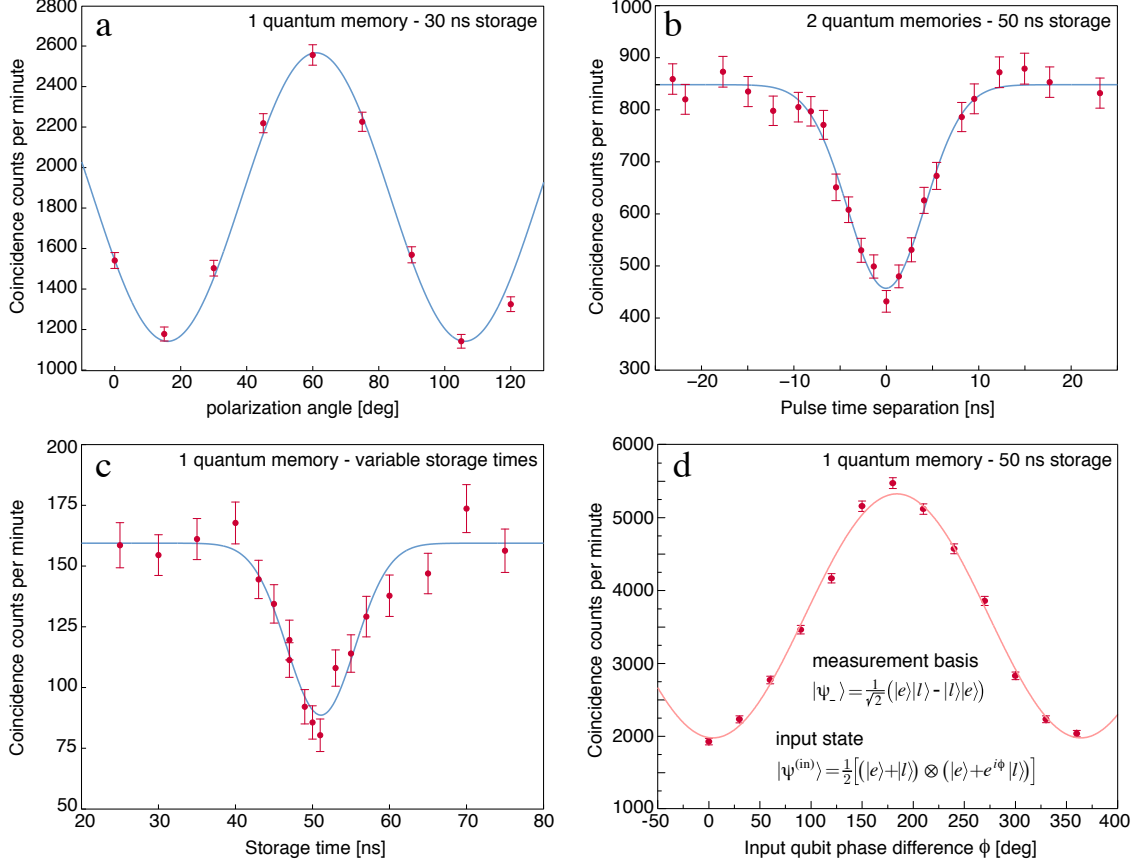
Figure 9.3: **HOM interference plot examples for one or two active memory configurations as labelled**. a) Varying mutual polarization difference. b) Varying temporal overlap by changing timing of pulse generation. c) Varying temporal overlap by changing storage time. d) Projection of pairs of time-bin qubits with relative phase ϕ onto $|\psi^-\rangle$. The acquisition time per data point is 60 s in a,b,d, and 120 s in c.

below one. Example data plots are shown in Fig. 9.3, while the complete set of plots is supplied in the Supplementary Information Figs. 9.6-9.8.

Coincidence counts rates as a function of the polarization of the recalled pulse for the case of one active memory are shown in Fig. 9.3a. The visibilities for all configurations (i.e. zero, one, or two active memories) extracted from fits to the experimental data are listed in column 2 of Table 9.1. They are – as in the case of single-photon-level inputs – equal to within the experimental uncertainty.

Next, in Fig. 9.3b, we depict the coincidence count rates as a function of the temporal overlap (adjusted by the timing of the pulse generation) for the two-memory configuration. Column

3 of Table 9.1 shows the visibilities extracted from Gaussian fits to the data, reflecting the temporal profiles of the probe pulses, for all configurations. Within experimental uncertainty, they are equal to each other. Alternatively, in the single-memory configuration, we change the temporal mode overlap by adjusting the storage time of the pulse mapped to the quantum memory. Again the measured visibility of $V = (44.4 \pm 6.9)\%$ (see Fig. 9.3c) is close to the theoretical maximum.

Finally, we vary the frequency difference between the two pulses (see Methods) to witness two-photon interference w.r.t. spectral distinguishability. For this measurement, we consider only the configurations in which either none, or a single memory is active. In both cases the visibilities, listed in the last column of Table 9.1, are around 43%. While this is below the visibilities found previously, for reasons discussed in the Supplementary Information, the key observation is that the quantum memory does not affect the visibility.

Table 9.1: Experimental two-photon interference visibilities (%) for different degrees of freedom

Storage	Single-photon level	Few-photon level		
configuration	Polarization	Polarization	Temporal	Spectral
No-storage	47.9 ± 3.09	50.7 ± 5.36	44.3 ± 1.76	43.7 ± 2.00
Single-storage	47.7 ± 5.44	55.5 ± 3.78	47.5 ± 2.45	42.5 ± 2.73
Double-storage	47.2 ± 3.37	52.8 ± 5.56	46.2 ± 2.71	N. A.

As stated above, Bell-state measurements (BSM) with photonic qubits recalled from separate quantum memories are key ingredients for advanced applications of quantum communication. To demonstrate this important element, we considered the asymmetric (and arguably least favourable) case in which only one of the qubits is stored and recalled. Appropriately driving the AOM, we prepare time-bin qubits [34] in the states $|+\rangle = \frac{1}{\sqrt{2}}(|e\rangle + |l\rangle)$ and $|\phi\rangle = \frac{1}{\sqrt{2}}(|e\rangle + e^{i\phi}|l\rangle)$, where e and l denote early and late temporal modes separated by 25 ns, and direct them to the memories of which only one is activated. The mean photon number in the qubit that is stored is set to 20, yielding a mean photon number of both qubits at the

HOM-BS input of 0.022. We ensure to overlap pulses encoding the states $|+\rangle$ and $|\phi\rangle$ at the HOM-BS and count coincidence detections that correspond to a projection onto the $|\psi^-\rangle = \frac{1}{\sqrt{2}}(|e\rangle |l\rangle - |l\rangle |e\rangle)$ Bell state as a function of the phase ϕ (see Fig. 9.3d). This projection measurement occurs if the two detectors click with 25 ns time difference [34]. Because $|\psi^-\rangle$ is antisymmetric w.r.t. any basis, the count rate is expected to reach a minimum value $R_\parallel$ if the two input pulses are prepared in equal states ($\phi = 0$), and a maximal value $R_\perp$ if prepared in orthogonal states ($\phi = \pi$). Accordingly, we define an error rate that quantifies the deviation of the minimum count rate from its ideal value of zero:

$$e \equiv \frac{R^\parallel}{R^\parallel + R^\perp} \, . \tag{9.2}$$

The error rate can be calculated from the visibility as $(1 - V_{\mathrm{BSM}})/(2 - V_{\mathrm{BSM}})$. For attenuated laser pulses the visibility has an upper bound of $V_{\mathrm{BSM}}^{\mathrm{theo}} = 66.67\%$, corresponding to a lower bound $e_{\mathrm{theo}} = 0.25$. From the fit to the measured coincidence count rates in Fig. 9.3d we obtain $V_{\mathrm{BSM}}^{\mathrm{exp}} = (62.9 \pm 0.5)\%$, resulting in an experimental error rate of $e_{\mathrm{exp}} = 0.271 \pm 0.003$, which only slightly exceeds e_{theo} (see the Supplementary Information for derivations).

9.1.4 Conclusion

Our demonstrations show that solid-state AFC quantum memories are suitable for two-photon interference experiments, even in the general case of storing the two photons an unequal numbers of times. With improved system efficiency [35] and multi-mode storage supplemented by read-out on demand [36,37], such memories can be used as synchronization devices in multi-photon experiments, which will allow increasing the number of photons that can be harnessed simultaneously for quantum information processing beyond the current limit of eight [38]. A subsequent goal is to develop workable quantum repeaters or, more generally, quantum networks, for which longer storage times are additionally needed. Depending on the required value, which may range from hundred micro-seconds [39] to seconds [1], this may be achieved by storing quantum information in optical coherence, or it may

require mapping of optical coherence onto spin states [30].

9.1.5 Methods

Memory operation and properties: A quantum memory is said to be activated when we configure the MEMS to allow the optical pumping light to reach the waveguide during the preparation stage and thus tailor an AFC in the inhomogeneously broadend absorption spectrum of thulium ions (see Fig. 9.2). If the optical pumping is blocked, the memory is said to be deactivated and light entering the waveguide merely experiences constant attenuation over its entire spectrum. If a memory is activated, incident an incident photon is mapped onto a collective excitation of thulium ions in the prepared AFC and subsequently re-emitted at a time given by the inverse of the comb tooth spacing [30], i.e., $t = 1/\Delta$ (see Fig. 9.2). In all cases, we adjust the mean photon number at the memory inputs so that mean photon numbers are equal at the HOM-BS inputs. This is required for achieving maximum visibility with attenuated laser pulses (see Supplementary Information).

The two Tm:LiNbO$_3$ waveguides are fabricated identically but differ in terms of overall length – memory a being ≈ 10 mm and memory $b \approx 15$ mm. This in turn yield optical depths of 2.7 and 3.2, respectively. As shown in Figure 1, memory a is placed at the centre of a solenoid in a uniform magnetic field, while memory b is placed outside the solenoid and thus experiences only a much weaker stray field. These differences cause the memories to operate in different regimes (see Supplementary Information) and have different efficiencies. Thus, to match the mean photon numbers at the HOM-BS we adjust the mean photon number at the input of the memories.

Changing degrees of freedom: a) The polarization degree is easily adjusted using the free-space half- and quarter-wave plate set at each HOM-BS input. For our measurements we rotate the half-wave plate in steps of 15 degrees (this applies only to the few photon measurements). **b)** The temporal separation δt between a pulse arriving at one of the HOM-BS inputs and the next pulse in the train arriving at the other input can be expressed as

$\delta t = \{nl/c\} \mod \delta t_r$, where n is the refractive index of the fibres, $l \approx 10$ km is the path-length difference for pulses interacting with memory a and b, and δt_r is the repetition period of the pulse train from the AOM, which is set to be around 395 ns. As we can change δt_r with 10 ps precision, we can tune δt on the ns scale. **c)** For the storage time scan, the recall efficiency decreases with storage time due to decoherence. Hence, we balance the mean photon number per pulse for stored and transmitted pulses for each storage time. **d)** Finally, to change the spectral overlap of the pulses input to the HOM-BS we can utilize that these pulses were generated at different times in the AOM and thus we can chose their carrier frequencies independently. We interchangeably drive the AOM by frequencies ν_a and ν_b and thus create two interlaced trains of pulses with different frequencies. Adjusting the pulse timing we can ensure that the pulses overlapped at the HOM-BS belong to different trains and thus have a spectral overlap given by $\delta\nu = \nu_a - \nu_b$. Due to the limited bandwidth of the AOM we are only able to scan $\delta\nu$ by 100 MHz, which, when compared to the 50 MHz pulse bandwidth, is not quite sufficient to make the pulses completely distinguishable. To achieve complete distinguishability, we supplement with a measurement using orthogonal polarizations at the inputs (see Supplementary Information). **e)** For the Bell-state projection measurement we interchangeably prepare the time-bin qubits $\frac{1}{\sqrt{2}}(|e\rangle + |l\rangle)$ and $\frac{1}{\sqrt{2}}(|e\rangle + e^{i\phi}|l\rangle)$ by setting the relative phase and intensity of the AOM drive signal. Adjusting the timing of the pulse preparation we ensure that qubits in different states overlap at the HOM-BS.

9.1.6   Supplementary Information

Properties of waveguide LiNbO$_3$ crystal and AFC

In the experimental configuration in which the HOM-interference occurs between two pulses recalled from separate quantum memories we pointed, in the main text, to the different properties of the two memory devices. In this section we wish to elaborate on the differences between the two memories based on their physical dissimilarity and measured optical depth. Memory crystal a is 10.4 mm long and crystal b is 15.4 mm long. The optical depths at

795.43 nm are around 2.5 and 3.2 for crystal a and b, respectively, as shown by the light-grey curves in Fig. 9.4 a,b. This corresponds to the case in which the memories are not activated.
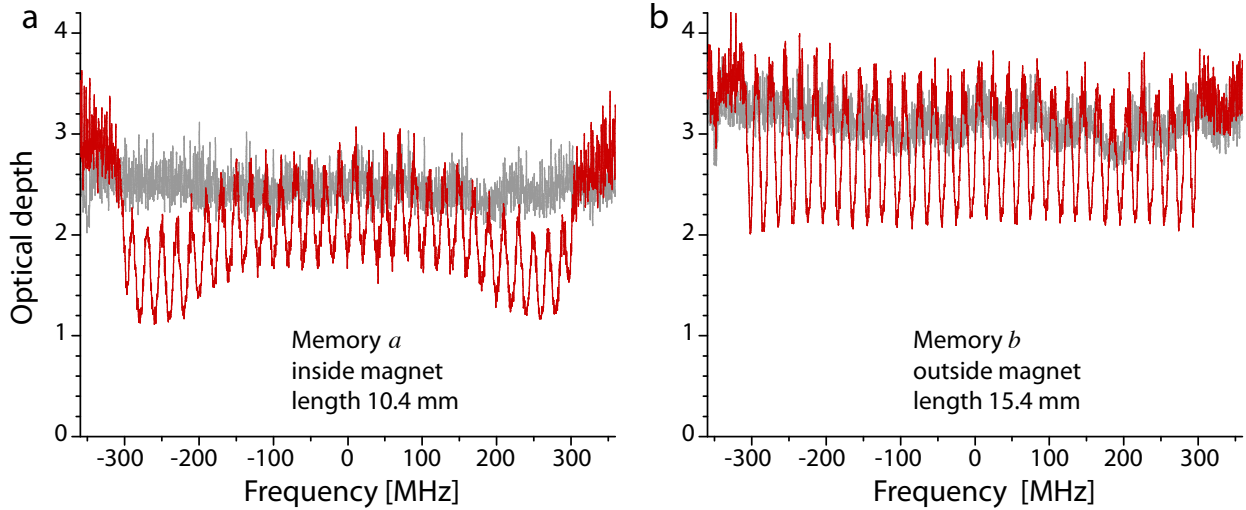
Figure 9.4: **Measured optical depths as a function of detuning (frequency) w.r.t the light carrier frequency of our two Tm:LiNbO$_3$ waveguides:** Light grey traces show optical depths when the memories are inactive, i.e. no AFC is prepared. Dark red traces show the prepared AFCs at a magnetic field of 900 Gauss at the centre of the solenoid.

In order to spectrally tailor an AFC in Tm:LiNbO3, a magnetic field must be applied along the crystal's c-axis so as to split the ground and excited levels into their two nuclear Zeeman sublevels [28]. The difference in excite and ground level splitting is around $\delta g_Z = 0.125 \ MHz/Gauss$ and thus, to generate an AFC yielding a storage time $t = 1/\Delta$, the magnetic field should ideally be set to either $B = \Delta/(2g_Z)$ or $B > W/(g_Z)$, where W is the total bandwidth of the AFC. Since the former field setting corresponds to a smaller field than the latter we coin them *low-* and *high*-field regime. In the low field regime atoms initially at frequencies in the comb throughs when in one of the Zeeman levels will be optically pumped to the comb's peaks when transferred to the other Zeeman level. In the high field regime atoms in the comb's throughs will be pumped outside the comb's bandwidth W. However, as one crystal is located at the centre of the setup's solenoid and the other outside the solenoid (see Fig. 9.2) it is not possible to apply the same B-field at the two crystals. In addition our magnetic field is limited so that only memory a can be operated in the high field regime.

As a result, when we operate both memories, we necessarily have to operate them in an intermediate regime, where the B-field is not optimal. We find that setting the B-field to 900 Gauss in the centre of the solenoid yields similar system efficiencies. The corresponding AFCs are shown in red in Fig. 9.4a,b.

Two-photon interference in imperfectly prepared memories

In all our demonstrations of the HOM interference we consistently observe that the HOM visibility is close to the theoretical maximum for coherent states. Yet, it is important to realize that an improperly configured AFC quantum memory does alter a stored photon's wavefunction, resulting in imperfect HOM interference with a non-stored photon.

To support this claim we activate only memory a, whose performance we change by varying the bandwidth of the AFC, and interfere the recalled pulses with pulses directly transmitted through the deactivated memory b. As the AFC bandwidth decreases below that of the probe pulses, the AFC effectively acts as a bandpass filter for the stored photons and we thus expect the recalled pulses to be temporally broadened w.r.t. the original pulse. This is observed in the insert of Fig. 9.5, which shows smoothed histograms of the photon detection events as a function of time. It is worth noting that the small bandwidth AFC also acts as a bandpass filter for the transmitted pulse by virtue of the different effective optical depths inside and outside the AFC. Thus the broadened transmitted pulse starts to overlap with the echo for the narrow AFC bandwidth traces, as is also observed in the insert of Fig. 9.5.

Another consequence of reducing the AFC bandwidth is that the overall efficiency of the quantum memory decreases, which causes an imbalance between the mean photon numbers at the HOM-BS inputs and thus reduced HOM interference visibility. We circumvent the change to the echo efficiency by adapting the mean photon number at the memory input so as to keep the mean photon number of the recalled pulse constant. With this remedial procedure, we assess the HOM visibility by changing the HOM-BS inputs from parallel
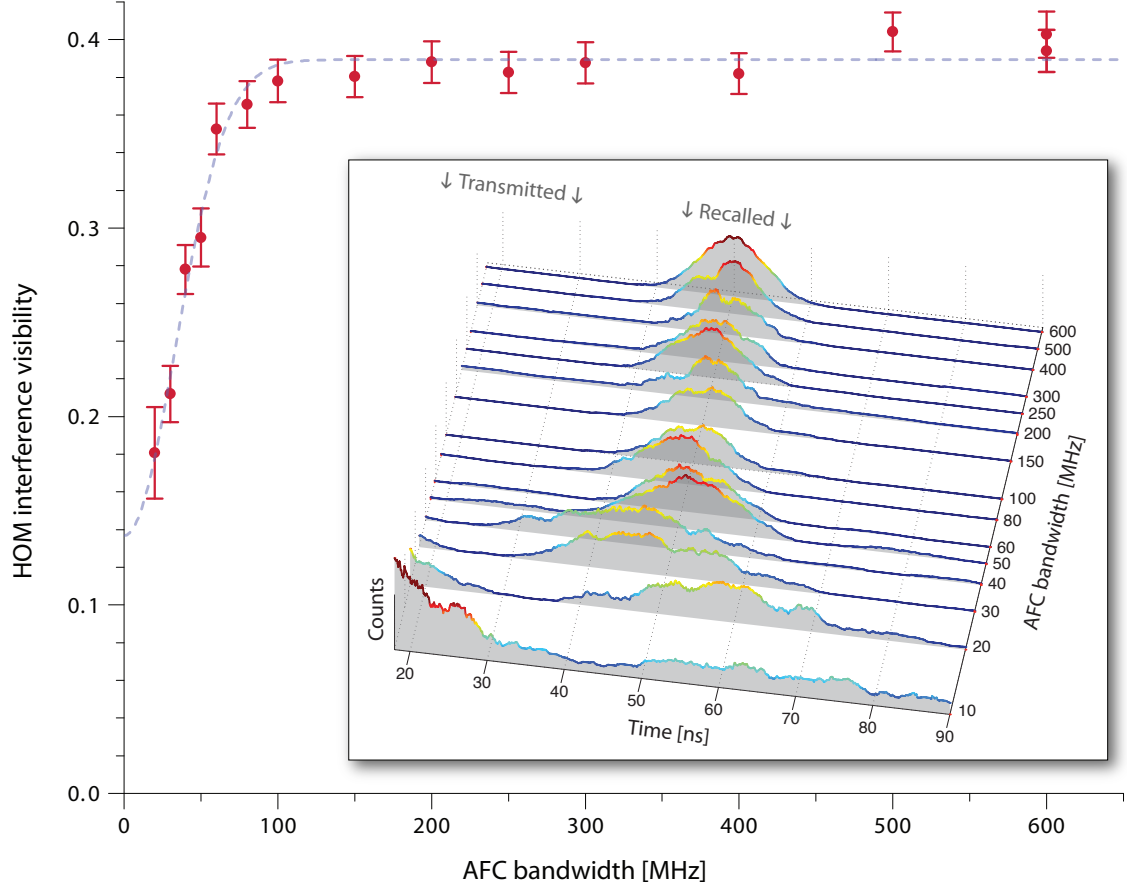
Figure 9.5: **HOM interference visibility if HOM-BS input pulses are recalled from AFCs with varying bandwidths.** Insert: Histograms of recalled pulse detection times for different AFC bandwidths. Traces taken for AFC bandwidths below 30 MHz also show temporally broadened transmitted pulses, as explained in the main text

to orthogonal polarizations for a series different AFC bandwidths. The HOM visibility in Fig. 9.5 is steady for bandwidths from around 100 MHz and up. However, below 100 MHz the visibility begins to drop significantly. The dashed line is a fit of the visibilities to a Gaussian function with full-width at half-maximum (FWHM) of $79 \pm 4\ MHz$. Note, that why the visibility is limited to around 40% is merely that, for this measurement, we do not go through the usual careful steps to optimize the visibility.

With these measurements we have illustrated how a quantum memory could alter the photonic wavefunction resulting in a reduced HOM interference visibility. A combination of spectral and temporal distortion of the photonic wavefunction is indeed a common type

of perturbation by quantum memories [40,41]. It is particularly worth noting that the gradient-echo memory (GEM) quantum memory protocol, though similar to the AFC protocol, imparts a frequency chirp to the recalled pulse. If not corrected, this feature constitutes a perturbation of the wavefunction of the recalled pulse, which may render it unsuitable for applications relying on two-photon interference.

Analytical model of second-order interference in coincidence measurements.

In the following theoretical treatment we will derive expressions for the coincidence and single-detector counts in terms of probabilities. By multiplying these probabilities with the average experimental repetition rate we can easily calculate the predicted experimental count rates. To a large extent though, we will mainly be interested in relative probabilities or count rates between different settings of the degrees of freedom of pulses.

It is reasonably straightforward to derive the rates of detection of light at the outputs of a BS (note that in this Supplementary Information, the HOM-BS of the main text will be referred to as just BS) In our case coherent states $|\alpha\rangle$ and $|\beta\rangle$, characterized by mean photon numbers $\langle \hat{a}^\dagger \hat{a} \rangle = |\alpha|^2$ and $\langle \hat{b}^\dagger \hat{b} \rangle = |\beta|^2$, occupy the two spatial input modes of the BS. In the Fock-basis the coherent state can be represented as

$$|\alpha\rangle = \sum_{n=0}^{\infty} e^{-\frac{|\alpha|^2}{2}} \frac{\alpha^n}{\sqrt{n!}} |n\rangle = \sum_{n=0}^{\infty} e^{-\frac{|\alpha|^2}{2}} \frac{\alpha^n}{n!} (\hat{a}^\dagger)^n |0\rangle, \tag{9.3}$$

and similarly for $|\beta\rangle$.

To account for the cases of photons being distinguishable and indistinguishable at the BS we must allow for an additional degree of freedom in each of the spatial modes, e.g. polarization, frequency, or time. Thus we write the input state at one of the BS inputs as $|\alpha_1, \alpha_2\rangle \equiv |\alpha_1\rangle \otimes |\alpha_2\rangle$, where α_1 and α_2 are the coherent state amplitudes in the two orthogonal modes of the auxiliary degree of freedom within the same spatial mode. We treat the coherent state at the other BS input in a similar way.

For the case in which the fields at the inputs of the BS are distinguishable with respect to the auxiliary degree of freedom, the inputs to the BS are described as being in the state

$|\alpha, 0\rangle|0, \beta\rangle \equiv |\alpha, 0\rangle \otimes |0, \beta\rangle$, whereas in the case of them being indistinguishable (up to a difference in the mean photon number) the input fields are written as $|\alpha, 0\rangle|\beta, 0\rangle$.

The BS is characterized by its reflection amplitude r and transmission amplitude $t = \sqrt{1 - |r|^2}$ that cause the input creation operators to transform as $\hat{a}^\dagger \rightarrow t\hat{c}^\dagger + ir\hat{d}^\dagger$ and $\hat{b}^\dagger \rightarrow ir\hat{c}^\dagger + t\hat{d}^\dagger$. With this in hand, we can compute the state in the BS outputs for any combination of Fock states at the inputs. When the two input states are indistinguishable, i.e. in the same auxiliary degree of freedom, we get [42]

$$|n, 0\rangle|m, 0\rangle \rightarrow \sum_{j=0}^{n} \sum_{k=0}^{m} K_\parallel(n, m, j, k) \, |j+k, 0\rangle|n+m-j-k, 0\rangle \tag{9.4}$$

$$K_\parallel(n, m, j, k) = t^{m-k+j}(ir)^{n-j+k} \sqrt{\binom{n}{j}\binom{m}{k}\binom{j+k}{j}\binom{n+m-j-k}{n-j}},$$

where the binomial coefficient $\binom{x}{y} = \frac{x!}{y!(x-y)!}$. For distinguishable input fields the output state is slightly simpler

$$|n, 0\rangle|0, m\rangle \rightarrow \sum_{j=0}^{n} \sum_{k=0}^{m} K_\perp(n, m, j, k) \, |j, k\rangle|n-j, m-k\rangle \tag{9.5}$$

$$K_\perp(n, m, j, k) = \sum_{j=0}^{n} \sum_{k=0}^{m} t^{m-k+j}(ir)^{n-j+k} \sqrt{\binom{j}{k}\binom{n-j}{m-k}}.$$

The above calculated output modes impinge on the single photon detectors (SPDs). These may be characterized by the probability of detecting an incident single photon. From this single photon detection probability η it is also possible to deduce the probability of detecting a pulse consisting of multiple photons, keeping in mind that, irrespective of the number of photons, only a single detection event can be generated. We write $p_1(n)$ for the probability for generating one detector event given n incident photons, and it is useful to note that it relates to the probability $p_0(n)$ of detecting nothing as $p_1(n) = 1 - p_0(n)$. The probability for not detecting n photons is, on the other hand, easily computed as $p_0(n) = (1-\eta)^n$. Since the two detectors at the BS outputs are independent, the probability $p_{11}(n, m)$ of generating a coincidence event, i.e. having simultaneous detection events in each of the detectors, given

154

n and m photons in one and the other output is simply $p_{11}(n,m) = p_1(n)p_1(m)$. Thus the probability for a coincidence detection becomes

$$p_{11}(n,m) = \left[1 - (1-\eta_1)^n\right]\left[1 - (1-\eta_2)^m\right],\qquad(9.6)$$

where η_1 and η_2 are the single photon detection probabilities for detector 1 and 2, respectively. Expressing the coincidence detection probability in terms of Fock states at the BS input we have

$$
\begin{aligned}
P_{11}^{\|(\perp)}(n,m) &= \sum_{j=0}^{n}\sum_{k=0}^{m}|K_{\|(\perp)}(n,m,j,k)|^2\, p_{11}(j+k,\,n+m-j-k) \qquad(9.7)\\
&= \sum_{j=0}^{n}\sum_{k=0}^{m}|K_{\|(\perp)}(n,m,j,k)|^2\left[1-(1-\eta_1)^{j+k}\right]\left[1-(1-\eta_2)^{n+m-j-k}\right],
\end{aligned}
$$

where $K_{\|(\perp)}(n,m,j,k)$ should be substituted with the appropriate factor from either (9.4) or (9.5). It is assumed that the detector at a given spatial output mode is equally sensitive to photons in both auxiliary modes, i.e. it detects the states $|k,j\rangle$ and $|j,k\rangle$ with equal probability.

We are now in the position to formulate an expression for the different detection probabilities given a particular set of coherent input fields. The probability to generate a detection event in both detectors, given coherent input fields of amplitude α and β, is

$$\mathcal{P}_{11}^{\|(\perp)}(\alpha,\beta) = \sum_{n=0}^{\infty}\sum_{m=0}^{\infty} e^{-|\alpha|^2-|\beta|^2}\frac{(\alpha^n\beta^m)^2}{n!\,m!}P_{11}^{\|(\perp)}(n,m).\qquad(9.8)$$

(Note that to distinguish Eq. (9.7), which is applicable to Fock states, from Eq. (9.8), which applies to coherent state inputs, we use P to denote the former and $\mathcal{P}$ for the latter probability.) This allows us to derive the visibility of the HOM interference on the two detectors as

$$\mathcal{V}_{11}(\alpha,\beta,\eta_1,\eta_2,r) = \frac{\mathcal{P}_{11}^{\perp}(\alpha,\beta) - \mathcal{P}_{11}^{\|}(\alpha,\beta)}{\mathcal{P}_{11}^{\perp}(\alpha,\beta)},\qquad(9.9)$$

where we have spelled out the parameters that affect the value of the visibility. The quantity $\mathcal{V}_{11}$ is usually referred to as the *HOM visibility*.

Simplified model for HOM visibility.

To gain some intuitive understanding of the way the HOM visibility is affected by the experimental parameters we resort to a couple of approximations. Firstly, we assume equal mean photon numbers at the inputs of the beam-splitter, $|\alpha|^2 = |\beta|^2 \equiv \mu$, the BS ratio to be 50:50 (i.e. $r = t = 1/\sqrt{2}$), and the detectors to have equal single photon detection probability $\eta_1 = \eta_2 \equiv \eta$. Secondly, since we normally work at very low mean photon numbers $\mu < 1$ only the first couple of terms of Eq.(9.3) need to be included. Specifically, we Taylor expand $e^{-\mu/2}$ and keep only terms in the sum up to 2nd order in μ. Thus, for the coincidence detection events we get the probabilities

$$\mathcal{P}_{11}^{\|} = \eta^2 \frac{\mu^2}{2} \tag{9.10}$$

$$\mathcal{P}_{11}^{\perp} = \eta^2 \mu^2 \,, \tag{9.11}$$

which results in a HOM visibility of

$$\mathcal{V}_{11} = \frac{1}{2} \,. \tag{9.12}$$

A key point is that the HOM visibility of 50% is independent of the mean photon number μ. This observation can be explained by noting that in this low order treatment the coincidences in the case of indistinguishable input modes stem mostly from events in which two photons are present at the same input, which occurs with probability $p_0 p_2 + p_2 p_0$. For distinguishable input modes the coincidences stem from all events that contain two photons at the input, i.e. $p_1 p_1 + p_0 p_2 + p_2 p_0$. Since, according to Eq. (9.3), for coherent input states, all of these probabilities scale in the same way with the mean photon number, their ratio, and thus the visibility of (9.9), is constant for all mean photon numbers.

Compilation of experimental results for HOM interference at the few-photon level.

Here we show the plots of coincidence count rates on which the few-photon values in Table 9.1 of the main text are based. We restate that coincidence count rates are proportional to

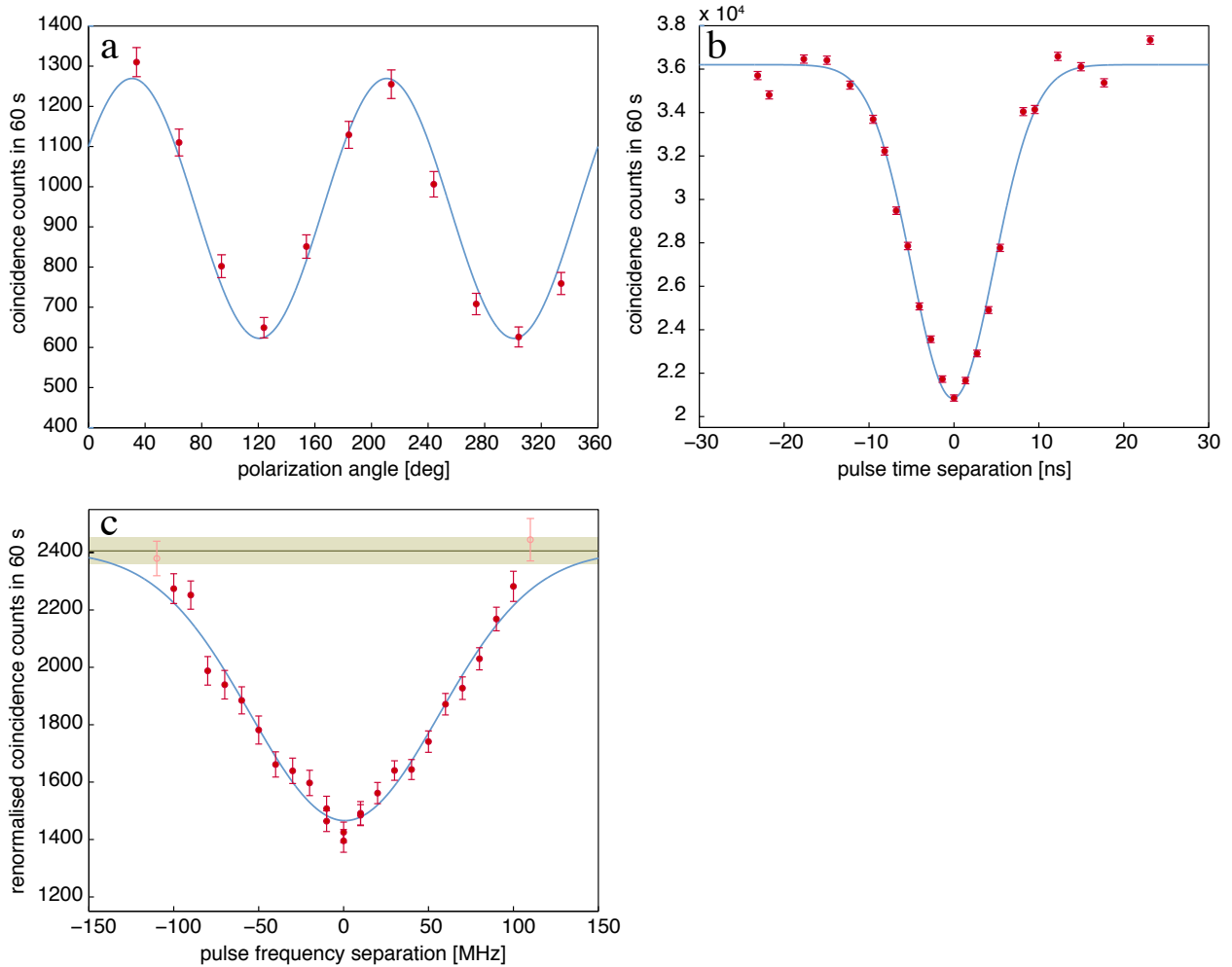Figure 9.6: **HOM interference manifested in coincidence counts between BS outputs with inactive memories:** a) Changing the polarization angle between the pulses yields a HOM visibility of $\mathcal{V} = 50.96 \pm 5.56\%$. b) Varying the temporal overlap of the pulses produces $\mathcal{V} = 42.43 \pm 2.27\%$. c) Altering the frequency overlap of the pulse spectra results in $\mathcal{V} = 39.06 \pm 1.52\%$.

coincidence probabilities by a factor that is given by the average experimental repetition rate. Moreover, when calculating the HOM visibility, only the relative probabilities or count rates in a measurement are important. In the experiments we change the mutual polarization, time separation, or frequency difference of the pulses at the BS (in the main text referred to as HOM-BS) input as explained in the Methods.

Deactivated memories: We present the data in order of the number of activated memories starting with none, i.e. pulses merely pass through attenuated to the BS. In Fig. 9.6a we show the coincidence counts as we vary the polarization difference of the pulses at the two inputs of the BS. Fitting the data with a squared-sine function we obtain a visibility of $\mathcal{V} = 50.96 \pm 5.56\%$. In Fig. 9.6b we display the coincidence counts as we step the temporal separation of the input pulses at the BS. The count rate for these measurements are generally higher than all the other count rates presented. This is because this data was acquired by looking at coincidences between the transmitted part of the probe pulses in the configuration of two active quantum memories (shown in Fig. 9.8b). Hence, the mean photon number per pulse is adjusted for the recalled pulses not for the transmitted pulses. Likewise, the balancing of the mean photon number in the transmitted pulses done less meticulously, which is the most likely reason for the observed lower visibility of $\mathcal{V} = 42.43 \pm 2.27\%$ in this case.

Fig. 9.6c shows the coincidence count rates as function of the frequency difference of the two pulses at the BS inputs. The horizontal line and surrounding shaded band shown in Fig. 9.6c – as well as in Fig. 9.7c – give the coincidence for completely indistinguishable input photons as obtained by making the polarizations orthogonal. As noted in the Methods, it is necessary to resort to the polarization degree of freedom in order to make the pulses completely indistinguishable. The visibility from the fit is noticeably lower than that we obtained by changing the other degrees of freedom. There are two main reasons for this. The first is that, in order to generate pulses with different frequencies, we drive the AOM at the limit of its bandwidth. This, in turn, necessitates setting the RF drive signal amplitude

high whereby the frequency purity of the signal is contaminated by higher-order harmonics. Although it is not expected to change the maximal interference value occurring when the pulses generated with the same modulation frequency, it will alter the shape of the interference as a function of the pulse frequency difference. Hence, the fitted Gaussian curve, assuming a Fourier limited pulse, may not correctly reproduce the actual frequency dependence of the interference. Indeed, the minimum coincidence rates consistently fall below the fitted curve. A second factor reducing the fitted visibility is related to the need to adjust the AOM drive amplitude to balance the bandwidth limitation. The limited accuracy with which we are able to estimate the appropriate RF amplitude results in significant scattering of the coincidence counts due to variations in input pulse intensities. To amend this we have found that it is necessary to normalize the points to the count rates on the individual detectors, as indicated on the y-axis of plot Fig. 9.7c. Unfortunately, the manifestation of the HOM interference in the single-detector count rates – which will be elaborated later in the Supplementary Information – means that such a normalization procedure tends to reduce the visibility in the coincidence counts.

One active memory: Next in line are the plots for the case in which only memory a is activated, while the other is left inactive. In Fig. 9.7 we present the coincidence count rates when changing the same degrees of freedom as in case of both memories being inactive. Additionally, in Fig. 9.7d, we plot the coincidence count rates when changing the storage time in the quantum memory.

Two active memories: Lastly, we present the plots for the case in which both memories are activated. Due to limitations in our current setup it is not possible to simultaneously generate two quantum memories with different storage times, and therefore we do not acquire a storage time scan when both memories are active. Furthermore, we skip the characterization with respect to the spectral degree of freedom. The coincidence count data for the remaining two degrees of freedom are plotted in Fig. 9.8, which also includes the appropriate fits.
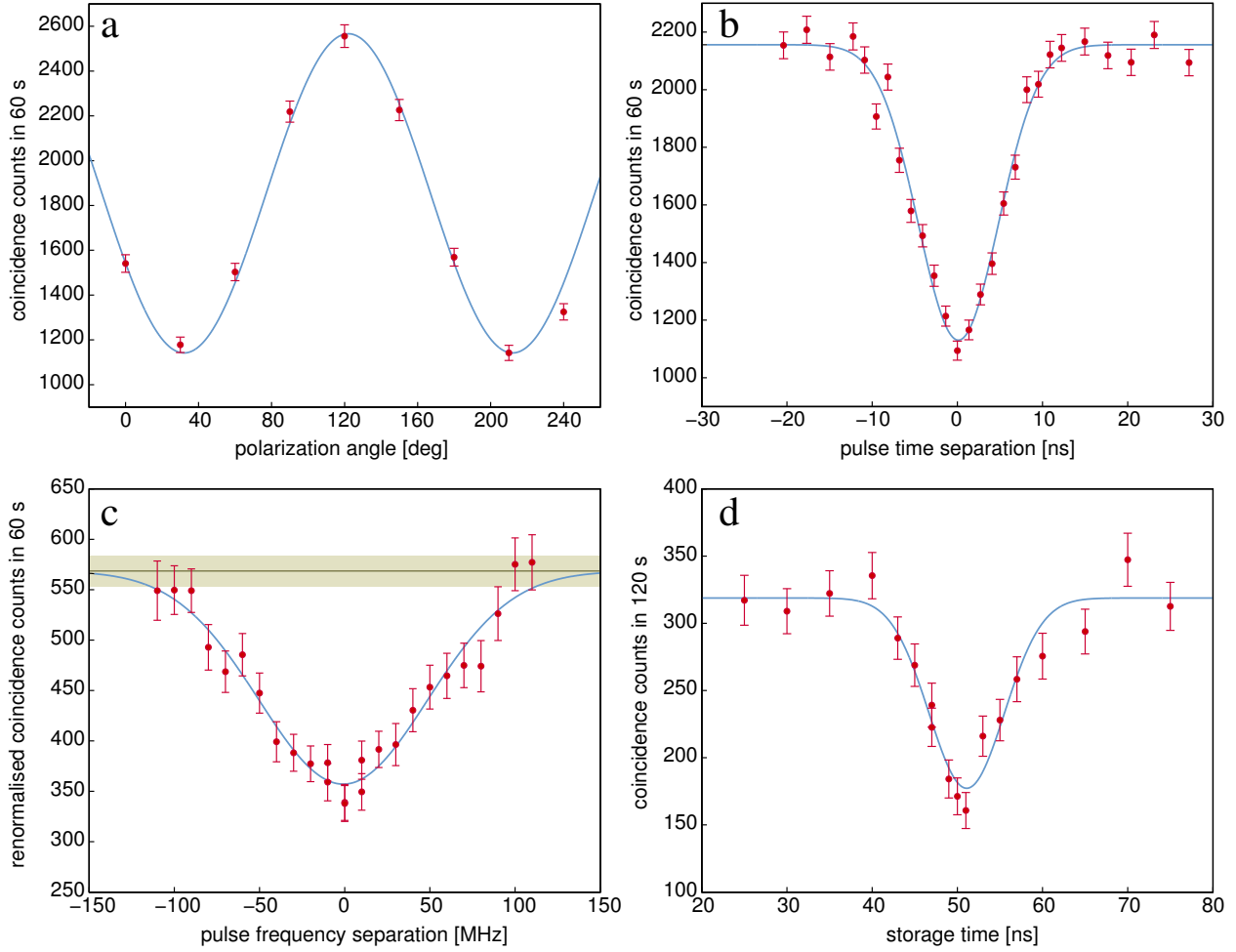
Figure 9.7: **HOM interference manifested in coincidence counts between BS outputs with one active memory:** a) Changing the polarization angle between the pulses yields a HOM visibility of $\mathcal{V} = 55.51 \pm 4.09\%$. b) Varying the temporal overlap of the pulses produces $\mathcal{V} = 47.57 \pm 2.96\%$. c) Altering the frequency overlap of the pulse spectra results in $\mathcal{V} = 37.18 \pm 2.50\%$. d) Varying the storage time of the quantum memory and thus the temporal overlap of the pulses yields $\mathcal{V} = 44.4 \pm 6.9\%$.
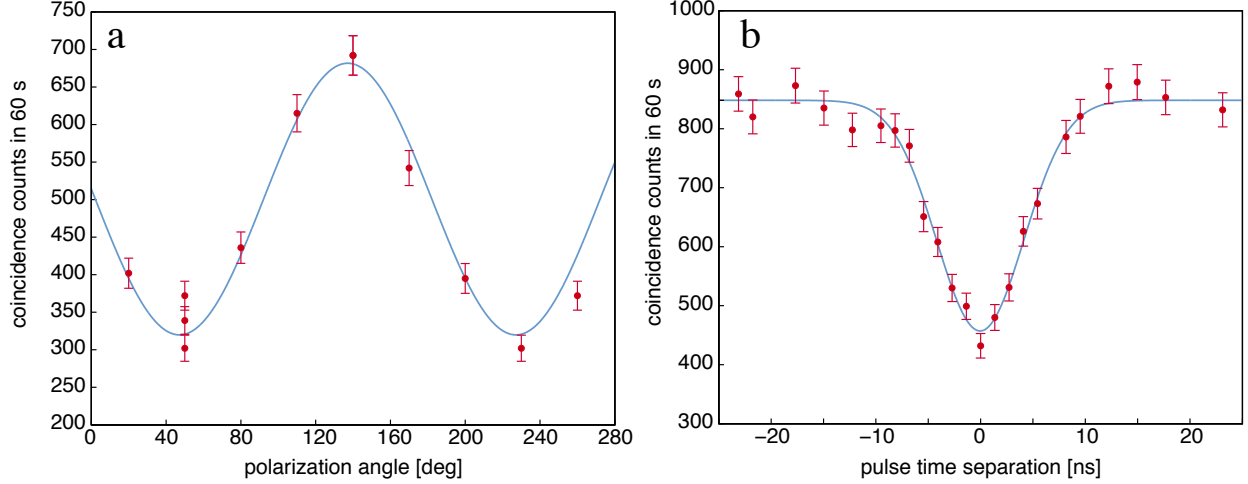
Figure 9.8: **HOM interference manifested in coincidence counts between BS outputs with two active memories:** a) Changing the polarization angle between the pulses yields a HOM visibility of $\mathcal{V} = (53.1 \pm 5.3)\%$. b) Varying the temporal overlap of the pulses produces $\mathcal{V} = (46.1 \pm 3.2)\%$.

Bell-state measurement visibility.

In this section we aim to arrive at an analytical expression for the coincidence count rates between time-bin qubits detected in the two detectors at the output of the HOM-BS. To that end, we will introduce a number of approximations as we did previously in order to calculate the HOM interference in the coincidence and single detector counts. In the limit of low mean photon numbers, two coherent states impinging onto the two inputs of a 50:50 BS can be represented in terms of Fock states as (without normalization)

$$|\psi\rangle_{ab} = \sqrt{p(1,1)}|11\rangle_{ab} + \sqrt{p(2,0)}|20\rangle_{ab} + \sqrt{p(0,2)}|02\rangle_{ab} \tag{9.13}$$

$$= \left(\sqrt{p(1,1)}(\hat{a}^\dagger \otimes \hat{b}^\dagger) + \frac{1}{\sqrt{2!}} \left[\sqrt{p(2,0)}((\hat{a}^\dagger)^2 \otimes I) + \sqrt{p(0,2)}(I \otimes (\hat{b}^\dagger)^2) \right] \right) |0\rangle_a \otimes |0\rangle_b,$$

where $p(n,m)$ denotes the probability of having n and m photons in the mode of a and b, and is given by $p(n,m) = |(_a\langle n| \otimes _b\langle m|)(|\alpha\rangle_a \otimes |\beta\rangle_b)|^2 = \frac{e^{-(|\alpha|^2 + |\beta|^2)}}{n!m!}(|\alpha|^2)^n(|\beta|^2)^m$. Stemming from the low mean photon number assumption, we only include terms with two photons. Terms with a total of one or no photons are also left out as they cannot generate any coincidence counts.

For a time-bin qubit, the Fock-state is created in an equal superposition of two temporal

modes, i.e., *early* and *late* modes, in the spatial input mode i ($i = a, b$) of the beam-splitter, as

$$(\hat{i}^{\dagger})^n|0\rangle_i \rightarrow \left[\frac{1}{\sqrt{2}}\left(\hat{i}_e^{\dagger} \otimes I + e^{i\phi_i}I \otimes \hat{i}_l^{\dagger}\right)\right]^n |0\rangle_{ie} \otimes |0\rangle_{il}, \tag{9.14}$$

where ϕ_i is the relative phase between the two temporal modes and i^+ is the photon creation operator making up the time bin. Inserting this expression in place of the $\hat{a}$ and $\hat{b}$ operators in (9.13) we get the low order expression for the wavefunction $|\psi(\phi_a, \phi_b)\rangle_{ab}$ for two superposition time-bin qubits at the HOM-BS inputs:

$$(\hat{a}^{\dagger} \otimes \hat{b}^{\dagger})|00\rangle_{ab} \rightarrow \frac{1}{4}\left[2e^{\frac{i(\phi+\pi)}{2}} \cos\left(\frac{\phi}{2}\right)(\hat{c}_e^{\dagger}\hat{c}_l^{\dagger} + \hat{d}_e^{\dagger}\hat{d}_l^{\dagger}) + 2e^{\frac{i(\phi+\pi)}{2}} \sin\left(\frac{\phi}{2}\right)(\hat{c}_e^{\dagger}\hat{d}_l^{\dagger} - \hat{c}_l^{\dagger}\hat{d}_e^{\dagger})\right.$$

$$\tag{9.15}$$

$$\left. + i(\hat{c}_e^{\dagger})^2 + i(\hat{d}_e^{\dagger})^2 + ie^{i\phi}(\hat{c}_l^{\dagger})^2 + ie^{i\phi}(\hat{d}_l^{\dagger})^2\right]|0000\rangle_{ce,cl,de,dl}$$

$$((\hat{a}^{\dagger})^2 \otimes I)|00\rangle_{ab} \rightarrow \frac{1}{4\sqrt{2}}\left[+ 2(\hat{c}_e^{\dagger}\hat{c}_l^{\dagger} - \hat{d}_e^{\dagger}\hat{d}_l^{\dagger}) + 2i(\hat{c}_e^{\dagger}\hat{d}_l^{\dagger} + \hat{c}_l^{\dagger}\hat{d}_e^{\dagger}) + 2i(\hat{c}_e^{\dagger}\hat{d}_e^{\dagger} + \hat{c}_l^{\dagger}\hat{d}_l^{\dagger})\right. \tag{9.16}$$

$$\left. + (\hat{c}_e^{\dagger})^2 - (\hat{d}_e^{\dagger})^2 + (\hat{c}_l^{\dagger})^2 - (\hat{d}_l^{\dagger})^2\right]|0000\rangle_{ce,cl,de,dl}$$

We first look for coincidence detection events that correspond to projections onto the Bell-state $|\psi_-\rangle_{cd} = \frac{1}{\sqrt{2}}(\hat{c}_e^{\dagger}\hat{d}_l^{\dagger} - \hat{c}_l^{\dagger}\hat{d}_e^{\dagger})|0000\rangle_{ce,cl,de,dl}$. Combining (9.15) with (9.13) we are thus able to compute the probability $P_-(\phi) = |_{cd}\langle\psi_-|\psi(0, \phi)\rangle_{cd}|^2$ as

$$P_-(\phi) \propto \mu^2 e^{-2\mu}\left[1 + 2\sin^2\left(\frac{\phi}{2}\right)\right] \tag{9.17}$$

where μ is the mean photon number per qubit at the HOM-BS input.

When two input qubits are orthogonal ($\phi = \pi$) the coincidence detection probability $P_-^{\perp}$, reaches its maximum and when they are identical ($\phi = 0$) it reaches a minimum $P_-^{\|}$. From these it is natural to define a Bell state measurement HOM visiblity $V_{\text{BSM}} = (P_-^{\perp} - P_-^{\|})/P_-^{\perp}$ analogous to (9.1). According to (9.17) we find the maximum visibility for coherent state inputs $V_{\text{BSM}}^{\text{theo}} = 0.667$.

We are now in a position to analyze the experimental data, which is reproduced in Fig. 9.3d where we plot the measured coincidence rates, which are all proportional to the probabilities by a common factor and thus equally applicable for calculating V_{BSM}. We fit the experimental data to a sine function and obtain $V_{\text{BSM}}^{\text{exp}} = 0.629 \pm 0.0052$, which is slightly below the theoretical bound. This indicates that either the detection suffers from imperfections such as noise or the modes at the BS are not perfectly aligned, which in turn could be due imperfectly created qubit states or imperfect storage of one of the one qubits in the quantum memory. To be conservative we assume that the entire reduction of the measured V_{BSM} is due to the quantum memory.

9.1.7 References

1. Sangouard, N., Simon, C., de Riedmatten, H. & Gisin, N. Quantum repeaters based on atomic ensembles and linear optics. Rev. Mod. Phys. 83, 33–80 (2011).

2. Kimble, H. J. The quantum internet. Nature 453, 1023–1030 (2008).

3. Kok, P. et al. Linear optical quantum computing with photonic qubits. Rev. Mod. Phys. 79, 135–174 (2007).

4. Lvovsky, A. I., Sanders, B. C. & Tittel, W. Optical quantum memory. Nat Photon 3, 706–714 (2009)

5. Saglamyurek, E. et al. Broadband waveguide quantum memory for entangled photons. Nature 469, 512–515 (2011).

6. Clausen, C. et al. Quantum storage of photonic entanglement in a crystal. Nature 469, 508–511 (2011).

7. Saglamyurek, E. et al. Conditional detection of pure quantum states of light after storage in a Tm-doped waveguide. Phys. Rev. Lett. 108, 083602 (2012).

8. Zhang, H. et al. Preparation and storage of frequency-uncorrelated entangled photons from cavity-enhanced spontaneous parametric downconversion. Nat Photon 5, 628–632 (2011).

9. Specht, H. P. et al. A single-atom quantum memory. Nature 473, 190–193 (2011).

10. England, D. G. et al. High-fidelity polarization storage in a gigahertz bandwidth quantum memory. Journal of Physics B: Atomic, Molecular and Optical Physics 45, 124008 (2012).

11. Hong, C. K., Ou, Z.-Y. & Mandel, L. Measurement of subpicosecond time intervals between two photons by interference. Phys. Rev. Lett. 59, 2044–2046 (1987).

12. Kaltenbaek, R., Blauensteiner, B., Zukowski, M., Aspelmeyer, M. & Zeilinger, A. Experimental interference of independent photons. Phys. Rev. Lett. 96, 240502 (2006).

13. Beugnon, J. et al. Quantum interference between two single photons emitted by independently trapped atoms. Nature 440, 779–782 (2006).

14. Maunz, P. et al. Quantum interference of photon pairs from two remote trapped atomic ions. Nature Phys. 3, 538–541 (2007).

15. Sanaka, K., Pawlis, A., Ladd, T. D., Lischka, K. & Yamamoto, Y. Indistinguishable photons from independent semiconductor nanostructures. Phys. Rev. Lett. 103, 053601 (2009).

16. Patel, R. B. et al. Two-photon interference of the emission from electrically tunable remote quantum dots. Nat Photon 4, 632–635 (2010)

17. Flagg, E. B. et al. Interference of single photons from two separate semiconductor quantum dots. Phys. Rev. Lett. 104, 137401 (2010).

18. Lettow, R. et al. Quantum interference of tunably indistinguishable photons from remote organic molecules. Phys. Rev. Lett. 104, 123605 (2010).

19. Bernien, H. et al. Two-photon quantum interference from separate nitrogen vacancy centers in diamond (2011).

20. Sipahigil, A. et al. Quantum interference of single photons from remote nitrogenvacancy centers in diamond. Phys. Rev. Lett. 108, 143601 (2012).

21. Felinto, D. et al. Conditional control of the quantum states of remote atomic memories for quantum networking. Nat. Phys 2, 844–848 (2006).

22. Chaneli'ere, T. et al. Quantum interference of electromagnetic fields from remote quantum memories. Phys. Rev. Lett. 98, 113602 (2007).

23. Yuan, Z.-S. et al. Synchronized independent narrow-band single photons and efficient generation of photonic entanglement. Phys. Rev. Lett. 98, 180503 (2007).

24. Chen, Y.-A. et al. Memory-built-in quantum teleportation with photonic and atomic qubits. Nat. Phys 4, 103–107 (2008).

25. Yuan, Z.-S. et al. Experimental demonstration of a BDCZ quantum repeater node. Nature 454, 1098–1101 (2008).

26. Weinfurter, H. Experimental Bell-state analysis. Europhysics Letters 25, 559–564 (1994).

27. Mattle, K., Weinfurter, H., Kwiat, P. G. & Zeilinger, A. Dense coding in experimental quantum communication. Phys. Rev. Lett. 76, 4656–4659 (1996).

28. Sinclair, N. et al. Spectroscopic investigations of a Ti:Tm:LiNbO$_3$ waveguide for photon–echo quantum memory. Journal of Luminescence 130, 1586–1593 (2010).

29. Reibel, R. R., Barber, Z. W., Fischer, J. A., Tian, M. & Babbitt, W. R. Broadband demonstrations of true-time delay using linear sideband chirped programming and optical coherent transients. Journal of Luminescence 107, 103–113 (2004).

30. Afzelius, M., Simon, C., de Riedmatten, H. & Gisin, N. Multimode quantum memory based on atomic frequency combs. Phys. Rev. A 79, 052329 (2009).

31. Mandel, L. Photon interference and correlation effects produced by independent quantum sources. Phys. Rev. A 28, 929–943 (1983).

32. de Riedmatten, H., Afzelius, M., Staudt, M. U., Simon, C. & Gisin, N. A solid-state light-matter interface at the single-photon level. Nature 456, 773–777 (2008).

33. Staudt, M. U. et al. Interference of multimode photon echoes generated in spatially separated solid-state atomic ensembles. Phys. Rev. Lett. 99, 173602 (2007).

34. Tittel, W. & Weihs, G. Photonic entanglement for fundamental tests and quantum communication. Quant. Inf. Comp. 1, 3–56 (2001).

35. Afzelius, M. & Simon, C. Impedance-matched cavity quantum memory. Phys. Rev. A 82, 022310 (2010).

36. Sinclair, N. et al. Frequency multimode quantum memory featuring recall on demand. (In preparation.)

37. Afzelius, M. et al. Demonstration of atomic frequency comb memory for light with spin-wave storage. Phys. Rev. Lett. 104, 040503 (2010)

38. Yao, X.-C. et al. Observation of eight-photon entanglement. Nat Photon 6, 225–228 (2012).

39. Munro, W. J., Harrison, K. A., Stephens, A. M., Devitt, S. J. & Nemoto, K. From quantum multiplexing to high-performance quantum networking. Nat Photon 4, 792–796 (2010).

40. Chaneliére, T. et al. Storage and retrieval of single photons transmitted between remote quantum memories. Nature 438, 833–836 (2005).

41. Eisaman, M. D. et al. Electromagnetically induced transparency with tunable single-photon pulses. Nature 438, 837–841 (2005).

42. Rarity, J. G., Tapster, P. R. & Loudon, R. Non-classical interference between independent sources. Journal of Optics B: Quantum and Semiclassical Optics 7, S171 (2005).

43. Bouwmeester, D. et al. Experimental quantum teleportation. Nature 390, 575–579 (1997).

44. Halder, M. et al. Entangling independent photons by time measurement Nat. Phys., 3, 692–659 (2007)

Chapter 10

Frequency Multimode Quantum Memory Featuring On-demand Selective Recall

After having demonstrated that our AFC-based quantum memory allows for two-photon interference required for quantum repeaters, in this chapter I will show how it can be employed in a quantum repeater even without on-demand recall in the time domain. First, I will introduce the concept of quantum repeaters with frequency multimode AFC memories and then I will report our initial experimental demonstrations. My contributions to this study were at the following stages : Designing and setting up the experiment, performing the initial measurements and the interpretation of the main results.

10.1   Introduction

The realization of practical quantum repeaters requires quantum memories with sufficiently high multimode capacity and on-demand retrieval [4, 23]. As explained in Section 3.2.5, in the operation of a quantum repeater based on temporal multiplexing, a sequence of entangled photon pairs, each well-localized in time, is created to increase the entanglement swapping rate. In this scheme[1], illustrated in Fig. 10.1a, one member of each entangled photon pair is directed to the beam splitter that is situated halfway across the each elementary link to establish entanglement between neighboring nodes, while the other member of the pairs is stored in the quantum memories. Only photons that form pairs with those photons that successfully created entanglement across the elementary link are retrieved from the memories. They are then used to extend entanglement across neighboring elementary links

---

[1]For the details of a quantum repeater based on multiplexing, see Section 3.1 (quantum repeaters) and 3.2.5 (operation of a multimode quantum memory in a quantum repeater).
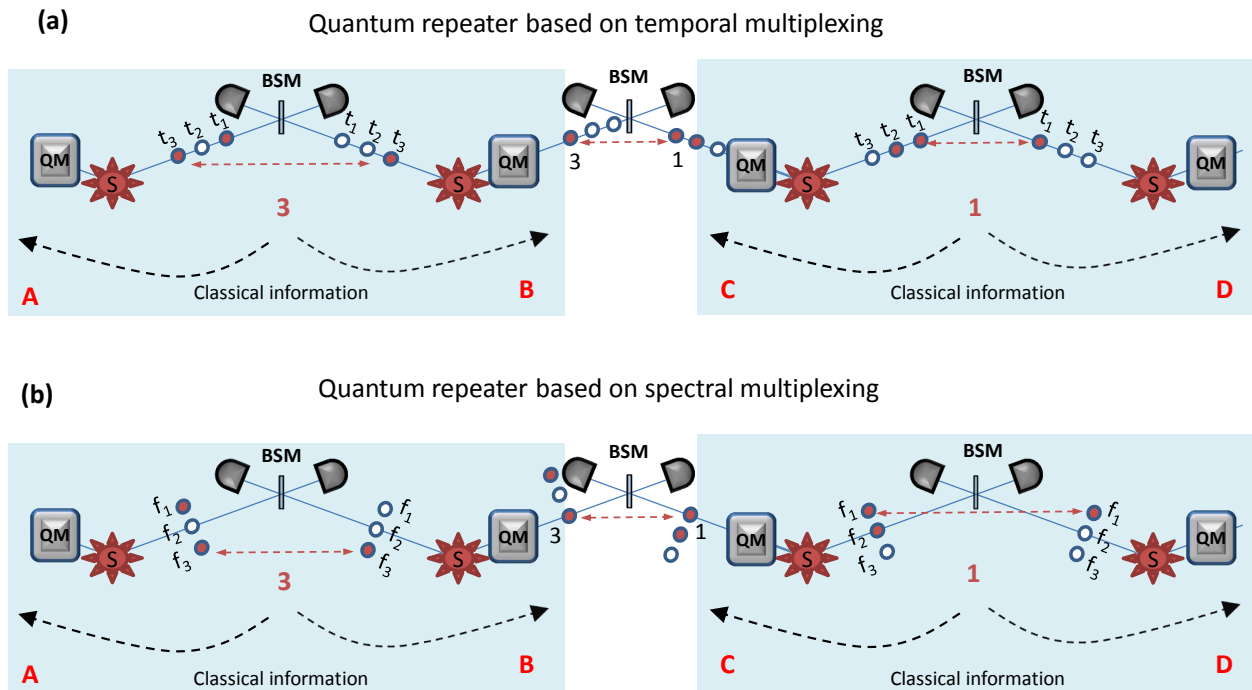
Figure 10.1: **Example of operational principle of quantum repeaters based on (a) temporal and (b) spectral multiplexing : (a)** In our example, the entire communication channel consists of two elementary links that extend from A to B and from C to D. In order to create entanglement across each elementary link, three attempts per clock cycle are made by generating entangled photon pairs at the same frequencies and at times t_1, t_2 and t_3. Entangled photons, generated at the time t_3 in link A-B and at t_1 in link C-D establish entanglement across the two links independently. This information is sent to the common node location B-C where quantum memories are placed. The quantum memories synchronize these photons by adjusting the storage time in such a way that the retrieved photons arrive on the central beam splitter at the same time. The Bell-State measurement then extends entanglement across the link A-D. **(b)** The communication channel is structured as in (a). Three attempts per communication time are made, but in this case, by simultaneously generating entangled photon pairs in frequency modes f_1, f_2 and f_3. The entangled photons, occupying the f_3 and f_1 modes, establish entanglement via independent Bell-state measurements across link A-B and link C-D, respectively. This information is sent to the common node location B-C where quantum memories are placed. In this case, there is no need to synchronize emission times from the quantum memories due to the synchronous nature of the quantum repeater architecture. Instead, it is necessary to selectively retrieve photons in particular frequency modes, and to equalize their frequencies, which can be done using filters and frequency shifters after the quantum memories.

via entanglement swapping with photons stored in the adjacent memory, which have been selected based on the same criterion. Note that the two photons did generally not arrive at the same time at their respective quantum memories. Thus the role of the quantum memories is to synchronize the arrival of the two recalled photons on the beam splitter that projects their joint state onto a Bell state by adjusting the storage time.

In Section 6.3, the large temporal multimode capacity of our AFC-based quantum memory was shown by the storage of 128 temporal modes. However, the missing feature for practical use in quantum repeaters is the on-demand retrieval of the stored modes. This is technically difficult to implement with AFC-based memories, for the reasons explained in Section 4.5. At this point, we take advantage of the high frequency multimode capacity of the AFC-based quantum memories to develop a novel approach for quantum repeaters without the requirement of on-demand retrieval in the time domain. In this approach, a set of simultaneously emitted entangled photon pairs, occupying different well-defined spectral modes, is created to increase the entanglement swapping probability. As before, one member per photon pair is directed to the beam splitter to establish entanglement between the nodes of each elementary link, while the other member is stored in a quantum memory, and eventually used to swap entanglement beyond the elementary link, as illustrated in Fig. 10.1b. However, unlike in the temporally multiplexed quantum repeater approach, synchronization of different temporal modes is not required due to the fact that all entangled photon-pair sources are operated in a synchronized manner. In this case, the necessary task is that of selecting the desired frequency modes and subsequently to shift the frequencies of the two recalled photons to be equal. These tasks can be carried out by employing frequency shifters and spectral filters at the output of frequency multimode memories. Consequently, this approach relaxes the requirement for on-demand retrieval in the time domain and benefits from the large frequency multimode capacity of the AFC memories.

Towards the implementation of this architecture, first we demonstrate the large frequency

multimode capacity of our broadband quantum memory by storing and retrieving several well-defined frequency modes. Furthermore, we simultaneously store multiple frequency modes in the memory and selectively retrieve a desired mode among these recalled ones. Finally, we demonstrate selective and high fidelity retrieval of time-bin qubits encoded into simultaneously stored photons in various frequency modes.
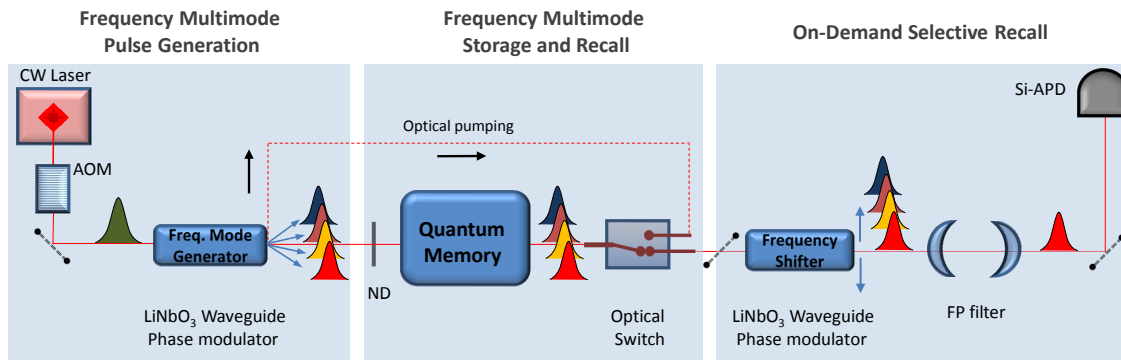
Figure 10.2: **Experimental setup for frequency multimode quantum memory:** The experimental setup consists of three main blocks: Frequency multimode pulse generation, a frequency multimode AFC memory, and on-demand selective recall. In the pulse generation block, CW laser light is sent to an AOM to generate pulses with nearly 12 ns duration at FWHM. Next, these pulses are directed to a phase modulator, either to shift the carrier frequency of the pulses by applying a serrodyne modulation signal, or to produce multiple frequency modes by applying an appropriate sinusoidal modulation. The generated pulses in single or multiple frequency modes are attenuated down to 10-50 photons on average by neutral density filters (ND) and passed to the AFC memory. The frequency multimode AFC memory in a Tm:LiNbO$_3$ waveguide is prepared using a Serrodyne technique. The optical pumping light is sent through the memory output in order to protect the single photon detector. After storage in the AFC memory, the retrieved pulses either are directed to the the selective recall block (shown in the figure) or directly sent to a Si-APD for detection. The frequency selective recall is achieved by using a phase modulator followed by a Fabry-Perot (FP) filter with 80 MHz linewidth and 23 GHz free-spectral range. The phase modulator allows for matching any desired frequency mode to the transmission window of the FP cavity by means of serrodyne chirping. In each experimental cycle, preparing AFC and waiting in order to avoid spontaneously emitted light last 3 ms and 2.2 ms, respectively. Following the wait time, the input pulses are sent to the memory at 2.7 MHz rate during 3 ms for storage and retrieval.

10.2 Frequency Multimode Storage in AFC

A quantum memory may have multimode storage capacity in time, space, frequency or in a combination of these depending on its properties. So far the temporal and spatial multimode capacity of quantum memories have been investigated and experimentally demonstrated in a few studies [85, 60, 61]. However, to our knowledge, there has not been any detailed research on developing frequency multimode quantum memories, which is partially due to the difficulty of achieving large bandwidths. In this respect, an AFC based quantum memory in a RE medium is naturally suitable for storing photons in multiple frequency modes, as will be demonstrated in the following.

The idea behind implementing a frequency multimode AFC memory is to sub-divide the total bandwidth of the AFC into many smaller bandwidth AFC segments such that each one defines a mode in the frequency domain. When an optical pulse, that contains multiple frequency modes compatible with the AFC segments is mapped to the memory, each mode can be simultaneously stored and retrieved after a pre-set time given by the peak spacing in the corresponding AFC segments.

To demonstrate this feature, we use the experimental setup depicted in Fig. 10.2. First, we prepare an AFC memory with 24 segments, each having 100 MHz bandwidth. We set different storage times for each AFC segment, as shown in Fig. 10.3, so that we can distinguish the retrieved frequency modes in the time domain. Next, for probing this AFC memory, we carve 12 ns long optical pulses using an AOM and shift the carrier frequency of the pulses to the desired frequency mode using a phase modulator driven by a serrodyne waveform. The pulses are attenuated down to the few photon level (containing on average 10-50 photons) using neutral density filters and then send to the prepared memory. In order to probe a particular AFC segment, we store pulses with a spectrum corresponding to a single segment, and detect the retrieved pulses using a Si-APD (In this measurement we bypass the FP filter and the output phase modulator). Fig. 10.4 shows the obtained detection
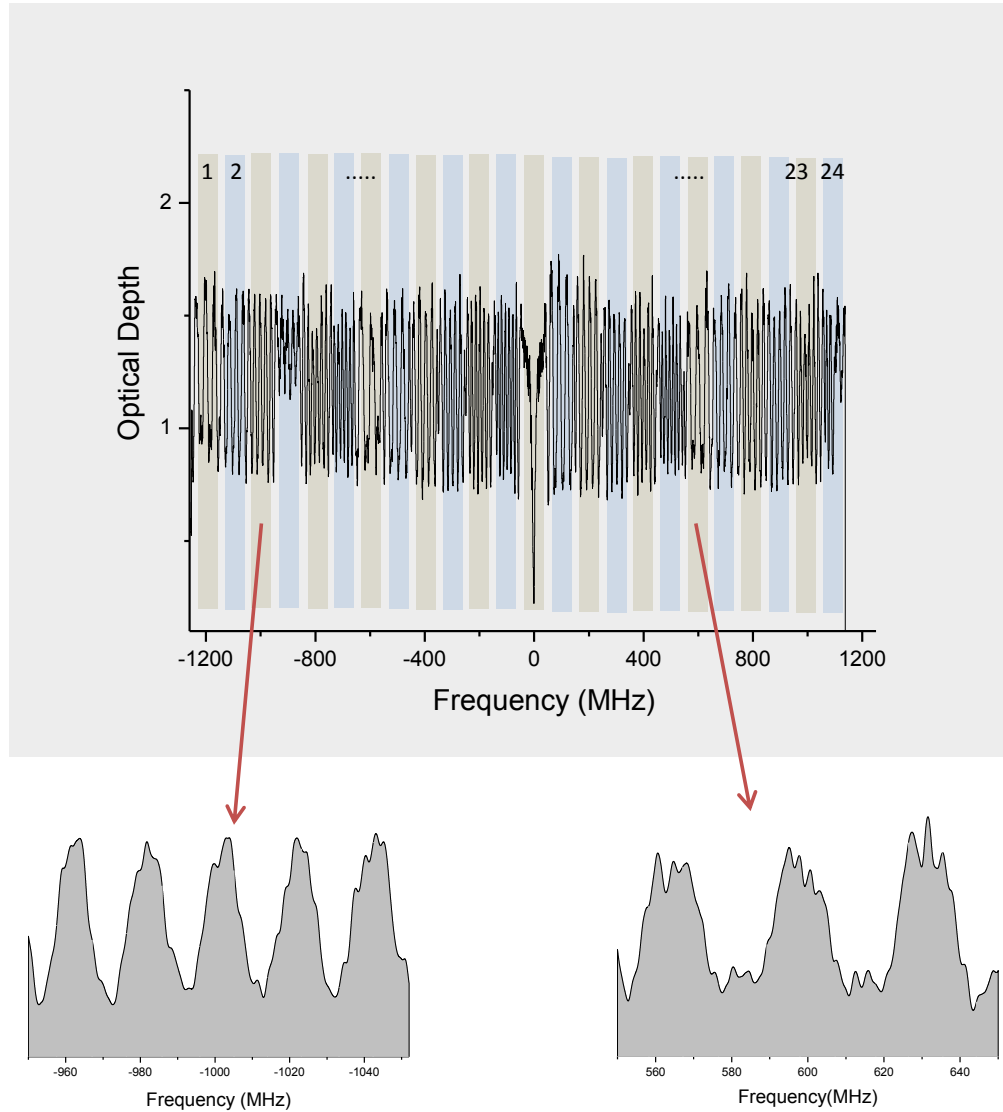
Figure 10.3: **Preparation of a frequency multimode quantum memory:** The total AFC bandwidth of 2.5 GHz was divided into 24 segments, each 100 MHz width. For each AFC segment, the peak spacing was set differently, leading to storage times between 25 ns and 75 ns. The applied magnetic field was adjusted such that the retrieval efficiency of all AFC segments was similar. The leaked light at zero detuning generated a large transmission window, which prevents us to set a comb at the center.
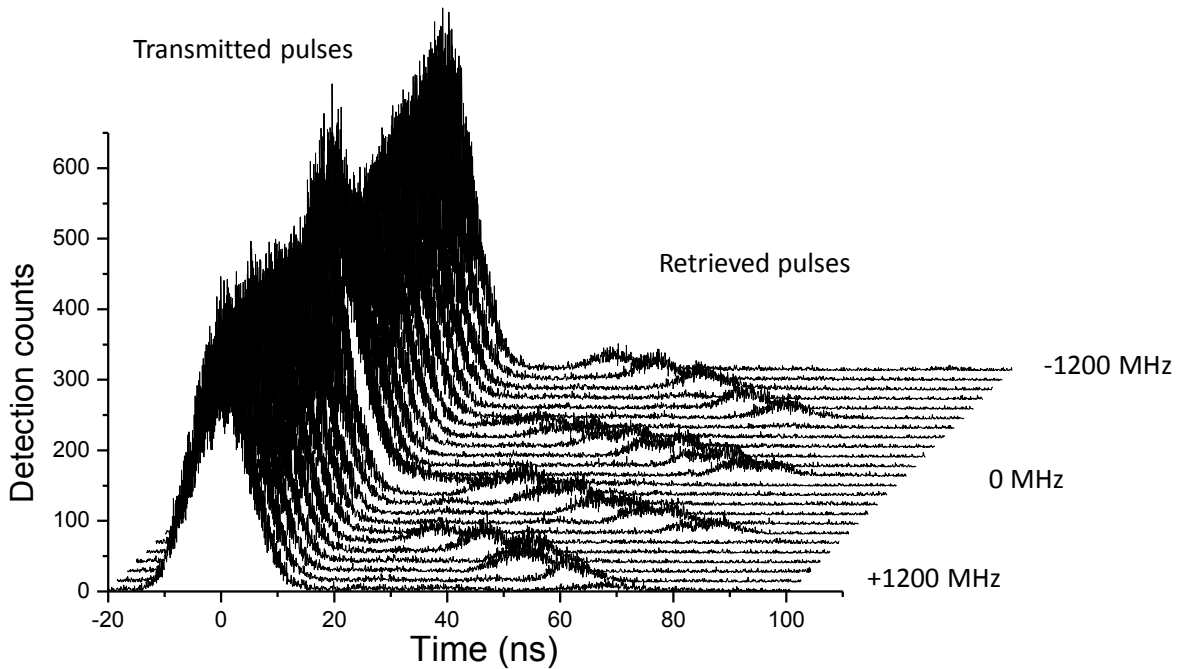
Figure 10.4: **Light storage in a frequency multimode AFC:** Each segment of the prepared AFC shown in Fig. 10.3 was individually probed by sending 12 ns long pulses. The pulses were retrieved at the storage times programmed into the different segments.

histograms for each AFC segment. As clearly seen, each frequency mode is retrieved with the corresponding programmed delay, which demonstrates the storage in the desired AFC segment.

Next, we simultaneously store multiple frequency modes that all occupy the same temporal mode. We generate five pulses by driving the input phase modulator with an appropriate sinusoidal waveform in a way that four strong frequency modes around the carrier frequency are generated. We send the pulses to an AFC prepared with four-segments, centered at each of the four generated frequency modes, each leading to different storage times, as shown in Fig. 10.5a. After storing the pulses in the memory, we detect four echoes at times given by the storage time of the corresponding AFC segment, as seen in Fig. 10.5b. The retrieval efficiency for each output mode is different due to the difference in the efficiency of each AFC
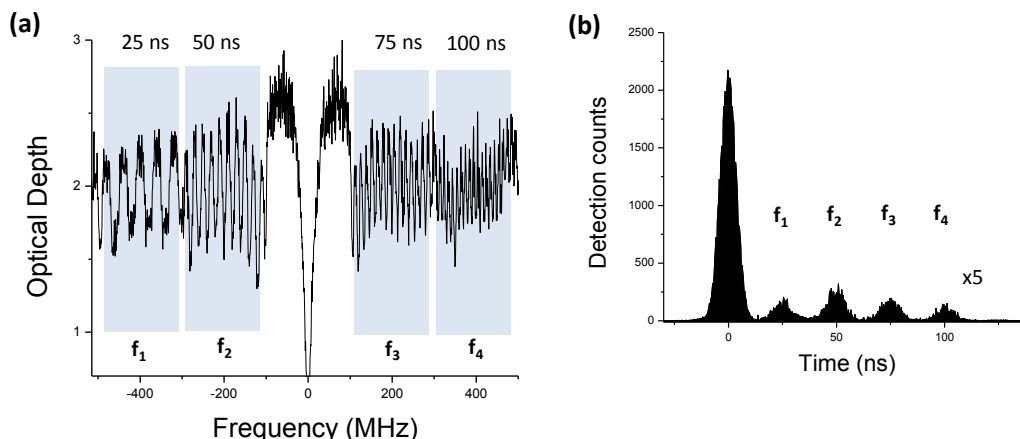
Figure 10.5: **Simultaneous storage of multiple frequency modes:** An AFC consisting of four-segments labeled f_1, f_2, f_3 and f_4 was prepared as shown in **(a)**. Each segment has a 200 MHz bandwidth and leads to 25 ns, 50 ns, 75 ns and 100 ns storage times, respectively. The strength of the applied magnetic field was optimized such that the retrieval efficiencies of all segment were almost equal. Four pulses at the four frequency modes compatible with the AFC segments were generated and simultaneously stored in the AFC. Each pulse was retrieved after the storage times programmed into the AFC segments as shown in **(b)**.

segment and in the power of the pulses. Considering the fact that we are able to generate up to 10 GHz bandwidth, it is possible to store around 100 frequency modes using our AFC memory.

10.3 On-demand Frequency Selective Retrieval

In this section, we turn our attention to the frequency selective recall process. We prepare an AFC with four segments with different storage times. Next, we generate four pulses in four well-defined frequency modes, matching the prepared AFC segments, as in Section 10.2. We map these pulses to the AFC memory from which they are retrieved after different pre-programmed storage times. As a reference, first we detect the recalled pulses while skipping the FP cavity and frequency shifter block. We thus observe the simultaneous storage of the four frequency modes, as shown in the far back trace of Fig. 10.6. Next, we want to
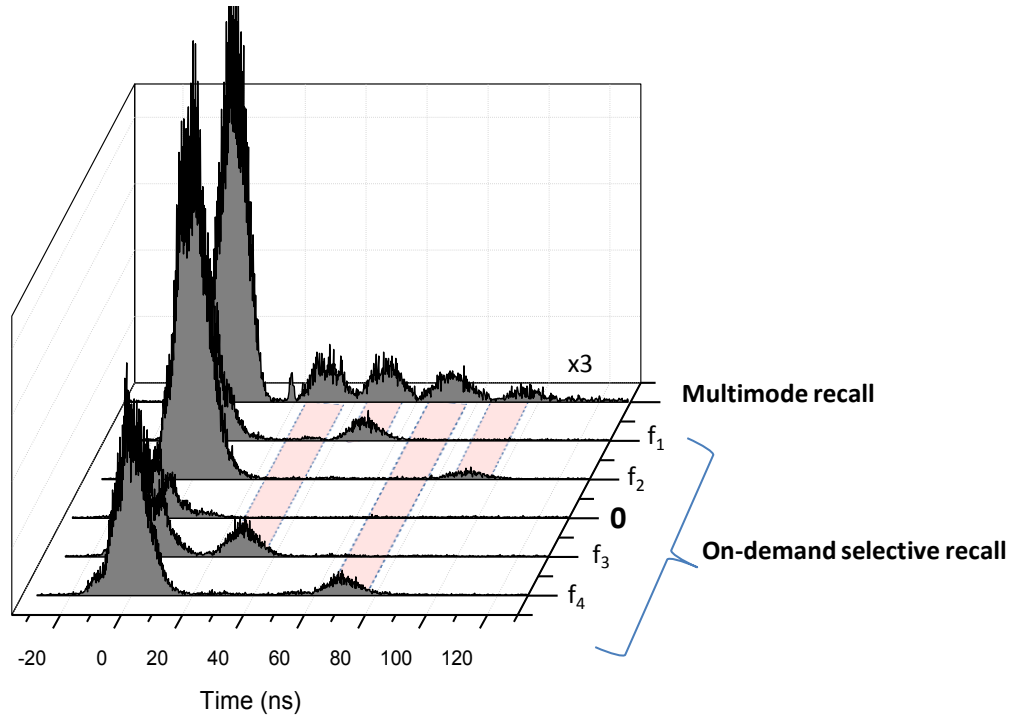
Figure 10.6: **Demonstration of on-demand selective retrieval from a multimode quantum memory:** An AFC consisting of four-segments, similar to the one shown in Fig. 10.5a was prepared. In this AFC, the storage time for each segment (f_1, f_2, f_3 and f_4) was set to 50 ns, 90 ns, 30 ns and 70 ns, respectively. Four pulses containing four well-defined spectral modes compatible with the AFC segments were simultaneously sent the prepared memory. All frequency modes were stored and retrieved at the different times programmed into the AFC. First, as a reference, all four pulses were detected after bypassing the selective recall block, as shown on the far back of the figure. Next, the retrieved modes were directed to the output phase modulator and FP filter with transmission window centered at zero MHz. By applying a frequency shift between -400 MHz and +400 MHz in increments of 200 MHz, each frequency mode was selectively recalled after the filter, as shown in the front figures. The applied magnetic field was optimized to maximize the echo efficiency for each recalled mode.

175

demonstrate that we can selectively recall any of the stored photons using the frequency shifter (a phase modulator) and the FP cavity, which is set to zero detuning with respect to the center of the AFC. This is done by applying an appropriate frequency shift to the retrieved modes so that only the desired frequency mode passes through the FP cavity and the rest is filtered out (reflected). After the FP filter, we detect the retrieved photons using the Si-APD. The front curves in Fig. 10.6 illustrate the obtained detection histograms for the selective recall of photons from each mode. As seen, selected modes are faithfully retrieved and the other modes are suppressed by more than 10 dB. The main reasons that we observe these spurious modes[2] are imperfections in the alignment of the FP cavity and in the settings of the modulation amplitude for the Serrodyne frequency shifting.

10.4   Storage of Time-Bin Qubits Encoded into Photons in Different Frequency Modes

After demonstrating the on-demand (selective) retrieval of pulses in different frequency modes, the final step will be probing the storage of qubits in the frequency multimode storage scheme. Unlike in the temporal multimode storage approach, the photons carrying the qubit states need to be in a set of well-defined frequency modes. On top of this, as described above, these frequency modes are translated to a certain fixed frequency for selective recall after storage in the quantum memory. We need to assess whether there is any degradation in the selectively retrieved quantum information at the end of the whole process. To do this, we prepare time-bin qubits in various spectral modes and analyze how faithfully they are retrieved after frequency shifting and filtering.

First, we generate photons in time-bin qubit states, early ($|e\rangle$) and late ($|l\rangle$), respectively

---

[2]Imperfections in the settings of the sawtooth waveform for the Serrodyne frequency shifting can cause the generation of harmonics higher than first order and/or oppositely signed harmonics. We refer to these modes as spurious modes. For example, in the experiment, to selectively retrieve the pulse at f_2=-200 MHz, a frequency shift of +200 MHz needs to be applied. Imperfections in the waveform setting can also result in the second order of f_1=-400 MHz mode. Therefore this mode (spurious) in addition to f_2=-200 MHz is shifted to zero MHz and transmitted through the cavity

f₁=200 MHz   f₂=400 MHz
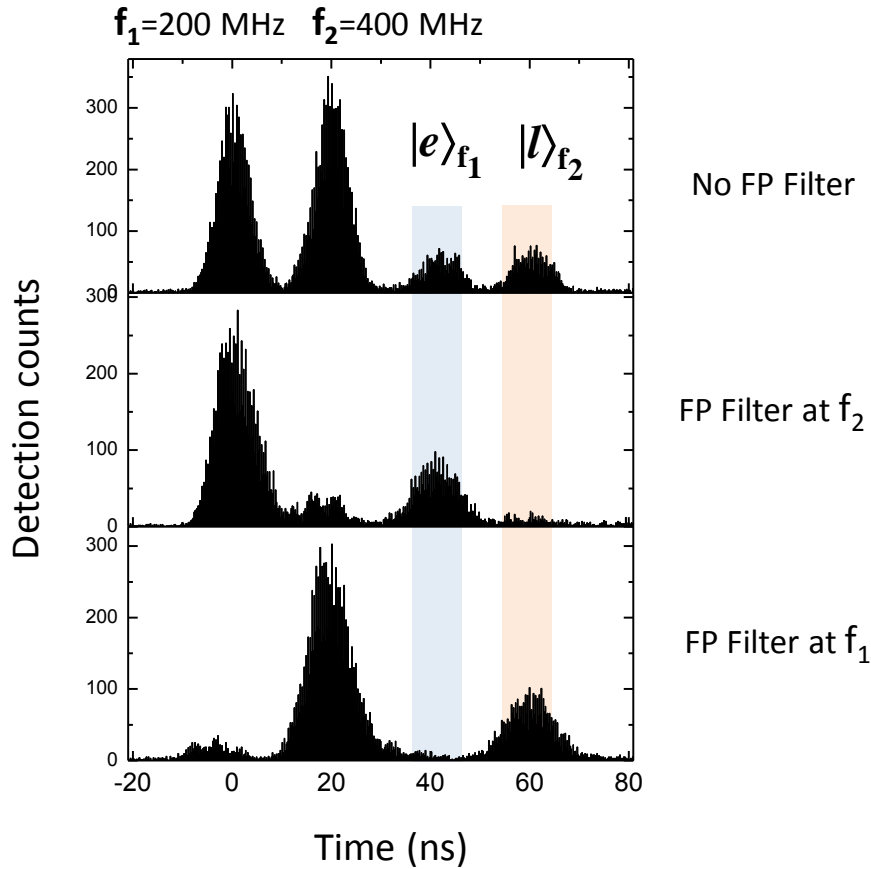
Figure 10.7: **Storage of $|e\rangle$ and $|l\rangle$ time-bin states occupying different frequency modes:** Pulses prepared in early and late temporal modes and centered at frequencies f_1 and f_2, respectively, were stored in a AFC memory prepared with two 200 MHz-wide segments centered at +200 MHz and +400 MHz. The pulses were retrieved after 40 ns and detected after bypassing the output phase modulator and FP filter for reference as shown in the top figure. Next, the retrieved pulses were directed the frequency shifter and the FP cavity for selective recall. The transmission window of the FP filter was centered at +400 MHz and a frequency shift of +200 MHz was applied to the pulses. This process allowed to recall only the $|e\rangle$ state as seen in the middle figure. Next, the transmission window of the FP filter was centered at +200 MHz and a frequency shift of -200 MHz was applied to the pulses, resulting in the selective recall of the $|l\rangle$ state as shown at the bottom figure.

and in different frequency modes. As a reference, these orthogonal states are simultaneously stored in an AFC memory, prepared with two-segments, and re-emitted after 40 ns as seen in the top trace of Fig 10.7. Next, we selectively retrieve one of the photons using the frequency shifter and the FP cavity. In the ideal case, when the $|e\rangle$ state is retrieved, no detection is expected to occur in the late temporal mode as the $|l\rangle$ state is encoded into the photon in the other frequency mode. Similarly upon retrieval of $|l\rangle$, there should be no detection in the early temporal mode. Based on this criterion, we can assess the fidelity of our scheme for storage of early and late qubit states, as described in Chapter 7. We calculate the fidelity for the ($|e\rangle$) state as $\mathcal{F}_e = C_{e|e}/(C_{e|e} + C_{l|e})$, where, e.g., $C_{l|e}$ denotes the number of detected counts in the late time-bin. If a photon in state $|e\rangle$ is recalled, we expect $C_{e|e}$ to be large and $C_{e|l}$ is zero. Any counts in $C_{e|l}$ are mainly due to detector dark counts (noise) and cross-talk between frequency modes. Similarly, we can find $\mathcal{F}_l$, enabling us to calculate the mean fidelity: $\mathcal{F}_{el} = (\mathcal{F}_e + \mathcal{F}_l)/2 = 0.895 \pm 0.02$, which beats the maximum recall fidelity allowed for classical memory of 0.67. The reduction of the fidelity compared to the results reported in Chapter 7 is due to imperfections in the Serrodyne frequency translation and filtering processes caused by cross-talk between the frequency modes. Nevertheless, it is possible to increase the fidelity to close to unity by careful optimization of these processes

The next step is to assess the fidelity for the storage and retrieval of a qubits in an equal superposition of early and late temporal modes and carried by the photons in particular frequency modes. The measurements presented here are only preliminary due to limitations of our current setup. More precisely, we can currently not prepare two orthogonal superpositions states in different frequency modes. Thus the assessment made here does not account for cross-talk between the frequency modes, which could cause a reduction of the fidelity. Following the approach taken in Chapter 7, we implement a double-AFC to store and analyze time-bin qubit states. Hence, we prepare qubits in a single frequency mode and store them a 1 GHz-wide AFC with 20 ns and 40 ns storage times. We vary the phase of the

projection measurement by shifting one of the comb's center peak in steps of 15 degrees. As demonstrated in Chapter 6 and 7, this results in the detection of photons in one out of three temporal modes. For each setting, we record the detections in the middle temporal mode after bypassing the cavity and FP filter. This yields a sinusoidal visibility curve, shown on the left hand side of Fig. 10.8. With visibility of $\mathcal{V} = 0.95 \pm 0.06$, this allows calculating the fidelity for superposition states $\mathcal{F}_\phi = (1 + \mathcal{V})/2 = 0.978 \pm 0.03$, leading to final fidelity $\overline{\mathcal{F}} \equiv (\mathcal{F}_{el} + 2\mathcal{F}_\phi)/3 = 0.95 \pm 0.05$, which exceeds again the limit allowed when using a classical memory. This confirms the faithful storage capability of our memory.

One crucial point, so far not considered in these measurements is that any translation in the frequency of photons, carrying the time-bin qubit states, changes the relative phase between the temporal modes of the qubit due to the intrinsic relation between the frequency (ω) and the phase of the light (ϕ) given by $\phi = \omega t$. Therefore preparing time-bin states in the different frequency modes and shifting these modes for the selective recall result in an unitary transformation of the originally encoded the state.

To assess this effect, we encode a certain time-bin qubit state, $\frac{1}{\sqrt{2}}(|e\rangle + |l\rangle)$, into the generated pulses using the AOM and then shift the frequency of these pulses into various frequency modes. The produced modes are individually stored in a 1 GHz-wide double AFC with a certain phase setting that allows a projection onto $\frac{1}{\sqrt{2}}(|e\rangle + |l\rangle)$. The retrieved photons are detected right after the memory and we record counts in the interfering (middle) temporal mode for each frequency shift setting. The plot, on the right hand side of Fig. 10.8, shows the results of these measurements. As seen, depending on the applied frequency shift, the originally prepared time bin qubit state unitarily transforms into a different state. Consequently, for high fidelity storage and retrieval, it is either necessary to account for this transformation or to transform the states back to the original ones. In our implementation, the latter can be accomplished by compensating the phase change using the phase modulator that facilitates frequency shifting. To demonstrate this possibility, we perform the same
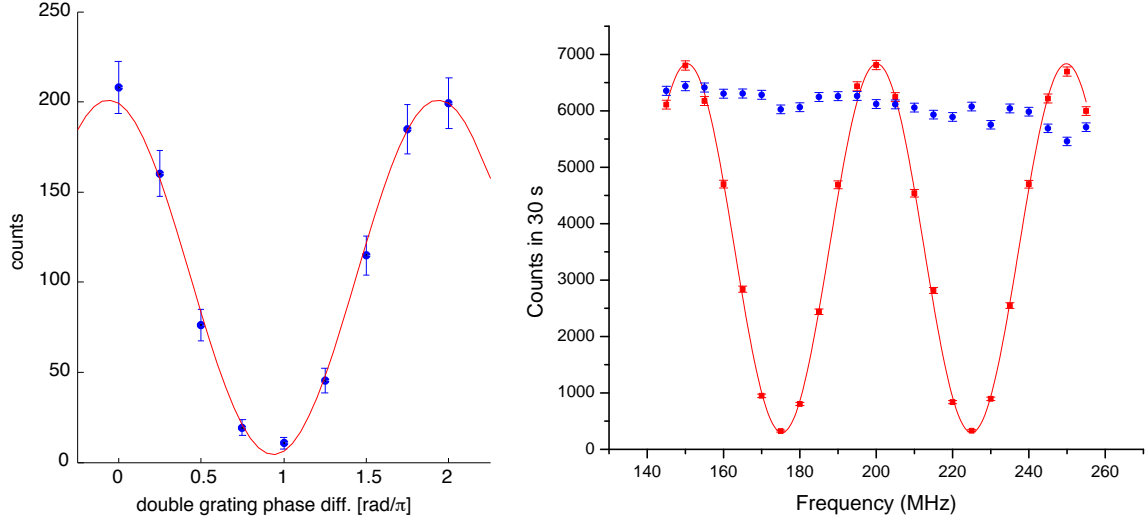
Figure 10.8: **Storage of superposition of time-bin states occupying single frequency mode and varying frequency modes in double-AFCs:** In the first experiment, a time bin qubit in $\frac{1}{\sqrt{2}}(|e\rangle + |l\rangle)$ was prepared using an AOM and its carrier frequency was shifted by 200 MHz by means of the input phase modulator. This state was stored in a 1 GHz-wide double AFC with 20 ns and 40 ns storage times, which allowed projection onto $\frac{1}{\sqrt{2}}(|e\rangle + e^{i\phi}|l\rangle)$, where ϕ is a phase setting determined by the frequency difference between the center peaks of the AFCs. The phase ϕ was changed by $\pi/6$ increments by shifting one of the AFC's center frequency. For each projection setting, the detections in the middle temporal were recorded during 30 s and the visibility curve shown on the left hand side of the figure was obtained. In the next experiment, a time-bin qubit state in $\frac{1}{\sqrt{2}}(|e\rangle + |l\rangle)$ was prepared using an AOM and its carrier frequency was shifted to the frequencies ranging from 146 MHz to 254 MHz in increments of 4 MHz by means of the input phase modulator. For each frequency shift, the time-bin qubit state was stored in the double AFC that allowed projection onto $\frac{1}{\sqrt{2}}(|e\rangle + |l\rangle)$. The detections in the middle temporal mode were recorded for each setting and the oscillating trace, shown in red on the right hand side plot, was obtained. Next, the same experiment was performed with compensation of the resulting transformations using the phase modulator. In this case, the flat trace, shown in blue, was obtained, which shows that encoded quantum states can be protected in the process of frequency translation.

experiment, but this time with appropriate phase compensation for each frequency shift. In this case, we obtain the flat trace shown in the figure, demonstrating that we can protect encoded quantum states in the process of frequency translation. In combination with the results of the previous measurements, these experiments demonstrate that our frequency multimode storage system featuring on-demand recall is expected to be capable of preserving quantum information with high fidelity.

To complete the picture, the final step will be simultaneously storing multiple qubits, each occupying different frequency modes and all in different time-bin qubit state, and faithfully retrieving the desired one. This work is in progress.

10.5 Conclusion

In this chapter, we demonstrated a frequency multimode quantum memory approach that features on-demand selective recall in the frequency domain. We also proposed a novel quantum repeater architecture, which is compatible with our storage system and relaxes the requirement of on-demand recall in the time domain. Hence If we can improve the storage time and the efficiency, our quantum memory approach would fulfill all requirements for frequency multiplexed quantum repeaters.

Chapter 11

Towards On-Chip Quantum Optical Processors

Faithful storage of quantum information encoded into photons has been the main purpose of the experiments presented in the previous chapters. In addition to storing, processing quantum information that requires coherent manipulation of photons is another important task for quantum communication and linear optics quantum computing. Towards this end, combining storage and manipulation in a light-matter interface is highly desirable. This task has received significant attention over the past decades, at least in what concerns standard photon-echo schemes and strong (classical) optical signals [80, 86, 87, 88, 89, 90, 91, 92, 93, 94]. However, at the single photon level, there have only been a few demonstrations and these are with limited capabilities. In this section, we show that our waveguide quantum memory can be turned into a processor for arbitrary temporal and spectral manipulation of quantum optical pulses. To this end, using weak coherent pulses at the few photon level together with light-matter interaction inspired by the AFC quantum state storage protocol, we experimentally demonstrate some basic pulse manipulation processes that are potentially useful for advanced quantum information processing.

My contributions to this study were the following: Designing and setting up the experiment, performing the measurements, analysis and interpretation of the results, writing the manuscript. Our findings will be submitted to a journal for publication. The following section is the current version of this manuscript, which has been re-formatted for consistency with the other chapters of this thesis.

11.1 Paper V

Towards On–Chip Quantum Optical Processor Using a Waveguide Quantum Memory

Erhan Saglamyurek[1], Neil Sinclair[1], Mathew George[2], Raimund Ricken[2], Daniel Oblak[1], Wolfgang Sohler[2], and Wolfgang Tittel[1]

[1]*Institute for Quantum Information Science, and Department of Physics and Astronomy, University of Calgary, 2500 University Drive NW, Calgary, Alberta T2N 1N4, Canada*
[2]*Department of Physics - Applied Physics, University of Paderborn, Warburger Str. 100, 33095 Paderborn, Germany*

Abstract

Faithful storage and coherent manipulation of quantum optical pulses are key for long distance quantum communications and quantum computing [6, 95, 4]. Combining these functions in a light-matter interface that can be integrated on-chip with other photonic quantum technologies, e.g. sources of entangled photons, is an important step towards these applications [95, 96, 97, 98]. To date there have only been a few demonstrations of coherent pulse manipulation compatible with quantum states, and that only in atomic gas media and with limited capabilities [99, 49, 100, 101, 102]. Here we describe how a broadband waveguide quantum memory based on the atomic frequency comb protocol [103, 58, 104] can be used as a programmable processor for essentially arbitrary spectral and temporal manipulations of individual quantum optical pulses. Using weak coherent optical pulses at the few photon level, we experimentally demonstrate re-sequencing, frequency-to-time multiplexing and demultiplexing, carving, splitting, compressing and stretching as well as on-demand delaying. Our integrated light-matter interface offers high-rate, robust and reconfigurable manipulations of optical pulses at the single photon level and brings fully practical optical quantum devices one step closer to reality.
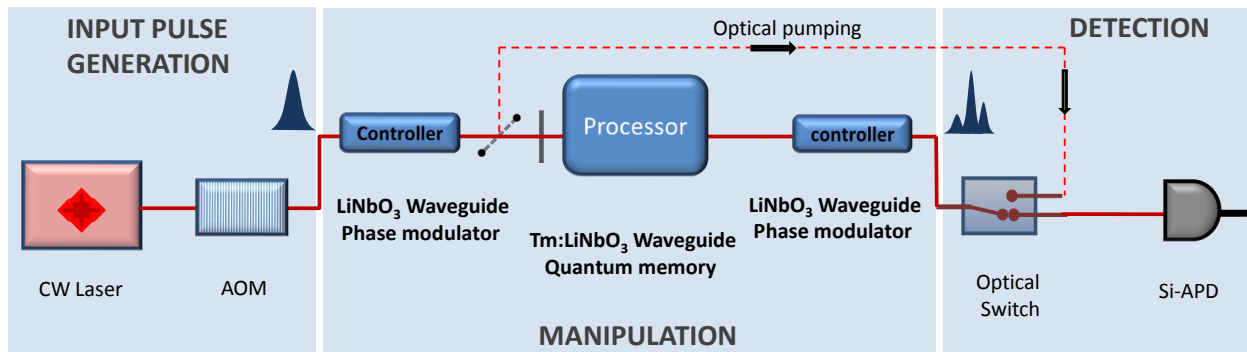
Figure 11.1: **Simplified diagram of experimental setup for optical pulse manipulation based on AFC processor.**

11.1.1 Introduction

Since the invention of the laser a lot of effort has been put into manipulating optical pulses for key applications in engineering and science. One recent example is photon-based quantum information processing, which promises unprecedented computational power [95] and unbreakable secret key distribution [4, 6]. The realization of these technologies requires coherently storing as well as manipulating quantum optical pulses in order to process and distribute quantum information. So far, efforts towards performing these tasks have yielded two separate developments: On the one side, optical quantum memories for the storage of quantum information, on the other side, photonic quantum devices for the manipulation of quantum information. Towards this end, combining storage and manipulation in a light-matter interface that can be integrated on-chip with other photonic quantum devices is an important step for future quantum technologies. To date there have only been a few demonstrations that employ a quantum storage device for coherent optical pulse manipulations [99, 49, 100, 101, 102]. However, these implementations are in gaseous atomic ensembles, show limited processing capabilities, and feature small bandwidth and small multimode capacities. In this study, we propose and demonstrate a universal approach for temporal and spectral manipulation of individual quantum optical pulses, which relies on the inte-

gration of our broadband waveguide quantum memories with waveguide photonic devices. Our implementation consists of two main components: a Tm:LiNbO$_3$ waveguide memory and two LiNbO$_3$ waveguide phase modulators placed before and after the memory. The idea behind this implementation is to use the large bandwidth capacity of the Tm:LiNbO$_3$ waveguide quantum memory in conjunction with the large frequency shift capacity of the LiNbO$_3$ waveguide phase modulators. The broadband nature of our memory device allows us to divide the entire bandwidth into several smaller-bandwidth AFC segments prepared for certain processing task, such as delaying by different amounts, splitting or compressing/decompressing of input pulses. The phase modulators are used to map the incoming pulses onto the relevant segments in the memory for desired manipulation, and to modify the frequency distribution of the retrieved pulses. This is accomplished with the serrodyne frequency translation technique [81]. In the following we demonstrate some of the basic temporal and spectral manipulations of weak laser pulses at the few photon level.

11.1.2 Experiment

Our experimental setup, depicted in Fig 11.1, consists of three main blocks: pulse generation, pulse manipulation, and detection. The pulse generation block features a continuous wave (CW) laser centered at 795.5 nm wavelength and an acousto-optic modulator (AOM) that is used to carve 12 ns-duration pulses from the CW laser light. These pulses are heavily attenuated down to $5 - 40$ photons on average. The pulse manipulation block is composed of a Tm:LiNbO$_3$ waveguide memory maintained at 3.5 K, and two commercial LiNbO$_3$ waveguide phase modulators at the input and output of the memory. We note that it is possible to combine these three elements on a single integrated photonic circuit that allowing a more compact setup. The detection block contains a Si-APD single photon detector, an optical switch used to protect the detector from optical pump light while preparing the AFC, and, a monolithic Fabry-Perot (FP) filter (not shown in the figure) used to demonstrate the ability to control the spectra of the retrieved pulses from the memory unit (this is
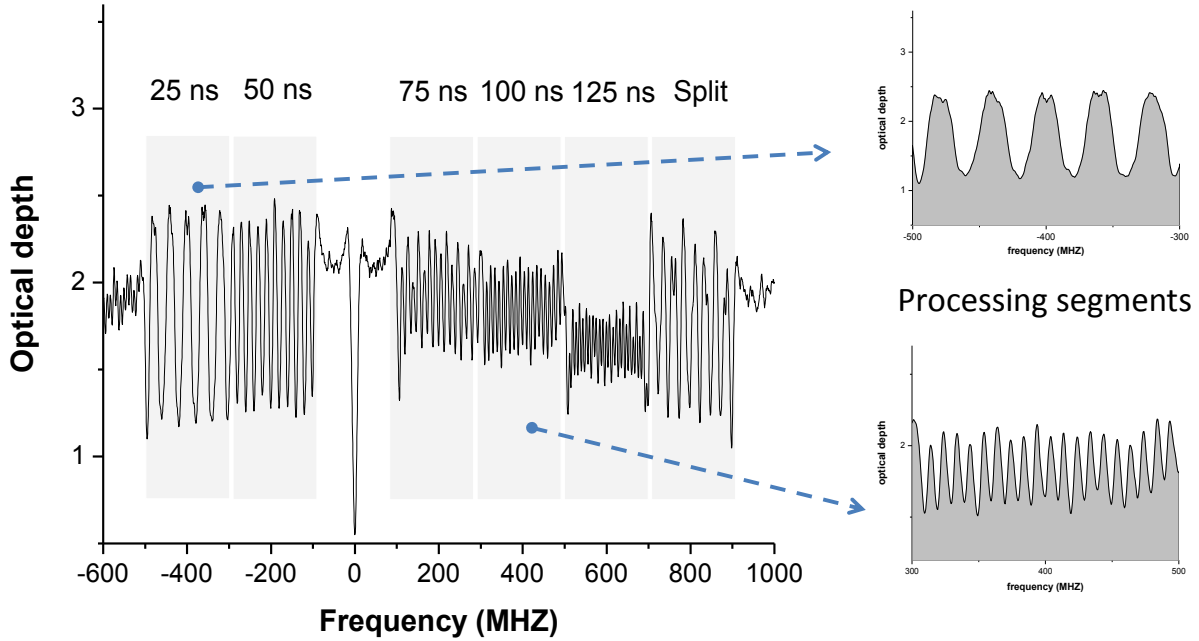
Figure 11.2: **An example of a programmed AFC memory.**

further explained in the Supplementary Information). Each experimental cycle has three stages: AFC programming, waiting in order to avoid noise from decaying excited atoms, and manipulating and detecting photons. The durations of these stages were 3 ms, 2.2 ms and 5 ms, respectively. Programming the AFC memory unit is achieved by frequency selective optical pumping, for which we control the frequency of the CW laser light using the phase modulator placed before the memory (see the Supplementary Information).

In a standard AFC memory, the inhomogeneously broadened absorption profile is tailored into a series of equally spaced absorption peaks. After mapping the photons onto this spectral feature, due to the periodicity, the atoms come to complete rephasing at $t_{storage} = 1/\Delta$, where Δ is the spacing between the peaks, resulting in re-emission of the input photons. The retrieval process can be achieved with unit efficiency provided that certain phase matching conditions are satisfied and AFC parameters such as finesse, effective optical depth are optimum [40].

Figure 11.3: **Demonstration of pulse re-sequencing:** An input pulse sequence consisting of three 25 ns separated pulses is generated using the AOM. The pulses are prepared wit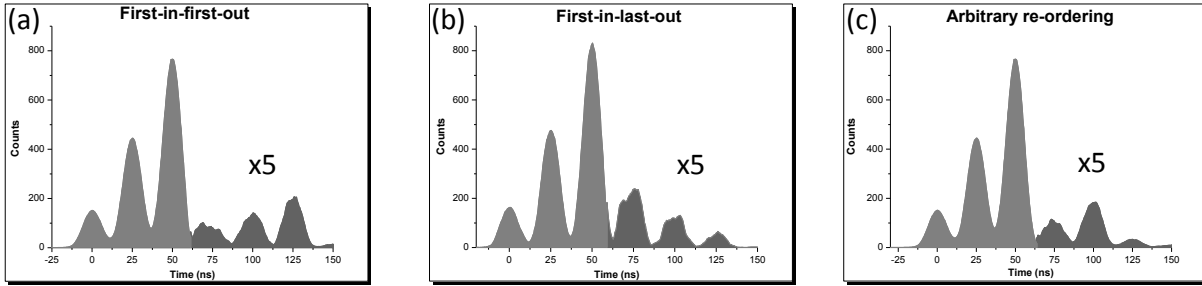h 12 ns duration, the same carrier frequency but different amplitudes. **(a)** Each input pulse is mapped onto the same AFC segment with +200 MHz detuning using the input phase modulator. They are stored with 75 ns duration and come out in the same order (First-in-first-out, FIFO). **(b)** The first, second and last pulses are mapped onto the AFC segments that yield 125 ns, 75 ns and 25 ns storage time, respectively. This results in a reversed order of the input sequence (First-in-last-out, FILO). **(c)** Similarly, by applying appropriate frequency shifts to each pulse, any time ordering can be obtained.

When the AFC is used for processing tasks, the peak spacing in different frequency intervals is typically set to different values resulting in storage times that vary as a function of frequency. An example of a programmed AFC memory is shown in Fig 11.2. In this example, the entire bandwidth is divided into six AFC segments with 200 MHz bandwidth. In each AFC segment, the peak separations are set by different amounts, allowing storage times from 25 ns to 125 ns with 25 ns increments. The last segment, prepared by superimposing two AFCs, is used to split a pulse into two temporal modes stored for 40 ns and 65 ns, respectively. Using this single re-configurable AFC processor, multiple processing tasks can be performed, as discussed in the following.

Pulse Re-sequencing

The first example is the re-ordering of pulses in a pulse sequence, which plays an important role in synchronizing and randomly accessing quantum information in quantum repeaters and optical quantum computers [99]. In the standard AFC storage scheme, one is restricted to simultaneously store pulses without changing their order, as shown in Fig. 11.3a. Now

187

we would like to re-order the pulses in this sequence. To accomplish this task, the phase modulator at the input of the memory applies appropriate frequency shift to each pulse in such a way that each pulse is mapped onto a different AFC segment, resulting in a reversed or arbitrary retrieved pulse sequences, as demonstrated in Fig. 11.3b and c, respectively. Moreover, the center frequency of each pulse retrieved from the memory unit can be set back to its original value through the output phase modulator, resulting in a manipulation only in time domain (see the Supplementary Information).
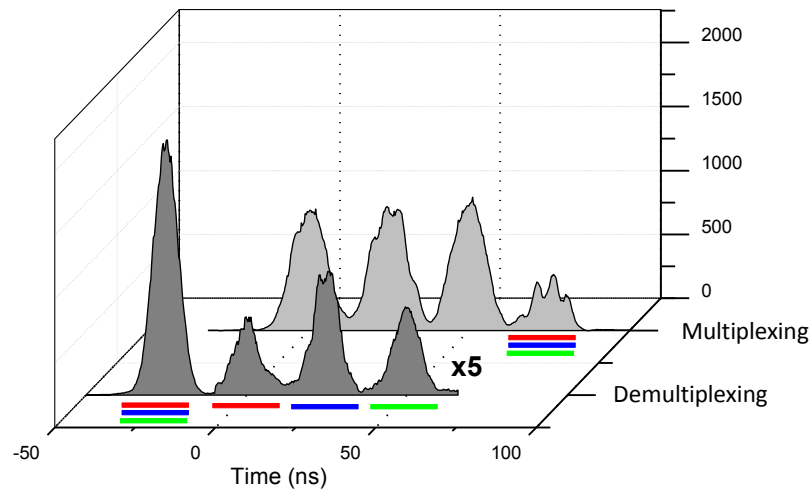
Figure 11.4: **Demonstration of frequency-to-time multiplexing and demultiplexing:** A pulse in three distinct frequency modes with -400 MHz, -200 MHz and +200 MHz detunings is generated using the input phase modulator driven by a sinusoidal waveform. This multimode pulse is sent to the programmed AFC (Fig. 11.2) and each frequency mode is mapped onto the corresponding AFC segment. This results in retrieving each pulse at a different time, as determined by the respective pre-programmed AFC segment. This is illustrated in the front curve (Demultiplexing). Next, three 25 ns-separated input pulses are prepared and their center frequencies are mapped to the AFC segments with +200 MHz, -200 MHz and -400 MHz detuning, respectively, using the input phase modulator. Having these pulses processed through the corresponding AFC segments allow them to be merged in the same temporal mode, as shown in the back curve (Multiplexing).

Frequency-to-time Multiplexing and Demultiplexing

The next example is to frequency-to-time multiplex and demultiplex pulses, which is an essential process for multiplexed quantum networks. When several frequency modes that

188

occupy the same temporal mode are mapped onto the programmed AFC, they are retrieved at different times (demultiplexing) as shown in the front of Fig. 11.4. Reversibly, pulses in different temporal modes can be merged in the same temporal mode (multiplexing) by applying the appropriate frequency shift to each input mode as demonstrated in the back of Fig. 11.4.
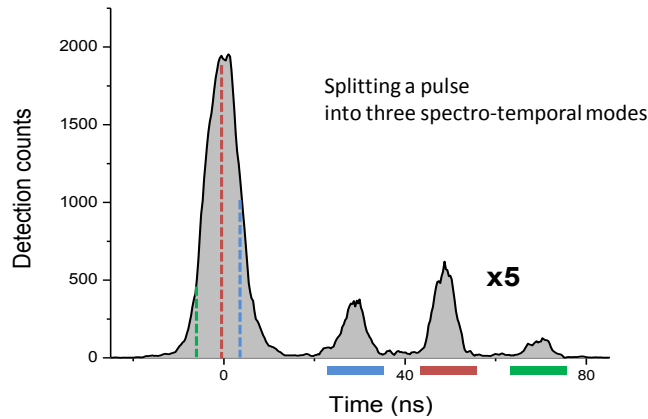
Figure 11.5: **Pulse splitting:** Three separate temporal portions of an input pulse, centered on the red, blue and green dashed lines, are mapped to three segments of the programmed AFC, leading to 75 ns, 50 ns and 25 ns storage times, respectively. After processing in the AFC, three spectro-temporal modes emerge from the memory as shown in the figure.

Pulse Splitting

Splitting a pulse into separate pulses in various spectral and temporal modes is another possibility, which could be used for generating high-dimensional quantum states. To demonstrate this feature, the input phase modulator maps three selected temporal portions of an input pulse onto different AFC segments such that each portion of the original pulse is retrieved in one of three well defined spectro-temporal mode as shown in Fig. 11.5. We note that it is also possible to recover the input pulse by re-processing each generated component in a subsequent system.
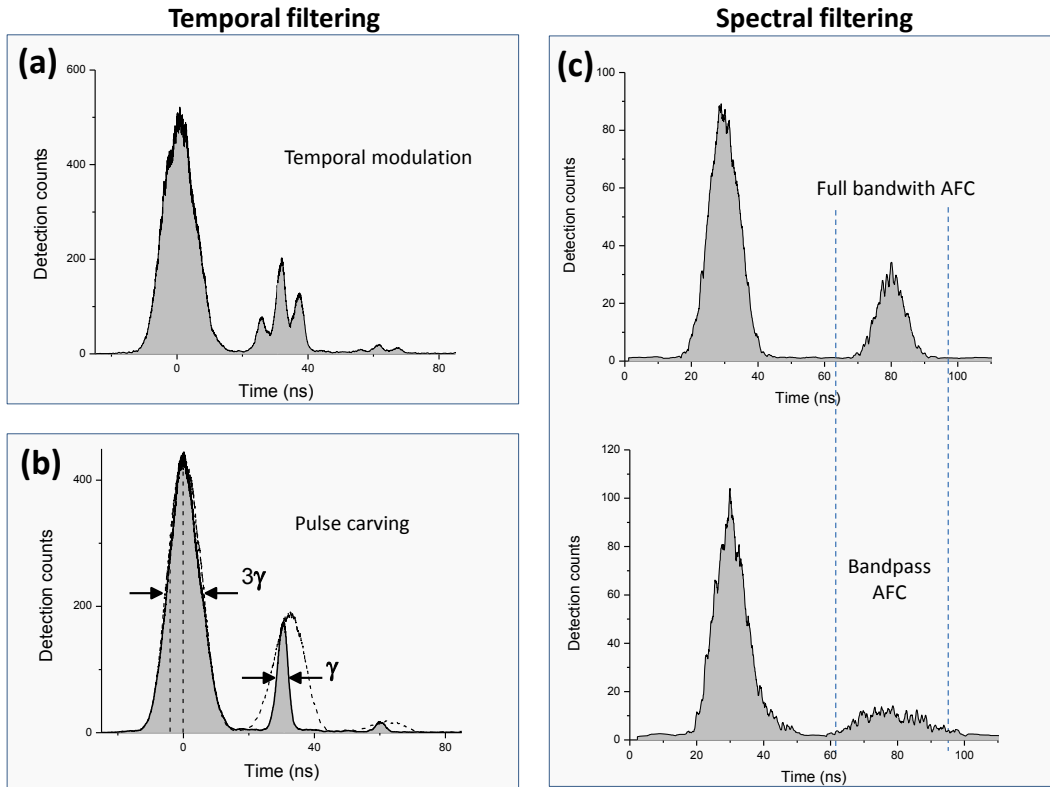
Figure 11.6: **Arbitrary temporal and spectral filtering:** **(a)** The input phase modulator maps three selected 3 ns-long temporal portions of a 12 ns long input pulse onto an AFC segment prepared with 600 MHz bandwidth and 33 MHz peak spacing. This allows generating arbitrary temporally modulated pulse as seen in the figure. **(b)** The input phase modulator maps a narrow temporal portion of an input pulse onto an AFC segment prepared with 600 MHz. This results in an echo almost three times shorter than the input pulse. The echo pulse, shown with the dashed line is obtained in the case in which the entire pulse is mapped to the same AFC. **(c)** An input pulse with nearly 70 MHz bandwidth is mapped onto an AFC segment prepared with 600 MHz bandwith and retrieved after 50 ns as shown in the top figure. An input pulss with the same bandwidth is mapped to an AFC with a bandwidth decreased to about 40 MHz. In this case the AFC acts as bandpass filter yielding an output pulse with increased duration.

Arbitrary Temporal and Spectral Filtering

Our integrated system can also be used as a reconfigurable temporal and spectral filter, which could be a tool for tailoring broadband single photons or to match the spectral and temporal properties of photons produced from independent sources. To demonstrate the

temporal shaping capability, the bandwith of an AFC segment is increased from 200 MHz to 600 MHz, and the input phase modulator maps three selected 3 ns long temporal portions of an incoming pulse onto the same frequency interval in this AFC segment. As shown in Fig. 11.6a, this allows arbitrarily modulating the temporal shape of a pulse while keeping the effective bandwidth the same. In addition, we can carve a narrow selected temporal portion from an input pulse which allows for generating a short pulse from a long one, as demonstrated in Fig. 11.6b.

To demonstrate the spectral filtering capability, the bandwidth of the AFC segment is decreased to about 40 MHz. An input pulse with nearly 70 MHz bandwidth is mapped onto this AFC. The excessive spectral portion is filtered out and the pulse is retrieved with longer duration (smaller bandwith) as seen in 11.6c.
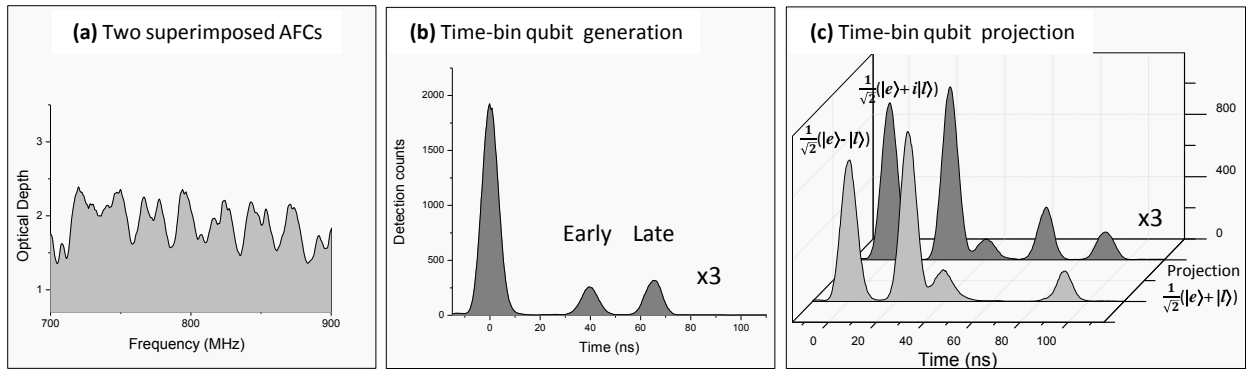
Figure 11.7: **Generating and Manipulating Time-bin Quantum States: (a)** The last segment of the programmed AFC with +800 MHz detuning (Fig. 11.2) is prepared by superimposing two AFCs (double AFC) with different comb spacings, leading to 40 ns and 65 ns storage times, as detailed in the figure. The strength of the applied magnetic field is carefully adjusted so that each comb has nearly the same retrieval efficiency. **(b)** Input photon, occupying a well-defined temporal mode is mapped to the double AFC. It is re-emitted in a superposition of two temporal modes.**(c)** Storing a superposition time-bin qubit state with temporal modes separated by the difference between the re-emission times of the AFCs leads to an overlap in the middle time slot after recall. This allows for performing any projection measurements onto time-bin qubit states, as represented in (c). In the measurements, input states, $|\psi\rangle = \frac{1}{\sqrt{2}}\left(|e\rangle - |l\rangle\right)$ (front curve) and $|\psi\rangle = \frac{1}{\sqrt{2}}\left(|e\rangle + i\,|l\rangle\right)$ are stored in a double AFC that allows projection onto $|\psi\rangle = \frac{1}{\sqrt{2}}\left(|e\rangle + |l\rangle\right)$. This result in complete destructive and a constructive interference in the middle temporal mode, respectively.

Manipulating Time-bin Qubit States

Generating and manipulating time-bin qubits can be easily accomplished using our integrated processing unit. In the programmed AFC shown in Fig. 11.2, the last segment is prepared by superimposing two AFCs with different comb spacings (see Fig. 11.7a). When a single photon pulse is mapped onto this AFC segment, it is re-emitted in a superposition of two temporal modes with a relative phase given by the difference between the corresponding combs' center frequencies. Thus this scheme can be used to generate any time-bin qubit state as represented in Fig. 11.7b. In addition, adjusting the difference between the emission times to the temporal separation of the two input modes leads the latter to overlap in the central time slot as shown in Fig. 11.7c. In this way, it is possible to project a time-bin qubit onto any arbitrary state, as shown in [104]. Furthermore our system is capable to convert a time-bin qubit to a frequency-bin qubit and to manipulate frequency-bin qubits, which could be useful for quantum communication protocols.

Pulse Compressing and Stretching

Compressing and stretching quantum optical pulses are other potential applications that could be used to increase quantum data rates and match bandwidths of input photons to quantum memories [102, 105]. An AFC memory is particularly well suited for this task, since it can be tailored in such a way that different frequency components can be rephased at different times instead of at one fixed time. Towards this end, we program a 500 MHz-wide AFC, whose peak separation is linearly decreasing from 30 MHz to 10 MHz across the entire bandwidth (Fig. 11.8a). In fact, this frequency segment could allow one to perform previously shown pulse manipulations in continuous time provided that the input pulse spectra are much smaller than the entire bandwidth. To compress an input pulse, the input phase modulator chirps the frequency of the incoming pulse linearly from high (200 MHz) end to low frequency (-200 MHz). When this pulse is absorbed in the memory unit, the frequency components from the pulse front rephase later than the components from the
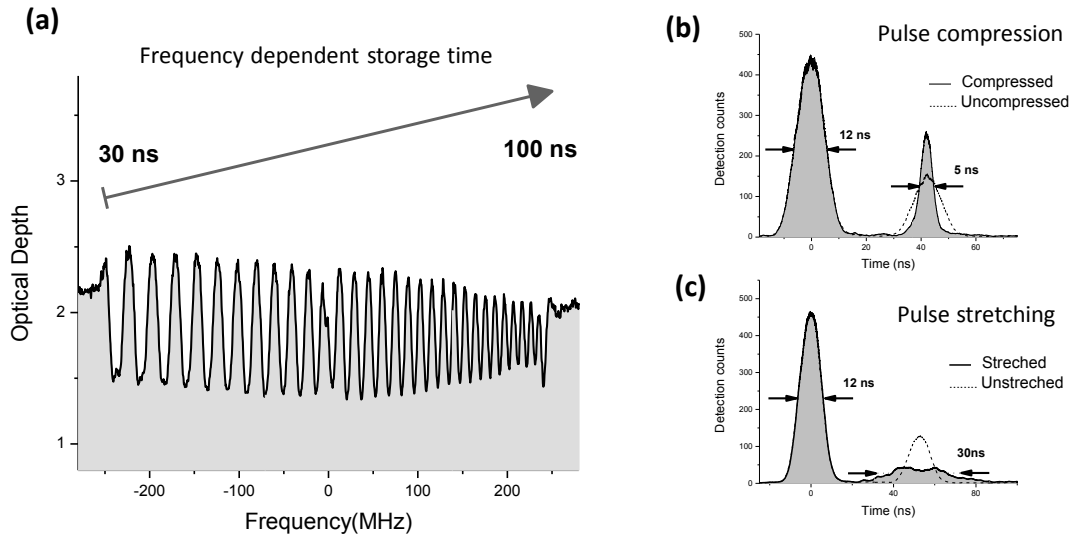
192

Figure 11.8: **Demonstration of Compressing and Stretching of pulses using an AFC with variable peak spacing: (a)** a 500 MHz-wide AFC with linearly decreasing peak spacing from 30 MHz to 10 MHz is programmed. **(b)** The frequency of an incoming pulse is linearly chirped from high (200 MHz) to low frequency (-200 MHz) using the input phase modulator. This pulse is mapped onto the programmed AFC. This results in the emission of a compressed pulse with a compression factor of nearly 2.4. The dotted plot shows the emitted echo after storage in a standard AFC. A clear difference can be seen between the peak level of the standard and compressed echo. **(c)**. Pulse stretching can be done in a similar way by having the frequency chirp for the input pulse from low to high frequency.

pulse end, allowing retrieval of a temporally compressed pulse as shown in Fig. 11.8b. Pulse stretching can be done in a similar way by having the frequency chirp from low to high as illustrated in Fig. 11.8c. We note that the compression and decompression are different from the previously described filtering process as, in principle, no loss is introduced to the input pulses.

Higher compression (decompression) factors can be easily obtained by extending the AFC bandwidth and/or increasing the duration of pulses as demonstrated in Fig 11.9. Considering the achievable bandwidths, up to 10 GHz in our current implementation, compression factors exceeding 100 are possible for the tens of nanosecond long pulses
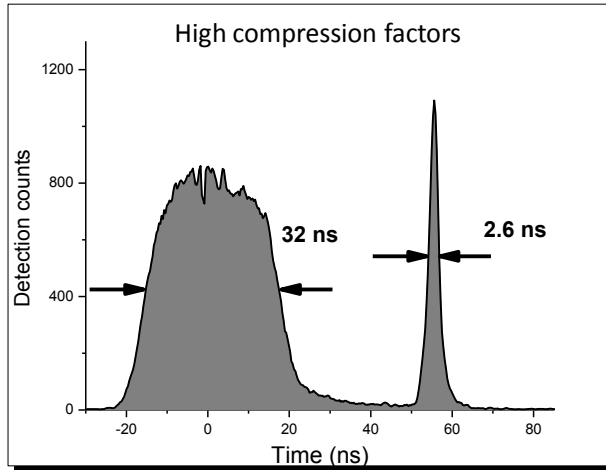
Figure 11.9: **Achieving high compression factors:** A 2 GHz-wide AFC with linearly decreasing peak spacing from 30 MHz to 10 MHz is programmed. The frequency of a 32 ns long pulse is chirped from 2 GHz to 0 GHz and mapped onto the programmed AFC. This results in a 2.6 ns long echo and a compression factor of 12.

On-demand Delaying

Having AFC segments with different peak spacing also allows one to select storage time on-demand without the (time intensive) need for the generation of different AFCs. In our new approach, the input phase modulator maps a pulse to a particular AFC segment for desired delay by serrodyne frequency translation as demonstrated in Fig. 11.10a. In addition, it is possible to compress the pulses during storage (as shown in previous section) using an AFC with continuously varying peak spacing. Changing the start frequency of the chirp allows one to choose non-discretized storage times before the memory unit as demonstrated in Fig. 11.10b. If necessary, the emitted pulse's carrier frequency can be set back to the original frequency using the output phase modulator. The described feature could be very useful for synchronization purposes in quantum communication protocols.

On-demand delay

Figure 11.10: **On-demand delaying: (a)** The input phase modulator maps an incoming pulse to a particular segment of the programmed AFC shown in Fig. 11.2 to obtain a desired delay. To achieve delay times of 25 ns, 50 ns and 75 ns, the pulses are mapped onto the segments with -400 MHz, -200 MHz and +200 MHz detuning, respectively and are retrieved after the corresponding storage time, as demonstrated in the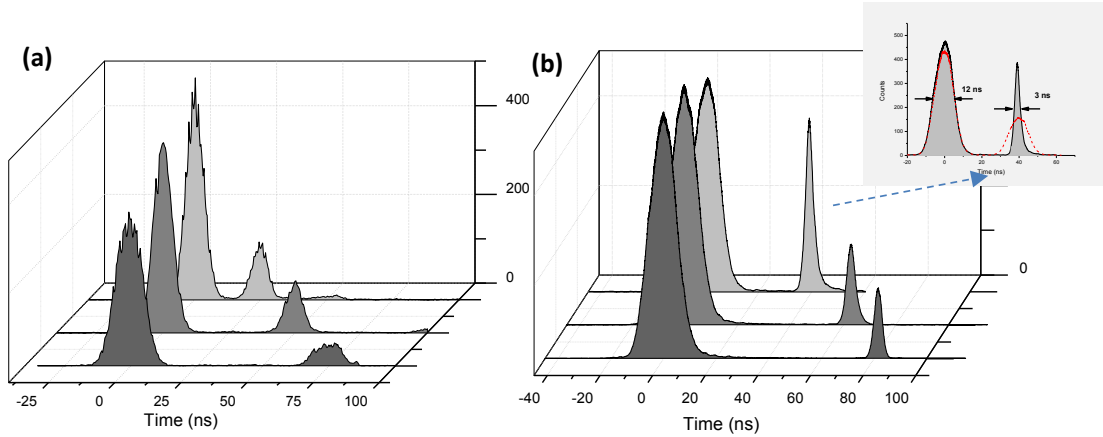 figure. **(b)** A 2 GHz-wide AFC with linearly decreasing peak spacing from 30 MHz to 10 MHz is programmed. The frequency of an incoming pulse is linearly chirped from high to low over nearly 800 MHz. This pulse is mapped onto the programmed AFC, resulting in the emission of a compressed pulse with a compression factor of nearly 4. Varying the start frequency of the chirp maps incoming pulse to different intervals of the AFC, which allows for setting storage time on-demand.

11.1.3   Conclusion

Integrated quantum memories have great potential in future quantum communication networks and in on-chip photonic quantum computers. Employing our device for manipulations of optical pulses at the single quantum level adds another direction to its potential use in advanced quantum information processing applications. In this study, we have shown that our broadband waveguide quantum memory can be turned into a processing unit for arbitrary temporal and spectral manipulations of light. Although in our demonstrations we used weak laser pulses at the few photon level, our approach can work equally well for laser pulses containing less than one photon on average, true single photons, or members of entangled pairs of photons. By combining the large bandwidth capacity of our quantum memory device

with high-speed waveguide electro-optic components, our implementation offers a wide range of pulse manipulation capabilities. Despite limited storage time and efficiency of our current implementation, our approach can open up new avenues for future quantum technologies.

11.2   Supplementary Information

In the following, some experimental details as well as a discussion on the limitations and possible improvements will be given.

Implementation: The main idea of the experiment is to use a cryogenically cooled Ti:Tm:LiNbO$_3$ channel waveguide quantum memory as a processor in conjunction with two commercial LiNbO$_3$ electro-optic modulators placed before and after the memory. Although in our experiments the LiNbO$_3$ phase modulators were outside the cryogenics system and connected to the input and output of the memory by single mode fibers, all components can in principle be implemented on a single chip. This can be achieved by fabricating a long LiNbO$_3$ channel waveguide with Thulium atoms doped only into the central part and electrodes are deposited at the beginning and end of the waveguide.

Material: The fabrication of the Tm:LiNbO$_3$ waveguide and basic spectroscopic properties of Tm atoms in this material have already been reported in [103]. The waveguide used in the experiments has 10.4 mm length and 3.5 μm diameter. The light was butt-coupled into and out of the waveguide using single mode fibers. End-to-end transmission was around 20 %. The crystal temperature was kept around 3.5 K during the experiments, which resulted in nearly 1.5 μs coherence time on the optical transition at 795.5 nm. A magnetic field of 50–130 G, depending on the measurement, was applied along the C$_3$ axis of the crystal in order to activate long-lived nuclear Zeeman spin level. These levels were used as shelving levels to generate persistent AFCs.

AFC Preparation: We prepared each AFC by means of frequency selective optical pumping of an inhomogenously broadened transition of Tm at 795.54 nm wavelength. As detailed

196

previously [58], this is achieved by chirping the laser frequency and simultaneously modulating its intensity. The interaction between the laser light and resonant atoms leads to excitation of the latter. The atoms may subsequently decay to the shelving state. Repeating this processes for a sufficienly long time leads to persistant spectral holes, which forms the troughs of the AFC. The atoms that are not excited by the laser are left in the ground state and form the peaks of the AFC. Adjusting the frequency spacing between the peaks (or throughs) allows to set the re-emission times.

An important point is that in the optical pumping process, reduced absorption at certain frequencies always comes with increased absorption in other frequencies, determined by the level structure. In our case, pumping atoms from one magnetic sub-level to the other magnetic sub-level results in decreased and increased absorption at frequencies whose separation is given by the difference between the excited and ground state splittings. Hence we have to adjust the magnetic field in such a way that the increased absorption and reduced absorption regions match the AFC peaks and troughs. However, this severely limits experiments that require variable peak spacing in the prepared AFC. Therefore, in some experimental configurations, the magnetic fields had to be optimized so that we obtained nearly equal efficiencies from each AFC segment, at the expense of reducing the overall memory efficiency. Typically, the efficiency was reduced by a factor 2–5 from the optimized efficiency of about 0.5–2 %.

As explained in ref. [58], in general, the low efficiencies of our implementation are due to unfavorable relaxation dynamics and a high decoherence rate in our specific sample. Substantial improvement in efficiency is possible by achieving closer to optimal conditions in the Tm doped waveguide fabrication, as discussed in reference [84].

Measurements: In each experimental cycle, optical pumping lasted for 3 ms. After the preparation of an AFC, a 2.2 ms wait time was set to eliminate any fluorescence coming from the excited atoms during the detections of the probe pulses. 12 ns probe pulses were then sent during 5 ms at 2.7 MHz repetition rate. Just before the memory, the pulses were

attenuated down to a mean photon number of 5-40. The retrieved and transmitted pulses were detected by a Si-APD single photon detector with 70% detection efficiency and low dark count rate. The estimated mean photon numbers after the memory were between 0.007 and 0.04 photon per pulse, depending on the experiment. For sufficient detection statistics, each measurement took $0.5 - 2$ minutes. To time-resolve and process the detections, a time-to-digital convertor was used. Strong optical pumping light with 5 to 15 μW peak power was sent from the backward direction, which protects the single photon detector. An optical switch allowed to share the memory output alternately between the optical pumping and probe pulse detections.

Ability to Spectrally Manipulate Pulses Retrieved from the Memory: In most of the pulse manipulations demonstrated, the center frequency or spectral distribution of the pulses are changed by the input phase modulator. The main role of the phase modulator that follows the memory unit is to undo these changes, if necessary. For example, when the pulses with the same carrier frequency are re-ordered in time, their center frequencies are automatically shifted by certain amounts as explained in Section 11.1.2. In this case, using the output phase modulator, the frequency of the re-ordered pulses can be shifted back to their original values.

To demonstrate this capability, we add a FP filter with 80 MHz linewidth and 23 GHz free-spectral range after the output phase modulator. We generate an AFC with 600 MHz bandwidth and 33 MHz peak spacing, leading to 30 ns storage time. We set the transmission window of the filter to the center of the AFC. First, we store pulses with 12 ns duration in the prepared AFC and detect retrieved photons after having set the frequency shift introduced by the output phase modulator to zero, as shown at the top of Fig. 11.11a. Next, we shift the frequency of the transmitted pulse by -200 MHz but leave the echo pulse's frequency unchanged. In this case, while the transmitted pulse is blocked by the filter, the echo passes through as seen in the middle of Fig. 11.11a. Finally we shift the frequency for transmitted
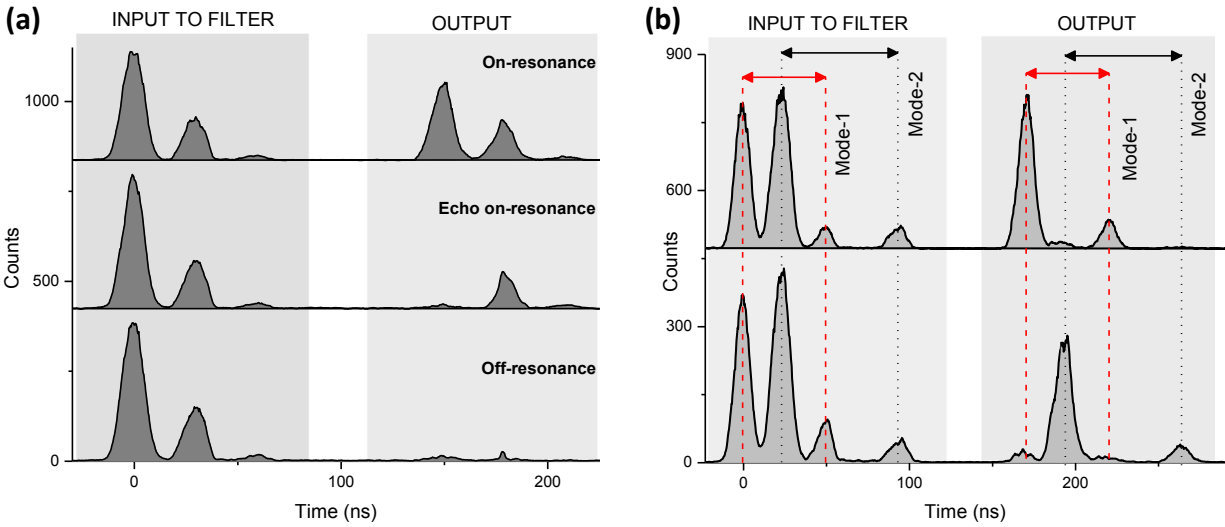
Figure 11.11: **Demonstration of spectral manipulation of the pulses retrieved from the memory unit using the output phase modulator: (a)** Pulses with 12 ns duration are stored in an AFC prepared with 600 MHz bandwidth and 33 MHz peak spacing. They are retrieved after 30 ns as shown on the left hand side column. The retrieved pulses are directed to the output phase modulator preceding the FP filter. The transmission window of the filter is tuned to the center of the AFC. First, no frequency shift is applied to the transmitted pulse nor the echo, and thus both pass through the filter, as shown in the top figure. Next, a 200 MHz frequency shift is applied to the transmitted pulse and then only the echo passes through the filter, as shown in the middle figure. Finally, a 200 MHz frequency shift applied to both and thus both are blocked by the filter. **(b)** Two 25 ns separated input pulses, occupying different frequency modes are simultaneously stored in a 2 segment AFC leading to 50 ns and 70 ns storage times, as shown on the left hand side column of the figure. After recall from the memory, by applying an appropriate frequency shift, we selectively retrieve one of these modes through the filter as shown on the right hand side column

and the echo pulses by 200 MHz allowing the filtering both as in the bottom of Fig. 11.11a.

In another demonstration, we prepare an AFC with two frequency segments, each having 200 MHz bandwidth centered at -100 MHz and +100 MHz detuning. We set the storage times to 50 ns and 70 ns, respectively. Next, we generate two 25 ns separated pulses with -100 MHZ and +100 MHz detuning and store them simultaneously in the prepared AFC. They are retrieved after 50 ns and 70 ns as shown on the left of Fig. 11.11b. We direct them to the phase modulator and the filter. Shifting the frequency by ±200 MHz we can recall

any desired frequency mode after the cavity as illustrated on the right hand side of 11.11b.

These experiments demonstrate that using the output phase modulator, we have full control over the processed pulses in the frequency domain. In particular, any temporal manipulation that requires the spectra of the pulses to be unchanged or spectral re-distribution that protects the encoded coherent information is achieved with the use of this component. On top of these, integrating a FP cavity to our system allows for the capability of on-demand selective recall in the frequency domain, as shown in [106].

Serrodyne Frequency Shifting: The Serrodyne frequency shift technique [81] that was employed in most of the pulse manipulations and AFC preparations is an essential tool in our experiments. The principle of this technique is to introduce a linearly varying time-dependent phase change to the light by applying a saw–tooth voltage to the electro-optic phase modulators. As a result of the linear phase change, the frequency of the light is shifted by the amount of the modulation frequency. The great advantage of this technique is that, in principle, all energy can be transferred to the desired frequency mode without producing higher order side bands. This feature allows fast frequency manipulations of short optical pulses, as demonstrated in our experiments. To generate a sawtooth modulation voltage, we used an arbitrary waveform generator (AWG) with 20 GS/s sampling rate. The output voltage of the AWG is amplified using a high-speed amplifier to achieve the 2π-voltage value of the electro-optic modulators. Our commercial electro-optic phase modulators have 10 GHz bandwidth and feature approximately 3 dB loss. With this system, we are able to shift the light frequency by up to ± 5 GHz. Imperfections in the applied saw tooth waveform cause imperfect energy transfer efficiency to the desired frequency mode. For instance, for a frequency shift of about 1 GHz, typically 80% of the unmodulated light's power is transferred.

Chapter 12

Outlook

There are three directions for our near future research activities. The first direction is to improve our quantum memory's performance. Increasing the memory efficiency and storage time are the primary goals. To achieve these goals, the first step is to test the performance of our existing waveguides in our new cryostat, which reaches temperatures down to a few hundred mK. The second step is to investigate various $Tm:LiNbO_3$ waveguides fabricated with different techniques as well as Thulium doped bulk crystals such as $Tm:LiNbO_3$ and $Tm:YAG$ crystals. In addition, Erbium doped crystals, which feature an optical transition within telecommunication band, will be characterized and studied for quantum state storage purposes.

The second direction is to perform further proof-of-principle experiments towards implementing a quantum repeater. The demonstration of quantum state teleportation into a RE based quantum memory is already planned. The next step is then to realize an elementary link of a quantum repeater, based on frequency multimode AFC quantum memories. The ultimate goal is to perform long distance quantum communication experiments with remote quantum memories.

The third direction is towards more fundamental physics aspects. Extending the storage time of a photon-echo quantum memory using the Zeno effect is one of the ongoing projects carried out in collaboration with Dr. Sergey Moiseev at Kazan Physical-Technical Institute of Russian Academy of Science. Quantum non-demolition measurement via cross phase modulation in a waveguide quantum memory is another ongoing investigation; it is pursued in collaboration with Dr. Christoph Simon's group at the University of Calgary.

Chapter 13

Conclusion

The end of the last century witnessed the emergence of quantum technologies that could underpin the scientific and engineering developments of the near future. Among those technologies, quantum cryptography, which enables unconditional security encryption, is the closest to becoming a part of our daily life. Quantum cryptography (or more precisely quantum key distribution) has already been commercialized to protect information transfer over short point-to-point links. However, quantum communication over more than a few hundred km, for instance between two cities, requires quantum repeaters. A key hardware for quantum repeaters is an optical quantum memory, which is used for the synchronization of quantum data by allowing storage and on-demand retrieval of quantum states of light. A quantum memory must meet certain specifications to be of use in a quantum repeater. For instance, high fidelity quantum state storage, and the preservation of entanglement during storage are essential features required in a quantum memory. In addition, a quantum memory must have a sufficiently long storage time and allow for on-demand recall, high efficiency, large bandwidth and high multimode capacity. Such a quantum memory is highly desirable not only for quantum communication, but also for linear optics quantum computing, which is another rapidly progressing field of research. Finally, a quantum memory needs to be easily integrated into existing communication infrastructure and compatible with existing photonic technologies.

The main goal of this thesis was to develop a quantum memory that is suitable for long distance quantum communication by satisfying the above requirements. Towards this goal, different steps from material characterization to proof-of-principle quantum memory experiments were performed. We developed a broadband quantum memory based on the atomic

frequency comb protocol in a Tm:LiNbO₃ waveguide. We demonstrated that our storage device is suitable for high fidelity quantum state storage and for the storage of photonic entanglement, and, that its large spectral multimode capacity allows for on-demand selective recall in conjunction with standard spectral filters and frequency shifters. In addition, by performing two-photon interference experiments and Bell-State measurements, we demonstrated that our memory preserves not only quantum information, but more generally, the photonic wavefunction in all degrees of freedom, which further confirms its suitability for quantum repeaters and for linear optics quantum computers. Finally, we showed that our integrated device can also be used for arbitrary temporal and spectral manipulation of quantum optical pulses, which could pave the way towards on-chip quantum optical processors. Despite this large number of new achievements, much work remains before our quantum memories meet all requirements for a quantum repeater. Most importantly, storage efficiency and storage time need to be improved, and this will determine our activities over next five years.

This thesis has focused on fundamental aspects of light-atom interaction in view of the development of high-performance quantum memory for light. I hope that it will trigger additional efforts, which will ultimately allow breaking the current distance barrier in quantum communication.

Appendix A

Structure of Tm:LiNbO$_3$ crystal

LiNbO$_3$ is a very important material for photonic applications due to its non-linear properties [96]. Using a LiNbO$_3$ crystal as host crystal for rare-earth ions offers attractive possibilities such as waveguide quantum memories as demonstrated in the thesis.
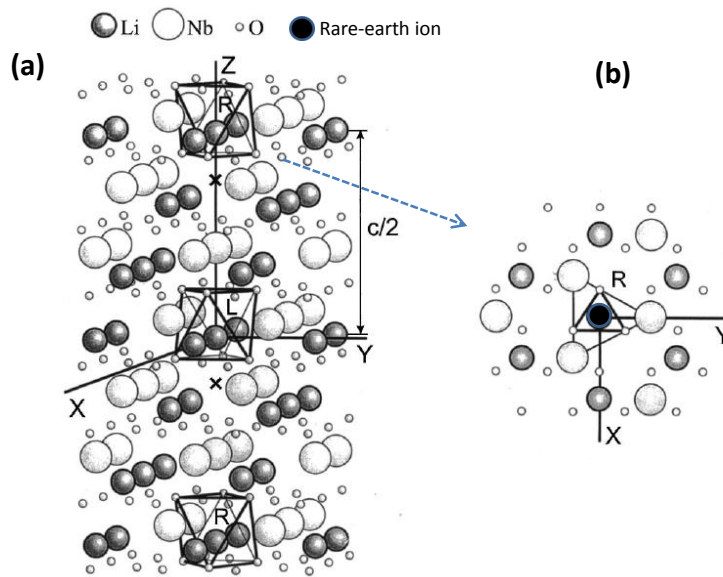

Figure A.1: **Structure of a rare-earth doped Tm:LiNbO$_3$: (a)** The ideal lattice of LiNbO$_3$. **(b)** Illustration of local C$_3$ symmetry for the nearest surroundings of a rare-earth ion doped into the Tm:LiNbO$_3$. A projection of three Li, Nb, and O layers on the **XY** plane (perpendicular to c-axis of the crystal) is shown. Image courtesy of Ref. [107]

The LiNbO$_3$ crystal belongs to the C$_{3v}^6$ space group [108]. Its elementary unit cell posses rhombohedral structure, which contains two LiNbO$_3$ molecules. Fig. A.1a shows an ideal lattice of LiNbO$_3$. As can be seen from the figure, the lattice is composed of planar layers of closely packed oxygen ions with small voids between them. These voids are filled by Li$^+$ and Nb^{+5} ions [107].

When rare-earth ions with triple charge like Tm^{+3} are doped into a LiNbO$_3$ crystal,

these ions substitute Li^+ ions, which are situated along the c-axis [108]. For low doping concentrations, these ions generate local C_3 (axial) symmetry centers as illustrated in Fig. A.1b. As seen from the figure, a $\pi/3$ rotation around the symmetry axis results in an identical configuration. In our experiments (performed with a $LiNbO_3$ waveguide), the magnetic field, which activates long-lived nuclear Zeeman sublevels, was applied along the symmetry axis, i.e c-axis of the crystal.

Bibliography

[1] N. Gisin and R. Thew. Quantum communication. *Nature Photonics*, 1:165–171, 2007.

[2] N. Gisin, G. Ribordy, W. Tittel, and H. Zbinden. Quantum cryptography. *Rev. Mod. Phys.*, 74, January 2002.

[3] H. J. Briegel, W. Dür, J. I. Cirac, and P. Zoller. Quantum repeaters : The role of imperfect local operations in quantum communication. *Phys. Rev. Let.*, 81:5932–5935, 1998.

[4] N. Sangouard, C. Simon, H. de Riedmatten, and N. Gisin. Quantum repeaters based on atomic ensembles and linear optics. *Rev. Mod. Phys.*, 83(1):33–80, 2011.

[5] H. J. Kimble. The quantum internet. *Nature*, 453:1023–1030, 2008.

[6] A. I. Lvovsky, W. Tittel, and B. C. Sanders. Optical quantum memory. *Nature Photonics*, 3(12):706–714, 2009.

[7] C. Simon et al. Quantum memories. A review based on the european integrated project. *Eur. Phys. J. D*, 58(1), 2010.

[8] W. Tittel and G. Weihs. Photonic entanglement for fundamental tests and quantum communication. *Quantum Inf. Comput.*, 1(2):3–56, 2001.

[9] D. Bouwmeester, A. K. Ekert, and A. Zeilinger (eds). *The physics of quantum Information.* Springer, 2000.

[10] N. Gisin, R. Ribordy, W. Tittel, and H. Zbinden. Quantum cryptography. *Rev. Mod. Phys.*, 74, 2002.

[11] V. Scarani, S. Iblisdir, and N. Gisin. Quantum cloning. *Rev. Mod. Phys.*, 77:1225–1256, 2005.

[12] N. J. Cerf and J. Fiurasek. Optical quantum cloning–a review. *Progress in Optics*, 49, 2005.

[13] W. K. Wootters and W. H. Zurek. A single quantum cannot be cloned. *Nature*, (802–803), 1982.

[14] V. Buzek and M. Hillery. Quantum copying : Beyond the no-cloning theorem. *Phys. Rev. A*, 54:1844–1852, 1996.

[15] S. Massar and S. Popescu. Optimal extraction of information from finite quantum ensembles. *Phys. Rev. Lett.*, 74(8), 1995.

[16] J. Bell. On the Einstein Rosen Padolsky paradox. *Physics*, 1(3):195–200, 1964.

[17] J. Longdell. Entanglement on ice. *Nature*, 469:475–476, 2011. News and Views.

[18] J. Clauser, M. Horne, A. Shimony, and R. Holt. Proposed experiment to test local hidden-variable theories. *Phys. Rev. Lett.*, 23(15):880, 1969.

[19] N. Lutkenhaus, J. Calsamiglia, and K. A. Suominen. Bell measurements for teleportation. *Phys. Rev. A*, 59:3295–3300, 1999.

[20] D. Bouwmeester et al. Experimental quantum teleportation. *Nature*, 390:575–579, 1997.

[21] M. Zukowski, A. Zeilinger, M. A. Horne, and A. K. Ekert. Event-ready detectors bell experiment via entanglement swapping. *Phys. Rev. Lett.*, 71:4287–4289, 1993.

[22] L. Duan, M. D. Lukin, J. I. Cirac, and P. Zoller. Long-distance quantum communication with atomic ensembles and linear optics. *Nature*, 414:413–418, 2001.

[23] C. Simon et al. Quantum repeaters with photon pair sources and multimode memories. *Phys. Rev. Lett.*, 98(190503), 2007.

[24] M. P. Hedges, J. J. Longdell, Y. Li, and M. J. Sellars. Efficient quantum memory for light. *Nature*, 465:1052–1056, 2010.

[25] M. Hosseini, B. M. Sparkes, G. Campbell, P. K. Lam, and B. Buchler. High efficiency coherent optical memory with warm rubidium vapour. *Nat. Commun.*, 2(174), 2010.

[26] J. Nunn et al. Multimode memories in atomic ensembles. *Phys. Rev. Lett.*, 101(260502), 2008.

[27] M. Mitsunaga. Time-domain optical data storage by photon echo. *Opt. Quantum Electron.*, 24(10):1137–1150, 1992.

[28] Y. C. Sun. *Spectroscopic Properties of Rare Earths in Optical Materials, Chapter 7 : Rare Earth Materials in Optical Storage and Data Processsing Applications*, volume 83 of *Material Science*. Springer, 2005.

[29] I. D. Abella, N. A. Kurnit, and S. R. Hartmann. Photon echoes. *Phys. Rev. Lett.*, 141:391–406, 1966.

[30] S. A. Moiseev and S. Kröll. Complete reconstruction of the quantum state of a single-photon wave packet absorbed by a doppler-broadened transition. *Phys. Rev. Lett.*, 87(17), 2001.

[31] M. Nilsson and S. Kröll. Solid state quantum memory using complete absorption and re-emission of photons by tailored and externally controlled inhomogeneous absorption profiles. *Opt. Commun.*, 247(393), 2005.

[32] A. L. Alexander, J. J. Longdell, M. J. Sellars, and N. B. Manson. Photon echoes produced by switching electric fields. *Phys. Rev. Lett.*, 96(043602), 2006.

[33] B. Kraus et al. Quantum memory for nonstationary light fields based on controlled reversible inhomogeneous broadening. *Phys. Rev. A*, 73(020302), 2006.

[34] W. Tittel et al. Photon-echo quantum memory in solid state systems. *Laser and Photon. Rev.*, 4(2):244–267, 2010.

[35] G. Hétet et al. Electro-optic quantum memory for light using two-level atoms. *Phys. Rev. Lett.*, 100(023601), 2008.

[36] G. Hétet et al. Photon echoes generated by reversing magnetic field gradients in a rubidium vapor. *Opt. Lett.*, 33(20), 2008.

[37] S. A. Moiseev and W. Tittel. Optical quantum memory with generalized time-reversible atom-light interaction. *New J. Phys.*, 13(063035), 2011.

[38] N. Sangouard, C. Simon, M. Afzelius, and N. Gisin. Analysis of a quantum memory for photons based on controlled reversible inhomogeneous broadening. *Phys. Rev. A*, 75(032327), 2007.

[39] M. Afzelius, C. Simon, H. de Riedmatten, and N. Gisin. Multimode quantum memory based on atomic frequency combs. *Phys. Rev. A*, 79(052329), 2009.

[40] H. de Riedmatten, M. Afzelius, M. U. Staudt, C. Simon, and N. Gisin. A solid-state light -matter interface at the single-photon level. *Nature*, 456:773–777, 2008.

[41] W. H. Hesselink and D. A. Wiersma. Picosecond photon echoes stimulated from an accumulated grating. *Phys. Rev. Lett.*, 43:1991–1994, 1979.

[42] V. Damon, M. Bonarota, A. Louchet-Chauvet, T. Chanelière, and J. L. Le Gouët. Revival of silenced echo and quantum memory for light. *New. J. Phys.*, 13(093031), 2011.

[43] D. L. McAuslan et al. Photon-echo quantum memories in inhomogeneously broadened two-level atoms. *Phys. Rev. A*, 84(022309), 2011.

[44] M. Fleischhauer and M. D. Lukin. Dark-state polaritons in electromagnetically induced transparency. *Phys. Rev. Lett.*, 84(5094), 2000.

[45] I. Novikova, R. L. Walsworth, and Y. Xiao. EIT-based slow and stored light in warm atoms. *Laser and Photon. Rev.*, 6(3):333, 2011.

[46] K. J. Boller, A. Imamoglu, and S. E. Harris. Observation of electromagnetically induced transparency. *Phys. Rev. Lett.*, 66(2593), 1991.

[47] L. V. Hau, S. E. Harris, Z. Dutton, and C. Behroozi. Light speed reduction to 17 metres per second in an ultracold atomic gas. *Nature*, pages 594–598, 1999.

[48] M. D. Eisaman et al. Electromagnetically induced transparency with tunable single-photon pulses. *Nature*, 438:837–841, 2005.

[49] D. Hockel and O. Benson. Electromagnetically induced transparency in cesium vapor with probe pulses on the single photon level. *Phys. Rev. Lett.*, 105(153605), 2010.

[50] T. Chanelière et al. Storage and retrieval of single photons transmitted between remote quantum memories. *Nature*, 438:833–837, 2005.

[51] K. S. Choi, H. Deng, J. Laurat, and H. J. Kimble. Mapping photonic entanglement into and out of a quantum memory. *Nature*, 452(67), 2008.

[52] M. Mücke et al. Electromagnetically induced transparency with single atoms in a cavity. *Nature*, 465:755–758, 2010.

[53] A. E. Kozhekin, K. Molmer, and E. Polzik. Quantum memory for light. *Phys. Rev. A*, 62(033809), 2000.

[54] J. Nunn et al. Mapping broadband single-photon wave packets into an atomic memory. *Phys. Rev. A*, 75(011401), 2007.

[55] A. V. Gorshkov, A. Andre, M. D. Lukin, and A. Sorensen. Photon storage in lambda-type optically dense atomic media 2 : Free-space model. *Phys. Rev. A*, 76(033805), 2007.

[56] K. F. Reim et al. Towards high-speed optical quantum memories. *Nature Photonics*, 4:218–221, 2010.

[57] J. J. Longdell, E. Fraval, M. J. Sellars, and N. B. Manson. Stopped light with storage times greater than one second using electromagnetically induced transparency in a solid. *Phys. Rev. Lett*, 95(063601), 2005.

[58] E. Saglamyurek et al. Broadband waveguide quantum memory for entangled photons. *Nature*, 469(513), 2011.

[59] K. F. Reim et al. Single–photon–level quantum memory at room temperature. *Phys. Rev. Lett.*, 107(053603), 2011.

[60] I. Usmani, M. Afzelius, H. de Riedmatten, and N. Gisin. Mapping multiple photonic qubits into and out of one solid-state atomic ensemble. *Nat. Commun.*, 1(12), 2010.

[61] M. Bonarota, J. L. Le Gouët, and T. Chanelière. Highly multimode storage in a crystal. *New. J. Phys.*, 13(013013), 2011.

[62] C. Clausen et al. Quantum storage of photonic entanglement in a crystal. *Nature*, 469:508–511, 2011.

[63] H. Zhang et al. Preparation and storage of frequency-uncorrelated entangled photons from cavity-enhanced spontaneous parametric downconversion. *Nature Photonics*, 5:628–632, 2011.

[64] K. Jensen et al. Quantum memory for entangled continuous-variable states. *Nat. Phys.*, 7:13–16, 2011.

[65] T. Chanelière, J. Ruggiero, M. Bonarota, M. Afzelius, and J. L. Le Gouët. Efficient light storage in a crystal using an atomic frequency comb. *New. J. Phys.*, 12(023025), 2010.

[66] M. Tian, D. Vega, and J. Dilles. Spatial configuration for atomic comb based quantum memory. HBSM 2012 workshop, Tübingen, Germany, August 27-30, 2012.

[67] M. Afzelius and C. Simon. Impedance-matched cavity quantum memory. *Phys. Rev. A*, 82(022310), 2010.

[68] S. A. Moiseev, S. N. Andrianov, and F. F. Gubaidullin. Efficient multimode quantum memory based on photon echo in an optimal QED cavity. *Phys. Rev. A*, 82(022311), 2010.

[69] M. Afzelius et al. Demonstration of atomic frequency comb memory for light with spin-wave storage. *Phys. Rev. Lett.*, 104(040503), 2010.

[70] N. Timoney, B. Lauritzen, I. Usmani, M. Afzelius, and N. Gisin. Atomic frequency comb memory with spin-wave storage in Eu^{3+}:Y_2SiO_5. *J. Phys. B. : At. Mol. Opt. Phys.*, 45(45124001), 2012.

[71] B. Lauritzen, J. Minar, H. de Riedmatten, M. Afzelius, and N. Gisin. Approaches for a quantum memory at telecommunication wavelengths. *Phys. Rev. A*, 83(012318), 2011.

[72] I. Iakopov and A. S. Sorensen. An efficient quantum memory based on two-level atoms. *arXiv:1301.0705*, 2012.

[73] R. M. Macfarlane and R. M. Shelby. *Spectroscopy of Solids Containing Rare Earth Ions, Chapter 2 :Coherent Transient and Holeburning Spectroscopy.* Elsevier, Amsterdam, 1987.

[74] Editors, G. Liu, and B. Jacquier. *Spectroscopic Properties of Rare Earths in Optical Materials.* Springer, Berlin, 2005.

[75] C. W. Thiel, Y. Sun, T. Böttger, W. R. Babbitt, and R. L. Cone. Optical decoherence and persistent spectral hole burning in Tm:LiNbO$_3$. *J. Lumin.*, 130(9), 2010.

[76] P. Goldner. Hyperfine structure of Tm in YAG for quantum storage applications. *Optical Materials*, 28:649–654, 2006.

[77] C. W. Thiel, Y. Sun, T. Böttger, W. R. Babbitt, and R. L. Cone. Optical decoherence, spectral diffusion and hyperfine structure of Tm:LiNbO$_3$ at 794 nm for quantum computing and signal processing applications. HBSM-09 Conference, Palm Cove, Australia, June 22-27, 2009, 2009.

[78] M. Bonarota, J. Ruggiero, J. L. Le Gouët, and T. Chanelière. Efficiency optimization for atomic frequency comb storage. *Phys. Rev. A*, 81(033803), 2010.

[79] R. R. Reibel, Z. W. Barber, J. A. Fischer, M. Tian, and W. R. Babbitt. Broadband demonstrations of true-time delay using linear sideband chirped programming and optical coherent transients. *J. Lumin.*, 107:62–74, 2004.

[80] C. J. Renner, R. R. Reibel, M. Tian, T. Chang, and W. R. Babbitt. Broadband photonic arbitrary waveform generation based on spatial-spectral holographic materials. *J. Opt. Soc. Am. B*, 24(12), 2007.

[81] L. M. Johnson and C. H. Cox. Serrodyne optical frequency translation with high sideband suppresion. *J. Lightwave Technol.*, 6(1), 1988.

[82] B. Lauritzen, S. R. Hastings-Simon, H. de Riedmatten, M. Afzelius, and N. Gisin. State preparation by optical pumping in erbium-doped solids using stimulated emission and spin mixing. *Phys. Rev. A*, 78(043402), 2008.

[83] G. Gorju et al. Stimulated optical pumping in a Tm^{3+}:YAG crystal. *J. Phys. : Condens. Matter*, 19(386226), 2007.

[84] C. W. Thiel, Y. Sun, R. M. Macfarlane, and T. Böttger. Rare-earth-doped $LiNbO_3$ and KTP for waveguide quantum memories. *J. Phys. B: At. Mol. Opt. Phys*, 45(124013), 2012.

[85] S. Y. Lan et al. A multiplexed quantum memory. *Opt. Express*, 17:13639–13645, 2009.

[86] Y. S. Bai and T. W. Mossberg. Photon-echo optical pulse compression. *Appl. Phys. Lett.*, 45:1269–1271, 1984.

[87] W. R. Babbitt and T. W. Mossberg. Time-domain frequency selective optical-data storage in a solid material. *Opt. Commun.*, 65:185–188, 1988.

[88] M. Mitsunaga and N. Uesugi. 248-bit optical data storage in Eu^3:$YAlO_3$ by accumulated photon echoes. *Opt. Lett.*, 15:195–197, 1990.

[89] S. Kröll, L. E. Jusinski, and R. Kachru. Frequency-chirped copropagating multiple-bit stimulated-echo storage in Pr^3:$YAlNO_3$. *Opt. Lett.*, 15:195–197, 1991.

[90] S. Kröll and U. Elman. Photon-echo-based logical processing. *Opt. Lett.*, 18(21):1834, 1993.

[91] M. Zhu, W. R. Babbitt, and C. M. Jefferson. Continuous coherent transient optical processing in a solid. *Opt. Lett.*, 20:2514–2516, 1995.

[92] F. R. Graf et al. Data compression in frequency-selective materials using frequency-swept excitation pulses. *Opt. Lett.*, 21:284–286, 1996.

[93] K. D. Merkel and W. R. Babbitt. Optical coherent transient header/data isolation techniques. *Opt. Lett.*, 21:71–73, 1996.

[94] Z. W. Barber, M. Tian, R. R. Reibel, and W. R. Babbitt. Optical pulse shaping using optical coherent transients. *Opt. Express*, 10(20):1145, 2002.

[95] J. O'Brien, A. Furusawa, and J. Vučković. Photonic quantum technologies. *Nature Photonics*, 3:687–695, 2009.

[96] W. Sohler et al. Integrated optical devices in lithium niobate. *Opt. and Photon. News*, 19(1):24–31, 2008.

[97] A. Martin, O. Alibart, M. P. De Micheli, D. B. Ostrowsky, and S. Tanzilli. A quantum relay chip based on telecom integrated optics technology. *New J. Phys.*, 14(2), 2012.

[98] B. Damien et al. Fast path and polarization manipulation of telecom wavelength single photons in lithium niobate waveguide devices. *Phys. Rev. Lett.*, 108(053601), 2012.

[99] M. Hosseini et al. Coherent optical pulse sequencer for quantum applications. *Nature*, 461(10), 2009.

[100] I. Novikova, R. L. Walsworth, and Y. Xiao. EIT-based slow and stored light in warm atoms. *Laser Photon. Rev.*, 2011.

[101] K. F. Reim et al. Multipulse addressing of a raman quantum memory: Configurable beam splitting and efficient readout. *Phys. Rev. Lett.*, 108(263602), 2012.

[102] B. M. Sparkes et al. Precision spectral manipulation: A demonstration using a coherent optical memory. *Phys. Rev. X*, 2(021011), 2012.

[103] N. Sinclair et al. Spectroscopic investigations of a Ti:Tm:LiNbO$_3$ waveguide for photon-echo quantum memory. *J. Lumin.*, 130(9):1586–1593, 2010.

[104] E. Saglamyurek et al. Conditional detection of pure quantum states of light after storage in a Tm-Doped waveguide. *Phys. Rev. Lett.*, 108(083602), 2012.

[105] S. A. Moiseev and W. Tittel. Temporal compression of quantum-information-carrying photons using a photon-echo quantum memory approach. *Phys. Rev. A*, 82(012309), 2010.

[106] N. Sinclair et al. On-demand retrieval of weak coherent pulses from a frequency multimode quantum memory. *In preparation*, 2013.

[107] G. Malovichko, V. Grachev, E. Kokanyan, and O. Schirmer. Axial and low-symmetry centers of trivalent impurities in lithium niobate : Chromium in congruent and stoichiometric crystals. *Phys. Rev. B*, 59(14), 1999.

[108] T. Nolte, T. Pawlik, and J. M. Spaeth. EPR study of Er^{3+} in congruent lithium niobate. *Solid State Comm.*, 104(9):535–539, 1997.